UNIVERSITY OF SOUTHAMPTON

Magnetic Properties of Rare Earth Superlattices

Caroline Jane Theresa Wilkins

A thesis submitted for the qualification of Doctor of Philosophy

DEPARTMENT OF PHYSICS AND ASTRONOMY

March 2001

UNIVERSITY OF SOUTHAMPTON

ABSTRACT

FACULTY OF SCIENCE

DEPARTMENT OF PHYSICS AND ASTRONOMY

Doctor of Philosophy

MAGNETIC PROPERTIES OF RARE EARTH SUPERLATTICES

by Caroline Jane Theresa Wilkins

Single-crystal Tm/Y and Tm/Lu superlattices have been grown using molecular beam epitaxy and their chemical structures have been determined using X-ray diffraction. Magnetisation measurements have revealed a more complicated phase diagram than that of pure Tm. Application of a field along the c-direction gave rise to an extra transition, and transitions were detected for the superlattices when the field was applied along the b-axis. In neutron diffraction studies, c-axis longitudinally modulated magnetic structures were found for both Tm/Y and Tm/Lu, which propagate coherently through the non-magnetic layers. In the case of Tm/Lu superlattices, there is evidence for ordering of the basal plane components.

Acknowledgements

I would like to thank my supervisor, Prof. Brian Rainford, under whose guidance it has been a pleasure and a privilege to study. I am grateful to Prof. Peter de Groot, Dr. Mohand Oussena and Dr. Mike Sawicki for useful discussions and to EPSRC for funding this research. My collaborator and co-experimenter, Dr. Jon Goff, has been a considerable source of input to this research. His expertise was essential to the X-ray and neutron diffraction experiments and his guidance and support throughout is highly appreciated by the author.

I would like to thank Dr. Mike Wells and Dr. Roger Ward for growing the good quality superlattice samples that feature in this research.

I have been extremely fortunate to receive a considerable amount of personal support. I would like to thank my friends and my family, in particular Vicki Platt, Mike Ternasky, Hazel Green, Minstrel, Shelley, Misty, Lord Ashby, William and Norma Wilkins, Helen and Jeff Knight, Malcolm and Jeni Wilkins. I would also like to acknowledge my early mentors, Mr. White (a great teacher is never forgotten), Donald Suskins (who once told a little girl that she should become a physicist) and the teachers and lecturers who have patiently answered my questions and given the gift of insight into the physical Universe.

Above all, I would like to thank my partner, Dr. Peter Hodges, who believes in me and supports everything I do. In a chaotic world, he is my rock and my light.

Contents

CHAPTER 1. MAGNETIC PROPERTIES OF RARE EARTH SUPERLATTICES 6

Introduction *6*
1.1 RARE EARTH MAGNETISM 8
1.1.1 Magnetic Moment of a Thulium atom *8*
1.1.2 The Crystal Field *10*
1.1.3 The Exchange Interaction *12*
1.1.4 Magnetic Order in Rare Earths *17*
1.1.5 The Magnetic Behaviour of Thulium *19*
1.2 SUPERLATTICES 21
1.2.1 Superlattice Growth *21*
1.2.2 Crystallographic properties of Tm, Y and Lu *23*
1.2.3 Giant Magneto-resistance *24*
1.3 RARE EARTH SUPERLATTICES 26
1.3.1 Gd/Y Superlattices *26*
1.3.2 Dy/Y Superlattices *29*
1.3.3 Ho/Y Superlattices *30*
1.3.4 Er/Y Superlattices *31*
1.3.5 Competing magnetic order in rare earth/rare earth Superlattices *31*

CHAPTER 2. EXPERIMENTAL TECHNIQUES 33

Introduction *33*
2.1 MAGNETIZATION 34
2.1.1 Introduction *34*
2.1.2 VSM : Principles of Operation *34*
2.1.3 VSM measurements *35*
2.1.4 VSM maintenance *37*
2.2 X-RAY DIFFRACTION 38
2.2.1 X-ray diffraction theory *38*
2.2.2 Instrumentation *40*
2.3 NEUTRON DIFFRACTION 41
2.3.1 Neutron diffraction theory *41*
2.3.2 Neutron diffraction Instrumentation - Zero Field *43*
2.3.3 Neutron diffraction Instrumentation - In Horizontal and Vertical Fields *47*

CHAPTER 3. SAMPLE GROWTH AND STRUCTURAL DETERMINATION 49

Introduction *49*
3.1 SUPERLATTICE GROWTH 50
3.2 XRAY SCATTERING FROM A SUPERLATTICE 52
3.3 EXPERIMENTAL DETAILS 55
3.4 X-RAY RESULTS 57
3.5 CONCLUSIONS 64

CHAPTER 4. MAGNETIC PHASE TRANSITIONS OF TM SUPERLATTICES 65

Introduction *65*
4.1 VSM MEASUREMENTS 66
4.2 SAMPLE HOLDER CONTRIBUTIONS 68
4.3 MAGNETISATION RESULTS 71
4.4 CONCLUSIONS 80

CHAPTER 5. MAGNETIC STRUCTURE DETERMINATION USING NEUTRON DIFFRACTION 81

Introduction *81*
5.1 ZERO FIELD NEUTRON DIFFRACTION 82
5.1.1 Experimental Details *82*
5.1.2 [00L] scans *84*

5.1.3 [10L] scans *88*
5.2 C-FIELD NEUTRON DIFFRACTION 95
5.2.1 Experimental Details *95*
5.2.2 20L measurements *96*
5.2.3 00L measurements *100*
5.3 B-FIELD NEUTRON DIFFRACTION 101
5.3.1 Experimental Details *101*
5.3.2 Results *102*
5.4 CONCLUSIONS 105

CHAPTER 6. CONCLUSIONS **107**

Introduction *107*
6.1 SUMMARY OF RESEARCH 108

APPENDIX A: MAGNETISATION RESULTS **112**

REFERENCES **151**

Chapter 1

Magnetic Properties of Rare Earth Superlattices

This chapter introduces rare earth superlattices. Section 1.1 discusses rare earth magnetism , specifically the magnetic behaviour and structures of Tm. Section 1.2 provides general information about superlattices and the crystallographic properties of the bulk elements used in the superlattice samples for the studies presented in later chapters. Section 1.3 summarises some of the previous research on rare earth superlatiices.

Introduction

Rare earth elements form a part of the periodic table in which the 4*f* shell is filled. Rare earth metals distinguish themselves from other members of the periodic table by forming fascinating magnetic structures. Rather than simply forming ferromagnetic or anti-ferromagnetic magnetic structures, rare earths exhibit structures such as helix, cone, fan and longitudinally modulated sinusoid [1]. These complex structures are the result of their strong magnetocrystalline anisotropy arising from the high angular momentum and spin-orbit coupling of the unfilled 4*f* shell, combined with the long range RKKY exchange mechanisms. The 4*f* wave-functions are highly anisotropic, see Fig. 1-1 [2];

Much of rare earth phenomena arises from the relative energies of the 4f, 5d and 6s electron levels and the angular momentum of electrons in these states. The 5d and 6s levels fall at a lower energy than the 4f, but the electron shells corresponding to 5d and 6s are physically outside the 4f shell. This means that, across the rare earth series, the 5d and 6s occupancy remains constant whilst the 4f states fill up.

The $[Xe]4f^n5d^26s^1$ outer electron structure that the rare earths share accounts for their chemical similarity and, hence, the difficulty associated with separation of elements. Rare earths gained their title from the difficulty involved in extracting pure samples, despite an abundance of the naturally occurring elements. The spins of the 4f electrons in a crystal are coupled via a super-exchange mechanism mediated by the 5d and 6s conduction electrons known as the Ruderman-Kittel-Kasuya-Yosida (RKKY) [3,4,5] interaction.

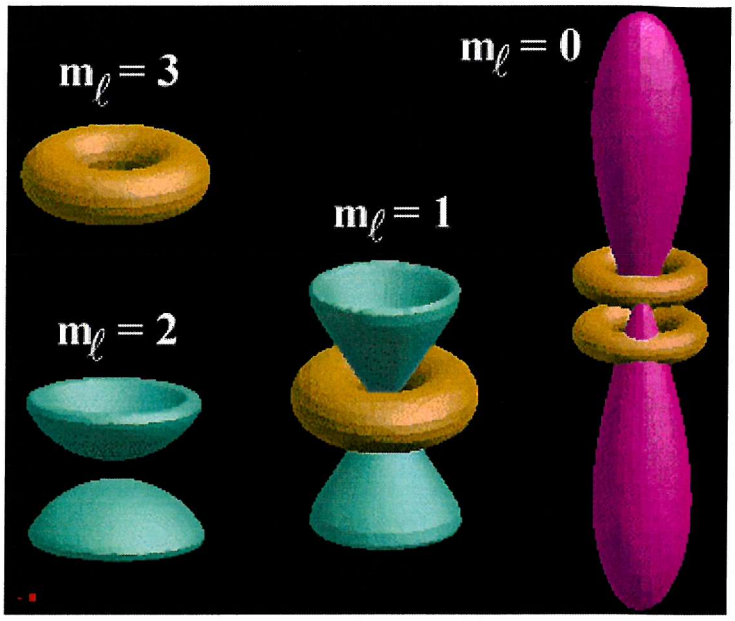

Figure 1-1. The angular variation of the 4f wavefunctions

During the 1950s, F.H. Spedding and collaborators at Iowa State University developed a technique to separate the rare earth elements and produce pure single crystals [6]. Around the same time, the techniques of neutron scattering were advancing and intense beams of neutrons from research reactors became available. These two developments led to the study of rare earths with neutron techniques and produced important data on their novel magnetic structures.

More recently (1980s) molecular beam epitaxy technology has enabled the growth of rare earth multilayers. This has typically involved alternating the growth of a number of atomic layers of rare earth element with a number of layers of chemically and electronically similar elements such as yttrium or lutetium. This process has the effect of introducing an artificial periodicity and imposing epitaxial strain on the rare earth. This thesis explores the structural and magnetic properties of a range of Tm/Y and Tm/Lu superlattices.

1.1 Rare Earth Magnetism

Since the $4f$ shell is localised rather deep in the atom, inside the filled $5p^6$ shell, it retains much of its atomic character. We begin with a brief description of the Hund's rule ground state, taking Tm as an example, then consider how the crystalline environment perturbs this state, leading to a description of the magnetic anisotropy in a solid. The exchange coupling between magnetic ions (Section 1.1.3) is responsible for magnetic order.

1.1.1 Magnetic Moment of a Thulium atom

The partly filled 4f shell of thulium is embedded well within the atom and is shielded by the 5s and 5p states from the surroundings. The consequence of this is that Tm has largely atomic properties. Hund's rules may therefore be applied to the 12 4f electrons to find values for the ground state configuration of $Tm^{3+}[4f^{12}]$:

1. The spins of the individual 4f electrons are coupled by the interatomic exchange interaction: $-J\underline{\mathbf{s}}_1.\underline{\mathbf{s}}_2$. The combination of spins, s, that gives the lowest energy (most stable) state is that with the highest value of $\mathbf{S}=\sum_i s_i$

2. The non-central part of the Coulomb interaction combines the angular momentum l_i into the total angular momentum $\mathbf{L}=\sum_i l_i$. If, when the first rule has been satisfied, there are several possible **L** values all having the same **S**, that with the largest value of **L** will be most stable (consistent with the Pauli exclusion principle).

3. The spin-orbit coupling acts to couple l_i and s_i together. If electron shell is greater than half full, J = L+S. If electron shell is less than half full, J = |L - S|. This is due to spin-orbit coupling which is associated with the magnetic field generated by the motion of electrons within the atom.

Hund's 1st rule gives the following value of S for Tm^{3+}:

$$S = 2.(½) = 1$$

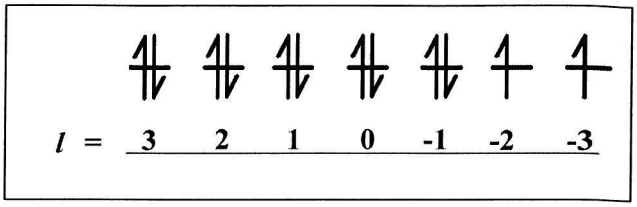

Figure 1-2 Occupation of the 4*f* level for Tm

Hund's 2nd rule gives the following value of L

$$L = (3 + 2 + 1 + 0 - 1 - 2 - 3) + 3 + 2 + 1 + 0 - 1$$
$$= 5$$

As the 4f electron shell is more than half full, Hund's 3rd rule gives the following value of J:

$$J = L + S = 6$$

Values of S, L and J give the Landé factor:

$$g = 1 + \frac{J(J+1) + S(S+1) - L(L+1)}{2J(J+1)}$$

$$g = 7/6$$

The Landé factor for the thulium atom gives it's paramagnetic moment:

$$\mu_J = g\sqrt{J(J+1)}\mu_B = 7.56\mu_B$$

However, for the ground state of Tm, we expect the saturation moment:

$$\mu_S = g\mu_B J$$
$$= (7/6)\mu_B \times 6$$
$$= 7\mu_B$$

This may be compared to the measured high-field value of $7.14\mu_B$ [7] for pure thulium. The discrepancy between the calculated and measured values is explained in terms of polarization of conduction electrons.

1.1.2 The Crystal Field

Having considered the magnetic moment of a single thulium atom, it is appropriate to consider the thulium atom in its crystal environment. The 4*f* electrons of the thulium atom interact with the electric field due to the charge distribution around ions in the crystal. This interaction is known as the crystal field and it has the point symmetry of the crystalline environment. The different (2J+1) components of the Hunds rule ground state $|Jm_J>$ have differently shaped spatial wavefunctions (Fig. 1-1) and therefore charge distributions. These charge distributions have different interaction energies within the anisotropic crystal field potential, and so the (2J+1)-fold degeneracy of the Hund rule state is lifted.

Hunds' third rule, defining total angular momentum in terms of the spin-orbit coupling, does not usually work for transition metals although it is successful for rare earth elements. The difference lies in the relative strengths of the crystal field and spin-orbit coupling. The crystal fields of transition elements dominate spin-orbit coupling and often quench the orbital angular momentum, so that **S** becomes a better measure of magnetic moment than **J**. The partly filled 4f shell of the rare earths is embedded well within the atom and is partly shielded from the effects of the crystal field. The crystal field is therefore less dominant in rare earths than in transition elements and Hunds' third rule remains reliable.

The crystal field splittings due to the raising of the 2J+1 fold degeneracy of the ground state are of the order 10meV for metals, which is significantly smaller than those due to the spin-orbit interaction; as such, the crystal field may be treated as a perturbation. The crystal field contributes to the Hamiltonian:

$$H = H_{CF} + H_{zeeman}$$

where $H_{zeeman} = g\mu_0 B J_z$ and $H_{CF} = \sum_i \sum_{lm} B^m_l O^m_l (J_i)$.

B^m_l are crystal field parameters and $O^m_l (J_i)$ are Stevens operators. For an ion with hexagonal point symmetry, the crystal field is specified by four parameters:

$$H_{CF} = \sum_i \left(\sum_{l=2,4,6} B^0_l O^0_l (J_i) + B^6_6 O^6_6 (J_i) \right)$$

McEwen et al have estimated these parameters for thulium from a detailed study of the excitations and bulk magnetic properties [8]:

$$B^0_2 = -0.096 \text{ meV}$$

$$B^0_4 = 0.0 \text{meV}$$

$$B^0_6 = -0.92 \times 10^{-5} \text{ meV}$$

$$B^6_6 = 8.86 \times 10^{-5} \text{ meV}$$

Considering the lowest order form of this crystal field:

$$H = B^0_2 O^0_2 + H_{Zeeman}$$

$$= B^0_2 (3J_z^2 - J(J+1)) + g\mu_0 B.J_z$$

For zero applied field:

$$\langle H \rangle = B^0_2 (3m_J^2 - J(J+1))$$

$$= -0.092 \ (3m_J^2 - J(J+1)) \qquad (1)$$

It can be seen from (1) that the lowest energy state is achieved when $m_J = \pm 6$. States of the system with lower values of m_J will possess higher energies due to the crystal field. Equation (1) allows one to locate the crystal field levels of thulium. McEwen et al. [8] calculated crystal field levels in thulium as a function of applied field.

1.1.3 The Exchange Interaction

The exchange interaction within the atom leads to the coupling between spins from which Hunds first rule follows. It arises from the Coulomb interaction between electrons, when the Pauli exclusion principle is taken into account. The same type of interaction can exist between electrons on different atoms. This is the origin of magnetic order. The name "exchange" comes from the underlying Pauli principle that electrons must have wave-functions that are anti-symmetric under exchange of space, r_n, and spin, r_s, co-ordinates i.e. no two electrons may have the same set of quantum numbers.

$$\psi(r_1, s_1 : r_2, s_2) = - \psi(r_2, s_2 : r_1, s_1)$$

The total wave function may have a symmetric spatial component and, therefore, an anti-symmetric X_s spin component. Alternatively, the total wave function will have anti-symmetric spatial component and symmetric spin component.

$$\Psi_{total} = \psi_{(symmetric)} X_{s\ (anti\text{-}symmetric)} \text{ OR } \psi_{(anti\text{-}symmetric)} X_{s\ (symmetric)}$$

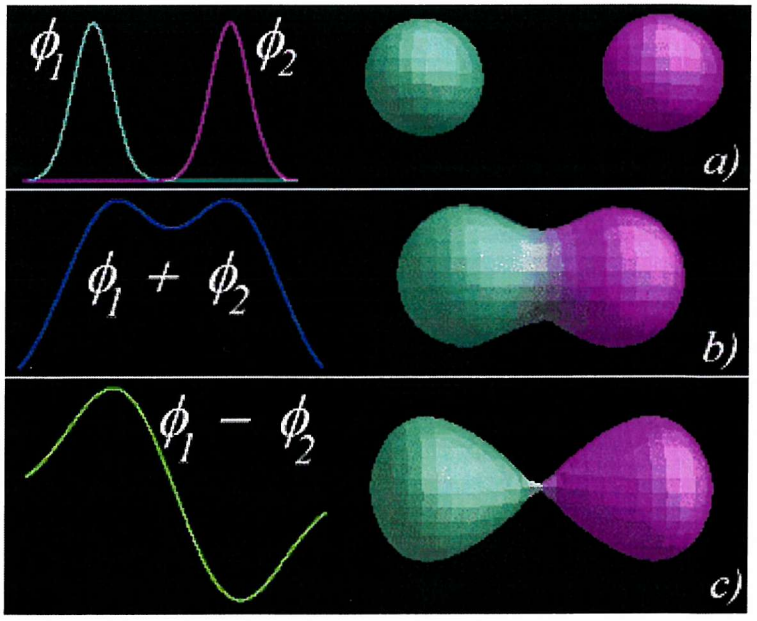

Figure 1-3: Symmetric and anti-symmetric forms of the spatial wave-function component

Figure 1-3 illustrates the symmetric (b) and anti-symmetric (c) forms of the spatial component of the wavefunction of a two electron system (a). The electronic charge distribution is clearly very different in the two cases, with a nodal plane in the

antisymmetric case and an enhancement of charge between the nuclei in the symmetric case.

The normalised spatial wave-function components may be expressed:

$$\Psi_s = \frac{1}{\sqrt{2}}(\phi_1 + \phi_2)$$

$$\Psi_a = \frac{1}{\sqrt{2}}(\phi_1 - \phi_2)$$

The spin components of the wavefunction take the following form:

$$X_s^0 = \frac{1}{\sqrt{2}}\left[|\uparrow\downarrow\rangle + |\downarrow\uparrow\rangle\right]$$

$$X_s^1 = |\uparrow\uparrow\rangle$$

$$X_s^{-1} = |\downarrow\downarrow\rangle$$

$$X_a = \frac{1}{\sqrt{2}}\left[|\uparrow\downarrow\rangle - |\downarrow\uparrow\rangle\right]$$

The total wave-function takes four possible forms corresponding to a spin singlet (S=0) with symmetric spatial component and anti-symmetric spin, $\Psi_s X_a$, and a spin triplet (S=1) with anti-symmetric spatial component and one of three forms of symmetric spin, $\Psi_a X_s$.

$$\Psi_s X_a = \frac{1}{2}(\phi_1 + \phi_2)\left[|\uparrow\downarrow\rangle - |\downarrow\uparrow\rangle\right]$$

$$\Psi_a X_s^1 = \frac{1}{\sqrt{2}}(\phi_1 - \phi_2)\left[|\uparrow\uparrow\rangle\right]$$

$$\Psi_a X_s^0 = \frac{1}{2}(\phi_1 - \phi_2)\left[|\uparrow\downarrow\rangle + |\downarrow\uparrow\rangle\right]$$

$$\Psi_a X_s^{-1} = \frac{1}{\sqrt{2}}(\phi_1 - \phi_2)\left[|\downarrow\downarrow\rangle\right]$$

These results may be substituted into the following expression to give the quantity $\underline{S}_1.\underline{S}_2$ for symmetric and anti-symmetric spins, in order to calculate the relative energies of the states:

$$\underline{S}^2 = (\underline{S}_1 + \underline{S}_2)^2 = \underline{S}_1^2 + \underline{S}_2^2 + 2\underline{S}_1.\underline{S}_2$$

This yields values of +¼ and -¾ for the $\underline{S}_1.\underline{S}_2$ of the triplet and singlet states respectively. The exchange energy of the states is then given by the Heisenberg-Dirac Hamiltonian:

$$H = -J\,\underline{S}_1.\underline{S}_2$$

Clearly the sign of J determines whether the triplet or singlet state lies at the lower energy level. Negative values of J favour anti-parallel (anti-ferromagnetic) alignment of spins.

So far we have not considered the Coulomb interaction:

$$V_C = \int \frac{\rho(r_1)\rho(r_2)}{4\pi\varepsilon_o r_{12}} dr_1 dr_2$$

The Coulomb interaction has a magnitude $\langle \Psi_{tot} | V_C | \Psi_{tot} \rangle$. Ψ_{tot} is a wavefunction which is antisymmetric with respect to interchange of electrons, as it describes Fermions.

Let's now consider the Coulomb interaction for the two possible cases where $\Psi_{tot} = \Psi_s X_a$ or $\Psi_a X_s$:

i) symmetric spin wavefunction

$$\langle \Psi_a X_s | V_C | \Psi_a X_s \rangle$$

ii) antisymmetric spin wavefunction

$$\langle \Psi_s X_a | V_C | \Psi_s X_a \rangle$$

Now V_C makes no mention of spin, but the charge distributions are very different (Fig 1-3) in the two cases, so the Coulomb energies are different too. We therefore expect to get an energy splitting for the singlet and triplet states (Fig 1-4). The size of this splitting can be modeled by an effective interaction proportional to $S_1.S_2$ since this parameter is different for the singlet and triplet states.

The point is that V_C is not spin dependant in itself but, because of Pauli, the spin states define the charge distribution, which clearly affects the Coulomb repulsion. Without V_C there would be no exchange interaction.

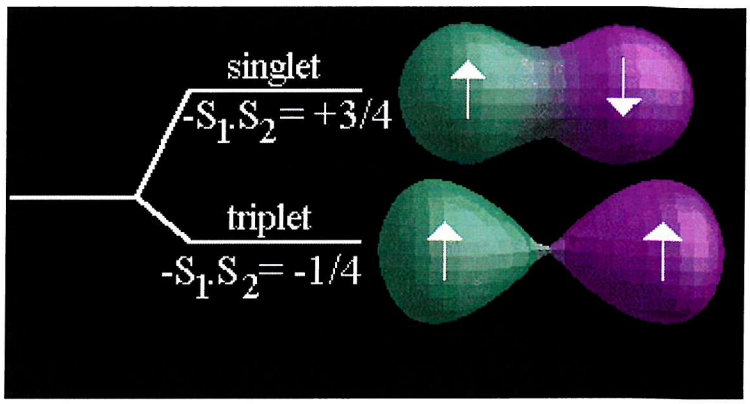

Figure 1-4. Energy splitting by the exchange interaction

The interaction described above is that of direct exchange. It is based on an overlap of wavefunctions on adjacent atoms. The magnetism of rare earths is due to the 4f shells, which are tucked well within the electron configuration and do not overlap with those of neighboring atoms. Direct exchange cannot therefore account for magnetic ordering in rare earth elements. Instead, an indirect exchange mechanism mediated by the conduction electrons is believed to be responsible. As the separation of the indirectly interacting 4f wavefunctions is increased, the sign of J is found to oscillate. This leads to a variety of exotic magnetic structures such as modulated anti-ferromagnetism.

Indirect exchange is the model that emerged from four major sources in the 1950s. In 1951, Zener [9] proposed an exchange interaction between conduction electrons and unfilled inner shell electrons (called s-d interaction). This was followed, in 1954 by a discussion of "Indirect exchange coupling of nuclear magnetic moments by conduction electrons" by Ruderman and Kittel [3], to explain the anomalous broadening of the absorption line in the nuclear magnetic resonance in metals. Kasuya developed the work of Zener and presented a careful investigation of the interaction between conduction electrons and localized *d*-electron spins in 1956 [4]. This included the concept of negative values of the exchange integral. In 1957, Yosida published a discussion of the importance of indirect exchange in CuMn alloys [5].

In honour of those who developed the theory, indirect exchange is known as the RKKY (Ruderman-Kittel-Kasuya-Yosida) interaction. Zener is curiously not similarly credited.

For a spherical fermi surface, the form of the RKKY interaction is long-ranged and oscillatory: $H_{exch} = -\sum_{i>j} J_{ij} \underline{S_i}.\underline{S_j}$ where $J_{ij} = \frac{1}{N}\sum_q J(q) e^{iq.(R_i - R_j)}$

More generally [78], the Fourier transform of the RKKY exchange interaction can be written:

$$J(q) = \frac{1}{\mu_B^2} |I(q)|^2 \chi(q)$$

where I(q) is the Fourier transform of the exchange coupling between the spin $\underline{S}$ of the local moment and the spin $\underline{s}$ of a conduction electron. $\chi(q)$ is the wavevector dependant susceptibility of the conduction electrons which may be obtained from the bandstructures. Many of the rare earths display a peak in $J(q)$ (Fig. 1-5) for a wavevector $\underline{q} = \underline{Q}$ along the [00L] direction. This peak arises from a nesting of flat portions of the Fermi surface, which gives rise to a large contribution to $\chi(q)$.

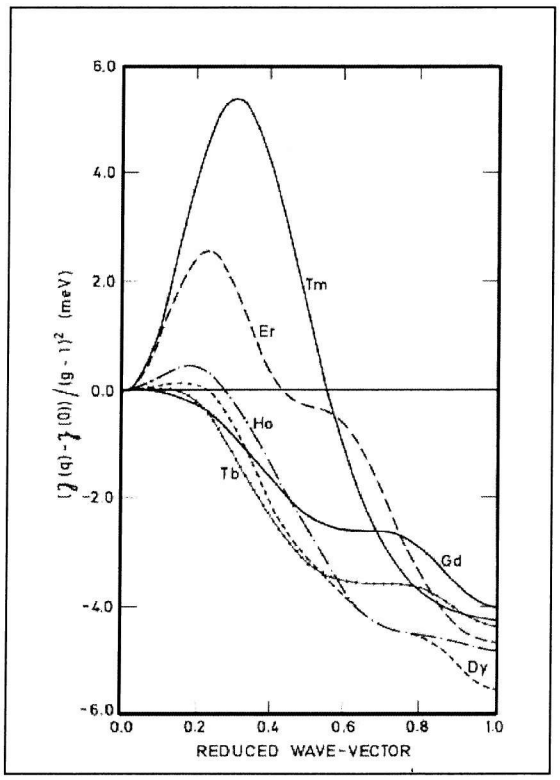

Figure 1-5. The exchange interaction, determined experimentally in the heavy rare earth metals. The magnitude of the peak, which stabilizes the observed periodic magnetic structures, increases monotonically with atomic number [77].

1.1.4 Magnetic Order in Rare Earths

Studies of the rare earth metals have revealed some rich phase diagrams and complicated magnetic structures. For example, terbium is ferromagnetic below 219.5K, paramagnetic above 231.5K and forms a helical magnetic structure in the temperature range 219.5K to 231.5K. These sorts of magnetic structures are largely a result of the RKKY interaction and the crystal field. The characteristic form of the RKKY exchange leads to the modulation of the magnetic order, while the crystal field determines the orientation of the magnetic moments with respect to the crystal *c*-axis. Thus Tb, Dy are easy plane magnets (moments align perpendicular to the *c*-axis) while Er, Tm tend to be easy axis systems (moments align parallel to the *c*-axis).

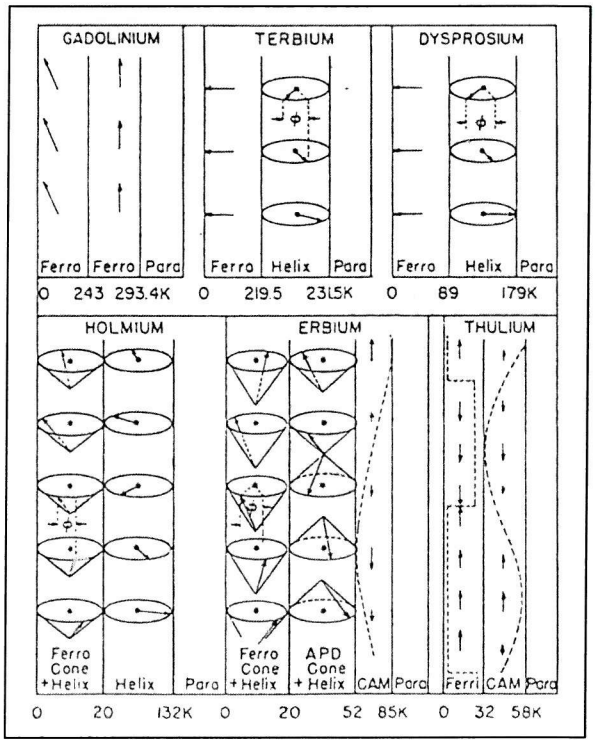

Figure 1-6. Magnetic ordering in the heavy rare earths, as found by neutron diffraction [14]

Magneto-elastic effects can also have an effect on the magnetic order; for example, in determining the temperature at which a helical modulation changes to a ferromagnetic structure. This is particularly important in the discussion of rare earth superlattices because the superlattice structure imposes epitaxial strain on the rare earth, consequently altering the inter-atomic distances and hence the crystal field and RKKY interactions. The phenomena of *Magnetostriction* is two-way: when a magnetic structure changes within a material there may be distortion of the crystal

structure; when a crystal is distorted, it's magnetic structure also may change. An equilibrium state results from competition between the elastic energy, which is quadratic in the strain, and the magnetoelastic energy which is linear in the strain.

1.1.5 The Magnetic Behaviour of Thulium

The magnetic behaviour of thulium is due to the 12 electrons in its 4*f* shell.The magnetic phase diagram has been established using magnetization measurements [7,11] thermal expansion [12], AC susceptibility [11], magnetostriction [12] and neutron diffraction [79].

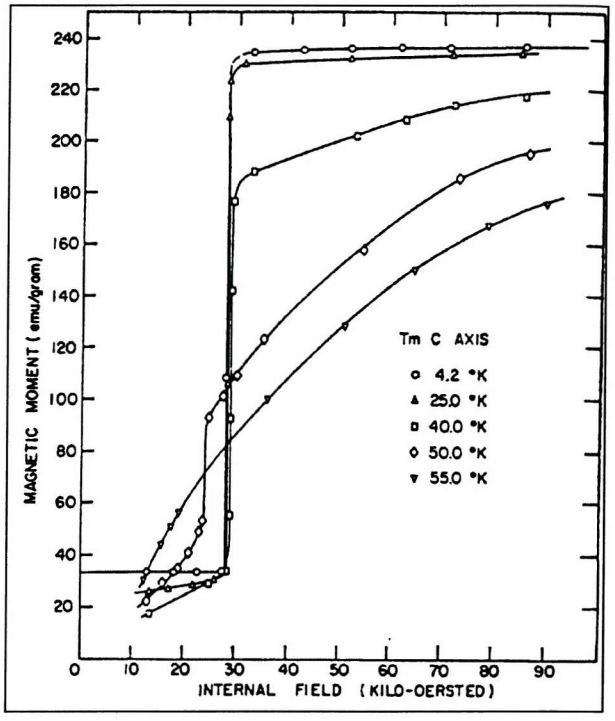

Figure 1-7: Magnetic moment as a function of internal field at fixed temperature for a c-axis Tm crystal [7]

The magnetic structure of thulium metal is dominated by the very strong uniaxial anisotropy arising from the crystal field. Below $T_N \sim 58K$, the moments order in a sinusoidal structure with modulation vector and moment directions both parallel to the crystallographic c-axis. At lower temperatures, the structure squares up and then locks into the ferrimagnetic 4-up/3-down structure below T = 32 K. This takes the form of a seven layer sequence, consisting of 4 atoms with magnetic moments aligned parallel to the c-axis, followed by 3 atoms with moments aligned anti-parallel to the c-axis [13,59]. Since the 4f moment is 7 μ_B [Section 1.1.1], the low temperature spontaneous moment is 1 μ_B[7] . The ferrimagnetic coupling can be overcome by

magnetic fields above 2.8T, yielding a ferromagnetic structure with a saturation magnetization of 7.14 μ_B per atom [7] (see Figure 1-7).

It is this meta-magnetic step that characterizes the magnetic behaviour of thulium at low temperatures and, when plotted against temperature, gives a magnetic phase diagram [Fig. 1-8].

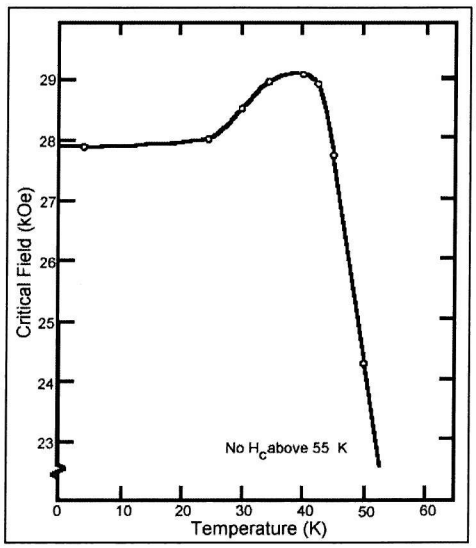

Figure 1-8. Magnetic phase diagram for Tm c-axis fields [7]

The b-axis of bulk thulium remains magnetically hard up to at least 10T [7]. No meta-magnetic transitions are observed and magnetic moments are an order of magnitude smaller than those observed for fields along the c-axis. (See Fig. 1-9) The anisotropy of Tm is due to the very strong crystal field and is related to the B^2_0 crystal field parameter which is dependant upon the c/a lattice spacings ratio [8].

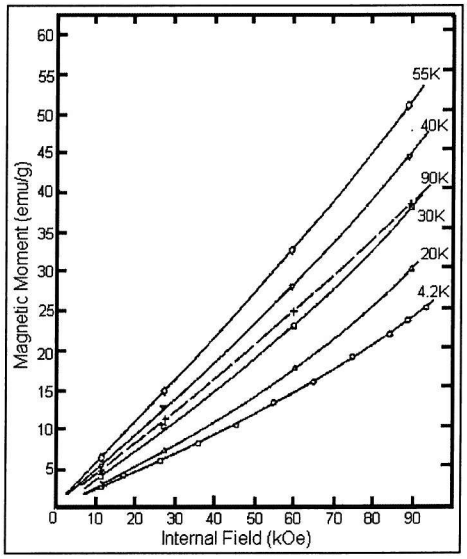

Figure 1-9. Magnetic moment as a function of internal field at fixed temperature for a b-axis Tm crystal [7]

1.2 Superlattices

1.2.1 Superlattice Growth

In 1986, Salamon et al [15] first reported results of measurements made on rare earth superlattices. The superlattice comprised alternating layers of Dy and Y and the emphasis of the report was on the coherency, over several multi-layers, of the incommensurate helical magnetic order.

In recent years, molecular beam epitaxy technology has enabled the growth of a range of rare earth superlattices. This has typically involved alternating the growth of a number of atomic layers of rare earth element with a number of layers of chemically and electronically similar elements such as yttrium or lutetium. This process has the effect of introducing an artificial periodicity and imposing epitaxial strain on the rare earth.

Superlattices are normally represented in the form $(A_xB_y)_z$. This means that a bi-layer consists of x atomic planes of element A followed by y atomic planes of element B; the bi-layer is repeated z times.

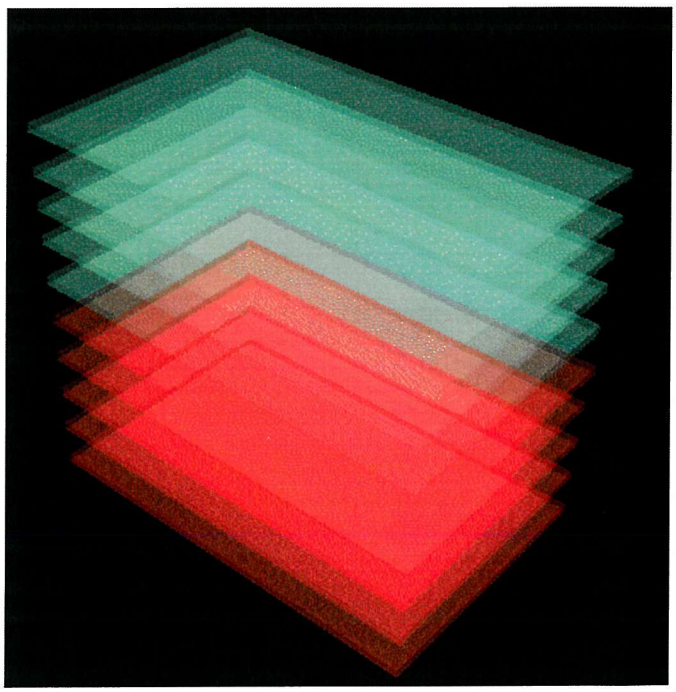

Figure 1-10. The atomic planes of magnetic and non-magnetic elements are layered to create a superlattice

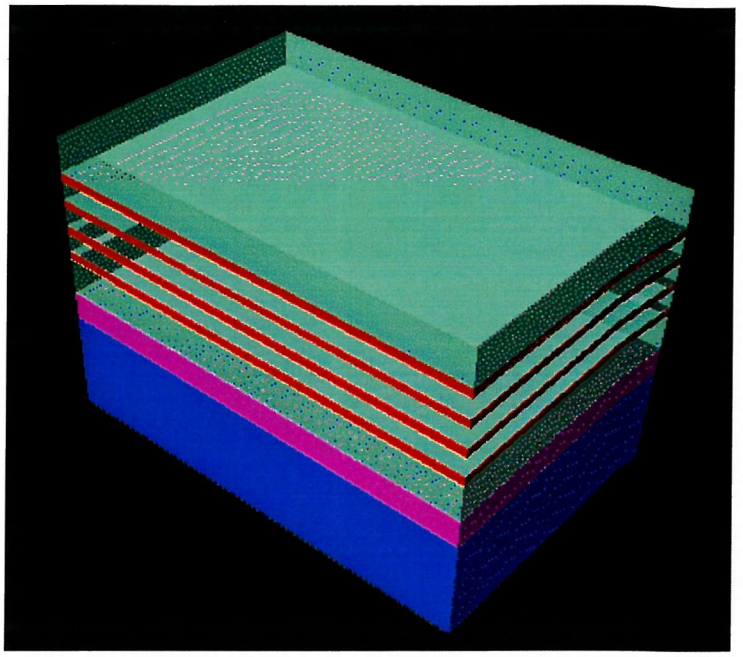

Figure 1-11. Superlattice illustration; sapphire substrate is depicted in blue, the niobium buffer layer in magenta, the magnetic layers in red and the non-magnetic spacer layers/seed/cap are shown in green.

A range of substrates, seeds and caps have been experimented with. A sapphire substrate with a Nb buffer layer (to prevent reaction between Y seed and sapphire) and a Lu or Y seed and cap is most popular. Y and Lu are chosen because they are chemically and electronically similar to the rare earths and yet non-magnetic.

1.2.2 Crystallographic properties of Tm, Y and Lu

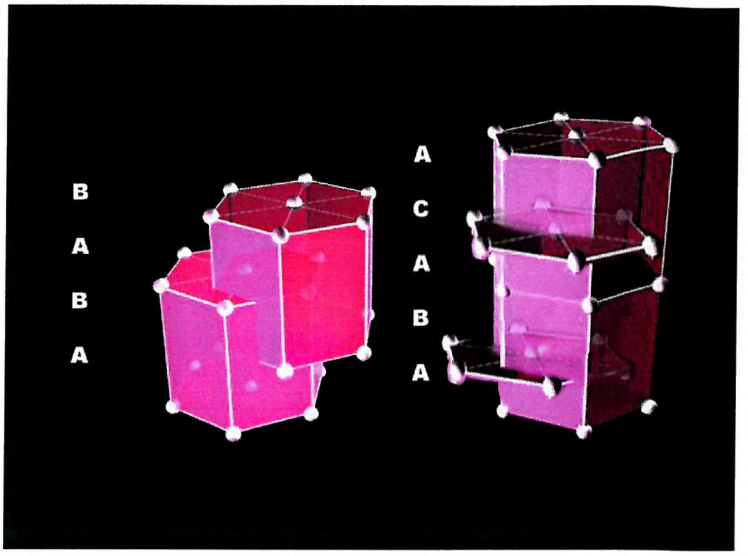

Figure 1-12. Hexagonal and double hexagonal close packed structures

Tm, Y and Lu share the crystallographic hexagonal close packed (hcp) structure, illustrated in Fig. 1-12 [17]. Atoms are arranged in hexagonal honeycomb sheets within an atomic plane, with alternate layers displaced as shown, in ABAB or ACAC sequences. The rare earths all have hexagonal structures; the heavy rare earths Gd, Tb, Dy, Ho and Er have hcp structure, whilst the lighter rare earths, La, Ce(β), Pr, Nd and Pm have the double hcp structure i.e. stacking sequence ABAC. The crystallographic a-axis lies along the line joining neighbouring atoms in the hexagonal plane, the c-axis is orthogonal to the hexagonal plane and the b-axis is orthogonal to the a and c axis.

Lu is found at the end of the rare earth series. It has the electronic structure of the rare earths, but with a full 4f shell. It is thus electronically and chemically similar but is not magnetic, which makes it ideal for superlattice growth. Y is a transition metal, located above Lanthanum in the periodic table. It is electronically similar to the rare earths, shares the hcp structure and is non-magnetic.

Element	*c* Lattice constant in Angstrom	*a* Lattice constant in Angstrom
Lu	5.549	3.505
Tm	5.554	3.538
Y	5.732	3.648

Table 1-1 . Crystallographic lattice parameters for Tm, Y and Lu [2]

1.2.3 Giant Magneto-resistance

Giant magnetoresistance (GMR) was first reported by Baibich et al [18] in 1988 for Fe/Cr superlattices. For superlattices with thin Cr layers, an applied of 2T was shown to reduce the magnetoresistance by 50% . See Fig. 1-13.

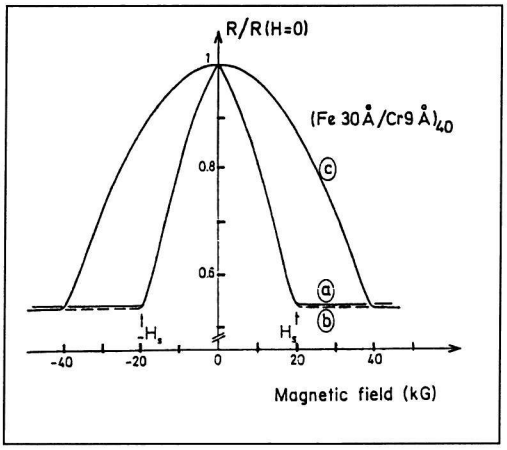

Figure 1-13. Magnetoresistance vs Applied field for Fe/Cr multilayer [18]

The GMR at low fields is explained in terms of antiferromagnetic coupling between neighbouring layers [19]. When a magnetic field is applied, neighbouring layers change their alignment from anti-parallel to parallel. The giant magneto resistance associated with the anti-parallel alignment of neighbouring layers is atrributed to spin-flip scattering of conduction electrons [20].

The magnitude of the GMR reduces with interlayer thickness, indicating that magnetoresistance is due to the exchange of polarized electrons from one ferromagnetic layer to the next [21] A model by Fujiwara and Parker [22], including both bi-linear(Heisenberg) and bi-quadratic(second-order Heisenberg) coupling, has been successful in describing magnetic characteristics (squareness, coercivity and hysteresis loop shape).

Since GMR was reported for Fe/Cr [18,20,23], much activity has been devoted to modelling this system [22,24] and to the investigation of other systems such as Co/Cu, Co/Ru and Co/Cr, which exhibit strong anti-ferromagnetic coupling across a non-magnetic spacer layer [25,26,27]. Furthermore, high quality epitaxial growth has

led to the discovery of anti-ferromagnetic coupling of Fe film across Al and Au spacer layers [28].

It is this Giant Magneto Resistive effect that gives superlattices their chief potential technological application i.e.data storage. Very little work has been done on the magnetoresistance of rare earth superlattices. This is probably partly because rare earth elements form interesting structures at temperatures too low for commercial exploitation. Nevertheless, the study of the complex magnetic behavior of rare earth superlattices provides valuable understanding of the nature of the interactions which determine the behavior of other materials.

1.3 Rare Earth Superlattices

Magnetic order in the rare earths is the result of competition between an anisotropic crystal field, magnetoelastic interactions and indirect exchange coupling between localized 4f electron moments which is mediated by conducting electrons (RKKY interaction). This competition is temperature dependent, giving rise to complex magnetic phase diagrams.

In a rare earth superlattice with layers of magnetic rare earth separated by non-magnetic but conducting material, the magnetic behavior of the bulk rare earth is modified. Epitaxial strain modifies the crystal field and magnetoelastic interactions and the RKKY interaction is modified by the spacer layers. In many rare earth superlattices, magnetic order propagates across several bi-layers, providing the spacer layer is not too thick. Magnetic order is rather remarkably conveyed across non-magnetic spacer layers by the conduction electrons.

1.3.1 Gd/Y Superlattices

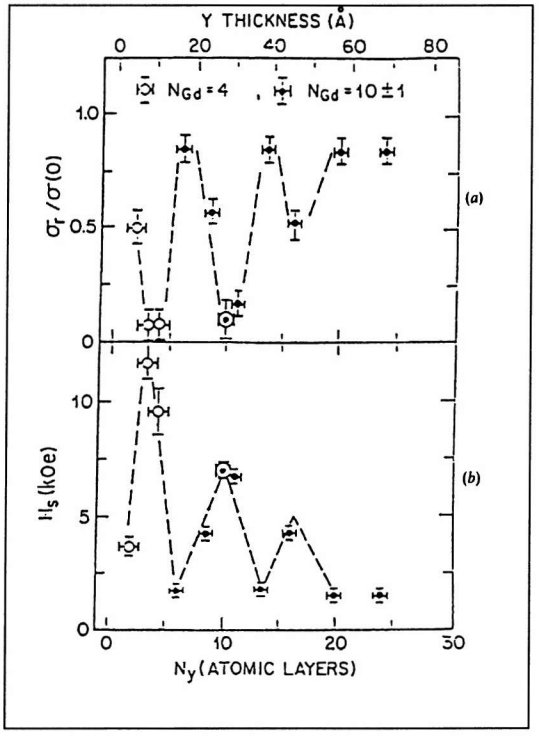

Figure 1-14. Remanence, σ_r, and saturation magnetisation, H_S, vs spacer thickness in a Gd/Y superlattice [29].

Magnetisation measurements, by Kwo et al [29], yielded results consistent with a model where the Gd within Gd slabs is ferromagnetically aligned, like bulk Gd,

with 1 to 2 atomic plane interfaces which are pinned and not ferromagnetically aligned. The Curie temperatures for these samples, with $N_{Gd} \geq 10$ were similar to the bulk value of 292K. Only the Gd_5Y_5 sample had a reduced T_c of 264K, indicating that the interfacial region over which inter-diffusion had occurred was significant for thinner Gd slabs.

Fig. 1-14 shows the oscillatory dependence of remanence and saturation magnetisation on the number of Y atomic planes per bi-layer in a Gd/Y superlattice [30]. Neutron scattering [31] led to an understanding of this oscillatory behaviour in terms of ferromagnetic and anti-ferromagnetic alignment of neighbouring Gd layers. (See Fig 1-15.) Samples with $N_Y = 6,14,20$ had low saturation fields and high remanence, corresponding to ferromagnetic alignment of adjacent magnetic layers. Samples with $N_Y = 3,4,9,10,11$ had high saturation fields and low remanence, corresponding to anti-ferromagnetic alignment of adjacent magnetic layers. An in-plane applied field of several thousand Oe was required to bring the anti-ferromagnetically coupled layers into ferromagnetic alignment. The width of superlattice satellite reflections in the neutron diffraction measurements indicated a magnetic coherence of over 17 bi-layers.

The oscillatory dependence of remanence and saturation magnetisation on Y spacer thickness demonstrates the dominance of the RKKY interaction in rare earth metals. The Y layers, whilst non-magnetic, conduct the electrons which mediate the interaction, thus propagating magnetic order.

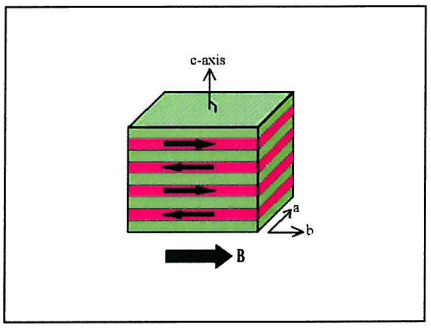

Figure 1-15. Anti-ferromagnetic alignment of adjacent magnetic layers.

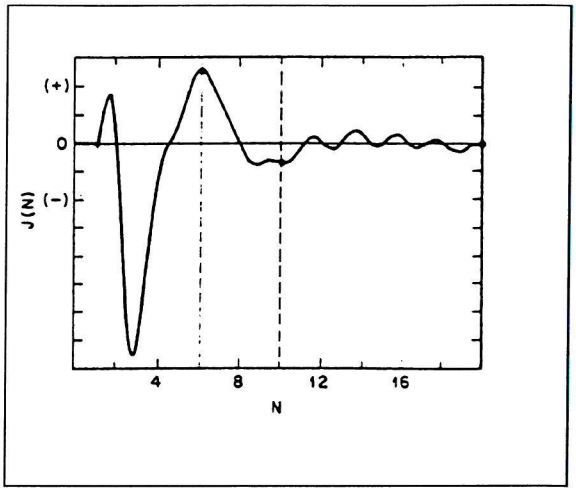

Figure 1-16. RKKY interaction for Gd/Y, as a function of the no. of ferromagnetic atomic layers per bi-layer [10]

Similar results have been reported for transition metal spacer superlattices and multilayers [32,33,34,35,25,36,30] and are generally interpreted in terms of the RKKY interaction which is mediated by the conduction electrons. The spacer slabs, while possessing no localised moment of their own, conduct the *s* and *d* electrons which provide an indirect exchange coupling between the 4*f* electrons of rare earth ions in neighbouring slabs.

A simple model for calculating the RKKY exchange interaction between layers of a magnetic rare earth metal separated by Y yields a RKKY interaction of the form shown in Fig. 1-16[10]. Positive values of the interlayer exchange interaction J(N) are associated with parallel(ferromagnetic) alignment of neighbouring rare earth layers. Negative values are associated with anti-parallel (anti-ferromagnetic) alignment. These calculations are supported by neutron diffraction measurements made by Majkrzak on Gd-Y superlattices [31].

A more general model for interlayer exchange coupling as a function of spacer thickness has been proposed by Bruno [37]:
A conduction electron, represented by a Bloch wave, travels across the paramagnetic spacer until it is incident upon the interface with the ferromagnetic layer which presents a potential barrier. Part of the incident Bloch wave is reflected off the barrier back into the paramagnet and this reflected wave interferes with the incident wave so that a standing wave is set up in the paramagnet. The reflection amplitude will, in general, depend upon whether the incident electron is parallel or anti-parallel to the majority spin direction in the ferromagnetic layer. i.e. the standing wave is

asymmetric in spin and an oscillatory spin polarisation is induced in the spacer. Furthermore, the reflected wave will pass back through the spacer until it encounters the other ferromagnetic layer that sandwiches the spacer. Multiple reflections occur and the corresponding interferences are associated with an interaction energy that oscillates as a function of the spacer thickness. This model is fairly general but, if one describes the reflection at the interfaces as due to 2-dimensional arrays of localised magnetic scatterers, it reduces to the RKKY model.

While the oscillatory dependence of the interlayer exchange interaction upon the thickness of the spacer layer is well supported, the dependence upon the thickness of the ferromagnetic or rare earth magnetic layer is a more contentious issue. Bruno's model for oscillatory interlayer coupling dependence on spacer layer thickness may be extended to include multiple reflections inside the ferromagnet which interfere with the reflection amplitude due to reflection at the spacer-ferromagnet interface. This theory was developed by Barnas [38].

Experimental evidence of the dependence of interlayer coupling upon ferromagnetic layer thickness was not found until 1994 [39,40,41,42], however not all publications report dependence of this kind [36].

1.3.2 Dy/Y Superlattices

Dy has a helical magnetic structure below 179K. Moments within an atomic plane are ferromagnetically aligned, with magnetization axis rotated by an average turn angle between successive layers. The turn angle decreases from 43.2° at T_N=185K to 26.5° at T_C=85K. In this phase, the helical magnetic structure can be pushed into ferromagnetic alignment by an in-plane field of around 15kOe. Below T_C, the spin structure falls into a ferromagnetic state, causing distortion of the crystal. This first order transition is magnetostriction driven and is affected by the epitaxial strain of the superlattice.

X-ray [43] and neutron diffraction [44] found that Dy/Y superlattices had c axis parameters that correspond to a weighted average of the Dy and Y constituents, structural coherence over several thousand Angstrom and 4 to 5 layer interfaces. The large lattice mismatch between Dy and Y (1.6%) means that Dy is expanded within the plane but contracted along c-axis when in the Dy/Y superlattice.

Salamon et al [15] demonstrated that helical order was not only present in Dy/Y superlattices, but that chirality and phase coherency of the Dy is preserved across the Y spacer layers. Erwin et al [44] found that magnetic order is coherent over many bi-layers but that the magnetic spiral wavevectors, which are parallel to the c-axis, are incommensurate with the superlattice chemical structure.

Hong et al [45] found that the spiral wave vector for Dy/Y superlattices had much weaker temperature dependence than for bulk Dy and that the helix-to-ferromagnetic transition does not occur at all. Instead the helical order locks into a fixed spiral wavevector at lower temperatures. Erwin et al [44] suggested that the helix-to-ferromagnetic transition is magnetoelastically driven and that the Dy is clamped as a result of epitaxial growth on to Y. Erwin et al [44,46] calculated that magnetoelastic energies are not sufficient to overcome the difference in exchange energy for the helix-to-ferromagnetic transition.

Rhyne et al [47] found that magnetic coherence length decreases with Y thickness. Rhyne and Erwin suggest that the propagation of helical order across the Y spacer layers is due to helical spin density waves which are induced in the Y conduction electrons.

1.3.3 Ho/Y Superlattices

Like Dy, Ho has a helical magnetic structure beneath its magnetic ordering temperature (T_N = 138 K) [48]. Beneath T_C = 20 K, there is a ferromagnetic component along the c-axis in addition to the in-plane helix. This results in a cone structure, with moments describing a cone around the c-axis. The magnetic moments of Ho, beneath around 80K, tend to bunch around the hexagonal basal plane easy directions of the crystal field. [48,49, 50, 51, 52,53, 54] This is because of competition between the low temperature turn angle, which is close to 30°, and the basal plane anisotropy.

The magnetic wavevector varies from ~0.3c* at 138 K to 1/6c* below T_C = 20K. As the magnetic wavevector decreases, the magnetic structure goes through a range of commensurate and incommensurate configurations, with the tendency to bunch around easy hexagonal directions, leading to various spin-slip phases. [51, 52, 54]

Bohr [53] calculated that, for a finite slab of Ho, there is a tendency to ferromagnetic alignment at the outermost 3-4 atomic layers. This suggests that adjacent slabs of Ho in a superlattice may couple ferromagnetically or anti-ferromagnetically, depending on the thickness of the Y slab, as for Gd. For superlattices with thin enough Y slabs, the alloying at the superlattice interfaces might be sufficient for the helical magnetic structure to propagate.

The spiral turn angles in Ho/Y superlattices are found to differ from those of bulk Ho [53]. Finite layer thickness is thought to be as important as strain when explaining these effects.

1.3.4 Er/Y Superlattices

Er has a magnetic structure, below its ordering temperature of ~85K, similar to that of Tm. The moments are aligned along the c-axis, but the moments' magnitude and direction are sinusoidally modulated with a repeat distance of approximately 7 atomic planes. Between 52K and 18K, the c-axis sinusoidally modulated moment is joined by an in-plane helical component with the same wavelength. This is best described as a tilted helix. At temperatures approaching 20K, tilted helix phase squares up and, beneath ~18K, Er has a ferromagnetic cone and helix magnetic structure. [55, 56, 57]

In an Er superlattice, magnetic order propagates through the Y spacer layers, as for other rare earth superlattices. The magnetic ordering temperature is similar for Er superlattices and Er bulk; the basal plane ordering occurs at approximately half the bulk temperature in a superlattice [58]. The low temperature magnetic phase transition, from tilted helix to ferromagnetic cone+helix, is suppressed for Er superlattices, although there is a resultant ferromagnetic moment. This phase transition suppression is attributed to epitaxial clamping [46]. The Er in an Er/Y superlattice is expanded within the basal plane. The magnetoelastic energy of this strain is sufficient to prevent the phase transition.

1.3.5 Competing magnetic order in rare earth/rare earth Superlattices

When two rare earths are combined in a superlattice formation, there is competition between the bulk magnetic properties of each. Cowley et al [16] studied Ho/Tm superlattices. The magnetic phases of the bulk elements are observed within blocks, but the coherence between blocks is disrupted. For predominantly Ho

samples, the helical order is coherent across blocks, whilst the Tm c-axis modulated order is localized. For predominantly Tm samples, the Tm order is coherent over several blocks whereas the Ho is not. Cowley *et al* concluded that two different types of magnetic ordering cannot simultaneously establish structures that are coherent over several bi-layers. This is attributed to competing crystal field anisotropies: the easy direction for Ho lies in basal plane, whereas for Tm, the easy direction is orthogonal to the plane, along the c-axis.

Chapter 2

Experimental Techniques

This chapter describes the principles and techniques employed in the studies of Tm/Y and Tm/Lu superlattices that are presented in Chapters 3 to 5. Section 2.1 contains experimental details relevant to the use of a Vibrating Sample Magnetometer for magnetization measurements. Section 2.2 presents the principles of X-ray diffraction and describes the Stöe rotating anode X-ray generator and triple axis diffractometer at Clarendon Laboratory, Oxford. Section 2.3 documents the experimental facilities used at Institut Laue Langevin, Grenoble, France and at Risø National Laboratory, Denmark for neutron diffraction measurements.

Introduction

This thesis presents the magnetic characterization of a range of Tm/Y and Tm/Lu superlattice samples. In order to understand the magnetic structures and behaviors that occur for such samples, a range of complementary experimental techniques have been employed. Extensive VSM measurements were performed at Southampton University in order to map out the phase diagram for each sample. These measurements yielded some interesting results which raised questions as to the magnetic structures within each region of the phase diagrams, some of which had additional phases not observed in bulk Tm. X-ray diffraction at Clarendon Laboratory, Oxford, was used to determine the chemical structure of the samples. Neutron diffraction was used to elucidate magnetic structures. Measurements in the absence of a magnetic field was performed at at Risø National Laboratory, Denmark. Neutron diffraction with horizontal and vertical magnetic fields was performed at Institut Laue Langevin, Grenoble, France.

2.1 Magnetization

Figure 2-1. The Vibrating Sample Magnetometer at Southampton University

2.1.1 Introduction

Measurements of magnetization were made using a computer controlled Vibrating Sample Magnetometer designed by Oxford Instruments for making precise measurements of magnetic moment over a range of temperatures (from 1.7 to 300K) and fields (+/- 12T) for samples with a width of less than approximately 5 mm.

2.1.2 VSM : Principles of Operation

The operation of a Vibrating Sample Magnetometer is based upon the principal that an EMF will be induced in a solenoid when subjected to a changing magnetic field.

A sample is oscillated along the centre axis of the pick-up coils, parallel to the applied field, and an EMF is generated which is proportional to the magnetic moment of the sample. When making measurements of magnetization for a steadily varying applied field, precautions must be taken to remove the effect of the induced EMF due to the changing applied field. This issue may be addressed by the use of 2 counter wound pick-up coils. See Fig. 2-2 for relative geometry of superconducting magnet and the pick-up coils.

The voltage due to the vibrating sample is added for the two identical coils and the voltage due to the changing applied field is subtracted out. In practice, it is hard to manufacture identical pairs of coils and so the equalization is achieved electronically by feeding the signals from the coils into variable gain amplifiers and balancing the signals precisely before summation to output.

2.1.3 VSM measurements

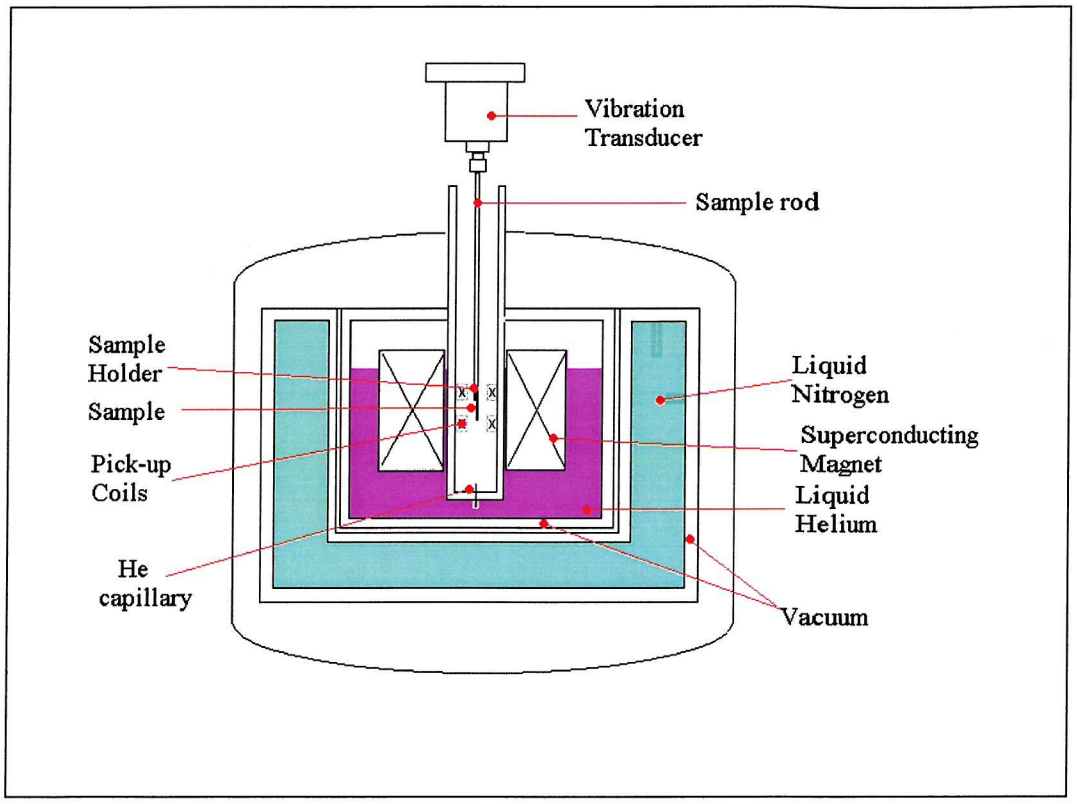

Figure 2-2. Cross-section of a VSM

A sample is mounted on a sample holder with vacuum grease and PTFE tape. The sample holder is screwed onto the sample rod, which is attached to the vibrating platform and then lowered into the sample chamber of the cryostat.

The sample chamber temperature is controlled by the variable temperature insert, which draws helium from the helium reservoir into the sample chamber. The temperature controller (ITC4) heats the He gas and feedback circuitry enables it to stabilize the temperature of the sample. The liquid He space holds approximately 40 litres and is insulated by a vacuum, layered reflective foil and a liquid nitrogen jacket.

The field applied to the sample is provided by a Nb_3Sn superconducting solenoid which is powered by an Oxford Instruments PS120 power supply. The sweep rate of the magnet is limited to less than 25mT/s in order to prevent a quench of the magnet [63].

The sample rod is vibrated along the line of its length at 66 Hz (avoiding noise from mains supply) with amplitude 0.75mm [63]. The magnetic moment induced in the sample by the solenoid is detected when the sample vibrates between the pick-up coils, which develop a voltage proportional to the moment. This voltage is amplified and processed with respect to an earlier calibration process (using a Nickel sample of known mass and, therefore, known magnetic moment) by the VSM computer and is displayed as a magnetic moment in emu.

At the beginning of an experiment, the optimum position of the sample with respect to the pick-up coils must be determined. A small field (approx. 0.01T to 0.1T, depending on the response of the sample) is applied and the magnetic moment as a function of position (z-axis) is measured over the 20mm potential travel. For a ferromagnetic or paramagnetic sample, a graph of the form shown will normally be obtained. The optimum position corresponds to the peak of this curve. For a diamagnetic sample, the form of the curve will be reflected in the z-axis and the lowest point will be the optimum position and will correspond to the calibration.

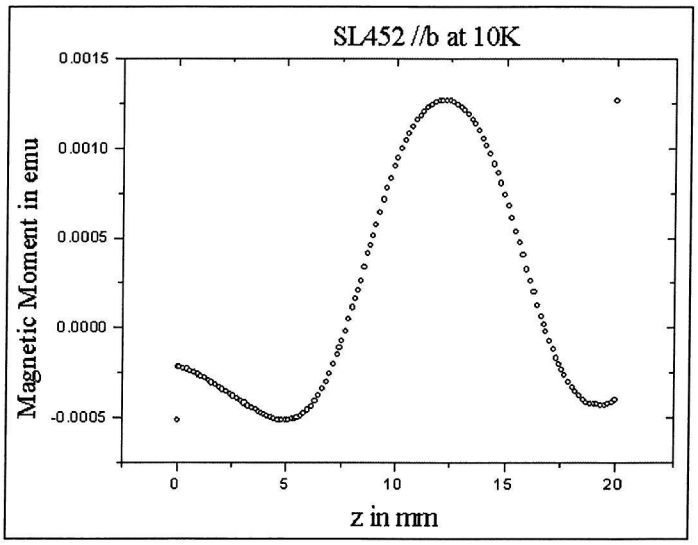

Figure 2-3 An example of a z-axis calibration curve

Having selected the optimum z position about which to oscillate, the operator may then program the VSM control PC. Control programs may run for any length of time, but they are normally designed to run for 1 to 2 days, which is usually a suitable period over which to characterize a sample for a given orientation with respect to temperature and applied field. Control programs consist of commands that enable manipulation of field and temperature and measurement of magnetic moment and time.

2.1.4 VSM maintenance

The VSM requires a nitrogen transfer every other day and a helium transfer approximately once every three days, although cryogen consumption varies with size of magnetic field and sweep rate.

If the magnet holds a high field for extended periods, as a consequence of a software error for example, helium will evaporate at a high rate and the helium level may drop beneath the height of the magnet. When a significant amount of the superconducting magnet is no longer immersed in helium, regions of the magnet will lose their superconductivity and behave as "normal" conductors with the Joule heating that would accompany the currents required for high magnetic fields. The Joule heating accelerates the helium evaporation in a run-away process that quickly expels all the helium in the cryostat. This process is known as a "quench" and presents a certain amount of hazard and inconvenience to the experimenter and may damage the magnet.

In addition to weekly maintenance, the VSM system requires maintenance of it's vacuum pump. This typically involves emptying oil-traps and changing or re-filling pump oil every month or two. The super-insulating vacuum would also be improved with a turbo pump during such an exercise.

The VSM is totally emptied of cryogenic liquids and allowed to warm up once a year so that any water or oil that may have got into the system can be removed.

2.2 X-ray Diffraction

2.2.1 X-ray diffraction theory

Whilst Bragg's Law relates the position of a diffracted beam to inter-planar spacings within a crystal, it makes no predictions about the intensities of diffracted beams. In order to predict the intensity of diffracted beams, we consider individual atoms within the crystal to absorb incident, plane waves and instantly re-emit the waves isotropically, in phase with the incident wave. The scattered amplitude from each atom, at position **R** and with form factor $f(\mathbf{Q})$, is:

$$A = f(\mathbf{Q})e^{(-i\mathbf{Q}.\mathbf{R})}$$

The scattered amplitude from the entire sample is the sum of the individual atomic contributions. **Q** is the scattering vector:

$$\mathbf{Q} = \mathbf{k}' - \mathbf{k}$$

i.e. it is the vector provided by the atom to divert the incident beam towards the diffracted beam.

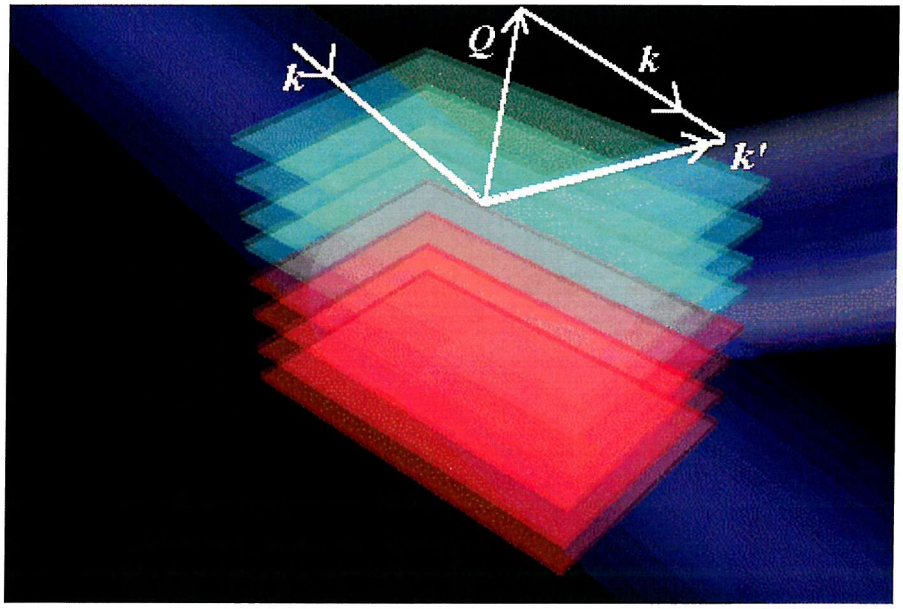

Figure 2-4 The scattering vector, Q, relative to incident and diffracted beams

For coherent-elastic X-ray scattering, the atomic form factor, $f(\mathbf{Q})$, has additional terms corresponding to dispersive and absorptive processes. These are important at X-ray wavelengths close to atomic absorption edges.

$$f(\mathbf{Q}) = f_0(\mathbf{Q}) + f' + if''$$

Values for f_0, f' and f'' were obtained from *The International Tables for Crystallography* [64].

The intensity of the elastically scattered X-rays may be written:

$$I(Q) \propto \left| \sum_n f_n(Q).\exp[iQ.R_n] \right|^2$$

This relation allows prediction of the intensity of scattering at any given position from knowledge of structure and chemical composition.

The Debye-Waller factor, which multiplies a factor of $e^{-2W(Q)}$ to the X-ray scattering cross-section, accounts for the thermal motion of atoms. It is particularly significant for light atoms, large Q or measurements over a range of temperatures [65]. It is considered to be constant for the purposes of these measurements.

The superlattice subjects of this study have fairly well known structures and compositions due to the level of control that the MBE growth method provides. It is therefore possible to make reasonable predictions about the result of X-ray scans along any direction in the crystal. A model for X-ray diffraction from a superlattice is presented in *Chapter 3, Section 3.2.*

2.2.2 Instrumentation

X-ray measurements were performed using a Stöe rotating anode X-ray generator and triple axis diffractometer at Clarendon Laboratory, Oxford. X-rays are generated in this apparatus by applying potentials (~kV) across a filament, causing electrons to boil off and accelerate towards a copper anode. The anode rotates to prevent any particular area of metal from over-heating and is thus able to produce a high flux of X-rays. Electrons, incident upon the anode, cause excitations in the copper atoms that then relax and isotropically emit $CuK_{\alpha 1}$ radiation with wavelength ~1.54 Å.

Some of these X-rays are incident upon a double-bounce silicon monochromator. The X-rays reflect off two surfaces within the hollowed silicon crystal, becoming more Gaussian-like in their wavelength distribution with each reflection.

Beyond the monochromator, the X-rays are incident upon a knife-edge which removes $CuK_{\alpha 2}$ photons and allows the $CuK_{\alpha 1}$ photons to continue along their path to the sample.

Upon diffraction from the sample, photons are filtered by a Germanium analyser, if high resolution measurements are required; otherwise, the photons are reflected directly from sample to detector. The Ge analyser selects X-rays according to their angle of incidence rather than their energy, as the energy of X-rays is sufficiently high to not be appreciably changed by interaction with the sample.

2.3 Neutron Diffraction

2.3.1 Neutron diffraction theory

Neutron diffraction shares much of the theory of X-ray diffraction. The properties of X-rays and neutrons lead to different interactions with materials.

An X-ray scatters off the charge cloud that surrounds a nucleus. The size of the charge cloud is comparable to the wavelength of an X-ray. This causes interference effects and, consequently, the form factor (intensity of interaction) drops off with Q. An X-ray carries no magnetic moment and so only interacts weakly with the magnetic moment of the atom. Standard X-ray diffraction only yields information about the chemical structure of a superlattice.

Properties of neutron	Value
mass	1.675×10^{-27}
charge	0
spin	½
magnetic dipole moment	−1.913 nuclear magnetons

Table 2-1 Properties of the neutron [60]

The properties of neutrons, given in table 2-1 [60], determine their interactions with matter. Their mass gives thermal neutrons a de Broglie wavelength according to:

$$\lambda = \frac{h}{mv}$$

where $E = k_B T = \frac{1}{2}mv^2 = \frac{h^2}{2m\lambda^2}$ and T is the temperature of the neutron moderator.

These wavelengths are of the order of the inter-atomic distances in solids, as shown in the table. Interference effects occur, therefore, and yield information about chemical structure.

Source	Energy E / meV	Moderator Temperature T / K	Wavelength $\lambda / 10^{-10}$m
cold	0.1 - 10	~25K (liquid H_2 or D_2)	30 - 3
thermal	5 - 100	~ 300K (water)	4 - 1
hot	100 - 500	~1000K (graphite)	1 - 0.4

Table 2-2. Energy, temperature and wavelength ranges for cold, thermal and hot neutron sources [61]

The uncharged nature of the neutron enables penetration of the Coulomb field of the atom. The neutron is scattered by the nucleus, which is very small compared to the wavelength of the neutron. The nucleus, therefore, scatters neutrons isotropically. Whereas the form factor for X-rays drops off with Q as a consequence of interference effects due to similar magnitudes of wavelength and scatterer, this does not occur for nuclear neutron diffraction and the form factor is constant in Q.

The magnetic moment of a neutron interacts with the unpaired electrons of the atom and so information about magnetic structure may be determined from elastic scattering. In this case there is a magnetic form factor $f(Q)$ corresponding to the distribution of magnetic moment density in the atom.

In summary, whereas X-ray diffraction yields only chemical structure information, neutron diffraction yields both chemical and magnetic structure information.

2.3.2 Neutron diffraction Instrumentation - Zero Field

Zero field neutron diffraction studies were conducted at Risø National Laboratory, Denmark. Neutron flux was provided by the research reactor DR3 and diffraction studies were performed on the triple axis spectrometers TAS1 and TAS7.

The Risø DR3 Reactor

The DR3 reactor is a heavy-water-moderated 10 MW thermal neutron research reactor. It has a moderator temperature of approximately 55°C and a nearly Maxwellian distribution peaking at 1.1 Å. Horizontal tubes through the peak flux positions act as guides from the cold and thermal sources positioned at these points. The cold source consists of a chamber filled with super-critical hydrogen at 16 atmospheres and 38K. The thermal source is a 10mm thick can containing light water.

There are two cold-beam ports within the DR3 Reactor Hall and one of these beams shares flux with a 25m guide tube that passes through the wall of the Reactor Hall and through to an adjoining building, "The Neutron House", where it supplies cold neutrons to four other instruments.

The instruments used were triple axis spectrometers TAS1 and TAS7, which are situated in the Reactor Hall and Neutron House respectively. Both are supplied with neutrons from the cold source.

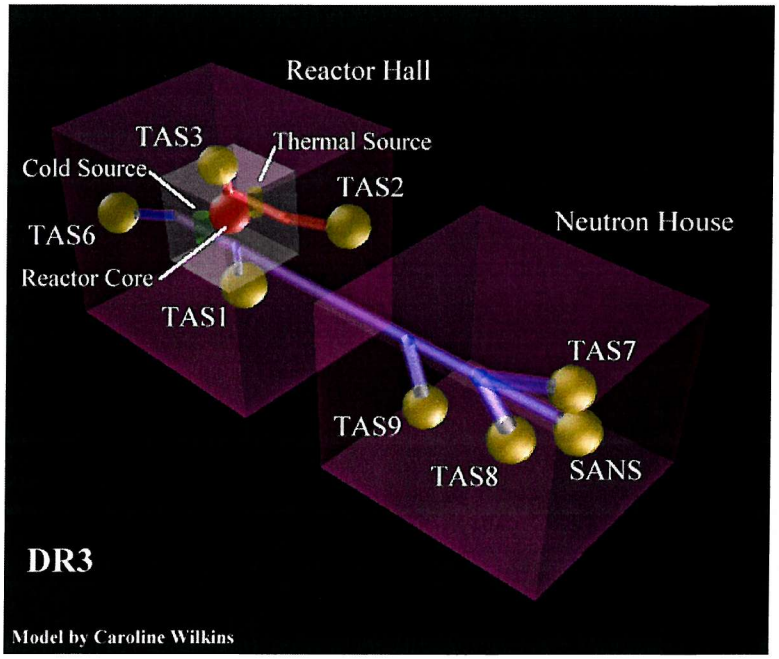

Figure 2-5. DR3 at Risø, Denmark, showing layout of reactor, neutron sources and spectrometers

TAS1

TAS1 is situated in the reactor hall of DR3 and shares the cold neutron beam with the guide-tube leading cold neutrons to the Neutron House. It is a conventional triple-axis spectrometer and, therefore, it has rotational freedom of the monochromator, sample table and analyser.

TAS1 has a pyrolytic graphite monochromator with four fixed- incidence take-off angles corresponding to first order neutrons of 13.7 meV, 7.2 meV, 5.0 meV and 3.6 meV for [002] reflections from the graphite. The monochromator consists of nine 1 cm high slabs of pyrolytic graphite crystals with a mosaicity of approximately 30' and is mounted so that it may be focussed and tilted.

The sample table comprises a 500 mm diameter turn-table, a relatively small motorised xy-goniometer (157× 157 mm^2, ± 15° tilt) and a manual xy-translation (± 10 mm) which can support cryostats and other types of sample environment.

The analyser unit moves on air cushions and the take-off angle from the analyser is continuously variable. The shielding wedges around the analyser are lifted pneumatically to allow for automatic changes of the analyser setting.

A liquid nitrogen cooled beryllium $\lambda/2$ filter and/or pyrolytic graphite can be inserted either in front of or behind the sample. Optical benches before and after the sample table and analyser allow the mounting of collimators. The neutron detector is a 2×10 cm^2 side-window ^3He detector similar to the one used at TAS7.

TAS7

TAS7 is a high resolution triple-axis spectrometer which is located at the end of the neutron guide in the Neutron House and, hence, benefits from the low ambient background. The resolution can be tailored to the experiment by choosing the optimal wavelength, collimations, distances between units, and if necessary, by using focusing monochromator and analyser. Depending on the configuration and length of the links between the monochromator, sample and analyser axes, a take-off angle up to 120° from the sample can be achieved.

The monochromator consists of fifteen 1 cm high slabs of pyrolytic graphite crystals with a mosaicity of approximately 30' and is mounted so that it may be focussed and tilted. The take-off angle of the monochromator may be varied

continuously from 40° to 140° by means of shielding wedges that are automatically lifted by pneumatic cylinders.

A liquid nitrogen cooled beryllium λ/2 filter and/or pyrolytic graphite can be inserted either in front of or behind the sample. Optical benches before and after the sample table and analyser allow the mounting of collimators.

The sample table has a 500 mm diameter turn-table, a motorised xy-goniometer (340×340 mm^2, ± 15° tilt) and an xy-translation (340×340 mm^2, ± 15 mm movement) which can support cryostats and other types of sample environment.

The analyser unit moves on air cushions and the take-off angle from the analyser is continuously variable. The shielding wedges around the analyser are lifted pneumatically to allow for automatic changes of the analyser setting. The instrument moves on air cushions and all angles may be set with a precision of a few hundredths of a degree. The neutron detector is a 20×100 mm^2 side-window ^3He detector similar to the ones used on TAS1.

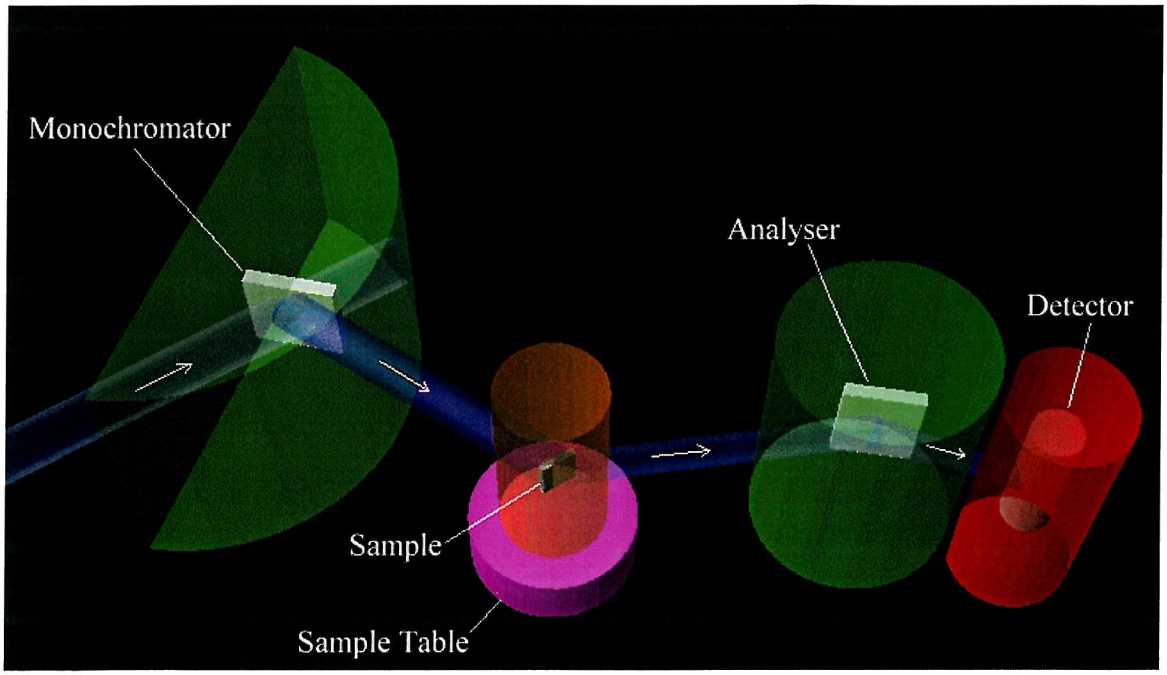

Figure 2-6. Schematic model of a triple axis spectrometer

Sample mount

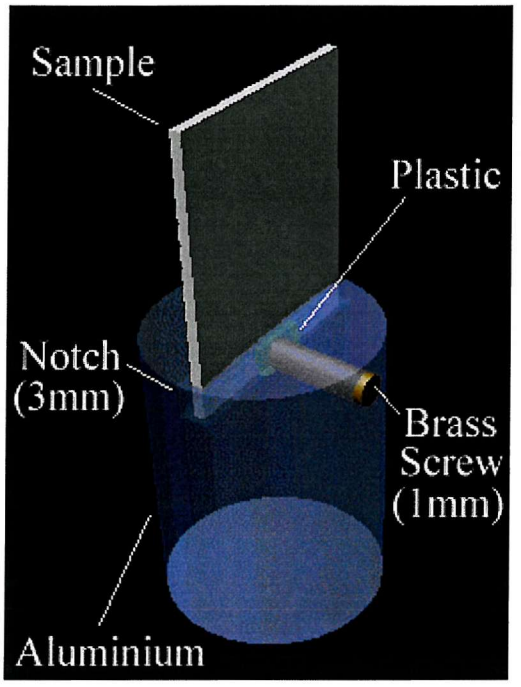

Figure 2-7. Design for a superlattice sample mount suitable for neutron scattering measurements

It was essential to design a sample mount that would hold the superlattice sample securely without obscuring a significant portion from the neutron beam. To this end a small flat notch, approximately 3 mm deep was cut into the end of the aluminium cylinder and 1 mm flat ended brass screw was drilled and fitted perpendicular to the notch. To mask the brass screw and the solid aluminium cylinder, a strip of cadmium was shaped around the outside of the holder. A hood of aluminium foil was secured over the sample and cadmium with a wire.

For the later ILL measurements, an aluminium can took the place of the foil hood and protected the sample from falling down inside the cryostat.

2.3.3 Neutron diffraction Instrumentation - In Horizontal and Vertical Fields

Neutron diffraction studies in horizontal and vertical fields were conducted at Institut Laue Langevin, Grenoble, France. Neutron flux was provided by the ILL high-flux reactor. Diffraction studies were performed on the triple axis spectrometer D10.

High-Flux Reactor

The ILL operates a single fuel element reactor, at a thermal power of 58MW, over approx. 4.5 cycles per year, each of 50 days. This single fuel element is cooled and moderated by heavy water. The thermal neutron flux, in equilibrium with the heavy water moderator (300 K), has a peak in the Maxwellian distribution at 1.2 Å. For certain beams and guide tubes this is modified by the inclusion of special moderators. Hot and cold neutrons are available from 3 sources. The hot source is a 10 dm^3 block of graphite, at 2400 K, which enhances the neutron flux at wavelengths below 0.8 Å. There are two cold sources, a 20 dm^3 vertical source and a 6 dm^3 horizontal source, both of liquid deuterium at 25 K, which enhances the neutron flux at wavelengths above 3 Å.

D10

D10 is a 4-circle diffractometer, with 3-axis energy analysis situated on thermal guide H24 of the ILL Guide Hall 1. It may be used in 4 or 2 circle configurations, and with or without energy analysis for inelastic and elastic measurements respectively. D10 consists of a fixed monochromator table with sample and analyser tables that move independently on air cushions.

Neutrons from the guide, which has a divergence of 3.5 λmrad Å are incident on the vertically focussing and continuously variable monochromator. A choice of two monochromators is available; pyrolytic graphite which selects neutrons of 1.8 Å to 6 Å and Cu (200) which selects neutrons 1.1 Å to 3 Å. The diffracted beam from the monochromator to the sample is 10x8 mm^2 in size and has a flux of 5 x 10^6 $cm^{-2}s^{-1}$ for $\lambda = 2.36$ Å and the pyrolitic graphite-monochromator and filter or 2 x 10^6 $cm^{-2}s^{-1}$ for $\lambda = 1.26$ Å and the Cu-monochromator.

For inelastic or 4 axis measurements, a vertically focussing pyrolytic graphite analyser may be used to select neutrons of appropriate energy. There are two high

pressure ^{3}He detectors are available. One detector is mounted directly on the sample table for the diffractometer configuration, another detector is mounted on the analyser table for the spectrometer configuration. The background rate for these detectors is < 3 cpm (without analyser) or 0.5 cpm (with special detector shielding or with analyser).

Chapter 3

Sample growth and structural determination

This chapter describes how X-ray diffraction measurements were used to determine the chemical structure of the range of superlattice samples for which neutron studies are presented in Chapter 5. Section 3.1 describes the growth of the samples. Section 3.2 presents a model for X-ray diffraction from a superlattice. Section 3.3 contains experimental details specific to these X-ray measurements and their computational modelling. The X-ray results are presented in Section 3.4. Section 3.5 summarises the conclusions that may be drawn from the X-ray experiments.

Introduction

The actual chemical structure of a superlattice may vary appreciably from the nominal growth parameters. What may have been designed and intended to have been a Tm_{40}/Y_{20} superlattice, may emerge from the growth process with an average chemical structure of Tm_{37}/Y_{22} for example. The intention of this thesis is to magnetically characterise a range of Tm superlattices. It is therefore important to determine, with reasonable accuracy, the chemical structure of the system for which magnetic behaviour has been studied.

X-ray diffraction is a technique that complements neutron diffraction well. Whilst the neutrons interact with magnetic moments as well as atomic sites, X-ray diffraction may be used to isolate the chemical structure from the magnetic structure.

3.1 Superlattice Growth

The superlattice samples described in this thesis were grown by Molecular Beam Epitaxy at the Clarendon Laboratory, Oxford, by Mike Wells and Roger Ward using a Balzers UMS30 facility. This technique provides high quality epitaxial films and superlattices.

Evaporation of the elements is achieved either by the use of an electron gun or by an effusion cell, according to the vapour pressure of the element (and hence the temperature) required for a deposition rate of ~0.5 Å/s.

The electron gun is suitable for elements with higher evaporation temperatures e.g. Lu: T_e = 1600 °C, Nb: T_e = 2500 °C. A beam of electrons from a filament is deflected by a magnetic field into a crucible containing the solid material. A constant flux of material is controlled by a feedback loop from a quadrupole mass spectrometer which is placed alongside the sapphire substrate.

The effusion, or Knudsen, cell relies on the resistive heating of a tungsten coil surrounding the crucible. This method is more suitable for elements with lower evaporation temperatures, up to about 1400 °C, e.g. Tm: T_e = 800 °C.

The flux of evaporated material is measured with a quartz crystal sensor whose resonant frequency is dependant upon the mass of material that has condensed on its surface. The response time of this mechanism is approximately 1 second. For precise calibration, this monitor can be positioned at the sapphire substrate position.

The substrates are normally 10mm x 12mm sapphire crystals of approximately 1.0mm thickness. The substrate is mounted on the underside of a Mo disk of about 10cm diameter and is held in place by two small clips.

Good epitaxial growth results from high mobility of atoms over the surface of the crystal. Surface mobility increases with temperature, however inter-diffusion also increases with temperature. The growth temperature is selected by trial and error to optimize the surface mobility whilst keeping interlayer diffusion to an acceptable minimum. This temperature is different for every metal and is related to its melting point. It is generally accepted [66,67] to be approximately 3/8 of the melting

temperature. Multilayer growth is therefore best obtained for elements with similar melting points e.g. Tm: T_m= 1545°C, Y: T_m = 1522°C.

Whilst the growth temperature is important for crystal quality, it is difficult to measure. Sapphire cannot be heated radiatively as it reflects incident heat energy. Instead the Mo disk upon which the sapphire is mounted, is heated from behind with a graphite resistive coil. Nevertheless, the surface temperature of the substrate is thought to be as much as 200°C below the temperature of the Mo disk. Attempts to calibrate this disparity have not met with success [67].

A 1000 Å seed of Y or Lu, depending on the choice of spacer material for the multilayer, is deposited over a buffer layer of 100 Å Niobium (+/- 10 Å). The multilayer is then deposited by alternating the source between the Tm effusion cell and the Y or Lu electron gun. Finally, a 200 Å Y or Lu cap is deposited to protect the reactive rare earth material from the atmosphere. The deposition rate is 0.5 $Å s^{-1}$. The pressure of the MBE chamber is of the order of 10^{-11}mbar [67].

3.2 X-ray Scattering from a superlattice

In order to model the X-ray scattering for scans of wavevector transfer along the c-axis (the [00L] direction), we follow the model by Jehan et al [62] and construct a function that identifies the location and chemical identity of each atomic plane in the superlattice. The superlattice consists of N bilayers, each comprising n_A and n_B atomic planes of elements A and B respectively. In this case, we take element A to be Tm and element B to be either Lu or Y. We use a series of tanh functions to smoothly step from one element to another, simulating the 3 to 4 atomic plane intermixing. The concentration of element A in the lth layer in the bilayer is given by:

$$c_A(l) = \frac{1}{2}[1 + \tanh((l+0.5)/\lambda_1) - \tanh((l+0.5-n_A)/\lambda_1) + \tanh((l+0.5-n_A-n_B)/\lambda_1)\ ]$$

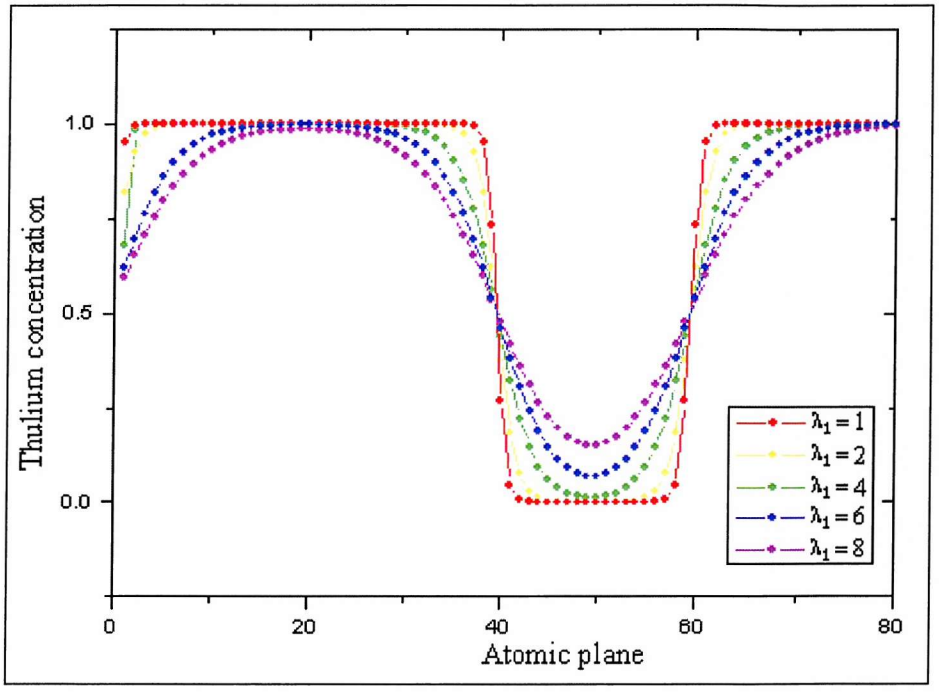

Figure 3-1 Modelled thulium concentration as a function of atomic plane

This gives a scattering amplitude for the *l*th layer:

$$f_l(Q) = c_A(l) f_A(Q) + (1 - c_A(l)) f_B(Q)$$

The inter-planar spacing does not necessarily change in precisely the way that the chemical composition does. In order to separate the two variables, they are allocated separate tanh widths λ_1 and λ_2. The concentration with regard to inter-planar spacing is given by a function that is centred on atomic, rather than inter-atomic, positions:

$$g_A(l) = \frac{1}{2}[1 + \tanh(l/\lambda_2) - \tanh((l - n_A)/\lambda_2 + \tanh((l + -n_A - n_B)/\lambda_2)\ ]$$

This function leads to the following expression for inter-planar distances where d_A and d_B are the interplanar distances for elements A and B respectively:

$$d_l = g_A(l)d_A + (1 - g_A(l))d_B$$

This expression allows the specification of the position of every atomic plane relative to an origin:

$$R_l = \sum_{m=0}^{l} d_m$$

The expressions for R_l and f_l can be substituted into the expression for the intensity of elastically scattered X-rays at a particular wave transfer vector,Q.:

$$I(Q) \propto \left| \sum_l f_l(Q).\exp[iQ.R_l] \right|^2$$

This expression can be separated into two terms, involving summation over a bilayer, multiplied by a summation of bi-layers over the superlattice:

$$I(Q) = \left| \left(\sum_{m=1}^{M} e^{iQmL} \right) \left(\sum_{l=0}^{n_1+n_2-1} f_l(Q) e^{iQ \cdot R_l} \right) \right|^2$$

The second term of the expression sums the contribution of atoms in planes l=0 to (n_1+n_2-1) within each bi-layer; the first term sums the contribution from bi-layers numbered from 1 to M.

It can be shown that the first summation may be expressed explicitly as:

$$\sum_{m=1}^{M} e^{iQmL} = e^{iQL(M-1)/2} \frac{\sin\left(QLM/2\right)}{\sin\left(QL/2\right)}$$

Furthermore, $|e^{i\theta}|^2 = 1$, and so the expression for scattered intensity from a superlattice simplifies to:

$$I(Q) = \left| \left(\frac{\sin(QLM/2)}{\sin(QL/2)} \right) \left(\sum_{l=0}^{n_1+n_2-1} f_l(Q) e^{iQ \cdot R_l} \right) \right|^2$$

3.3 Experimental Details

As part of systematic studies of the magnetic phase diagrams of rare earth superlattices, thulium superlattices with non-magnetic Y and Lu spacer layers [68,69] have been studied. All of the samples are epitaxial superlattices grown on sapphire substrates by molecular beam epitaxy at the Clarendon Laboratory, Oxford, as described in section 3.1.

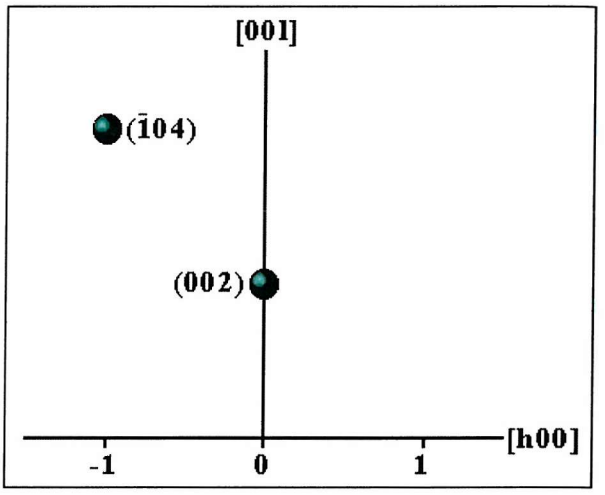

Figure 3-2 Reciprocal space illustration for X-ray measurements

X-ray diffraction was used to characterize the superlattice structure. These measurements were carried out by the author and J.P Goff using the Stöe rotating anode X-ray generator and triple axis diffractometer at the Clarendon Laboratory, Oxford, as described in section 2.2.3.

Detailed scans along the [00L] crystallographic direction were performed in the vicinity of the (002) Bragg peak. These were complemented by a set of theta scans through the superlattice features observed around the (002) peak. (A theta scan involved rocking the crystal so that an arc was described about the origin of Fig.3-2, with constant Q.)

In order to extract structural parameters for each superlattice from the X-ray scans, the model by Jehan et al [62] described in Section 3.2 was fitted to the data. Computer modeling software was written that calculated the X-ray diffraction

intensity at **Q** for an atom at position **R**, based on the Jehan model [62]. This was summed over all the atomic planes in the superlattice to give a value of intensity that would correspond to a modeled point on a [00L] scan. Repeating this for every value of Q in the experimental scan produced a simulated data set. The simulated data set was fitted to the experimental results by passing the nominal input parameters and the chi-squared (the difference between simulated and experimental data) to a least squares fitting routine [70]. The fitting routine makes a series of small changes to parameters and uses the simulation code to evaluate the effect in terms of a change in chi-squared. The fitting routine makes a series of steps in multi-dimensional parameter space, continuing to work towards decreasing values of chi-squared. When the routine meets a minimum in chi-squared it quits, returning least squares fit values of the parameters that it was initially fed.

It was found that the model was extremely sensitive and the fitting software was prone to getting stuck in local minima within multi-dimensional parameter space. In order to find a reliable solution, it was necessary to start fitting routines from a position in multi-dimensional parameter space that was very close to the final answer.

3.4 X-ray results

Scans along the [00L] crystallographic direction are sensitive to structural patterns orthogonal to the basal plane, along the hexagonal-close-packed c-axis. Bragg peaks are observed, corresponding to the two atomic plane repeat pattern of the hcp structure. A series of more frequent superlattice peaks are observed, displaced from the Bragg peaks by *nq*, where n is the order of the superlattice peak relative to the main Bragg reflection and q, the separation of the superlattice reflection in Q, is related to the superlattice bi-layer thickness:

$$L_{bi\text{-}layer} = 2\pi/q$$

The Tm/Y samples showed strong superlattice reflections, with up to fourth order superlattice peaks being strongly evident either side of the Bragg (002) peak. The intensity of the superlattice features closely matched that of the (002) peak, so that modelling of results was required in order to identify each. The large lattice mismatch between Tm and Y and the significant contrast in form factor are likely to have been responsible for the strong superlattice reflections.

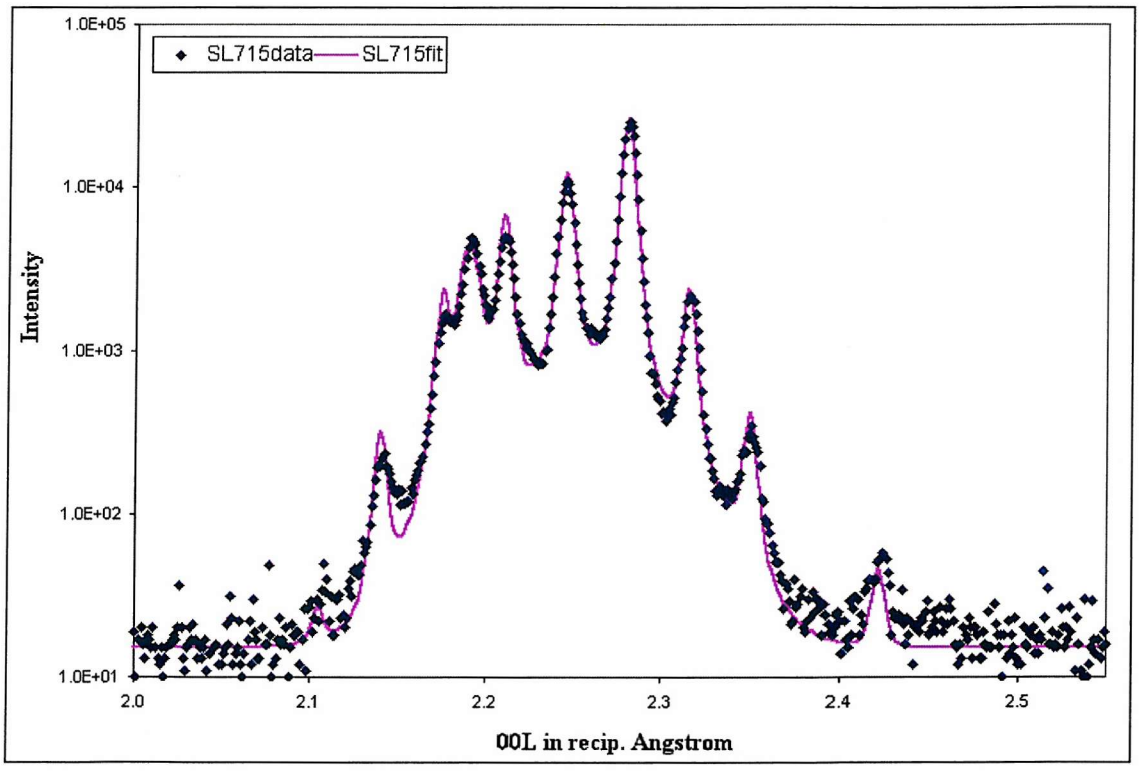

Figure 3-3 X-ray diffraction scan along [00L] for SL715 $(Tm_{40}/Y_{20})_{52}$

Figure 3-3 shows the [00L] scan for SL715 $(Tm_{40}/Y_{20})_{52}$, on a logarithmic intensity scale, together with the theoretical curve resulting from least squares fit to the model. This scan for SL715 is representative of all three Tm/Y samples. Each showed a very similar form, with strong multiple superlattice reflections either side of the (002) Bragg reflection.

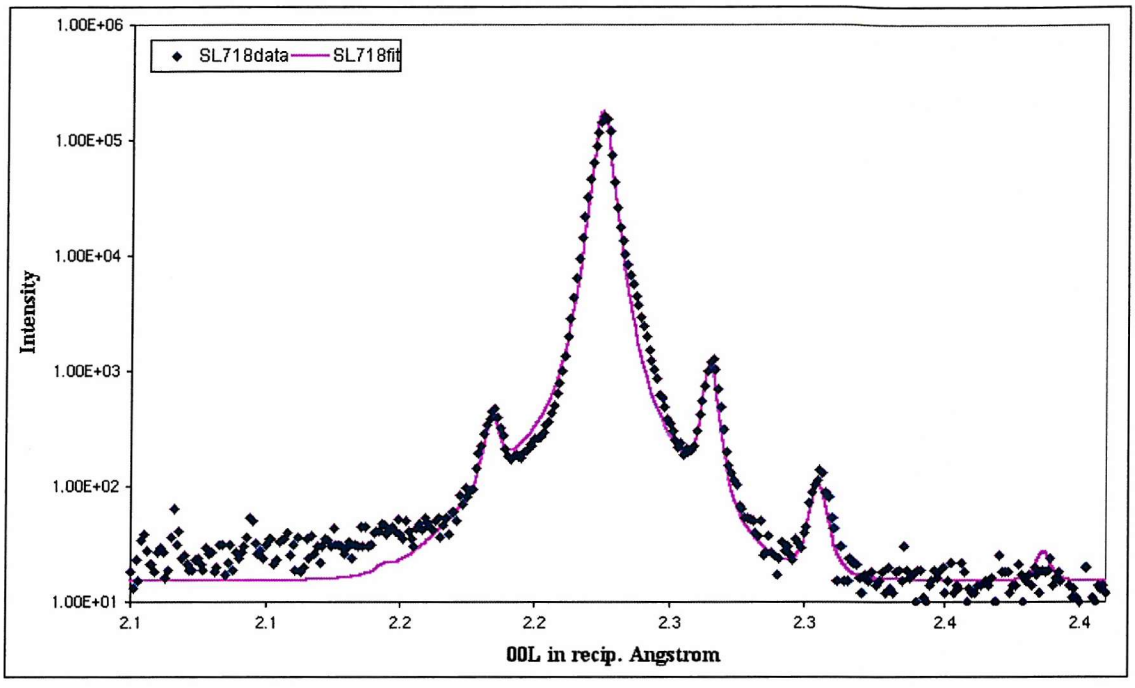

Figure 3-4 X-ray diffraction scan along [00λ] for SL718 $(Tm_{40}/Lu_{20})_{52}$

Figure 3-4 shows the [00L] scan for SL718 $(Tm_{40}/Lu_{20})_{52}$, on a logarithmic intensity scale, together with the theoretical curve resulting from least squares fit to the model. Just as the three Tm/Y samples yielded very similar-looking scans, so did the three Tm/Lu scans. The scan for SL718 is representative of all three Tm/Lu samples. Each displayed fewer superlattice reflections either side of the (002) Bragg reflection than for the Tm/Y samples. The superlattice reflections were also of weaker intensity than those for Tm/Y samples. Whereas there were up to fourth order superlattice reflections for the Tm/Y samples, the Tm/Lu samples had 1 to 2 superlattice peaks below the (002) and 2 to 3 superlattice peaks above. The relative weakness of the Tm/Lu superlattice peaks is likely to be due to similar number of electrons for Tm and Lu and, hence, almost identical form factors.

Sample	Composition		c_{Tm}	c_{spacer}	λ	a_{SL}	Strain (%)
	Nominal	Measured					
SL715	Tm_{40}/Y_{20}	$Tm_{43.37}/Y_{21.13}$	5.516	5.764	3.00	3.580	+ 1.182
SL716	Tm_{20}/Y_{40}	$Tm_{19.37}/Y_{39.13}$	5.510	5.760	2.05	3.589	+ 1.450
SL717	Tm_{50}/Y_{10}	$Tm_{49.39}/Y_{10.11}$	5.518	5.756	2.44	3.568	+ 0.842
SL718	Tm_{40}/Lu_{20}	$Tm_{35.94}/Lu_{19.82}$	5.556	5.536	0.08	3.516	- 0.636
SL719	Tm_{50}/Lu_{10}	$Tm_{50.14}/Lu_{10.86}$	5.556	5.526	2.75	3.524	- 0.410
SL720	Tm_{20}/Lu_{40}	$Tm_{17.63}/Lu_{40.88}$	5.572	5.538	1.96	3.502	- 1.026

Table 3-1 Nominal and measured composition of samples

Table 3-1 gives the nominal growth composition and the composition obtained from modeling of X-ray diffraction data. The primary objective of the X-ray measurements was to obtain this information. We see that SL715 and SL719, whilst nominally similar but for the choice of spacer element, are actually quite different. SL715 has ~43 atomic planes of Tm per bilayer whereas SL718 has ~36. It is important to appreciate such differences when making direct comparisons between Tm/Y and Tm/Lu samples with the same nominal magnetic/non-magnetic superlattice ratio.

The crystallographic *a* lattice parameter may be obtained from a scan along [h00] through the (100) peak. For a hexagonal lattice, the d-spacing of the (*h,k,l*) reflection is given by:

$$d = \left\{ \left(\frac{4}{3} \right) \left(\frac{h^2 + hk + k^2}{a^2} \right) + \frac{l^2}{c} \right\}^{-1/2}$$

The position in Q ($Å^{-1}$) of the (100) peak is given by:

$$Q_h = \frac{2\pi}{d} = \frac{2\pi}{a}\sqrt{\frac{4}{3}}$$

Values of the in-plane crystal parameter, *a*, were calculated thus and are also presented in table 3-1. Strain is calculated as the ratio of the superlattice *a* parameter to that of bulk thulium and is expressed as a percentage.

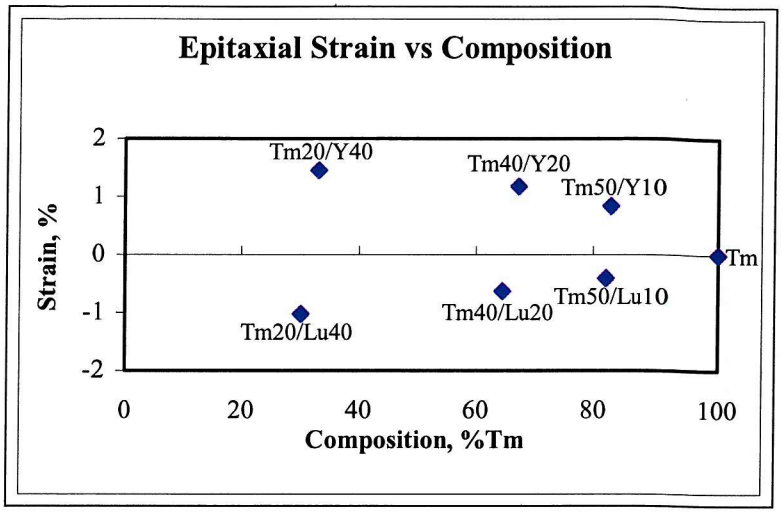

Figure 3-5. Strain as a function of composition. (Sample labels refer to nominal composition.)

The plot of strain as a function of composition, Fig.3-5, demonstrates that yttrium imposes a strain on thulium within a superlattice and that lutetium compresses the thulium within the basal plane. A smooth, non-linear, relation is indicated between composition and strain.

The Tm crystallographic lattice parameters in the superlattices may be compared with the bulk values of c_{Tm}=5.554Å and a_{Tm}=3.538 Å [8]. In a Tm/Y superlattice, Tm has tensile strain within the basal plane but is compressed along the c direction; Y is compressed within the basal plane and has tensile strain along the c direction. In a Tm/Lu superlattice, Tm is compressed within the basal plane and has tensile strain along the c direction; Lu has tensile strain within the basal plane and is compressed along the c direction.

The basal plane *a* parameter is constant throughout the superlattice and is a compromise between the *a* parameters of each of the constituents of the superlattice, weighted by composition. The c parameter for each element is determined by the tendency for cell volume to remain constant for an element in a superlattice, as shown in Table 3-2.

The cell volume for the hcp structure is given by:

$$V = \frac{\sqrt{3}}{2} a^2 c$$

Sample	Nominal Composition	c_{Tm}	c_{spacer}	a_{SL}	Tm Cell Vol. (Å^3)	Y/Lu Cell Vol. (Å^3)
SL715	Tm_{40}/Y_{20}	5.516	5.764	3.580	61.22	63.98
SL716	Tm_{20}/Y_{40}	5.510	5.760	3.589	61.47	64.25
SL717	Tm_{50}/Y_{10}	5.518	5.756	3.568	60.84	63.46
SL718	Tm_{40}/Lu_{20}	5.556	5.536	3.516	59.48	59.27
SL719	Tm_{50}/Lu_{10}	5.556	5.526	3.524	59.75	59.43
SL720	Tm_{20}/Lu_{40}	5.572	5.538	3.502	59.18	58.82

Table 3-2 Crystal parameters and hcp cell volume

Table 3-2 demonstrates that the cell volume of Tm does not stray far from the bulk value of 60.19 Å^3, but that it is increased when combined with Y which has a larger cell volume and decreased when combined with Lu which has a smaller cell volume. Lu maintains a cell volume close to its bulk value of 59.05 Å^3 but Y is compressed a little more, relative to its bulk value of 66.06 Å^3.

As well as yielding lattice paramaters, X-ray scans also contain information about the quality of the crystal. The width of the (002) peak yields the length over which the hcp lattice order is maintained in the superlattice, the structural coherence length. Table 3-3 gives the widths, $W_{[002]}$,, of the [002] peaks for each sample, from the least squares fits to the [00L] scans. These are related to structural coherence lengths, L, by the relation:

$$L = 2\pi/W_{[002]}$$

Sample	Nominal Composition	$W_{[002]}$ (Å^{-1})	L (Å)	Fitted bi-layer thickness (Å)	L (bi-layers)
SL715	Tm_{40}/Y_{20}	0.007	900	180	5
SL716	Tm_{20}/Y_{40}	0.004	1600	166	10
SL717	Tm_{50}/Y_{10}	0.007	900	165	5
SL718	Tm_{40}/Lu_{20}	0.005	1300	155	8
SL719	Tm_{50}/Lu_{10}	0.004	1600	168	10
SL720	Tm_{20}/Lu_{40}	0.003	2100	162	13

Table 3-3 Structural coherence lengths

The superlattices have structural coherence of between 5 and 13 bi-layers, indicating the quality of the MBE growth. Over the regions of coherence, c-axis crystal parameters vary according to a function similar to the tanh function described in the model, whilst in-plane crystal parameters maintain constant values. These constant values of in-plane crystal parameters are a fundamental quality of a superlattice and differentiate it from a multi-layer, which may not share this coherence.

The Tm/Lu samples have greater structural coherence lengths than the Tm/Y samples. This is probably because the lattice parameters of Tm are closer to those of Lu than those of Y. Tm/Lu superlattices are therefore less strained and likely to be coherent over greater lengths.

Sample	Nominal Composition	$W_{Background}$ ($Å^{-1}$)	$L_{hcp\ stack}$ (Å)
SL715	Tm_{40}/Y_{20}	0.094	66.8
SL716	Tm_{20}/Y_{40}	0.141	44.6
SL717	Tm_{50}/Y_{10}	0.088	71.4
SL718	Tm_{40}/Lu_{20}	0.060	104.7
SL719	Tm_{20}/Lu_{40}	0.060	104.7
SL720	Tm_{50}/Lu_{10}	0.050	125.7

Table 3-4. Width of background gaussian and corresponding hcp stacking lengths.

There is a broad gaussian feature, beneath the series of structural and superlattice peaks in the [00L] scans, which varies in magnitude. This is attributed to stacking faults in the hexagonal lattice, such as an interface between an ABABAB region and an ACACAC region, and is accounted for in the model. The width of the broad gaussian feature, from the least squares fit, and its corresponding hcp stacking length is given in table 3-4. The Tm/Lu superlattices have approximately half the stacking faults of the Tm/Y superlattices. This is likely to be due to the smaller lattice mismatch for Tm/Lu superlattices. Figure 3-6 demonstrates the linear relation between strain (calculated in section 3.4) and the lengths over which either hcp ABAB or ACAC stacking is maintained for the samples.

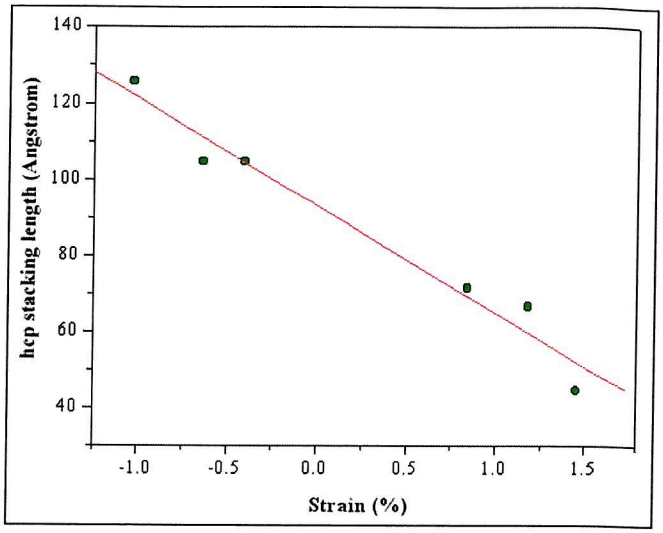

Figure 3-6. hcp stacking length vs basal plane strain

3.5 Conclusions

X-ray diffraction measurements have been made for the range of superlattices for which neutron diffraction measurements are presented in Chapter 5. A computer model has been created and used to model the X-ray scans. This has yielded values for the hcp *a* and *c* lattice parameters and the width of the interface between superlattice bilayers. Structural coherance lengths and hcp stacking lengths have been calculated directly from the widths of the (002) and background gaussian respectively.

Superlattice samples may have varying degrees of structural disorder, which are related to their growth. In general, one would seek to minimize the disorder through careful choice of growth temperature and deposition rate so that the best quality crystals may be studied and the fundamental magnetism of superlattice systems may be isolated. However, some of the disorder may be modeled and useful information deduced. Any production environment will be subject to fluctuations that lead to a range of sample quality and so it is important to quantify the likely effects. Furthermore, it is possible that the effects of structural disorder may be interesting in their own right.

The main sources of superlattice disorder may be summarized as follows:

- Structural incoherence; quantified by the size of crystallites and deduced from the width of the [002] reflection. For these samples, structural coherence lengths were between 900 Å and 2100 Å.
- Stacking faults; where ABAB hcp structure interfaces to ACAC regions. This is reflected in the broad feature under sharp peaks. For these samples, hcp ABAB or ACAC stacking was maintained over an average of between 45 Å and 125 Å.
- Mosaic spread (orientation difference between crystallites): smears peaks over an arc of approx. 0.2 degrees about the origin. This effect is not appreciable at [002] but is observable at [104]. [002] gives the cleanest value of structural coherence length whilst [104] gives information about mosaic spread.

Chapter 4

Magnetic phase transitions of Tm superlattices

This chapter describes how magnetisation measurements were made to magnetically characterise a range of Tm/Y and Tm/Lu superlattice samples. Section 4.1 contains experimental details for these magnetisation measurements. Section 4.2 describes the contribution to the magnetic measurements from the sample holders. The magnetisation results are presented in Section 4.3. Section 4.4 discusses the conclusions that may be drawn from the magnetisation experiments.

Introduction

Magnetisation measurements were performed using the Vibrating Sample Magnetometer at the Department of Physics and Astronomy, University of Southampton . Measurements were made in fields up to 12T and temperatures between 5K and 290K, for fields both parallel and normal to the basal plane. Magnetic phase diagrams were obtained for each sample and sample-field orientation. The magnetisation studies revealed some remarkable departures in the behaviour of the superlattices from that of pure Tm. First, for fields parallel to the c-axis, a double metamagnetic step is found: the first step is to roughly 50% of the saturation moment. Secondly, when fields are applied in the basal plane a large in-plane moment develops. This is an extraordinary result which implies that uniaxial anisotropy has been drastically reduced in the superlattice compared to bulk Tm, perhaps as a consequence of epitaxial strain which alters the c/a ratio.

The surprising magnetisation results led to the neutron and X-ray diffraction studies described in Chapters 5 and 3.

4.1 VSM measurements

Magnetisation measurements were made for the range of samples in Table 4-1, using techniques and apparatus described in Section 2.1 of Chapter 2. These measurements were made over a period of three years and, as such, the range and choice of measurements varied as the type of magnetic behaviour typically exhibited became better understood. All samples have been well characterised by magnetic moment versus applied field sweeps at least every 5K between 10K and 70K as well as magnetic moment versus temperature sweeps at 0.1 Tesla in the range 10 to 100K, for field-cooled and zero-field-cooled conditions. Supplementary measurements included magnetic moment versus applied field at additional set temperatures (typically every 2K between 40K and 60K) and magnetic moment versus temperature at higher fields (typically 40K to 60K sweeps at set fields between 0.5 and 5.0T). Measurements were made for fields applied parallel to the crystallographic c-axis (i.e. normal to the basal plane of the sample) and for fields applied in the basal plane, parallel to the b-axis.

The magnetisation results presented illustrate transitions between magnetic phase structures and these are seen as sudden changes in magnetic moment with applied field. The sharpness of the phase transition is smoothed by the effect of the demagnetising field of a flat sample. The internal field, H, may be obtained by subtracting the product of the magnetisation, M, and the demagnetisation factor, D, from the applied field, B: D=1 for thin flat sample [71]. However, whilst this deduction was possible for Richards and Legvold, (who measured a sphere of bulk Tm), it could not be achieved with meaningful accuracy for our superlattice samples; as the volume of the thin film could not easily be measured. Hence, the magnetic moment of the sample could not be converted to an absolute value of magnetisation.

In the absence of an absolute measure of transition field, a consistent approach to determining this point was adopted. In order to construct a phase diagram, first order differentials of the magnetic moment versus applied field data were plotted and the peaks in these differential plots taken to represent the mid-point of the phase transition. The values of applied field at these phase transition midpoints were plotted against temperature to construct phase diagrams for each sample and sample orientation. These phase diagrams then formed the basis of the experimental planning process for neutron scattering measurements.

An extremely large amount of data was collected to magnetically characterise the samples. It would not be feasible to display it in its entirety within this document. Much of the data collected is represented in the phase diagram and so only the following are presented for each sample and orientation:

1) Magnetic Moment versus Applied Field at 10K
2) Magnetic Moment versus Temperature at 0.1T
3) Phase diagram

This data is presented in Appendix A.

Sample Number	Superlattice Structure
SL701	$(Tm_{20}/Y_6)_{60}$
SL702	$(Tm_6/Y_{20})_{60}$
SL703	$(Tm_{20}/Y_{20})_{60}$
SL706	Tm film, 2000 atomic planes
SL707	$(Tm_{40}/Y_{20})_{50}$
SL708	$(Tm_{20}/Y_{40})_{50}$
SL709	$(Tm_{20}/Lu_6)_{60}$
SL710	$(Tm_6/Lu_{20})_{60}$
SL711	$(Tm_{20}/Lu_{20})_{60}$
SL712	$(Tm_{40}/Lu_{20})_{50}$
SL713	$(Tm_{20}/Lu_{40})_{50}$
SL714	Substrate/buffer/seed only
SL717	$(Tm_{50}/Y_{10})_{52}$
SL719	$(Tm_{50}/Lu_{10})_{48}$

Table 4.1: MBE Samples

4.2 Sample Holder contributions

Two sample holders were used, both made of Tufnol. For c-axis measurements, a cylindrical sample holder was used and for b-axis measurements, a cylinder with a flat cut-away surface was used. Each contributed different components of magnetisation to the total moment measured and, at times, this was significant, since the total amount of magnetic rare earth in a superlattice was very small.

The sample holders were found to have magnetic moments that varied with z-axis position, applied field and temperature. This is illustrated in figures 4.1 to 4.6. The response was quite complex and not a straightforward matter to remove from further magnetic measurements on superlattice samples as these measurements occurred over a range of z-axis positions, fields and temperatures. Instead, it was thought sufficient to broadly characterise the contribution of the sample holder so that estimates and subtractions could be made where necessary. The b-axis sample holder was found to have a magnetic moment about one tenth of that of the c-axis sample holder. This was likely to be a reflection of the mass of material involved.

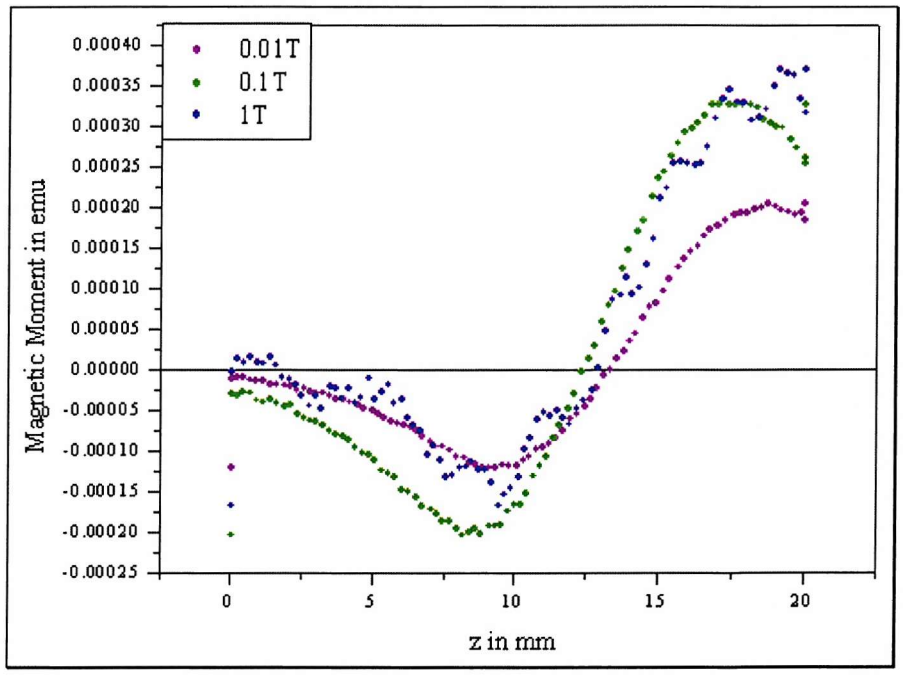

Figure 4-1. Variation of Magnetic Moment with VSM z-axis position at 5K for c-axis Sample Holder

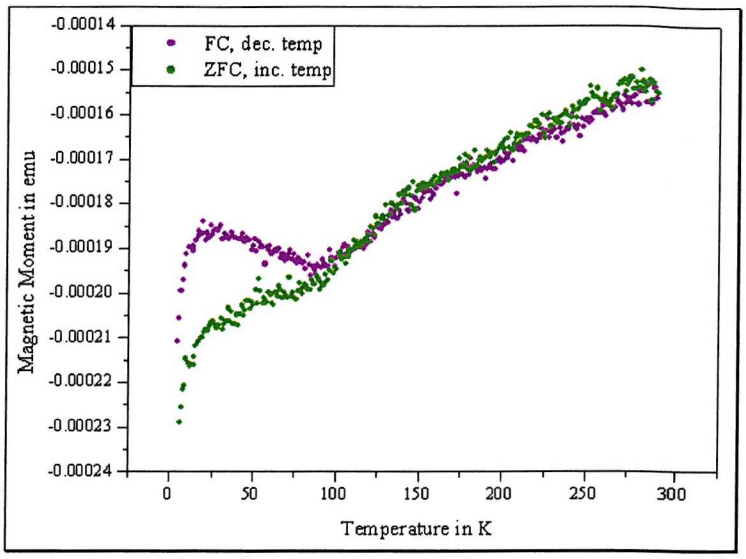

Figure 4-2. Variation of Magnetic Moment with Temperature in a field of 0.1T for c-axis Sample Holder

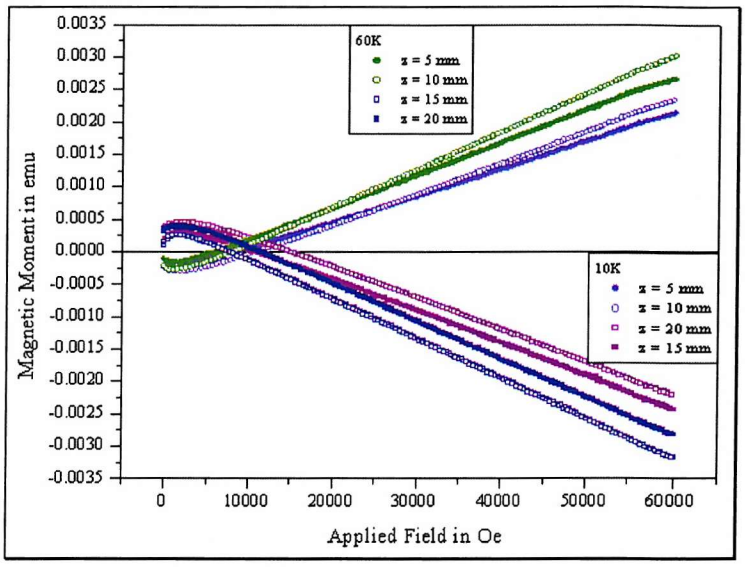

Figure 4-3. Variation of Magnetic Moment with applied field for c-axis Sample Holder

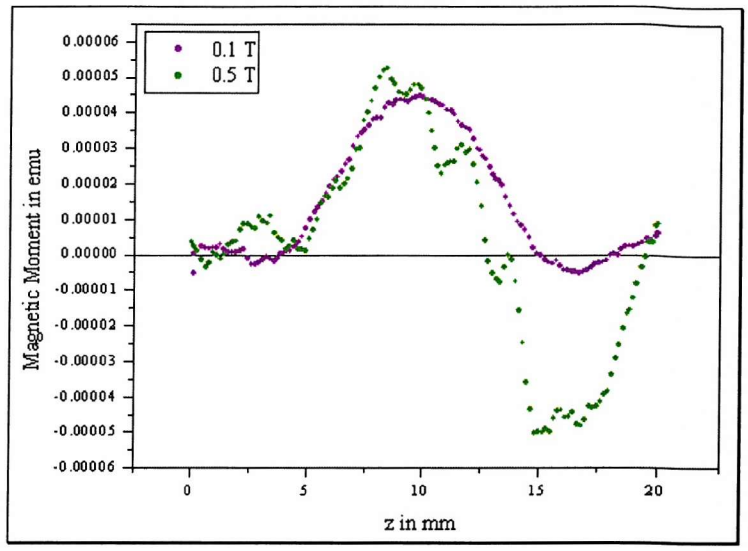

Figure 4-4. Variation of Magnetic Moment with VSM z-axis position at 5K for b-axis Sample Holder

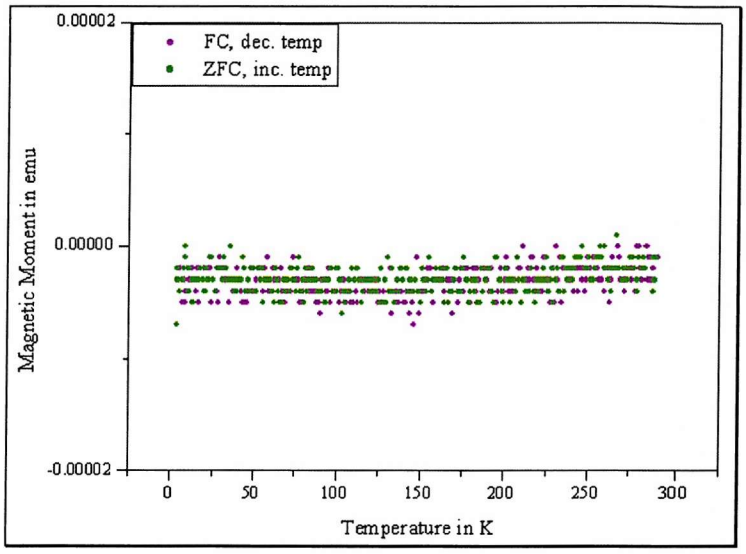

Figure 4-5. Variation of Magnetic Moment with temperature for b-axis Sample Holder

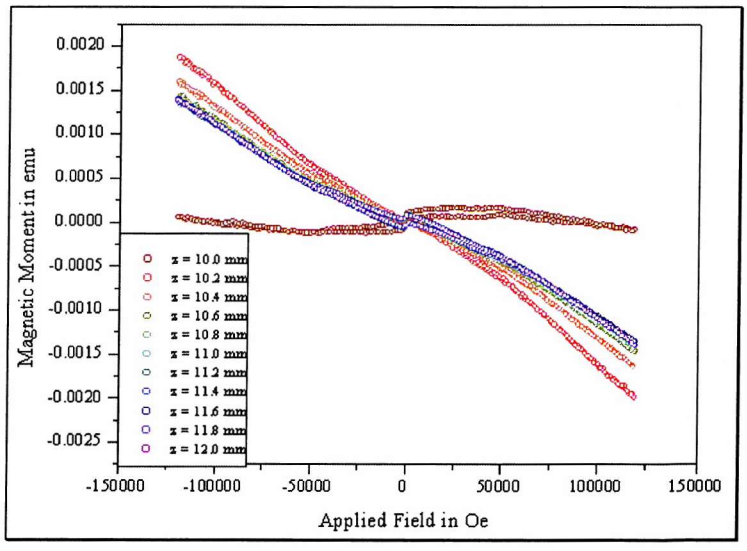

Figure 4-6. Variation of Magnetic Moment with applied field for b-axis Sample Holder at 10K

4.3 Magnetisation Results

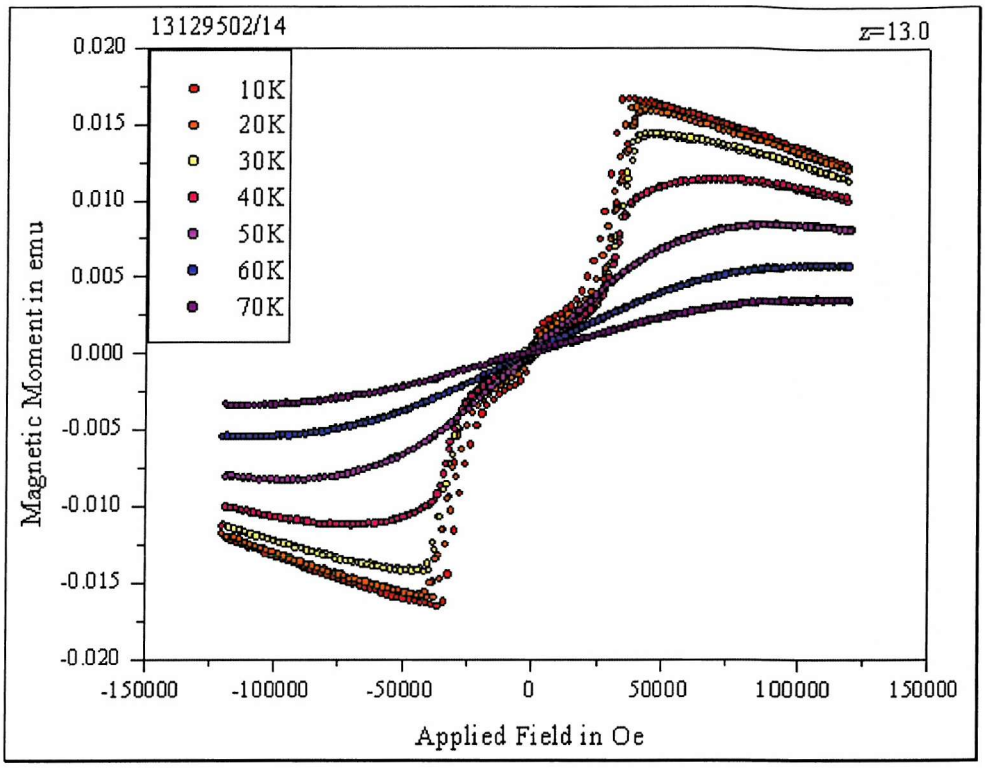

Figure 4-7. Magnetic Moment as a function of c-axis applied magnetic field at a range of temperatures for $(Tm_{20}/Y_6)_{60}$

The magnetic moment as a function of applied field data for fields applied parallel to the c-axis took the form shown in Figure 4-7, for the Tm film and samples with nominal structures of $Tm_{20}Y_6$, Tm_6/Y_{20}, Tm_{20}/Y_{20}, Tm_6/Lu_{20}. This is similar to the form of the Richards and Legvold data for a pure Tm crystal [7]. The shape of the curves may be interpreted as the result of two transitions:

- Tm switching from 4up/3down square wave anti-ferromagnetic structure to 7up saturated ferromagnetic structure. This transition occurs at ~2.8T for pure Tm.
- Tm switching from 4up/3down to 3up/4down square-wave anti-ferromagnetic structure. This transition occurs around 0T when the applied field changes direction.

When attempting to construct a phase diagram (showing the applied field at which each transition takes place with respect to temperature), distinguishing the correct transition field is obscured by the smoothness of the transition (which is caused by the demagnetising field and domain effects). This problem has been dealt with by differentiating the magnetic moment with respect to applied field; a sharp peak in the

differentiated graph indicates the midpoint of the transition. For consistency, this approach was taken towards determining every point on the phase diagram. Each phase transition is surrounded by hysteresis due to the crystal field anisotropy that causes magnetic moments to align preferentially along the *c*-axis. The phase transition is taken as the average of the increasing and decreasing field transitions.

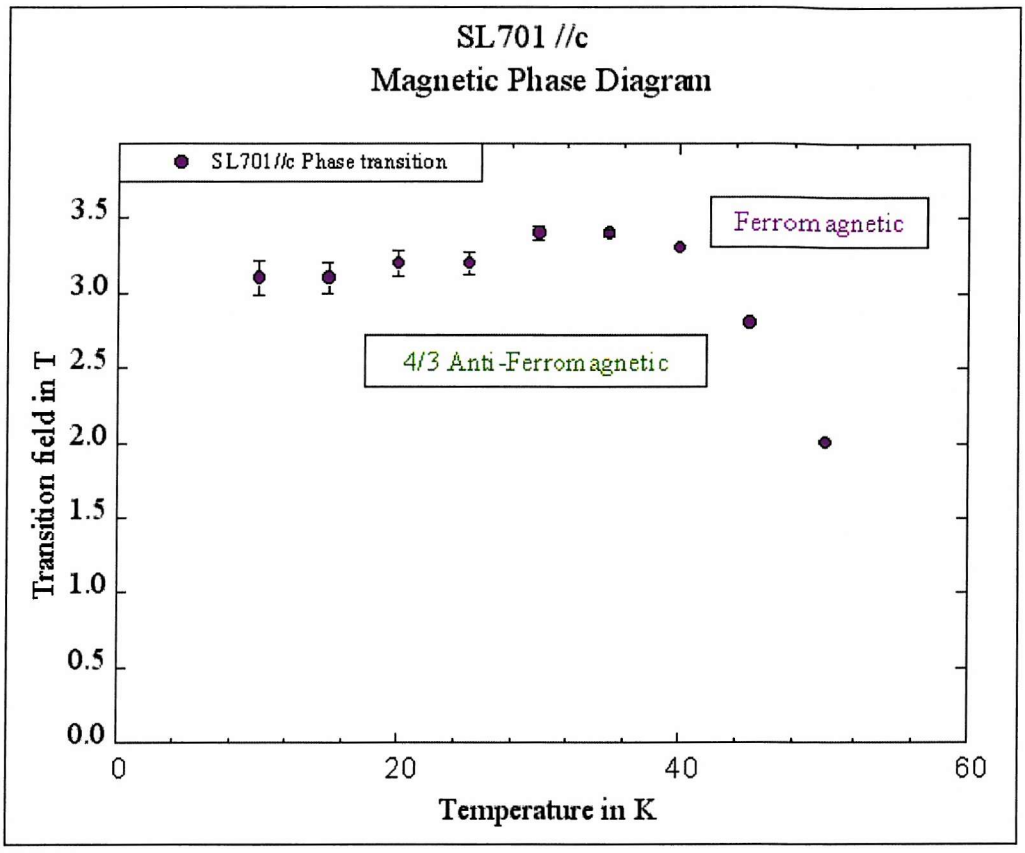

Figure 4-8. Phase diagram for $(Tm_{20}/Y_6)_{60}$ with field parallel to c-axis. Error bars indicate difference between increasing and decreasing field sweeps.

Figure 4-8 is representative of the phase diagrams that were constructed for $Tm_{20}Y_6$, Tm_6/Y_{20}, Tm_{20}/Y_{20}, Tm_6/Lu_{20} and the Tm film. The phase transition field varied however. The samples with very little Tm in them, Tm_6/Y_{20} and Tm_6/Lu_{20}, had transition fields of 0.6T and 1.37T respectively at 10K, considerably lower than the bulk Tm value of ~2.8T. As superlattice interfaces are typically around 3 atomic layers, it is likely that these samples are more like alloys than superlattices. This may explain the lower transition field. With a value of 2.6T at 10K, Tm_{20}/Y_{20} was close to the bulk value for the magnetic phase transition, whilst Tm_{20}/Y_6 was a little higher than the bulk value at 3.1T at 10K. Interestingly, the Tm film had a single magnetic phase transition at 3.8T at 10K. This strongly demonstrates the effect of epitaxial strain alone on the magnetic behaviour of Tm thin film samples.

Whilst the phase diagrams for the thinner superlattices (26 atomic layers/bilayer) take forms that resemble the phase diagram for pure thulium[7], the thicker superlattices - Tm_{40}/Y_{20},Tm_{20}/Y_{40}, Tm_{20}/Lu_{20}, SL712 and SL713 (with 40 - 60 atomic planes/bilayer) (except SL703) exhibit an additional transition, suggesting that an additional phase occurs other than ferrimagnetic and ferromagnetic. Figure 4-9 demonstrates the typical form of the magnetic moment with respect to applied magnetic field. The additional transition can be clearly seen.

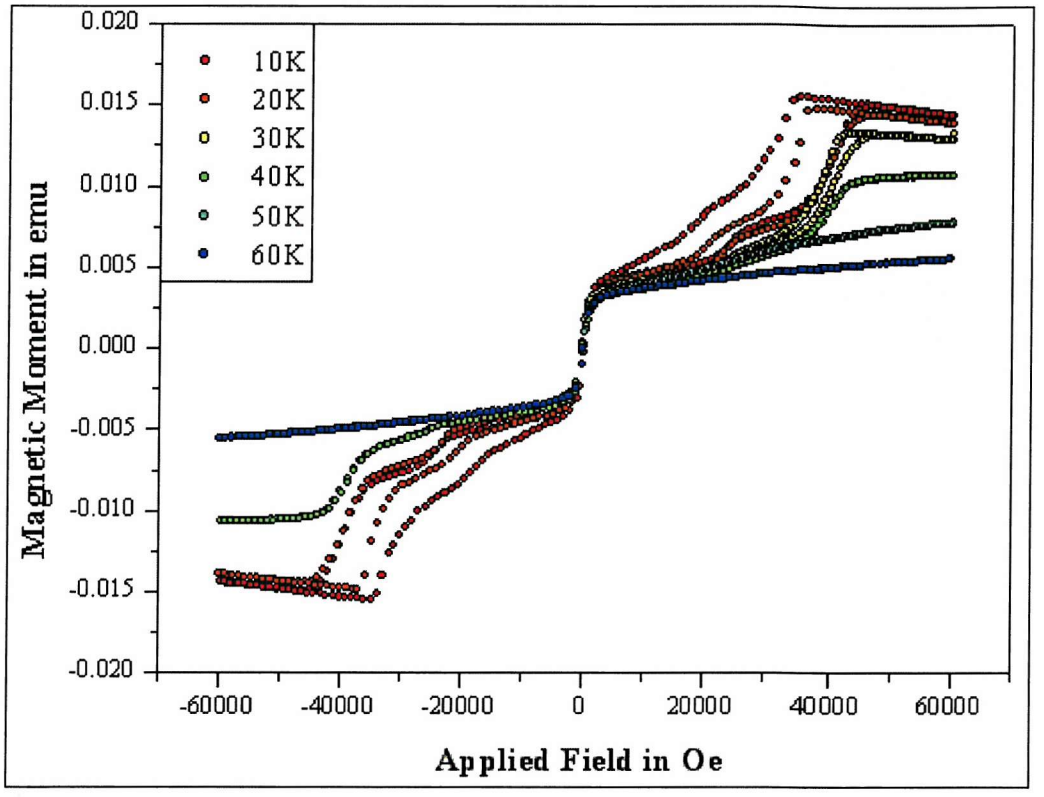

Figure 4-9. Magnetic Moment as a function of c-axis applied magnetic field at a range of temperatures for $(Tm_{20}/Lu_{40})_{50}$.

The additional magnetic phase transition was observed for the three thicker Tm/Y samples, Tm_{40}/Y_{20}, Tm_{20}/Y_{40}, Tm_{50}/Y_{10}, and all the Tm/Lu samples, except for Tm_6/Lu_{20}. The lower magnetic transition occurred between 1.7 and 2.5T; the higher magnetic transition occurred between 2.8 and 3.9T at 10K. There was no obvious pattern in the magnetic phase transition field, although samples containing more Tm had higher transition fields.

The additional magnetic phase transition is one of the novel findings of this research. Whilst it could be said with confidence that the highest region of the phase diagrams corresponds to ferromagnetic alignment of moments within the sample, the magnetic structures in the lower areas of the phase diagram are less obvious. This

uncertainty was the motivation for the neutron and complementary X-ray diffraction studies that followed.

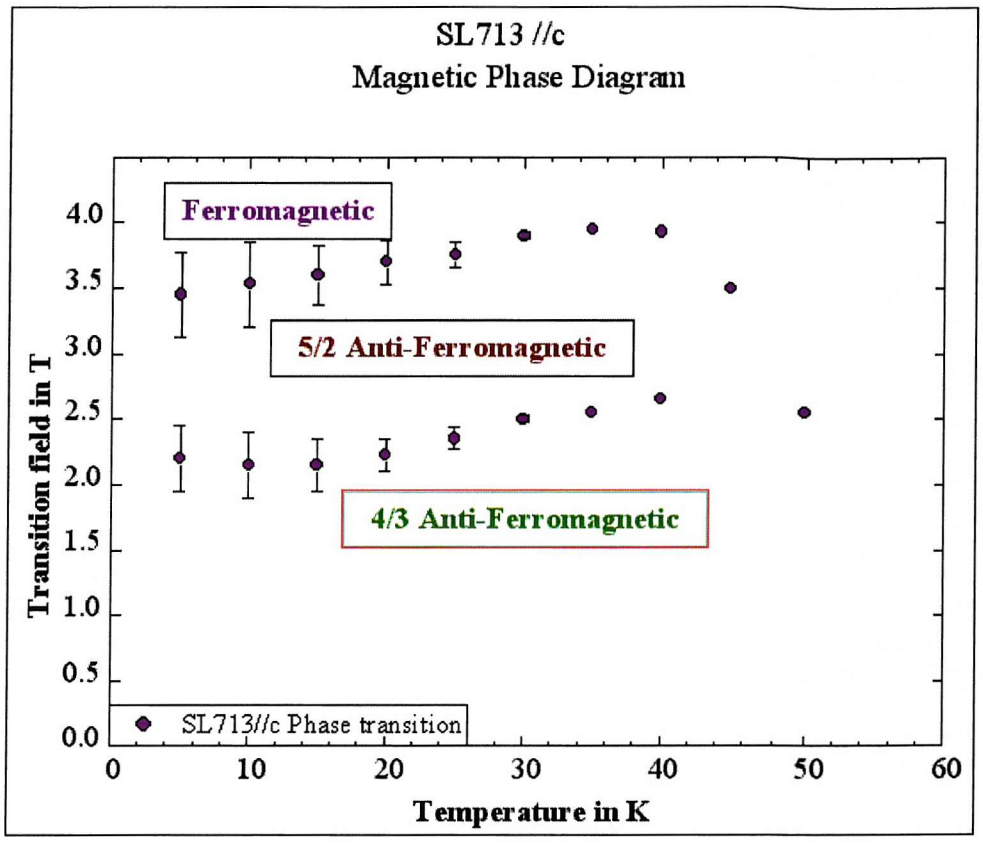

Figure 4-10. Phase diagram for SL713 with field parallel to c-axis. Error bars indicate difference between increasing and decreasing field sweeps.

Figure 4-10 is representative of the general form of the phase diagram for the thicker Tm/Y samples and the Tm/Lu samples (except Tm_6/Lu_{20}). It was thought most likely that the additional mid-region in the phase diagram corresponds to a magnetic structure within Tm layers where 5 consecutive moments aligned parallel to the field, along the *c*-axis, followed by 2 moments aligned anti-parallel. This 5up/2down structure would seem a natural variation on the 4up/3down structure observed in the bulk at low fields and temperatures [7].

An alternative explanation would be in terms of an anti-ferromagnetic interaction between neighbouring Tm superlattice slabs, which switch into ferromagnetic alignment at a certain field, as was observed for Gd/Y superlattices [31]. For this model, below the lower transition there is anti-ferromagnetic coupling between Tm slabs and a 4up/3down structure within the Tm slabs. The mid-range phase would then correspond to ferromagnetically aligned superlattice slabs, with the 4up/3down structure within the Tm slab. The higher transition would be the transition from the 4up/3down structure to ferromagetic alignment of Tm moments within the Tm slabs.

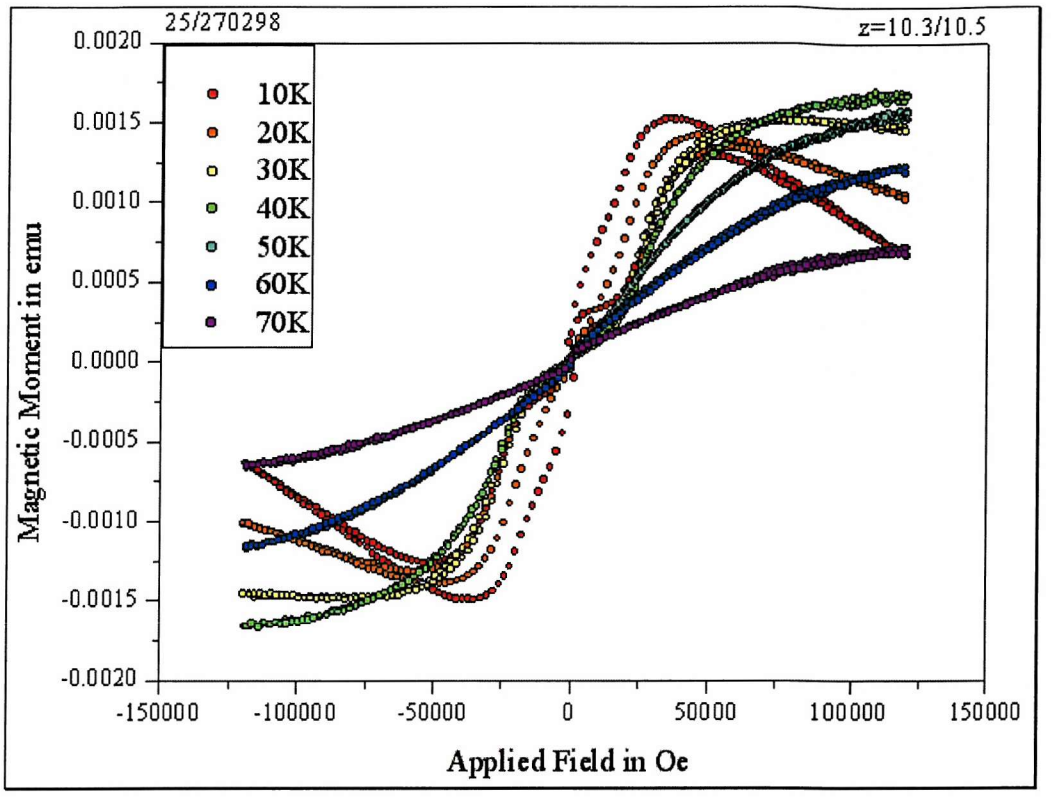

Figure 4-11. Magnetic Moment as a function of b-axis applied magnetic field at a range of temperatures for SL707

Figure 4-11 shows rather unexpected magnetic behaviour for SL707 for fields applied parallel to the b-axis. Although pure Tm is magnetically hard and exhibits no transitions for fields applied parallel to the b-axis [7], transitions were observed for all the samples except the alloy samples, Tm_{20}/Y_{20} and the Tm film. These magnetic phase transitions have been plotted against temperature, as for the c-axis field data, to form magnetic phase diagrams. The hysteresis surrounding the magnetic transition is broad at 10K, but closes much more rapidly with temperature than the hysteresis around the transition for c-axis applied fields.

The first question to answer is why some of the superlattices exhibit transitions and others do not. The Tm moments which normally order along the c-axis are pulled away from the c-axis by the applied field and a component of the moment is developed along the b-axis. It seems likely that the magnetic moments are not aligned perfectly along the c-axis for zero applied field. A likely reason is that the epitaxial strain reduces the uniaxial anisotropy so that moments are inclined at an angle to the *c*-axis, as for Er, and there is a component of the moment within the basal

plane. This would fit well with the idea of anti-ferromagnetic coupling between Tm slabs.

It is less clear why this effect is observed for Tm superlattices and not for pure Tm. It is assumed that the effect is, therefore, linked to either strain or interlayer coupling as these are the features that distinguish a Tm superlattice from pure Tm.

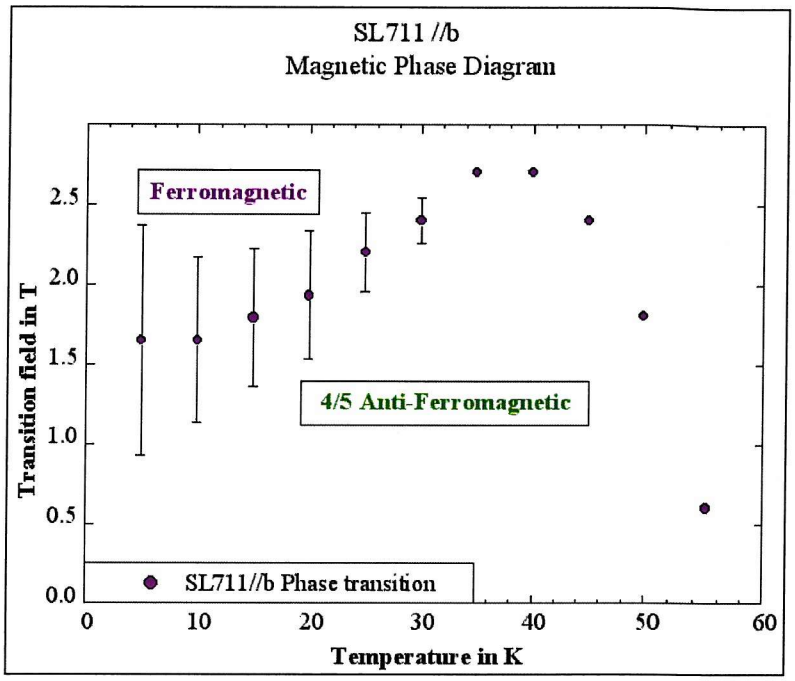

Figure 4-12. Phase diagram for SL711 with field parallel to b-axis. Error bars indicate difference between increasing and decreasing field sweeps.

Figure 4-12 is representative of the phase diagrams obtained for the samples that exhibited magnetic phase transitions for fields along the b-axis. Some samples had more exaggerated peaks, but all followed the basic form observed for the single magnetic transitions of bulk Tm [7].

With the exception of Tm_{20}/Y_6, samples that exhibited the double transitions for fields applied along the c-axis also exhibited the magnetic transition for fields along the b-axis. This is an interesting result that suggests that the in-plane component of magnetisation could be responsible for the additional transition, supporting the model of a canted 4up/3down structure with a net in-plane moment within each Tm slab and anti-ferromagnetic coupling between the in-plane moments of consecutive slabs.

Alternatively, there may be no appreciable anti-ferromagnetic coupling. The moments in the 4up/3down structure may be pulled away from the c-axis by the b-axis applied field and then switch to a ferromagnetically aligned structure with both c-

axis and b-axis components. It cannot be determined which of these models is most accurate from magnetisation measurements alone.

Sample	Nominal Structure	*c*-axis Transition Fields (T)	*b*-axis Transition Fields (T)
SL701	Tm_{20}/Y_6	3.1	1.7
SL702	Tm_6/Y_{20}	0.6	
SL703	Tm_{20}/Y_{20}	2.6	
SL706	Tm film	3.8	
SL707	Tm_{40}/Y_{20}	1.9, 3.37, 3.67	2.22
SL708	Tm_{20}/Y_{40}	1.73, 2.85	1.2
SL717	Tm_{50}/Y_{10}	2.14, 3.57	1.69
SL709	Tm_{20}/Lu_6	2.05, 3.61	1.74
SL710	Tm_6/Lu_{20}	1.37	
SL711	Tm_{20}/Lu_{20}	2.2, 3.6	1.65
SL712	Tm_{40}/Lu_{20}	2.34, 3.84	2.98
SL713	Tm_{20}/Lu_{40}	2.15, 3.53	1.54
SL719	Tm_{50}/Lu_{10}	2.495, 3.92	1.72

Table 4-2. Transition fields for Magnetisation versus Applied c-axis and b-axis magnetic field at 10K.

Table 4-2 summarises the magnetic phase transition fields for each of the samples and sample-field orientations at 10K. It illustrates the connection between double c-axis transitions and the unexpected b-axis transition. Figure 4-13 shows a plot of the c-axis transitions as a function of calculated epitaxial strain, assuming a composition weighted in-plane lattice parameter. There are insufficient data points to draw any strong conclusions, but the plot suggests that the transition fields are reduced as Tm is strained further away from its bulk lattice parameters.

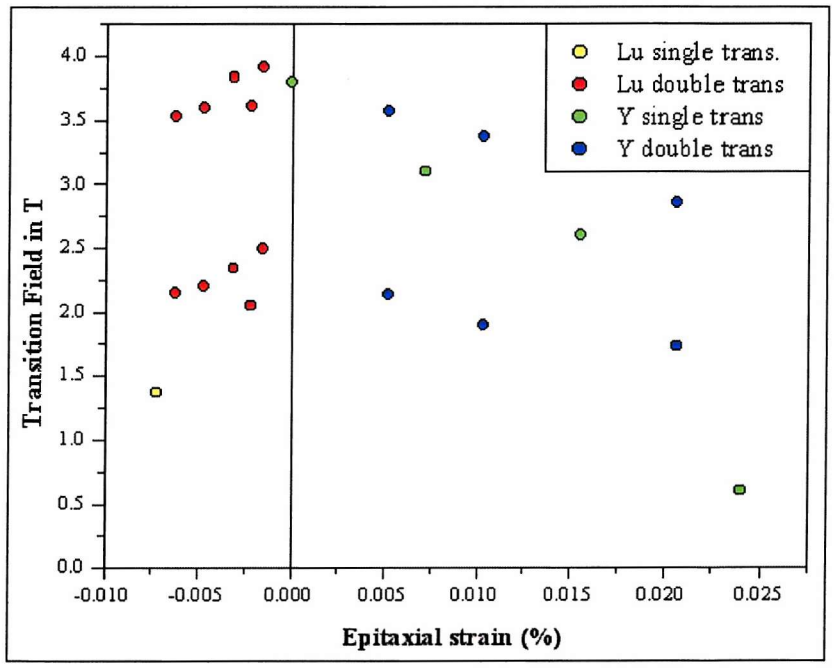

Figure 4-13 Phase transition at 10K as a function of calculated epitaxial strain

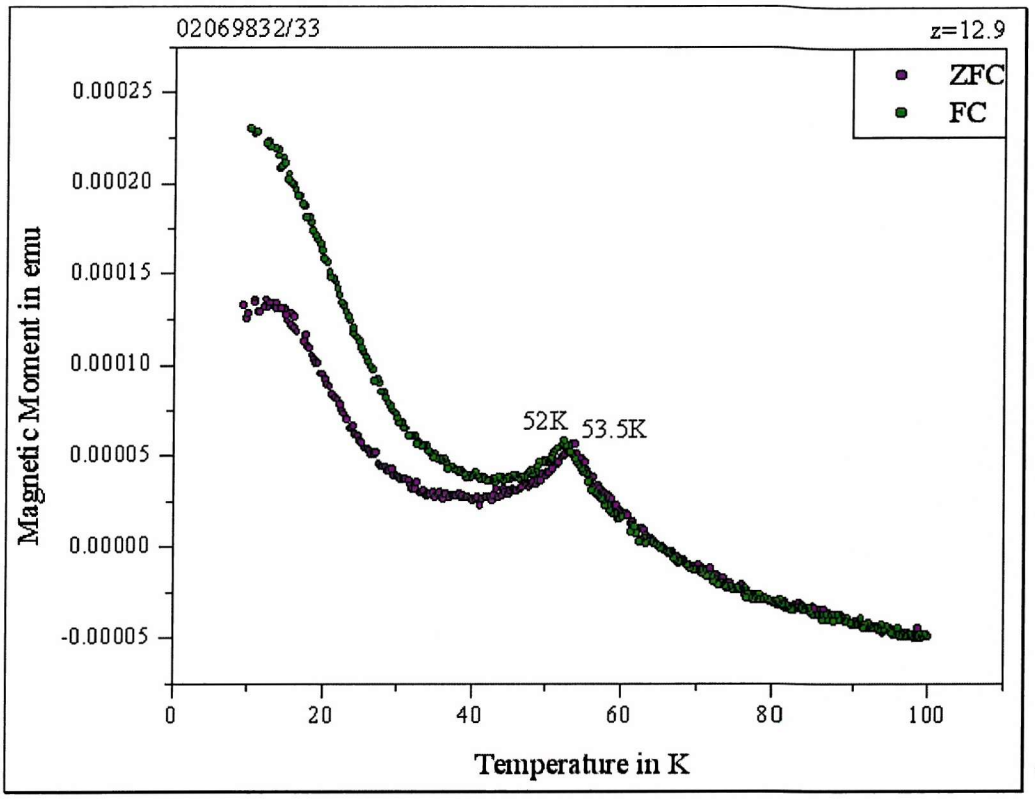

Figure 4-14. Magnetic Moment as a function of temperature with 0.1T applied magnetic field parallel to the c-axis for $(Tm_{20}/Lu_6)_{60}$.

Plots of magnetic moment with respect to temperature for an applied field of 0.1T for each superlatttice (for fields both parallel to b-axis and parallel to c-axis) may be found in Appendix A. A peak in the magnetic moment is observed for all zero field cooled (ZFC) temperature sweeps for fields parallel to the c-axis and most field-cooled (FC) temperature sweeps, this is illustrated in Figure 4-14. The peak is characteristic of a metamagnetic step and the discontinuity indicates a phase transition. Similar peaks are observed for temperature sweeps where fields of 0.1T were applied along the b-axis for the samples that also exhibited transitions in their magnetisation as a function of applied field graphs. These peaks occur at the Neél temperature and signify the on-set of magnetic ordering. A plot of Neél temperature as a function of epitaxial strain (Fig. 5-15), calculated from nominal structures, showed very little strain dependence. This is mainly because the exchange interaction, which determines the magnetic ordering temperature, is relatively unaffected by strain, unlike the crystal field which is demonstrated in Chapter 5 to be strain dependent.

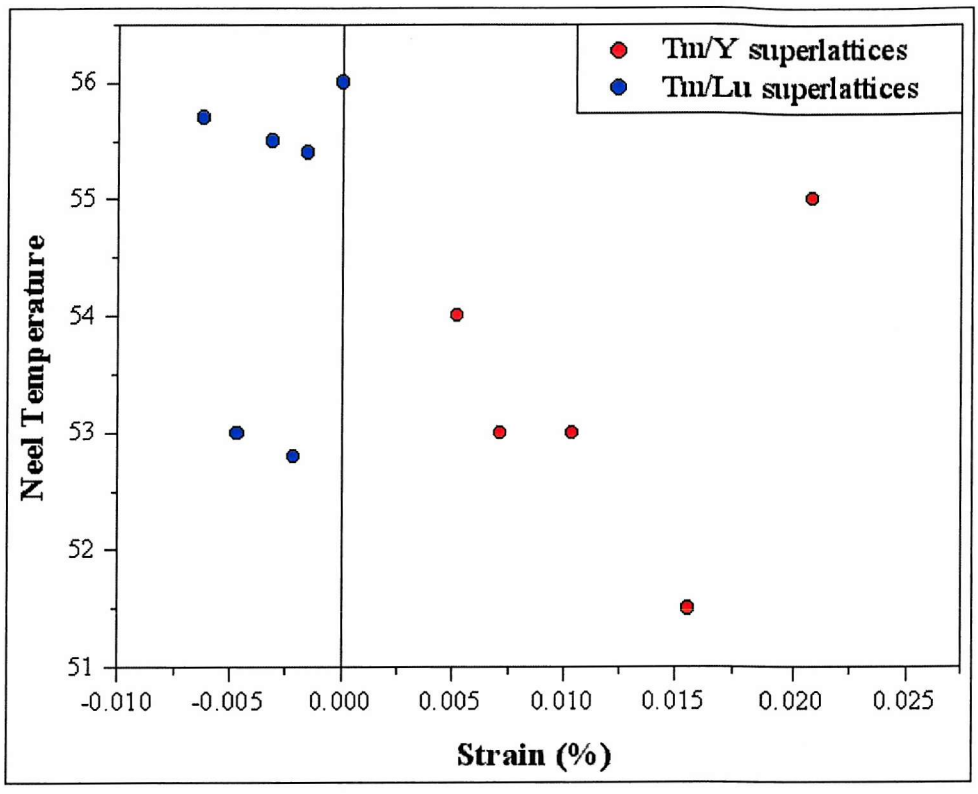

Figure 4-15. Neél temperature as a function of calculated strain for applied magnetic field parallel to the c-axis for Tm/Y and Tm/Lu superlattices.

It was hoped that a plot of saturation magnetisation (at a given temperature) as a function of number of Tm layers per bi-layer may give some indication of the form of the interlayer RKKY interaction, as was found for Gd/Y [30]. However, only a single point on the graph is contributed by each superlattice and these ten points reveal very little.

For plots of these sorts to be at all conclusive, many more superlattices need to be measured. Alternatively a different experimental technique, such as Magneto-Optic Kerr Effect (MOKE), using wedge shaped tri-layers may be used to investigate interlayer coupling as a function of spacer layer and of thulium layer thickness may be employed.

4.4 Conclusions

The magnetic phase diagrams of a range of Tm/Y and Tm/Lu superlattices have been constructed from measurements of magnetic moment vs applied field. These phase diagrams were more complex than that of bulk Tm for the thicker Tm/Y superlattices and all of the Tm/Lu superlattices, with the exception of Tm_6/Lu_{20} which is thought to be more of an alloy sample than a superlattice. An additional phase transition was observed, leading to 3-zone phase diagrams rather than the 2-zone phase diagrams of bulk Tm. The additional phase is thought to either be a phase for which Tm forms another localised magnetic structure, such as a 5up/2down anti-ferromagnetic square wave, or a phase for which there is anti-ferromagnetic coupling between Tm slabs which switch into ferromagnetic alignment at a certain field.

The second surprising result was that magnetic phase transitions were observed for in-plane applied magnetic fields, for the same range of samples that exhibited the additional phase transition for fields applied along the *c*-axis. This is very different to the behaviour of bulk Tm [7], which remains magnetically hard and exhibits no magnetic transitions for applied fields of up to 10T.

The *b*-axis magnetic behaviour is consistent with the model where there is an in-plane component of magnetisation that is antiferromagnetically coupled between successive Tm blocks. In order to establish a model that best describes the magnetic structures within these superlattices, neutron diffraction measurements were required. Nevertheless, it is clear that the epitaxial strain of a superlattice environment has a strong effect on the magnetic structures and behaviour of Tm.

Chapter 5

Magnetic structure determination using neutron diffraction

This chapter describes how elastic neutron diffraction measurements were performed in order to elucidate the magnetic structures of a range of Tm/Y and Tm/Lu superlattice samples. Section 5.1 presents the results from zero field neutron diffraction experiments. Section 5.2 presents the results from c-axis magnetic field neutron diffraction experiments. Section 5.3 presents the results from b-axis magnetic field neutron diffraction experiments. Conclusions are drawn in Section 5.4.

Introduction

The magnetisation measurements presented in Chapter 4 uncovered additional phases in the magnetic phase diagrams of Tm/Y and Tm/Lu superlattices for fields applied along the c-axis. Magnetic transitions were also discovered for fields applied within the basal plane. These unexpected results were the motivation for the neutron diffraction experiments described in this chapter. Neutron diffraction was used to deduce the magnetic structures in various regions of the phase diagram.
Elastic neutron scattering measurements, in zero applied magnetic field were performed at Risø National Laboratory, Denmark. Further experiments, employing vertical and horizontal magnets were performed at Institut Laue Langevin, Grenoble, France.

5.1 Zero field neutron diffraction

5.1.1 Experimental Details

Zero field neutron diffraction measurements were performed at Risø National Laboratory, Denmark by the author, J.P. Goff and D. F. McMorrow using apparatus and techniques described in Chapter 2, Section 2.3. For these experiments, neutrons with an energy of around 5 meV (corresponding to a wavelength of ~4Å) were selected. Beryllium filters were employed to filter out the λ/2 contamination.

Measurements for Tm/Y superlattice samples were performed on TAS1 using a variable temperature cryostat with a base temperature 1.8 K. Measurements for Tm/Lu superlattice samples were carried out on TAS7 using a closed-cycle cryostat with a base temperature of 6 K.

Sample Number	Superlattice Structure
SL715	$(Tm_{40}/Y_{20})_{52}$
SL716	$(Tm_{20}/Y_{40})_{52}$
SL717	$(Tm_{50}/Y_{10})_{52}$
SL718	$(Tm_{40}/Lu_{20})_{48}$
SL719	$(Tm_{50}/Lu_{10})_{48}$
SL720	$(Tm_{20}/Lu_{40})_{48}$

Table 5-1. Neutron Diffraction Samples

New superlattice samples were grown for neutron scattering measurements (See Table 5-1), using the apparatus and techniques described in Chapter 3 Section 3.1, because the set of samples SL701 to SL714 had been cut to approx. 5 mm square pieces for the magnetisation measurements that had happened previously. It was important to use larger samples for neutron scattering in order to present a greater sample surface area to the neutron beam and maximise counting statistics. The Tm_{40}/Y_{20}, Tm_{40}/Lu_{20}, Tm_{20}/Y_{40}, Tm_{20}/Lu_{40} structures were grown again. Tm_{50}/Y_{10} and Tm_{50}/Lu_{10} were also selected in order to investigate the extreme points on Kwo's[30] plot of saturation moment, and remanence, against Y spacer width for Gd-Y superlattices. These extremes correspond to maxima and minima in the exchange interaction [See Fig. 1-14].

For each sample, the basic measurements included:

- scans along [H00] through (1,0,0)
- scans along [00L] through (002)
- scans along [10L] through (100) and (101)

Depending on the results yielded by these scans, closer studies of magnetic features were performed as a function of temperature. This normally involved measurements of temperature dependence for either the (1,0,q) or the (1,0,1-q) first-order magnetic peak. In some cases, higher order harmonics were also measured.

The [H00] scans locate the position of (100) and this yields the in-plane lattice parameter. The [00L] scans locate the position in Q of the (002) peak, which gives the hcp (out-of-plane) c-axis parameter. From these locations in reciprocal space, any other scans and peaks could be referenced. The scans along [10L], from just before (100) up to the other side of the (101) peak, allowed observation and measurement of magnetic structures with periodicity parallel to the hcp c-axis.

Bulk Tm has a 7-atom 4up/3down square wave magnetic structure at base temperature and zero field [13,59]. This corresponds to magnetic satellites occurring at $\pm q$ in the [10L] scan, where $q=(2/7)\ Q_{(101)}$. Harmonics of these magnetic peaks were observed and measured, in some cases, at $\pm 3q$ and $\pm 5q$. The intensity of these magnetic peaks was measured as a function of temperature for these zero field measurements to investigate the changing magnetic structures.

5.1.2 [00L] scans

Scans along [00L] for Tm/Y superlattice samples showed a flat background between 1.0 and 2.1 $Å^{-1}$ and strong (002) nuclear peaks, modulated by superlattice periodicity, between 2.2 $Å^{-1}$ and 2.3 $Å^{-1}$. The superlattice features are strong for the Tm/Y samples because of the larger lattice mismatch between Tm and Y and the contrast in their scattering lengths. There were no signs of magnetic peaks in the [00L] scans for Tm/Y samples. This demonstrates that there is no observable magnetic moment parallel to the hcp basal plane direction for zero applied magnetic field at base temperature. Fig. 5.1 shows the [00L] scan for $(Tm_{20}/Y_{40})_{52}$; the similarity in the peaks at low and high temperature demonstrate that they are structural and not magnetic. The scans for $(Tm_{40}/Y_{20})_{52}$ and $(Tm_{50}/Y_{10})_{52}$ were very similar.

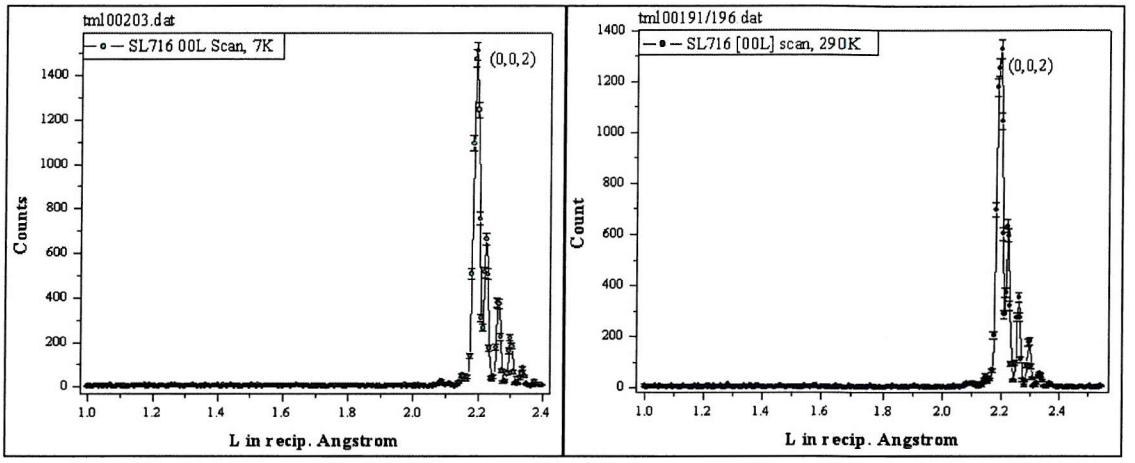

Figure 5-1. [00L] scan for $(Tm_{20}/Y_{40})_{52}$ at a) 7K and b) 290K

Scans along [00L] for the Tm/Lu samples were of similar form to the Tm/Y scans, but they contained an important extra feature. An additional peak was observed at around 1.96 $Å^{-1}$, indicating that there is a component of magnetisation within the basal plane, with a *c*-axis repeat pattern of about 7 atomic planes. This result supports the conclusions regarding in-plane components of magnetisation drawn from magnetisation measurements in Chapter 4. The magnetic peak is clearly observable for $(Tm_{40}/Lu_{20})_{48}$ and $(Tm_{50}/Lu_{10})_{48}$. It is less pronounced for $(Tm_{20}/Lu_{40})_{48}$; longer counting times would be necessary to determine its presence with certainty. Figure 5-2 displays the [00L] scan for $(Tm_{40}/Lu_{20})_{48}$.

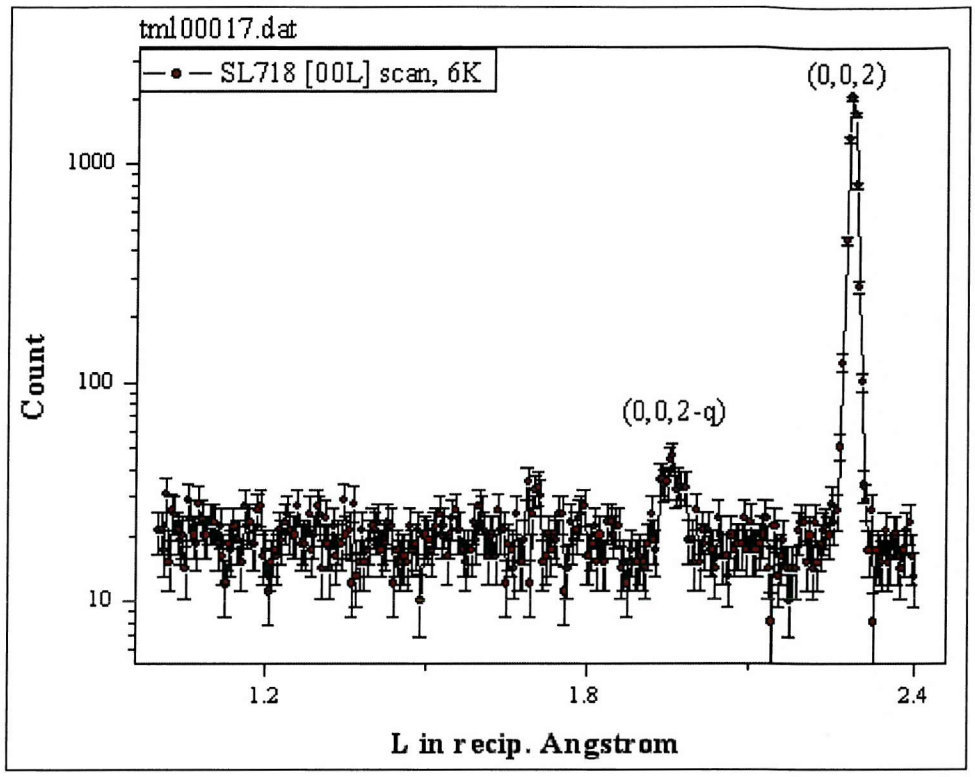

Figure 5-2. [00L] scan for $(Tm_{40}/Lu_{20})_{48}$ at 6K

The Tm/Lu [00L] scans had much smaller counting statistics than the Tm/Y scans. They also lacked the superlattice features around the (002) nuclear peak. This is because Tm and Lu have almost identical scattering lengths.

The magnetic peaks observed for $(Tm_{40}/Lu_{20})_{48}$ and $(Tm_{50}/Lu_{10})_{48}$ were investigated over a range of temperatures. Fig 5-3 shows these results for $(Tm_{40}/Lu_{20})_{48}$. The superlattice features split the magnetic peak so that there appears to be two peaks; thus complicating analysis. Fig 5-4 demonstrates how the magnetic peak was seen to die away with increasing temperature and Fig. 5- Fig 5-5 shows that it is locked in to a steady q value at low temperature. Fig 5-6 plots the width of the magnetic peak as a function of temperature, before corrections for instrumental resolution. The range of the magnetic order is seen to decrease and, at 6K, lock-in to a magnetic coherence length of about 413 Å, which is around 149 planes of Tm or 2.5 bi-layers. The results for $(Tm_{50}/Lu_{10})_{48}$ were similar, with a smoothly decaying intensity for increasing temperature, a peak position that increases and locks in to around 1.953$Å^{-1}$ at lower temperatures and a low temperature coherence length of

around 455 Å, which is around 164 planes of Tm or 2.7 bi-layers. This indicates that the in-plane component of magnetic order was coherent over several bi-layers.

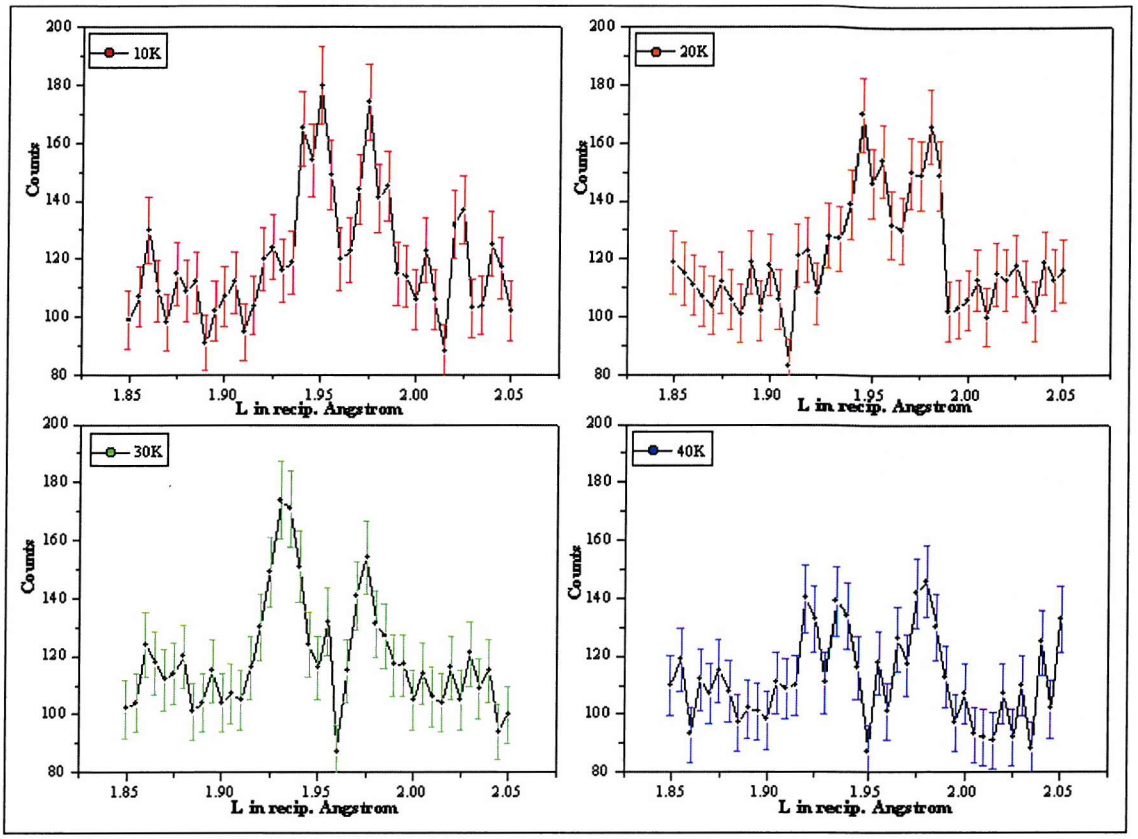

Figure 5-3. [00L] scan through the (0,0,2-q) peak for $(Tm_{50}/Lu_{10})_{48}$ at various temperatures

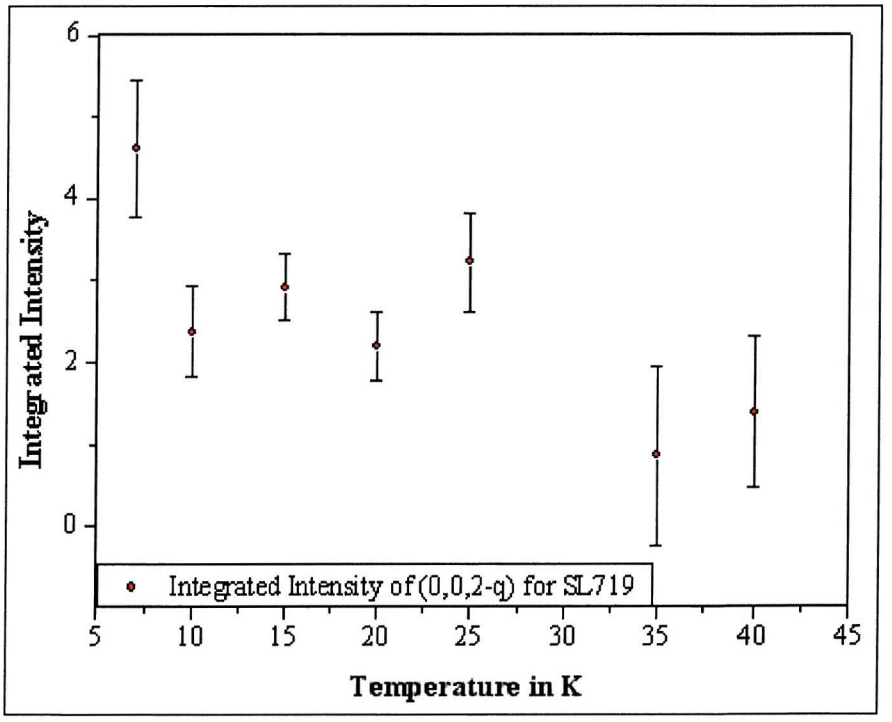

Figure 5-4. Integrated intensity of magnetic (0,0,2-q) peak for $(Tm_{50}/Lu_{10})_{48}$ versus temperature

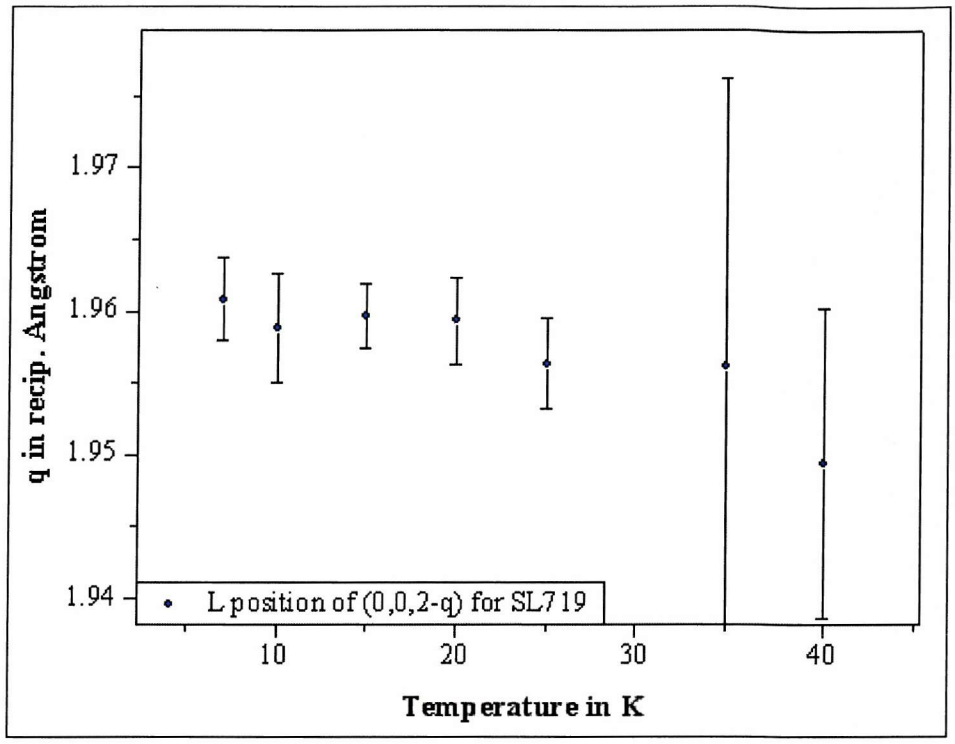

Figure 5-5. Position of magnetic (0,0,2-q) peak for $(Tm_{50}/Lu_{10})_{48}$ versus temperature

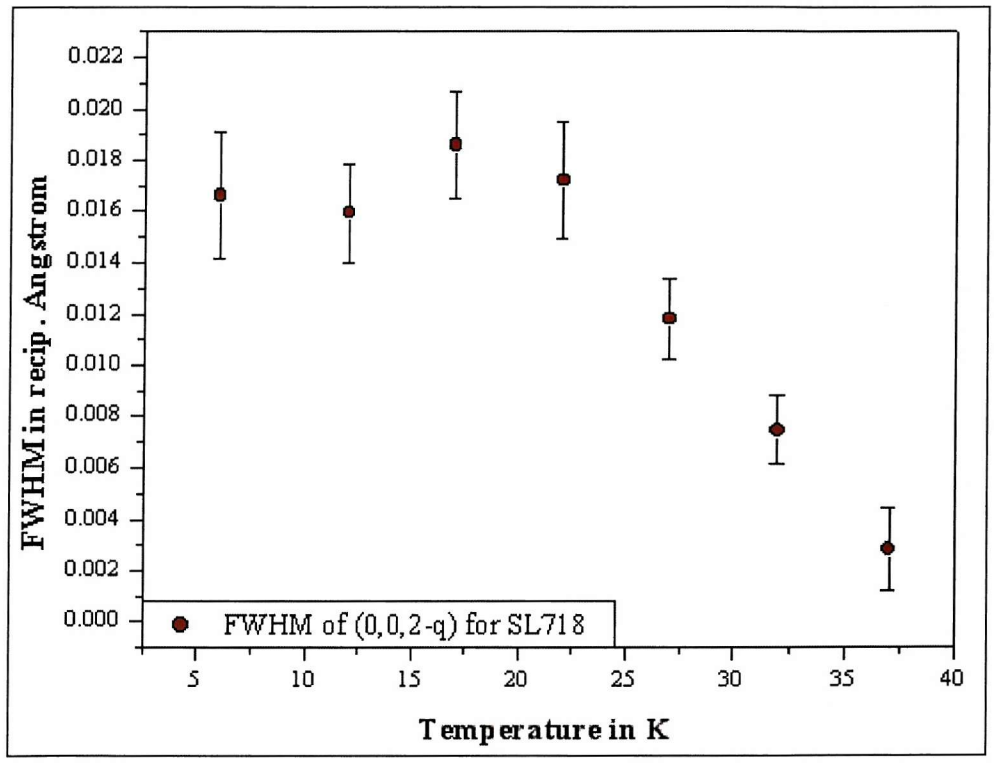

Figure 5-6. Width of magnetic (0,0,2-q) peak for $(Tm_{40}/Lu_{20})_{48}$ versus temperature

5.1.3 [10L] scans

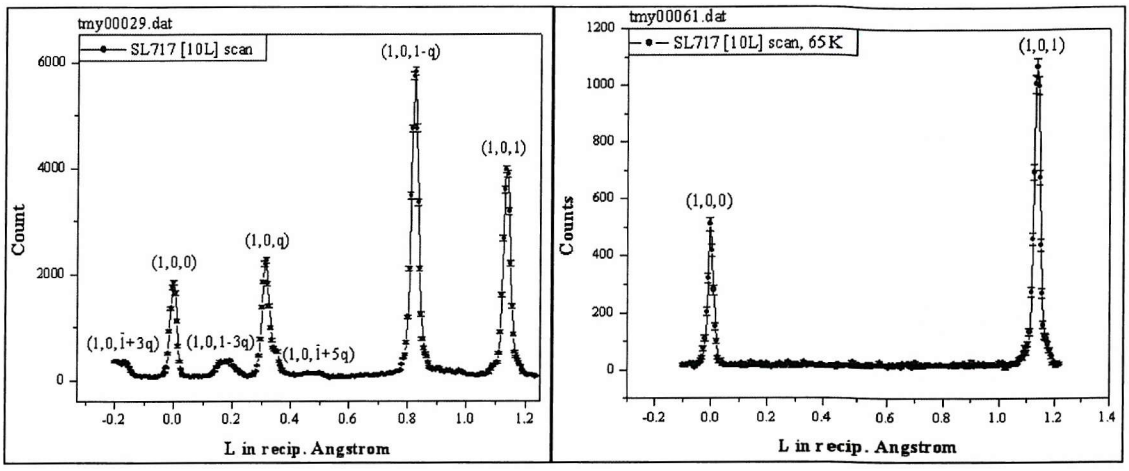

Figure 5-7. [10L] scan for $(Tm_{50}/Y_{10})_{52}$ at a) 1.8K and b) 65K

Figure 5-7 shows the [10L] scan from the (100) to the (101) nuclear peaks for $(Tm_{50}/Y_{10})_{52}$ at a base temperature of 1.8K. [10L] scans are sensitive to components of magnetisation both along the basal plane and the hcp *c*-axis. The scan shows clear first order magnetic peaks at L=0.32 $Å^{-1}$ and 0.82 $Å^{-1}$, corresponding to a 7 atom repeat magnetic structure aligned along the c-axis. There are also third and fifth order harmonics of the magnetic peaks, suggesting a square wave-like geometry of the magnetic structure. The [10L] scan for $(Tm_{40}/Y_{20})_{52}$ was very similar to that for $(Tm_{50}/Y_{10})_{52}$ in general form and relative intensities of chemical and magnetic peaks, although the counting statistics were less good for $(Tm_{40}/Y_{20})_{52}$ due to the lower Tm composition.

The base temperature [10L] scan for $(Tm_{20}/Y_{40})_{52}$ is shown in Fig. 5-8. It differs from the [10L] scans for the other Tm/Y samples in two ways. Firstly, the (1,0,1-q) magnetic peak is considerably smaller than the (101) chemical peak for $(Tm_{20}/Y_{40})_{52}$, whereas it was higher for the other Tm/Y sample. Secondly, the magnetic harmonics are not apparent. Both these effects are due to the relative Tm composition and, hence, the total magnetic moment of the sample.

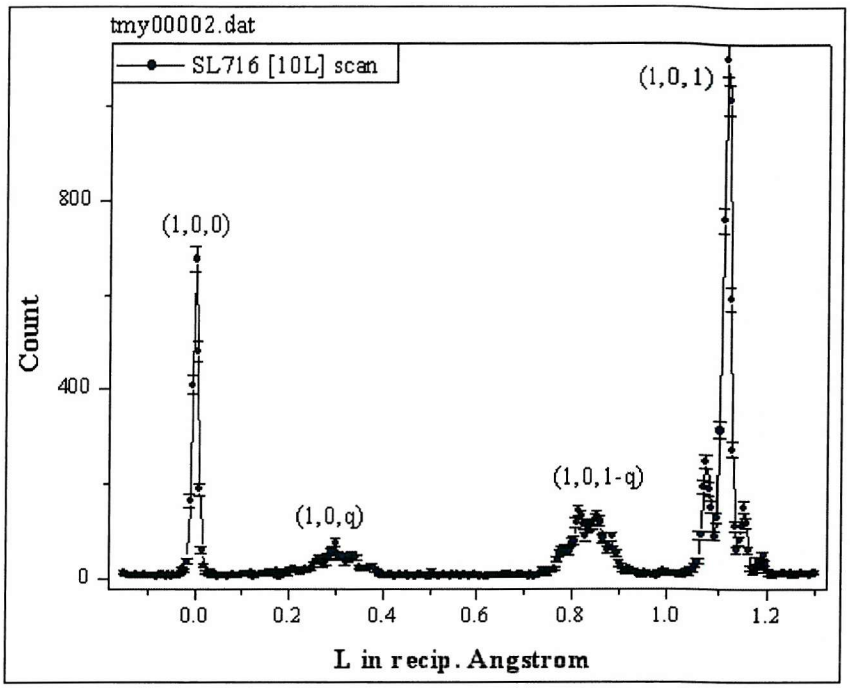

Figure 5-8. [10L] scan for $(Tm_{20}/Y_{40})_{52}$ at 1.88K

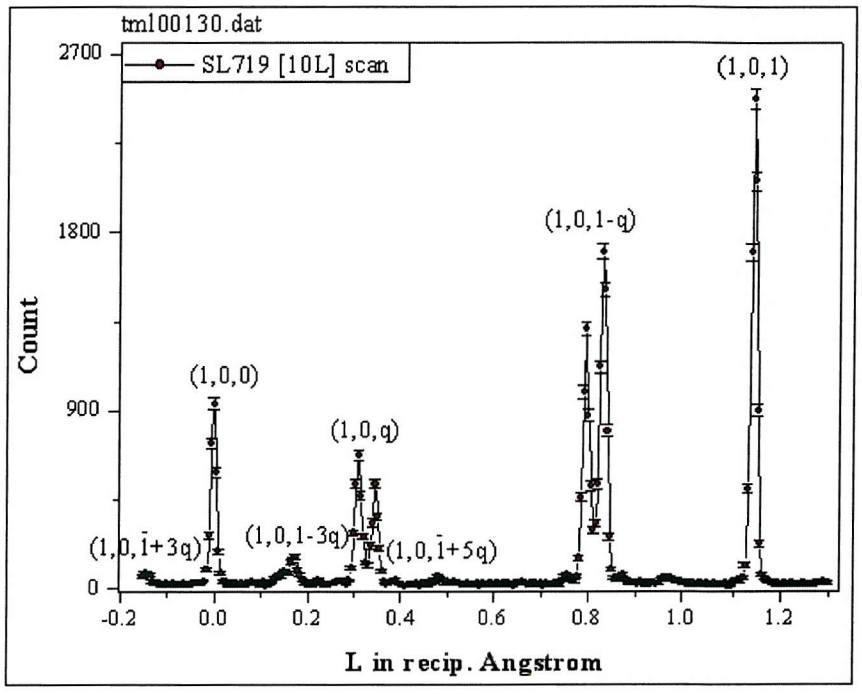

Figure 5-9. [10L] scan for $(Tm_{50}/Lu_{10})_{48}$ at 8K

Figure 5-9 displays the [10L] scan for $(Tm_{50}/Lu_{10})_{48}$ at the base temperature of 8K. It is similar to the scans for $(Tm_{40}/Y_{20})_{52}$ and $(Tm_{50}/Y_{10})_{52}$, displaying first, third and fifth order magnetic peaks in addition to the (100) and (101) nuclear peaks. The [10L] scan for $(Tm_{40}/Lu_{20})_{48}$ is very similar, although the lower Tm composition is reflected in poorer counting statistics. The harmonics are nevertheless apparent. The [10L] scan for $(Tm_{20}/Lu_{40})_{48}$, The [10L] scan for $(Tm_{20}/Lu_{40})_{48}$ (Fig 5-10), like that

for $(Tm_{20}/Y_{40})_{52}$, lacks the magnetic harmonics and peak intensities of the other Tm/Lu samples. This is again explained in terms of total Tm content of the sample and hence total magnetic moment. The base temperature [10L] scans for all three Tm/Lu samples show clear superlattice modulations to the magnetic peaks, suggesting coupling between the Tm blocks.

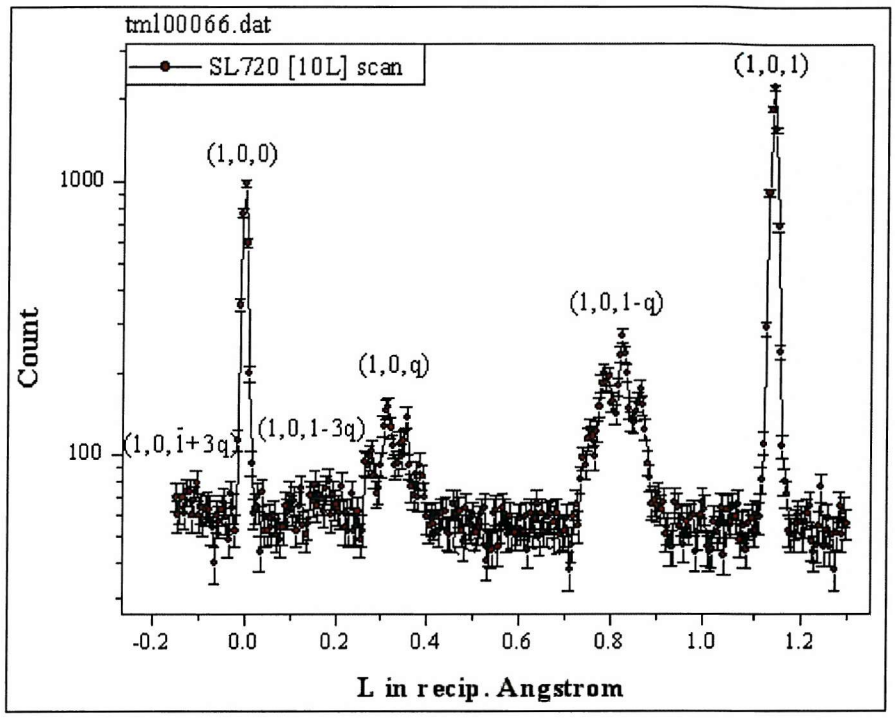

Figure 5-10. [10L] scan for $(Tm_{20}/Lu_{40})_{48}$ at 8.3K

The magnetic peaks were measured over a range of temperatures for each of the samples. In each case, the value of q was seen to increase and lock in to a steady value as temperature decreased, as shown in Fig. 5-13, corresponding to approximately 7 atomic planes of Tm. For the (1,0,q) peaks, this meant that the position along [00L] decreased with temperature, bringing the magnetic peak closer to the (100) structural peak. For the (1,0,1-q) peaks, this meant that the position along [00L] increased with temperature, bringing the magnetic peak closer to the (101) structural peak. Figure 5-11 demonstrates this for $(Tm_{40}/Y_{20})_{52}$. The amplitude of the (100) structural peak shows very little variation with temperature whilst the amplitude of the magnetic peaks smoothly decreased from a steady value at lower temperatures, as shown in Fig. 5-12.

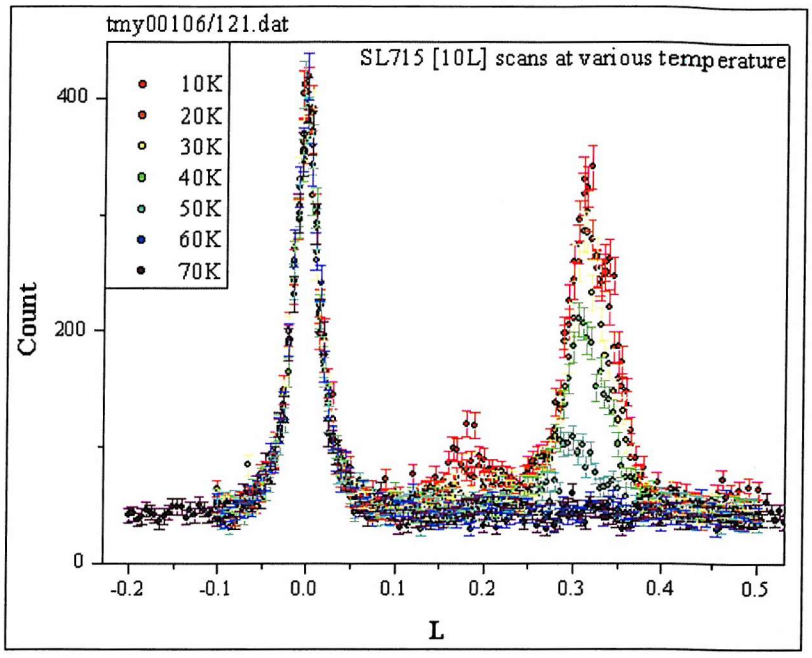

Figure 5-11. $(Tm_{40}/Y_{20})_{52}$ [10L] scans at temperatures between 10K and 70K

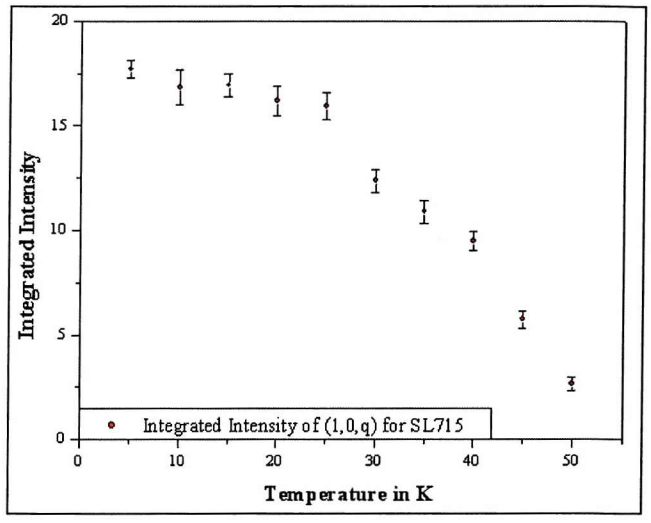

Figure 5-12. Integrated intensity of magnetic (1,0,q) peak for $(Tm_{40}/Y_{20})_{52}$ versus temperature

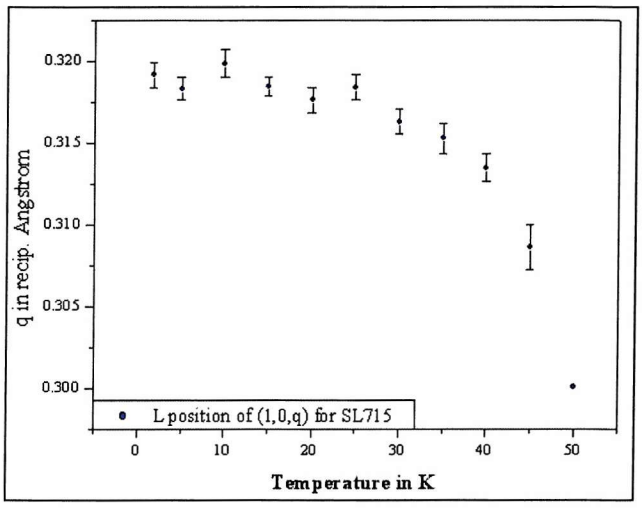

Figure 5-13. Position of magnetic (1,0,q) peak along [10L] for $(Tm_{40}/Y_{20})_{52}$ versus temperature

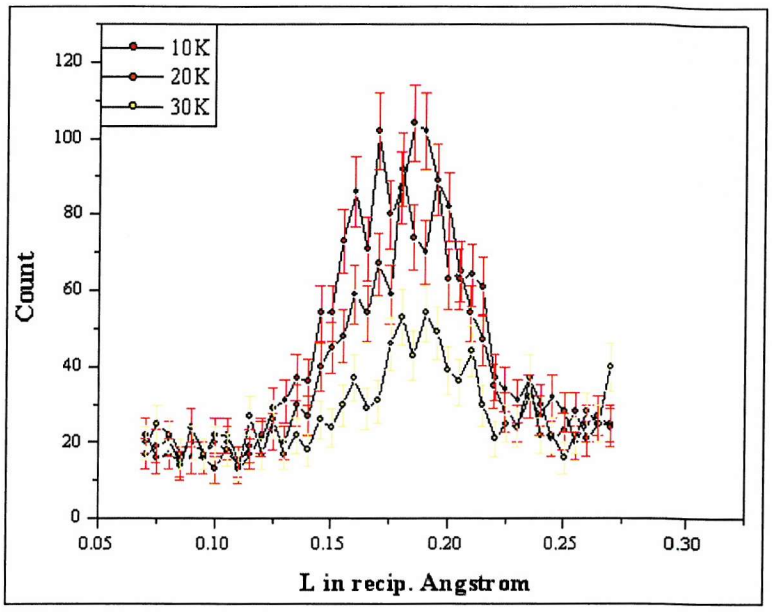

Figure 5-14. [10L] scan through the (1,0,1-3q) peak for $(Tm_{50}/Y_{10})_{52}$ at various temperatures

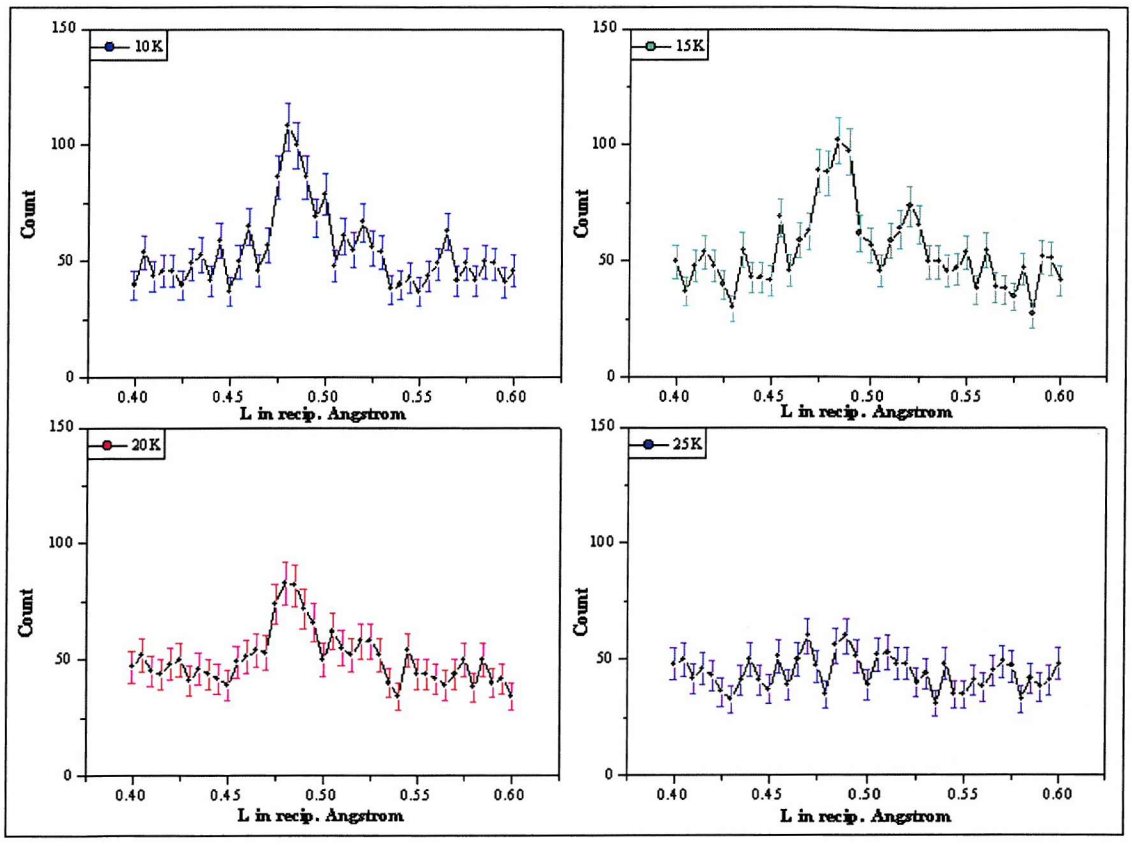

Figure 5-15. [10L] scan through the (1,0,-1+5q) harmonic for $(Tm_{50}/Lu_{10})_{48}$

Scans along [10L] through the third (Fig. 5-14) and fifth (Fig. 5-15) order harmonic magnetic peaks as a function of temperature showed that these harmonic peaks are only present beneath around 30K. The *c*-axis modulated magnetic structure in bulk Tm squares up from a smoother sinusoidal structure above 32 K [2,3] to form a square-wave structure below this temperature. The presence of the higher order

harmonics beneath 30K, for these Tm superlattices, is likely to indicate the same squaring-up process. Magnetic harmonic peaks were more prevalent amongst the samples with higher concentrations of Tm. $(Tm_{20}/Y_{40})_{52}$ exhibited no magnetic harmonics, whilst $(Tm_{50}/Lu_{10})_{48}$ had very clear third and fifth order harmonics. Third order harmonics were clearly observed for the remaining samples.

The width of the first order magnetic peaks is related to the magnetic coherence length according to:

$$\text{Magnetic coherence length} = 2\pi/w_{(\text{mag. peak})}$$

The magnetic coherence length has been calculated from the [10L] scans for each of the samples. The results of these calculations are presented in Fig. 5-16, with instrumental resolution accounted for. The magnetic coherence length appears to have some dependence on the Tm thickness within the spacer layer, although the spacer thickness was not constant for the samples. The superlattices with thicker Tm also have thinner spacer layers and it is this that gives the greater coherence length. Dependence of interlayer coupling on ferromagnetic layer thickness has been found in other systems [39,40,41,42], although not all publications report dependence of this kind [36]. The magnetic coherence lengths indicate that magnetic coherence is close to a single bi-layer for Tm_{20} samples, but is propagated across 2 to 4 bilayers for the samples with 40 or more atomic planes of Tm/bilayer and spacer layers of 20 planes or thinner.

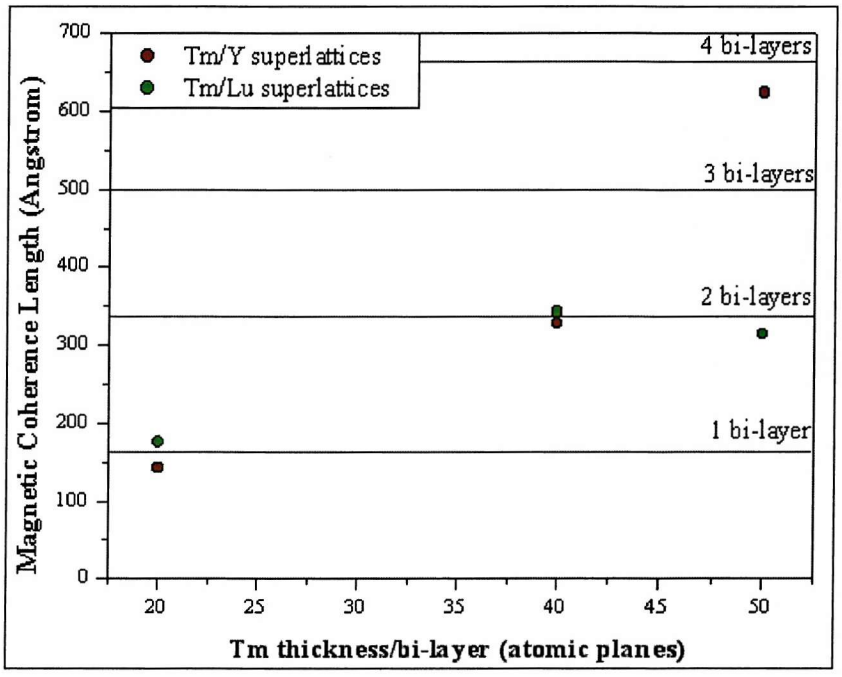

Figure 5-16. Magnetic coherence length as a function of Tm thickness/bi-layer (corrected for instrumental resolution)

	Base temperature		>65°		% change
Sample	$L_{(101)}$ in $Å^{-1}$	c in Å	$L_{(101)}$ in $Å^{-1}$	c in Å	in c
$(Tm_{40}/Y_{20})_{52}$	1.13412	5.540	1.13098	5.556	+0.29
$(Tm_{20}/Y_{40})_{52}$	1.10656	5.678	1.10795	5.671	-0.12
$(Tm_{50}/Y_{10})_{52}$	1.13672	5.527	1.135	5.536	+0.16
$(Tm_{40}/Lu_{20})_{48}$	1.14043	5.509	1.13153	5.553	+0.80
$(Tm_{50}/Lu_{10})_{48}$	1.14087	5.507	1.13839	5.519	+0.22
$(Tm_{20}/Lu_{40})_{48}$	1.13921	5.515	1.13302	5.546	+0.56

Table 5-2 Chemical structure at base temperature and over 65 degrees

Scans along [10L] were performed both at base temperature, which was 1.8K for the Tm/Y experiments carried out on TAS1 and around 6K for the Tm/Lu measurements, and also at temperatures above 65 °. Table 5-2 illustrates how scans along [10L] at base temperature and at temperatures above 65° reveal a change in the c-axis parameter with temperature. The % change is of the same order as the epitaxial strain.

5.2 c-field neutron diffraction

5.2.1 Experimental Details

Neutron diffraction measurements in *c*-axis fields of up to 5T were performed at Institut Laue Langevin, Grenoble, France by the author, J.P. Goff, B. D. Rainford and G. J. McIntyre using apparatus and techniques described in Chapter 2, Section 2.3.

The motivation for these measurements was the experiments that had gone before. Magnetisation and zero-field neutron studies had yielded interesting results which could be investigated further with neutron diffraction in a magnetic field. Magnetisation measurements revealed extra magnetic phases in the phase diagram for some samples and magnetic moments and transitions for fields applied along the basal plane. Zero field neutron scattering demonstrated that, for at least $(Tm_{40}/Lu_{20})_{48}$ and $(Tm_{50}/Lu_{10})_{48}$, a component of magnetisation exists parallel to the basal plane for zero applied field.

In order to make the best use of the 7 days ILL neutron time available for this experiment, the experimental focus was restricted to a single sample, SL718 $(Tm_{40}/Lu_{20})_{48}$. SL712, a sample with the same nominal composition as SL718, had exhibited a double magnetic transition for fields along c-axis and a clear single transition for fields along b-axis during magnetisation measurements. SL718 had shown a component of magnetisation parallel to the basal plane for zero applied field during zero field neutron measurements.

Working with a horizontal magnet seriously restricted the regions of reciprocal space that were accessible and not obscured by pole pieces of the magnet. It was possible to reach the (0,0,2) peak for [00L] scans and the (2,0,-3) and (2,0,-4) for [20L] scans, although intensity was diminished by the form factor; measurements were performed over these ranges for magnetic fields applied along the c-axis up to 4.5T. Neutrons of wavelength 1.53 Å were chosen and a pyrolytic graphite filter was used to filter out $\lambda/2$ contamination.

5.2.2 20L measurements

Scans along [20L] for magnetic fields applied along the c-axis of $(Tm_{40}/Y_{20})_{48}$ showed a fairly noisy background, strong nuclear peaks and weaker magnetic peaks, modulated by superlattice periodicity. The intensity of the (2,0,-3) was significantly greater than the (2,0,-4), and increased with applied field. This demonstrates that there is a ferromagnetic component of magnetisation that increases with applied field.

The intensity of the (2,0,-3-q) magnetic peak increased up to 1.6T, but decreased at higher fields. This indicates that the anti-ferromagnetic component of magnetisation along the c-axis increases with applied field up to a certain applied field and then dies away. This would be consistent with a metamagnetic phase transition from a 4up/3down magnetic structure to a completely ferromagnetically aligned state, as for bulk Tm [7].

Figs. 5-17 shows the [20L] scans for this sample at base temperature, with an applied field of 1T. The scans at higher fields were of a similar form, but with peak intensities that varied as previously described. The peak at (2,0,-3.05) is a powder line.

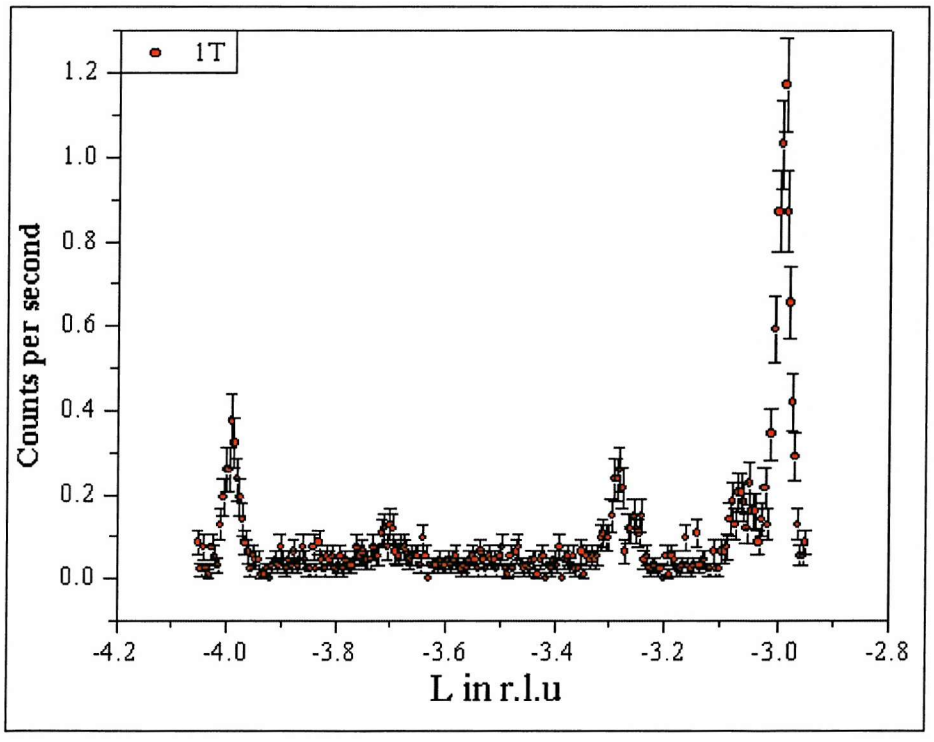

Figure 5-17. [20L] scan for $(Tm_{40}/Y_{20})_{48}$ at 2K and 1T

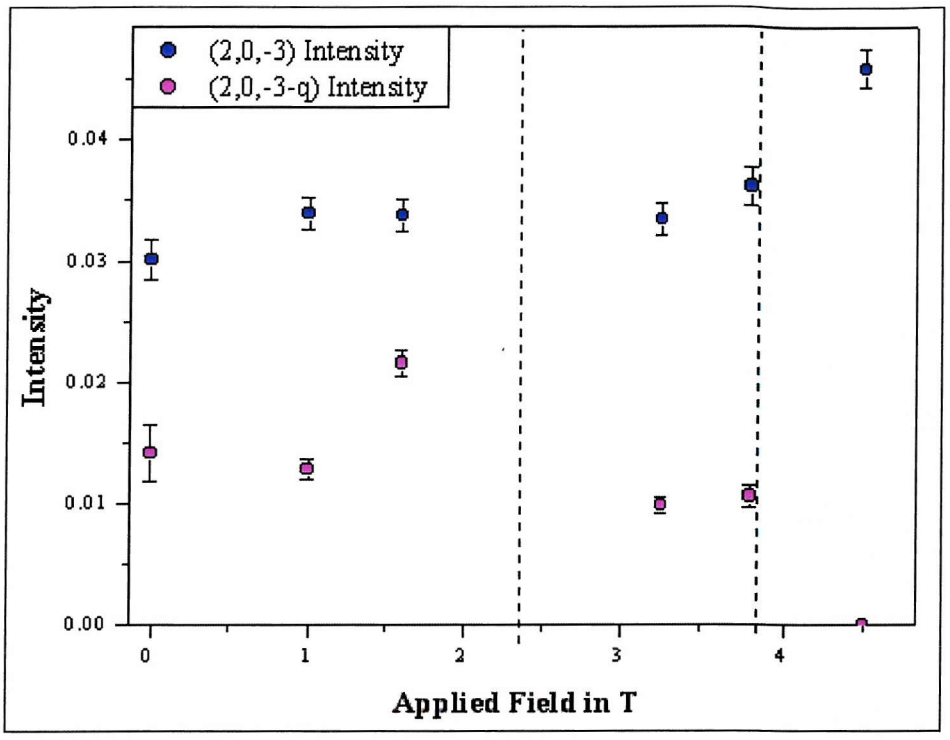

Figure 5-18. Intensity of the [20L] (2,0,-3) and (2,0,-3-q) peaks as a function of applied c-axis field for $(Tm_{40}/Lu_{20})_{48}$

Figure 5-18 plots the intensity of the structural and magnetic peaks observed in the [20L] scans as a function of applied field along the hcp *c*-axis. The dotted lines at 2.34T and 3.84 indicate the fields at which SL712, a sample with the same nominal structure, exhibited magnetic phase transitions during magnetisation measurements. It is important to note that our X-ray measurements and modelling showed that there can be significant disparity between nominal and physical superlattice specification and so the magnetic phase transitions for SL718 may be quite removed from those of SL712. They are included in Fig. 5-18 as a guide to what may be expected.

The intensity of the magnetic (2,0,-3-q) peak demonstrates the magnitude of the anti-ferromagnetic component of magnetisation along the c-axis as a function of field. The three phases for the anti-ferromagnetic component indicated in Figure 5-18 suggest a model with a 4-up/3-down structure below the first transition (~2.34T), a 5-up/2-down structure between the first and second magnetic transitions (~2.34 to 3.84T) and ferromagnetic alignment above the second transition. The presence of the magnetic peak at 3.2T and 3.8T confirms that the magnetic structure is ferrimagnetic in this phase. This supports the 5-up/2-down structure that is postulated.

The intensity of the (2,0,-3) peak includes both the structural reflection and the zeroth order magnetic reflection, corresponding to the magnitude of the ferromagnetic component of magnetisation.

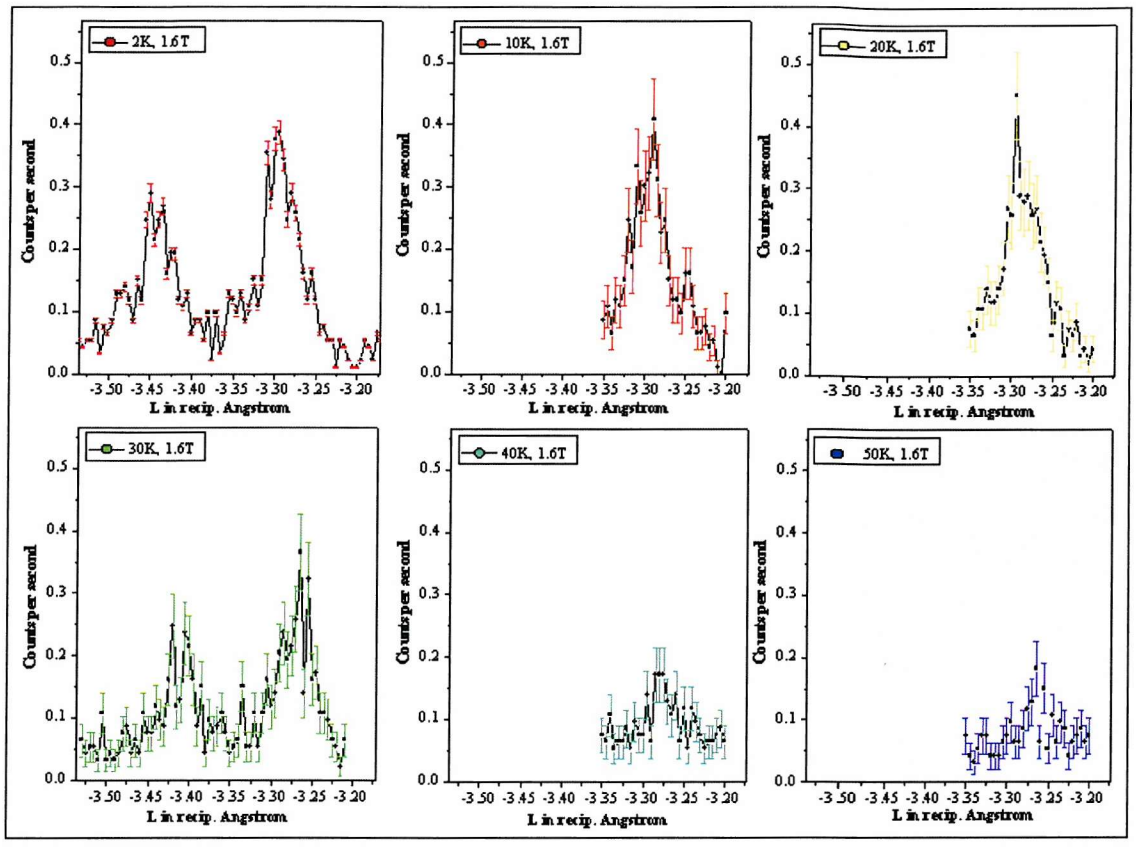

Figure 5-19. $(Tm_{40}/Lu_{20})_{48}$ (2,0,-3-q) magnetic feature at 1.6T and a range of temperatures

Figure 5-19 plots the magnetic peak observed in the [20L] scan at various temperatures for a constant applied field of 1.6T. The intensity of this peak was significantly greater at 1.6T than for lower or higher fields, so it was important to establish that it was a magnetic feature and to establish its temperature dependence. Omega scans eliminated the possibility of powder contributions. The intensity decreased with increasing temperature, whilst q decreased, consistent with the lock-in of magnetic order observed in earlier zero field measurements.

Figure 5-20 shows how the magnetic coherence length, obtained from the width of the (2,0,-3-q) magnetic peak, varies with applied magnetic field along the *c*-axis. The dotted lines at 2.34 and 3.84 correspond to the phase transition fields for SL712, a sample with the same nominal superlattice specification. The coherence increases from approx. 2.5 bilayers at zero field to around 4 bilayers at 3.2T. At 3.8T the coherence length is less than two bi-layers. At this field the sample is likely to be

mid-transition from a 5up/2down ferrimagnetic structure to ferromagnetic alignment. By 4.5T, there is ferromagnetic alignment throughout the sample and so no (2,0,-3-q) peak is observed.

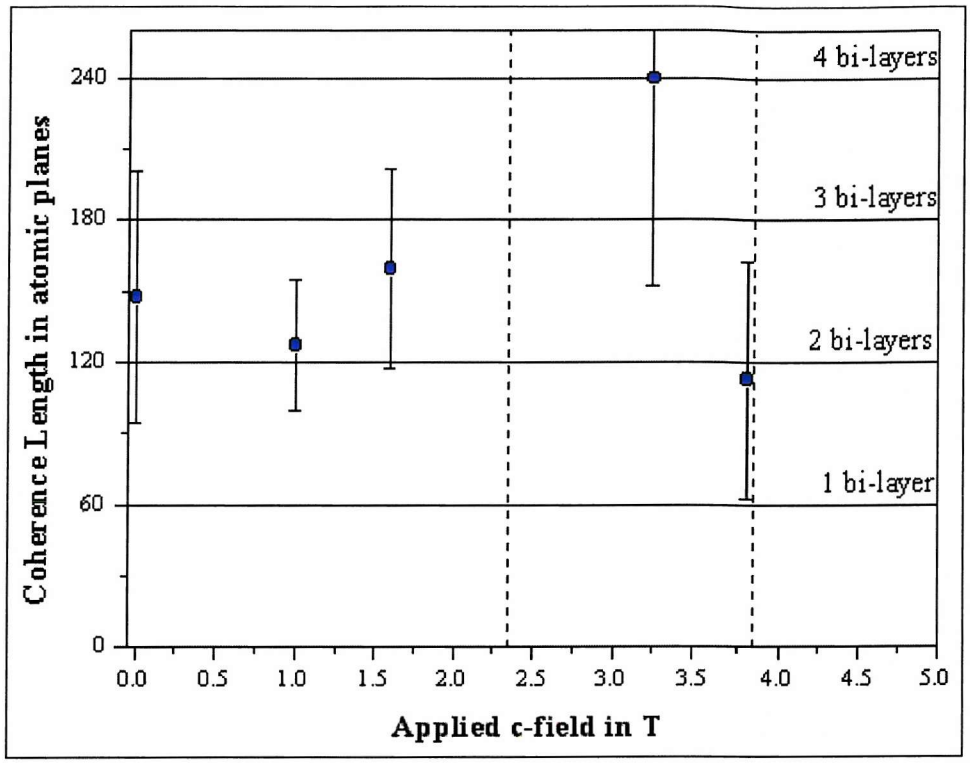

Figure 5-20. Magnetic coherence length as a function of applied c-field for $(Tm_{40}/Lu_{20})_{48}$.

5.2.3 00L measurements

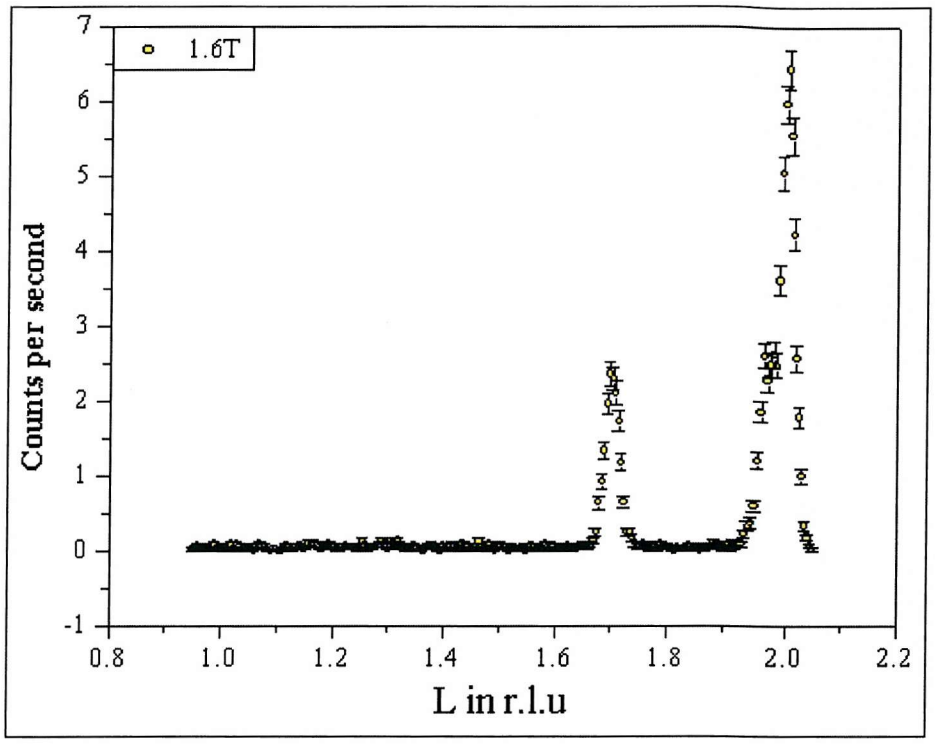

Figure 5-21. [00L] scan for $(Tm_{40}/Lu_{20})_{48}$ at 2K and 1.6T

Scans along [00L] at base temperature for $(Tm_{40}/Lu_{20})_{48}$ showed a flat background with well-defined structural peaks and peaks at (0,0,1.7) for applied c-fields of 0T and 1.6T. The superlattice modulations that were observed for zero field and [20L] c-field magnetic peaks are not particularly evident here. This may be due to counting statistics or because there is no pattern in the long-range magnetic structure that relates to the c-axis periodicity of the superlattice.

The peak at (0,0,1.7) turned out to be a powder peak that appeared following a helium fill. An omega scan confirmed this. The peak was no longer present after the temperature was raised above 80K and the chamber evacuated.

The magnetic peak that was expected in this region, and had been observed for the zero field measurements at Riso, was not observed due to insufficient sensitivity.

5.3 b-field neutron diffraction

5.3.1 Experimental Details

Neutron diffraction measurements in *b*-axis fields of up to 4.5T were performed at Institut Laue Langevin, Grenoble, France by the author, J.P. Goff, B.D. Rainford and G.J. McIntyre using the apparatus and techniques described in Chapter 2, Section 2.3.

The motivation for these measurements was the experiments that had gone before. Magnetisation measurements had revealed extra magnetic phases in the phase diagram for some samples and magnetic moments and transitions for fields applied along the basal plane. Zero field neutron scattering demonstrated that, for at least $(Tm_{40}/Lu_{20})_{48}$ and $(Tm_{50}/Lu_{10})_{48}$, a component of magnetisation exists parallel to the basal plane for zero applied field. Neutron diffraction measurements for fields applied along the *c*-axis had led to the interpretation of the extra *c*-axis phase in terms of a 7-layer repeat CAM structure with 5 moments aligned along the c-axis and 2 moments aligned anti-parallel, with in-plane components that are reduced with increasing *c*-fields.

Having established the magnetic behaviour of sample $(Tm_{40}/Lu_{20})_{48}$ for fields along the *c*-axis, the corresponding behaviour for in-plane magnetic fields was studied in this experiment.

Working with the vertical magnet restricted the regions of reciprocal space that were accessible and not obscured by pole pieces of the magnet, although access to the scattering plane is much better for the vertical than the horizontal magnet. It was possible to reach the (0,0,2) peak for [00L] scans and the (-1,-1,2) and (-1,-1,3) for [-1,-1,L] scans; measurements were performed over these ranges for magnetic fields applied along the *b*-axis up to 4.5T.

Neutrons of wavelength 2.36 Å were chosen and a pyrolytic graphite filter was used to filter out $\lambda/2$ contamination.

5.3.2 Results

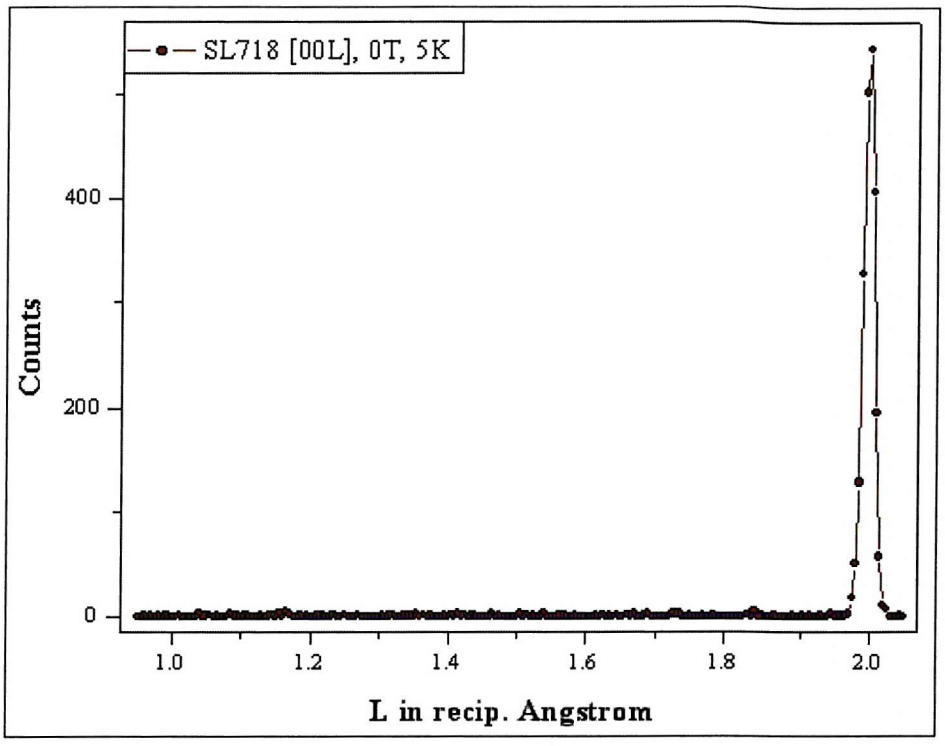

Figure 5-22. [00L] scan for $(Tm_{40}/Lu_{20})_{48}$ at base temperature for zero applied field

Scans along [00L] at base temperature for zero applied field did not feature the (0,0,2-q) magnetic peak observed for previous measurements. Figure 5-22 demonstrates this. Scans at fields up to 5T were equally flat in the region where the (0,0,2-q) was expected. This meant that the antiferromagnetic component of magnetisation could not be studied.

The intensity of the [002] contains intensity due to the chemical structure and intensity due to the ferromagnetic component of magnetisation. Measurements of the [002] as a function of applied field at base temperature demonstrate the development of the in-plane component of magnetisation with applied *b*-field. Fig. 5-23, a plot of [002] intensity as a function of applied field, illustrates this. Given the anisotropy of Tm, a basal-plane ferromagnetic component will be small and difficult to detect above the nuclear peak. Domain effects may explain why this plot does not indicate a smooth relationship between applied *b*-field and in-plane magnetisation. The dotted line in Fig. 5-23 corresponds to the field at which magnetic transitions were observed for SL712, a sample with the same nominal superlattice structure. There is no

dramatic increase in (002) intensity at this field, so a phase change in the local magnetic structure is not indicated.

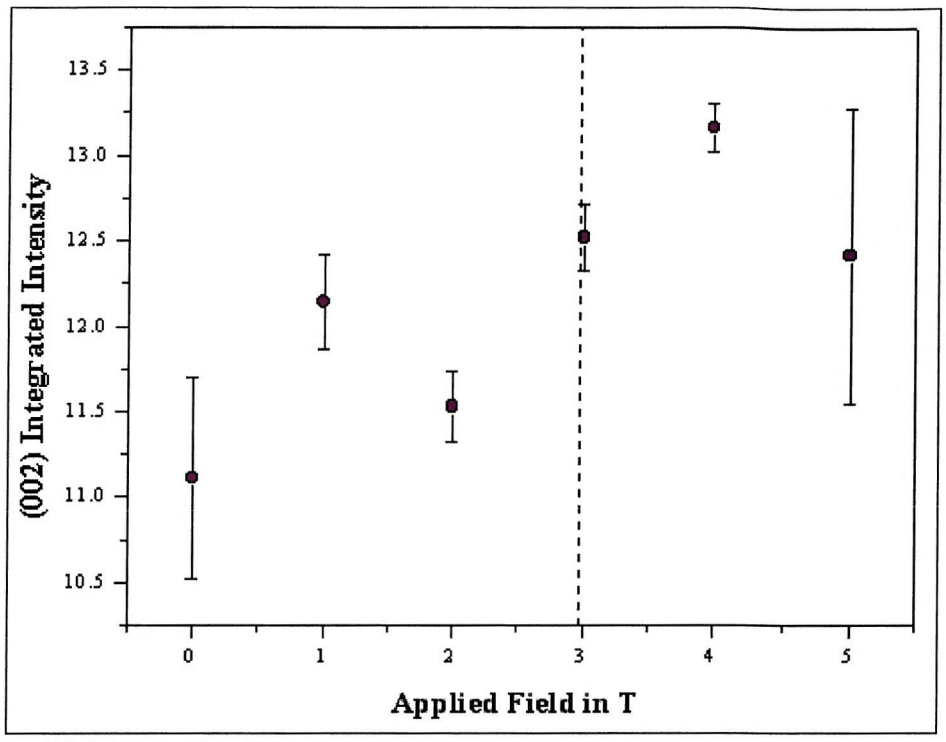

Figure 5-23. (002) intensity as a function of applied b-field

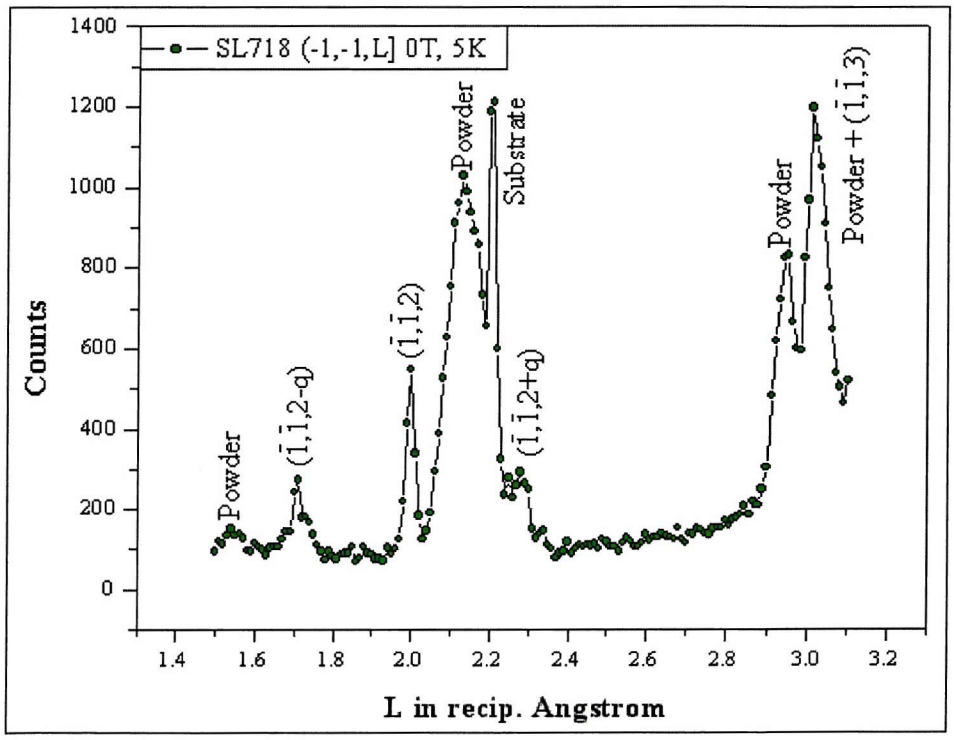

Figure 5-24. [-1,-1,L] scan for $(Tm_{40}/Lu_{20})_{48}$ at base temperature for zero applied field

Fig. 5-24 presents the [-1,-1,L] scan for $(Tm_{40}/Lu_{20})_{48}$ at base temperature and for zero applied field. The same scan at an applied *b*-field of 5T differed only in the intensity of the peaks. This is summarised in table 5-3.

Peak	0T Peak Intensity	5T Peak Intensity
(-1,-1,2)	12.02 ±0.48	13.81 ±0.77
(-1,-1,2+q)	9.85 ± 0.35	8.86 ±0.30
(0,0,2)	11.11 ± 0.59	12.42 ± 0.87

Table 5-3 Intensity of structural and magnetic peaks at 0T and 5T

The (0,0,2) and (-1,-1,2) increase with *b*-field due to an increase in the in-plane ferromagnetic component of magnetisation as the moments get pulled away from the c-axis towards the direction of the *b*-field. The (-1,-1,2+q) peak loses intensity because the *c*-axis component of magnetisation is diminished as this occurs.

5.4 Conclusions

Neutron diffraction measurements were performed in order to elucidate the magnetic structures of Tm/Y and Tm/Lu superlattices at a range of temperatures and for applied magnetic fields both within and orthogonal to the basal plane.

Zero field neutron measurements were performed for a range of Tm/Y and Tm/Lu superlattice samples. A magnetic peak at (0,0,2-q) was observed for Tm/Lu superlattices, but not for Tm/Y samples. This meant that the Tm/Lu superlattices had a component of magnetisation within the basal plane, with c-axis modulation of 7 atomic planes. The width of the (0,0,2-q) indicated that the magnetic order had a coherence length less than the bi-layer thickness.

Zero field [10L] scans demonstrated how magnetic order locks into a commensurate structure, at low temperature, with a 7 atom repeat distance and a coherence length of 2-4 bi-layers for samples with thin spacer layers and ~1 bi-layer for samples with thick spacer layers. Superlattice features in the magnetic peaks supported the model of antiferromagnetic coupling between Tm blocks.

Neutron diffraction measurements in applied *c*-axis fields were performed for only one sample. $(Tm_{40}/Lu_{20})_{48}$ was chosen for its anticipated 3-zone phase diagram and the clear b-axis component of magnetisation that had been identified for zero field neutron measurements. The intensity and position of the (0,0,2) and (0,0,2-q) peaks with *c*-field indicate that the Tm goes through 3 localised magnetic structures. At low fields there is the 7-plane CAM 4up/3down structure observed for bulk Tm [7] and at high fields there is ferromagnetic alignment along the *c*-axis. The intermediate phase is another 7-plane CAM structure, which is likely to be of the form 5up/2down. The presence of (2,0,L ± q) peaks in the [20L] scans for intermediate *c*-fields shows that there are antiferromagnetic components to the magnetic structure in this region.

Neutron diffraction measurements in applied *b*-fields were performed for the same sample as the *c*-field measurements, $(Tm_{40}/Lu_{20})_{48}$. The increase in the intensity of the (002) with applied *b*-field demonstrated the development of the ferromagnetic component of magnetisation within the plane for increasing *b*-fields, suggesting that the *b*-field pulls the canted magnetic moment further from the *c*-axis towards the *b*-axis.

The general picture of magnetic behaviour for Tm/Lu superlattices suggested by these neutron diffraction results is of a 4up/3down CAM structure at zero field,

where moments are canted so that there is an in-plane component of magnetisation for the CAM structure. Application of a *c*-field pulls the magnetic moments back towards the c-axis and drives metamagnetic transitions to firstly a 5up/2down CAM structure and then a ferromagnetic transition. Application of a *b*-field pulls the localised moments towards the b-axis.

Chapter 6

Conclusions

This chapter summarises the experimental results obtained in the course of this research and summarises their interpretation.

Introduction

The purpose of this research was to characterise the magnetic behaviour of a range of Tm/Y and Tm/Lu superlattices. This was initially achieved through detailed magnetisation measurements at the Dept. of Physics and Astronomy, Southampton University. Magnetisation measurements indicated that the magnetic behaviour of Tm superlattices can be more complex than that of bulk Tm. The additional magnetic phases and in-plane magnetic behaviour was investigated with neutron diffraction in zero field and fields orthogonal to and within the basal plane. X-ray diffraction and computer modelling of X-ray results were used to establish the chemical structure of the samples used for neutron measurements.

A model for the magnetic behaviour of a Tm superlattice in zero, *c*- and *b*-fields is presented.

6.1 Summary of research

This research has focused on the magnetic properties of rare earth superlattices, specifically thulium superlattices. A range of experimental techniques have been employed to magnetically characterise and analyse the magnetic behaviour of a range of Tm/Y and Tm/Lu superlattice samples.

As part of systematic studies of the magnetic phase diagrams of rare earth superlattices, we have been studying thulium superlattices with non-magnetic Y and Lu spacer layers [68,69,72,73,74,75,76]. All of the samples are single-crystal superlattices grown on sapphire substrates using molecular beam epitaxy at the Clarendon Laboratory. The chemical structures have been determined using detailed X-ray diffraction studies, which show that the superlattices form coherent hcp structures. The in-plane lattice parameters are found to be the same for both constituents of the superlattice, and the individual interplanar spacings were obtained by fitting the model of Jehan et al. to the intensities of the superlattice reflections [62].The c/a ratio is increased compared to pure Tm in Tm/Lu, whereas it is decreased for Tm/Y.

The bulk magnetisation has been studied using a vibrating-sample magnetometer at Southampton University, and the magnetic structures have been determined using neutron diffraction techniques. The zero-field neutron measurements were performed using triple-axis spectrometers at RISØ National Laboratory; energy analysis was used to separate the elastic magnetic diffraction from the inelastic background from the substrate and cryostat. Neutron scattering studies were also performed with a fields applied both in-plane and perpendicular to basal plane on D10 at the Institut Laue-Langevin, using vertical and horizontal superconducting cryomagnets.

The magnetisation studies have revealed some remarkable departures in the behaviour of the superlattices from that of pure Tm, the magnetic structures for which are illustrated in Figure 6-1. Firstly, for fields parallel to the c-axis, a double metamagnetic step is found: the first step is to roughly 50% of the saturation moment. Secondly, when fields are applied in the basal plane a large b-axis moment develops. This is an extraordinary result which implies that uniaxial anisotropy has been drastically reduced in the superlattice compared to bulk Tm, perhaps as a consequence of epitaxial strain which alters the c/a ratio.

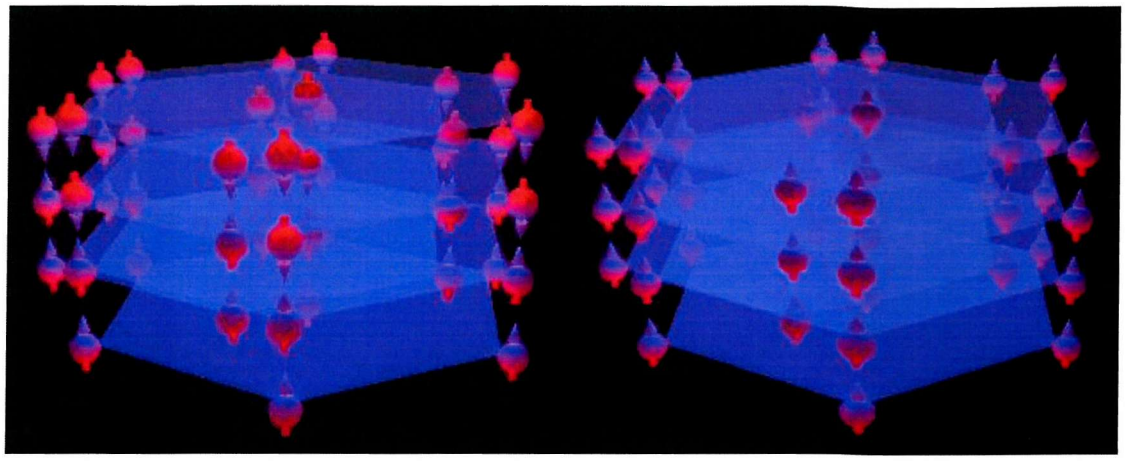

Figure 6-1. The magnetic structures of bulk Tm a) 4-up/3-down structure b) Ferromagnetic

In order to construct a phase diagram, first order differentials of the magnetic moment versus applied field data were plotted and the peaks in these differential plots taken to represent the mid- point of the phase transition. The values of applied field at these phase transition mid-points were plotted against temperature to construct phase diagrams for each sample and sample orientation. These phase diagrams then formed the basis of the experimental planning process for neutron scattering measurements. The extra metamagnetic transition and the unexpected behaviour for fields applied along the b-axis led to both zero field elastic neutron diffraction investigations as well as measurements in c-axis and basal plane fields up to 5T.

Magnetic diffraction peaks were observed below $T_N \sim 60K$, displaced from nuclear peaks along **Q**=[10L] by the incommensurate modulation vector **q**. With decreasing temperature, **q** increases until it locks into a commensurate value and, below this temperature, higher harmonics of the modulation are observed. Thus, the magnetic moments form longitudinal modulated structures along the c direction.

Zero field neutron diffraction measurements revealed a component of magnetisation within the basal plane for Tm/Lu but not Tm/Y superlattices, with *c*-axis modulation of 7 atomic planes. This suggests that the 4-up/3-down CAM structure is canted away from the *c*-axis so that there is a ferromagnetic component within the basal plane. Basal plane magnetic order is coherent within a Tm block and there is coupling between the b-axis components of magnetisation in successive Tm blocks.

Zero field [10L] scans demonstrated how magnetic order locks into a commensurate structure, at low temperature, with a 7 atom repeat distance and a coherence length of 2-4 bi-layers for samples with thin (≤20 atomic planes) non-magnetic spacer layers and ~1 bi-layer for samples with thick non-magnetic spacer layers(40 atomic planes). Superlattice features in the magnetic peaks indicated coupling between Tm blocks.

Fields along the *c*-axis of up to 5T and temperatures down to 2K were employed in order to investigate the regions of the phase diagram for Tm_{40}/Lu_{20}. The low-field scattering shows the expected modulation of 7 atomic planes and, by 4.5T, the system is ferromagnetic. The intermediate phase shows a reduction in anti-ferromagnetic component, accompanied by an increase in ferromagnetic component, but the modulation vector is unchanged from low field. This scattering is therefore consistent with a 5-up/2-down ferrimagnetic structure. This is illustrated in Figure 6-2a).

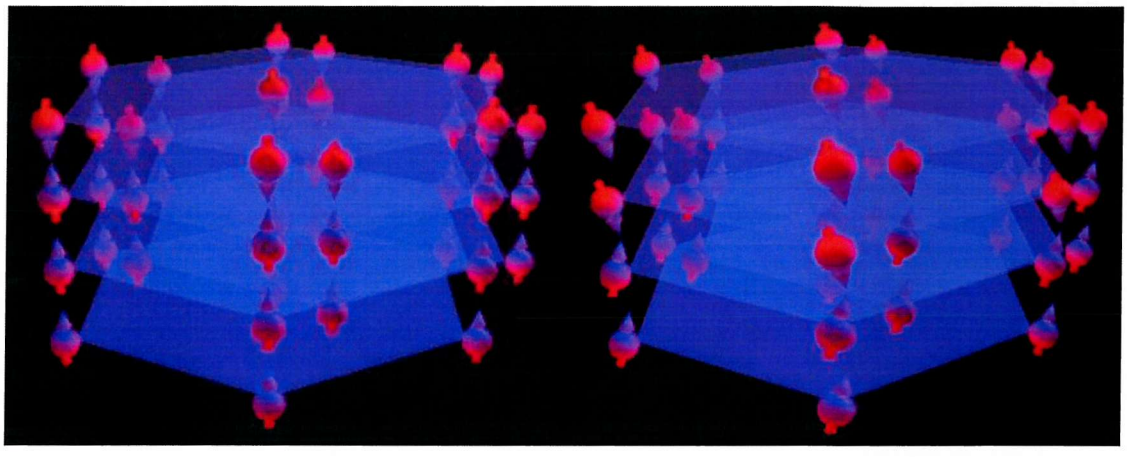

Figure 6-2 a)The 5-up/2-down magnetic structure b) The canted 4-up/3-down structure

Neutron diffraction measurements in *b*-fields were performed for $(Tm_{40}/Lu_{20})_{48}$. The magnetic peak that had clearly been observed in [00L] measurements for zero field measurements was not observed. Nevertheless the increase in the intensity of the (002) with applied *b*-field demonstrated the development of the ferromagnetic component of magnetisation within the plane for increasing *b*-fields, suggesting that the *b*-field pulls the canted magnetic moment further from the *c*-axis towards the *b*-axis. This is illustrated in Figure 6-2b).

The magnetic behaviour of Tm/Lu superlattices has been demonstrated to differ from that of bulk Tm. The epitaxial strain alters the crystal field and diminishes

the uniaxial anisotropy so that there is an in-plane component of magnetisation even in zero applied field. In plane components are ferromagnetically aligned within a Tm block and are coupled between successive blocks via spin waves in the spacer layer. Application of a *c*-field pulls the magnetic moments back towards the c-axis and drives metamagnetic transitions to first a 5-up/2-down CAM structure and then a transition to ferromagnetic alignment. Application of a *b*-field pulls the localised moments towards the b-axis.

In summary we have found a surprisingly rich magnetic phase diagram for Tm/Lu and Tm/Y superlattices, and have identified the magnetic structures using neutron diffraction. This unusual behaviour is attributed to the effects of epitaxial strain.

Appendix A: Magnetisation results

SL701 $(Tm_{20}/Y_6)_{60}$

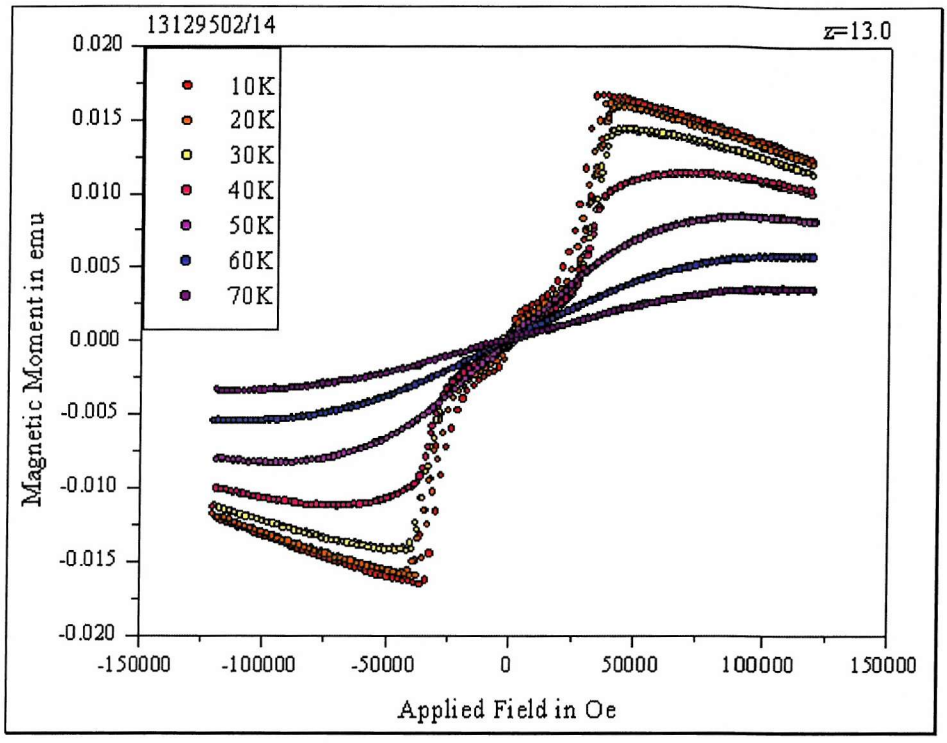

Figure A-1. Magnetic Moment as a function of c-axis applied magnetic field at a range of temperatures for SL701 $(Tm_{20}/Y_6)_{60}$

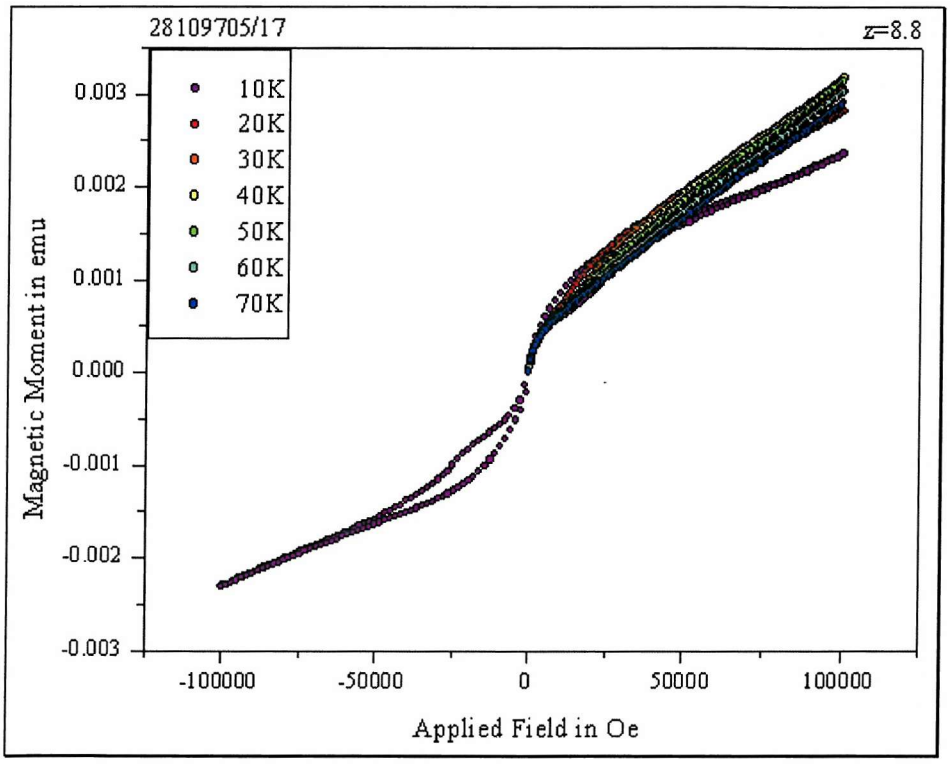

Figure A-2 Magnetic Moment as a function of b-axis applied magnetic field at a range of temperatures for SL701 $(Tm_{20}/Y_6)_{60}$

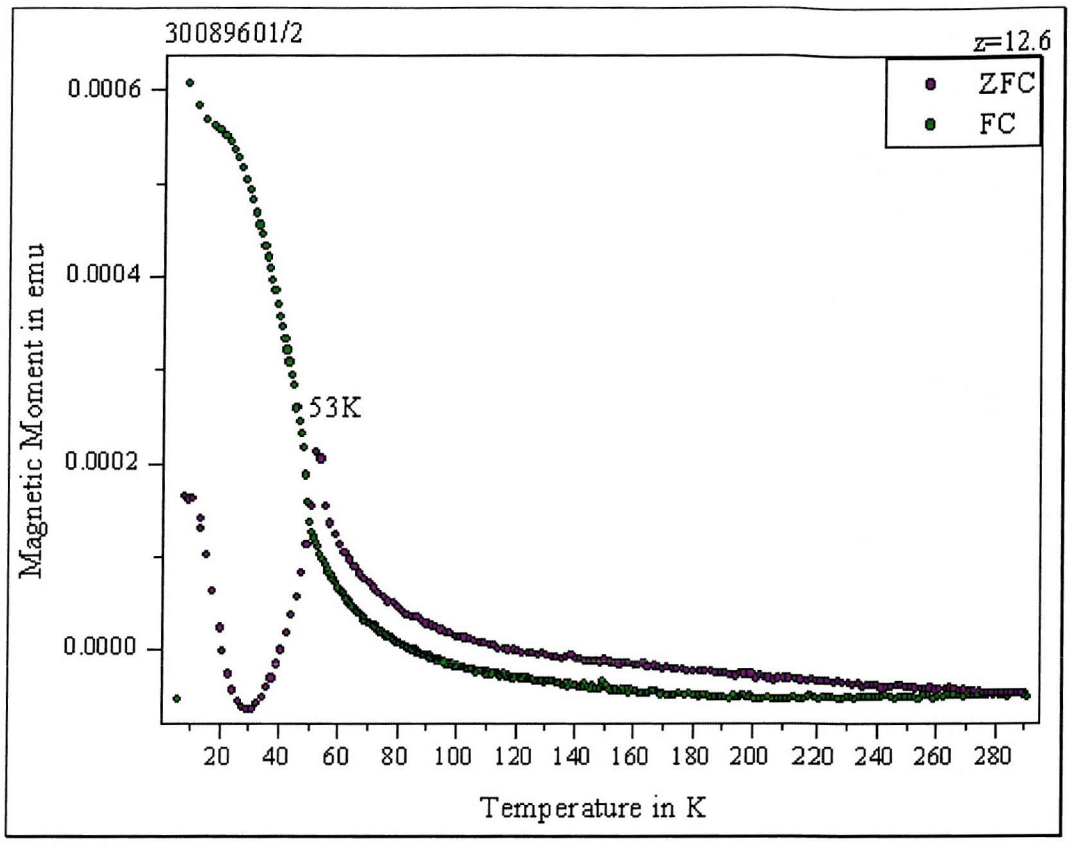

Figure A-3 Magnetic Moment as a function of temperature with 0.1T applied magnetic field parallel to the c-axis for SL701 $(Tm_{20}/Y_6)_{60}$

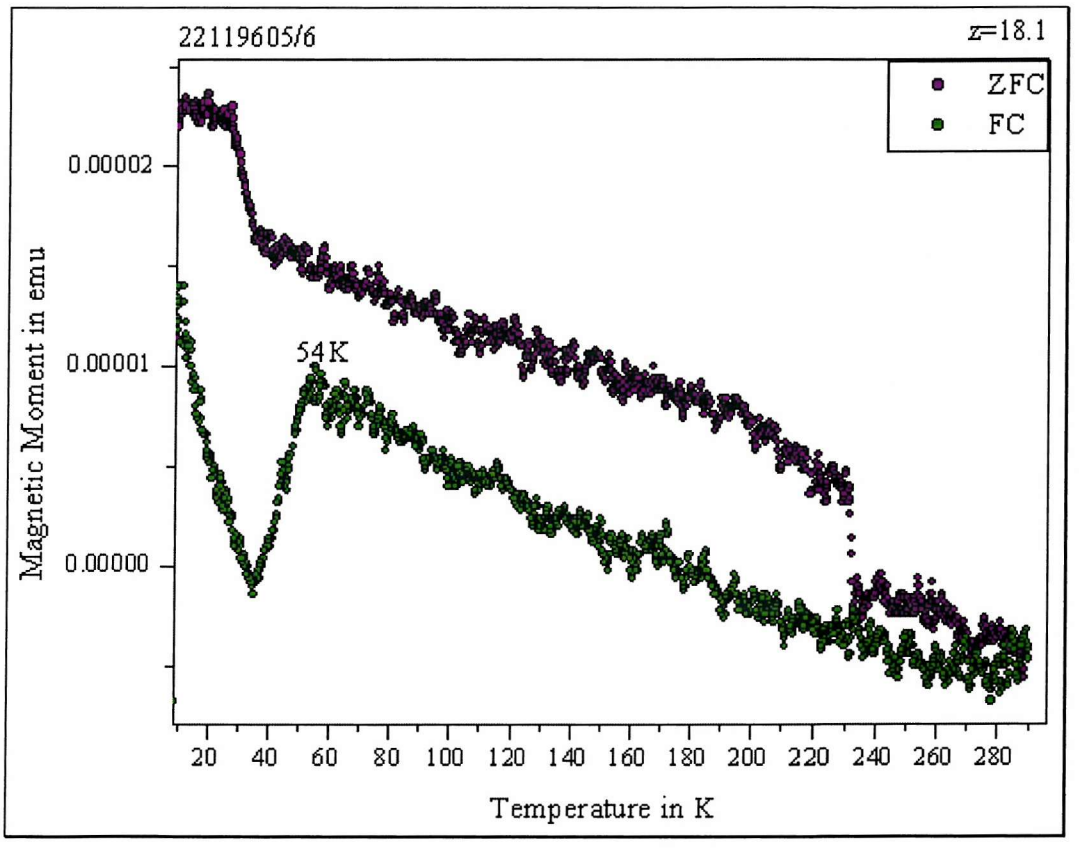

Figure A-4. Magnetic Moment as a function of temperature with 0.1T applied magnetic field parallel to the b-axis for SL701 $(Tm_{20}/Y_6)_{60}$

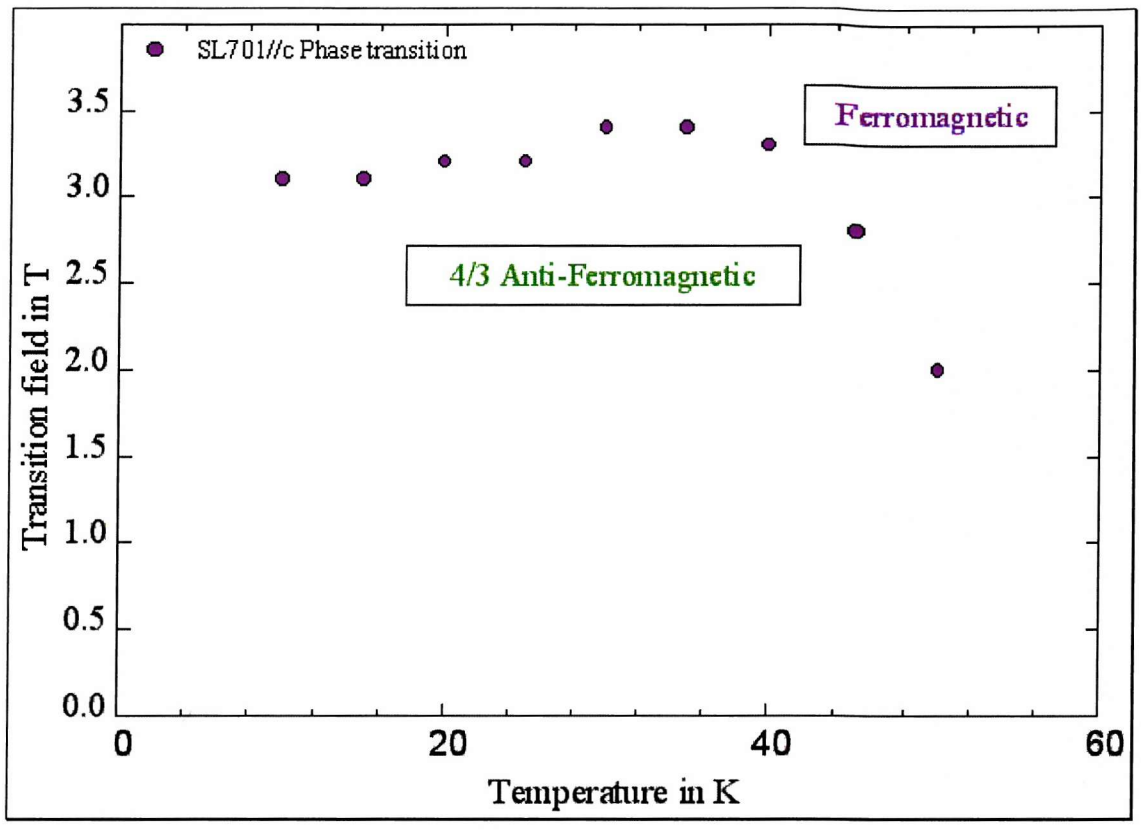

Figure A-5 Phase diagram for SL701 $(Tm_{20}/Y_6)_{60}$ with field parallel to c-axis.

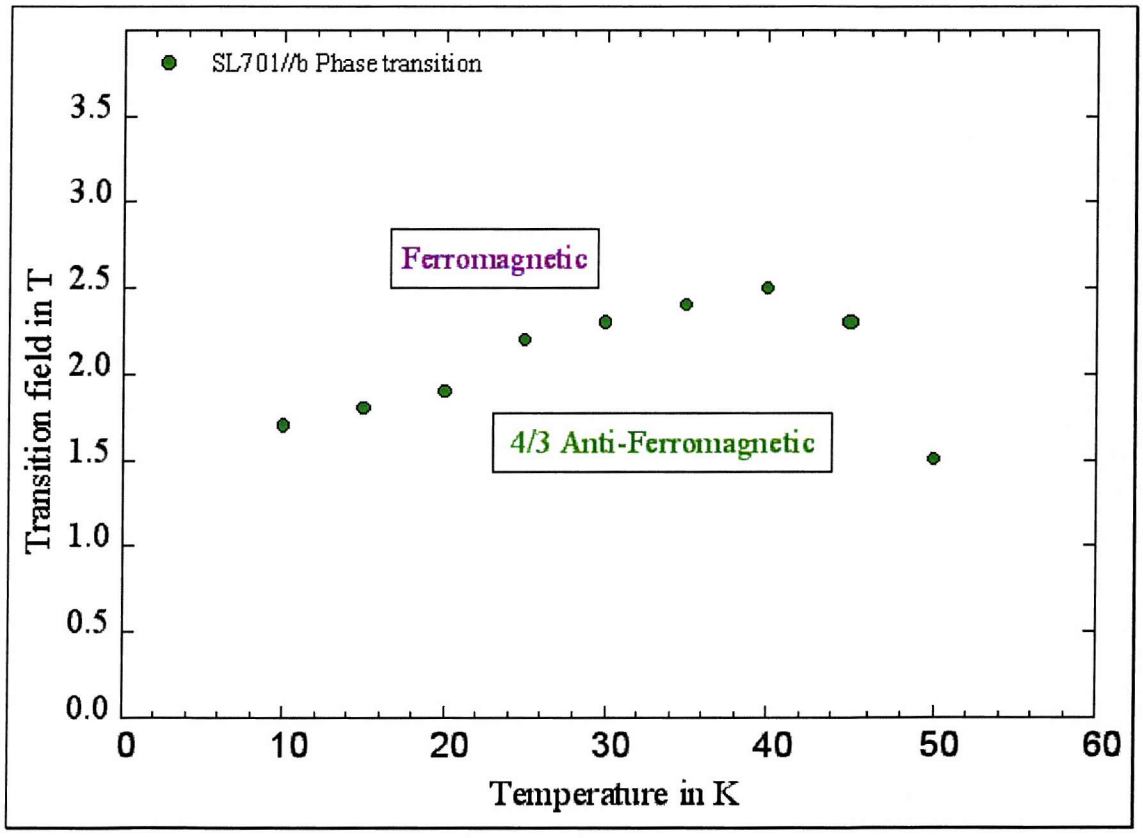

Figure A-6. Phase diagram for SL701 $(Tm_{20}/Y_6)_{60}$ with field parallel to b-axis

SL702 $(Tm_6/Y_{20})_{60}$

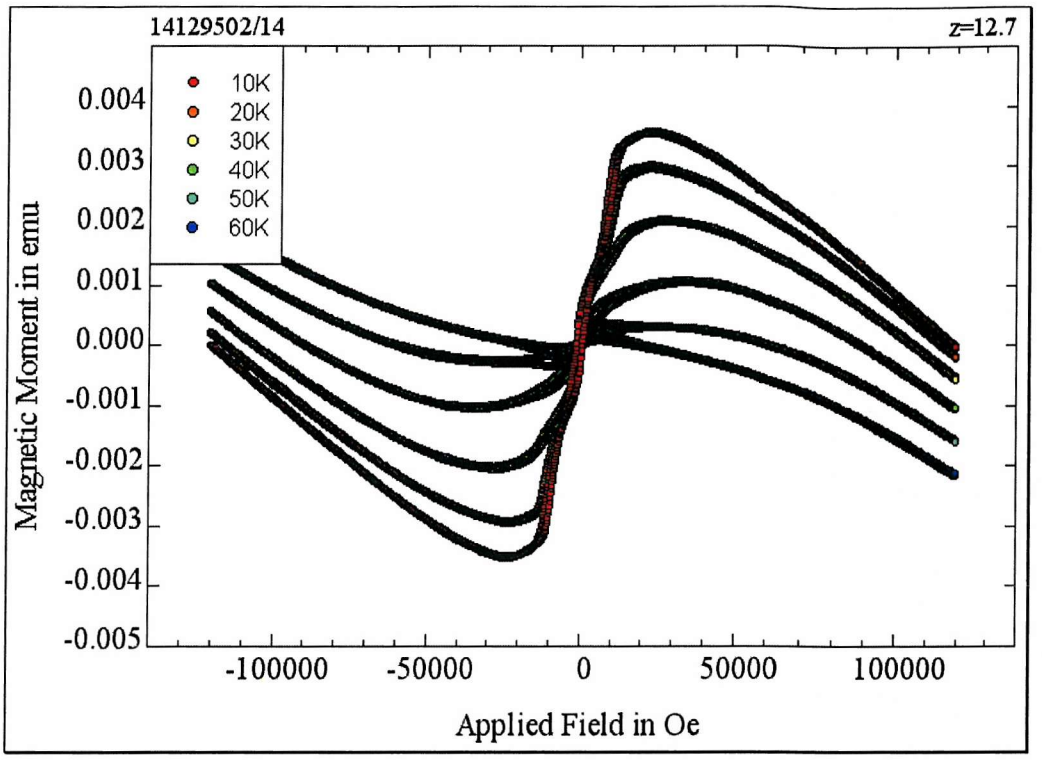

Figure A-7. Magnetic Moment as a function of c-axis applied magnetic field at a range of temperatures for SL702 $(Tm_6/Y_{20})_{60}$

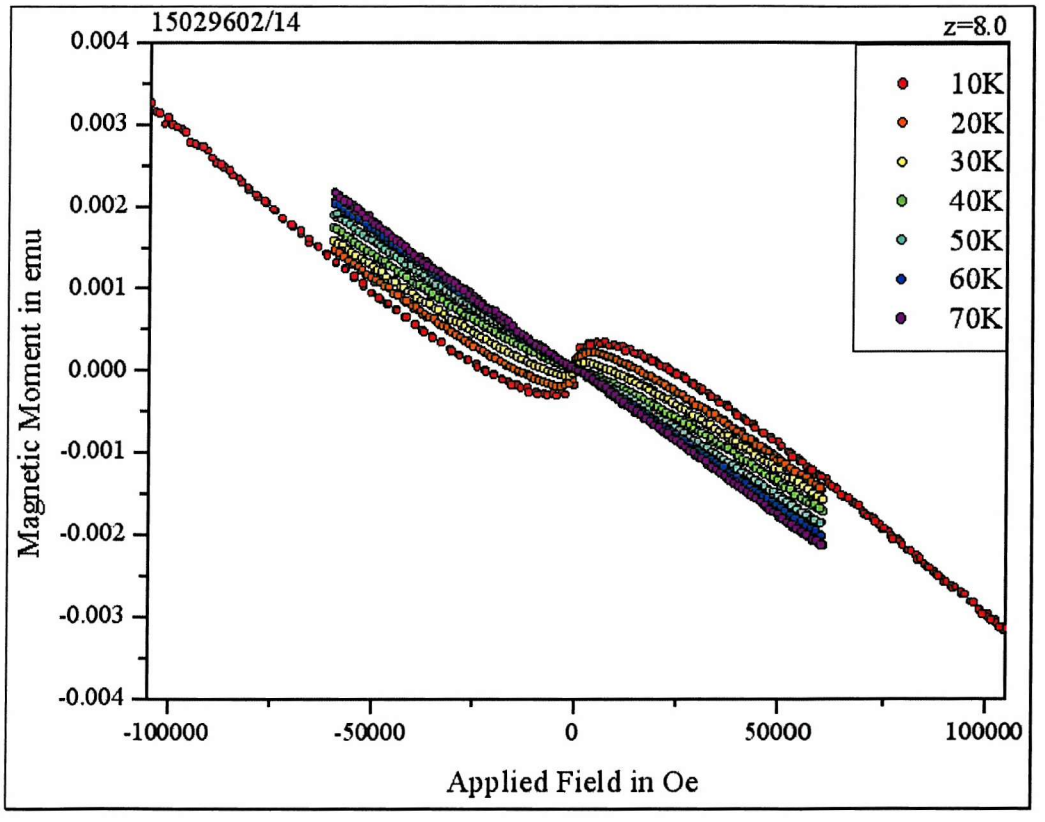

Figure A-8. Magnetic Moment as a function of b-axis applied magnetic field at a range of temperatures for SL702 $(Tm_6/Y_{20})_{60}$

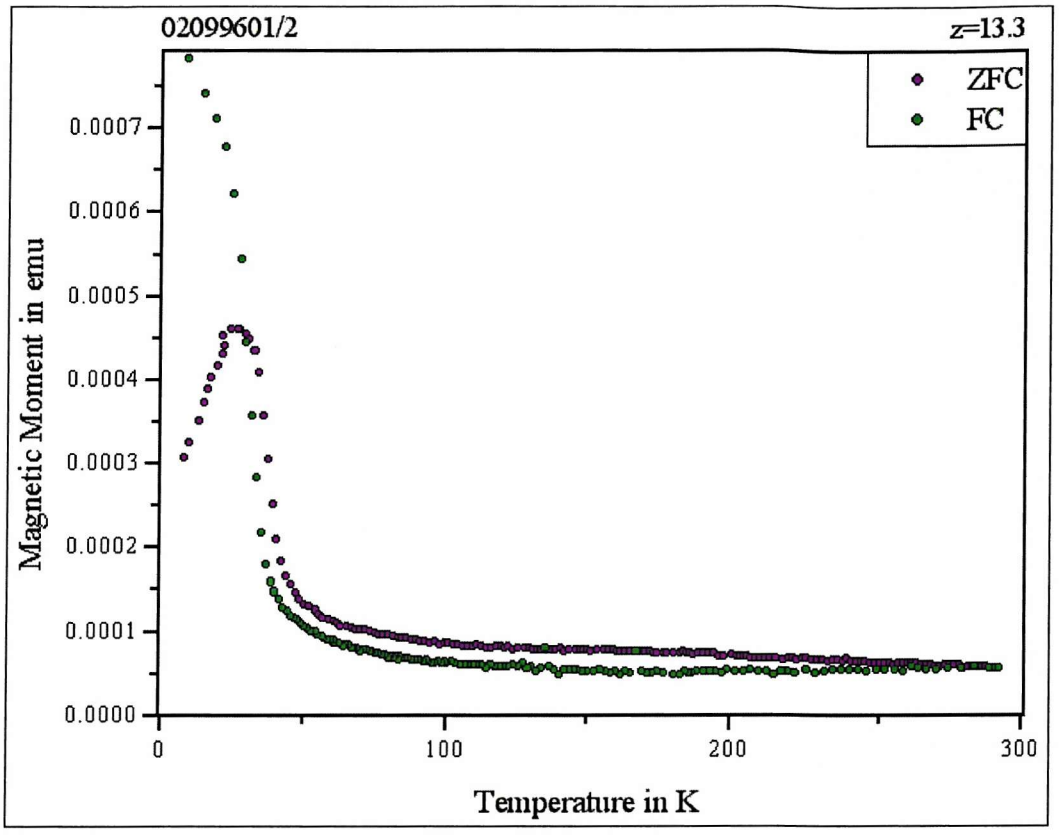

Figure A-9 Magnetic Moment as a function of temperature with 0.1T applied magnetic field parallel to the c-axis for SL702 $(Tm_6/Y_{20})_{60}$

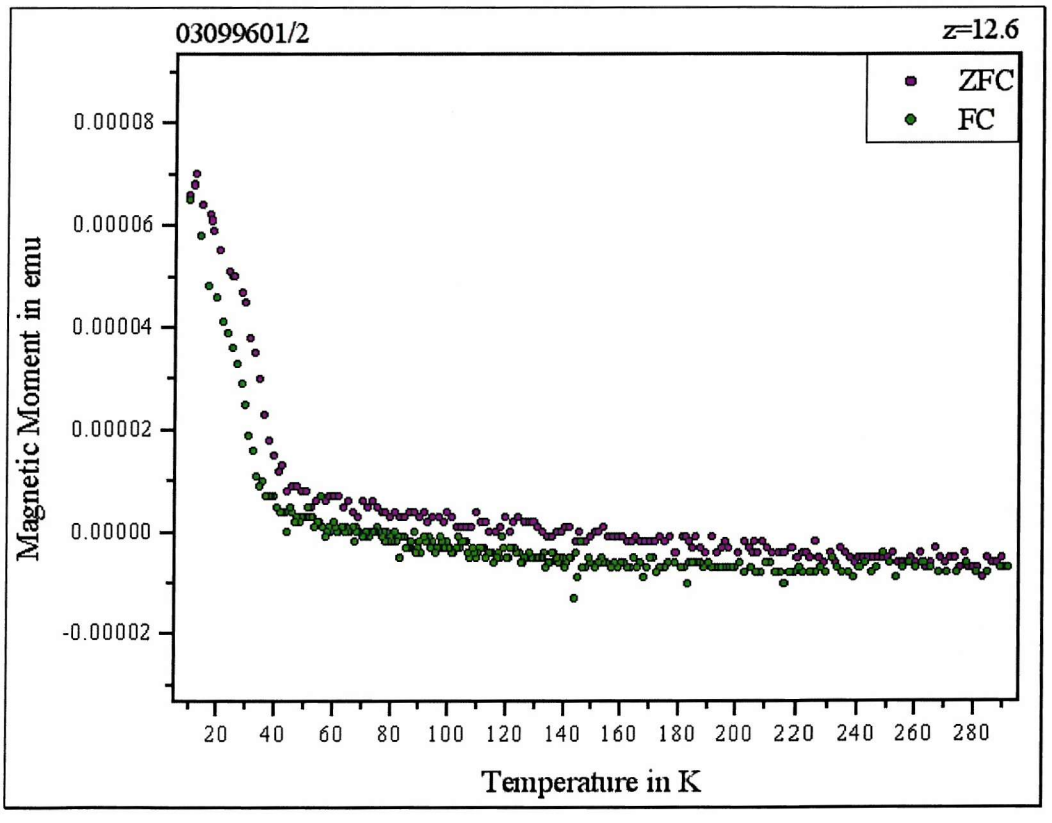

Figure A-10. Magnetic Moment as a function of temperature with applied 0.1T magnetic field parallel to the b-axis for SL702 $(Tm_6/Y_{20})_{60}$

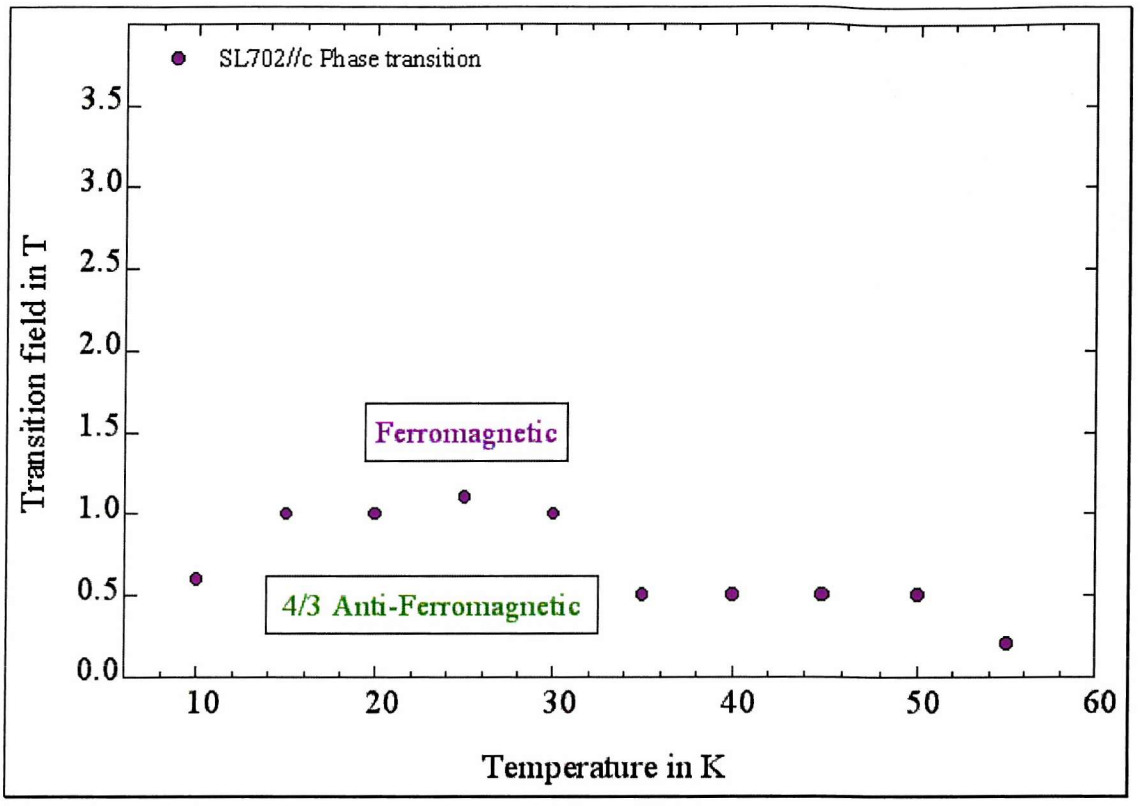

Figure A-11 Phase diagram for SL702 $(Tm_6/Y_{20})_{60}$ with field parallel to c-axis.

The magnetisation as a function of applied field does not suggest a detectable phase transition. No phase diagram is, therefore, presented for SL702 $(Tm_6/Y_{20})_{60}$ with field parallel to b-axis.

SL703 $(Tm_{20}/Y_{20})_{60}$

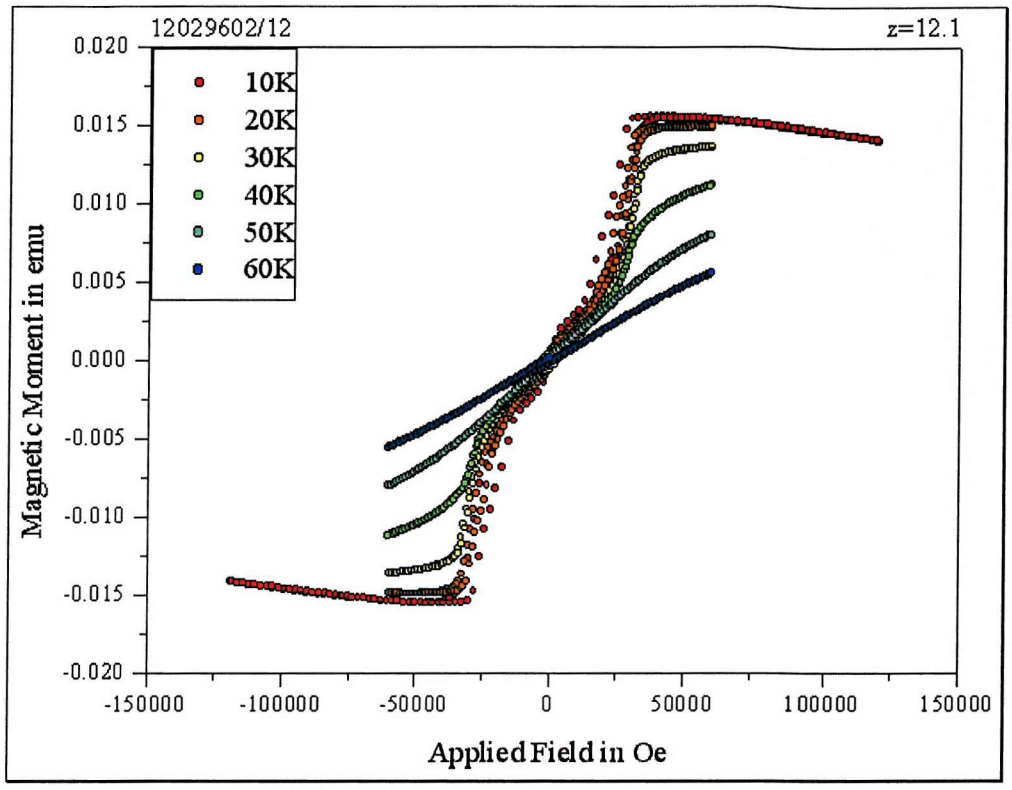

Figure A-12. Magnetic Moment as a function of c-axis applied magnetic field at a range of temperatures for SL703 $(Tm_{20}/Y_{20})_{60}$

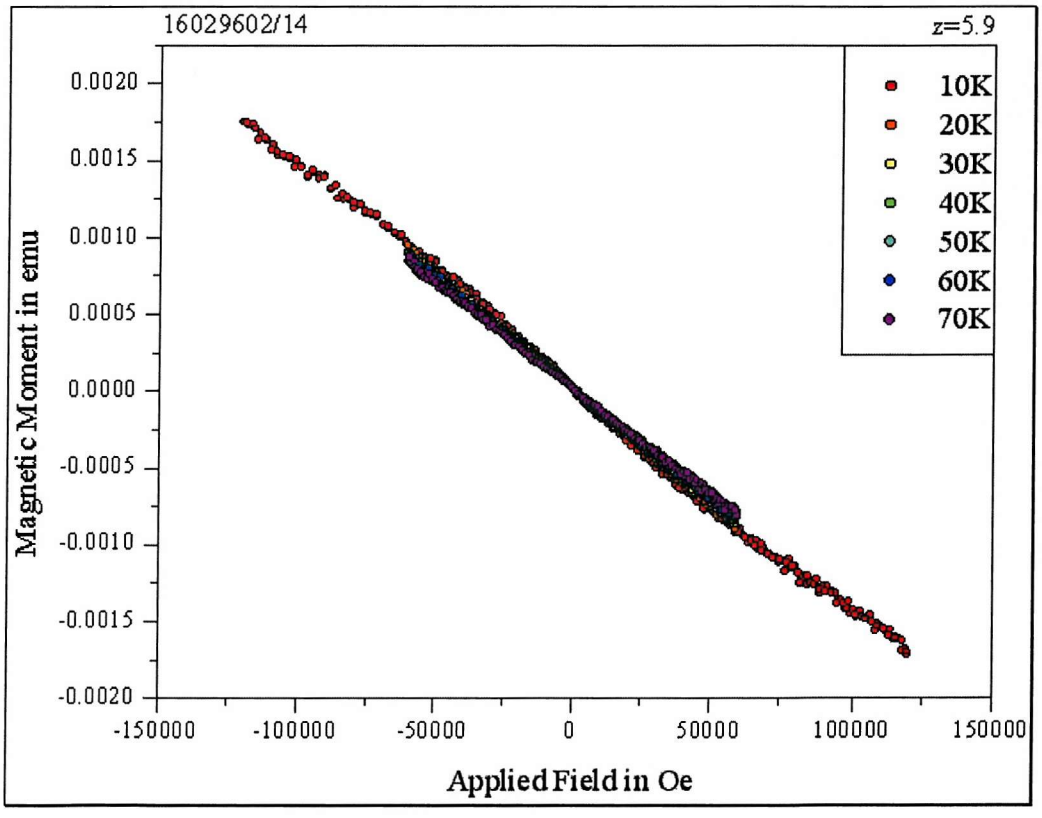

Figure A-13. Magnetic Moment as a function of b-axis applied magnetic field at a range of temperatures for SL703 $(Tm_{20}/Y_{20})_{60}$

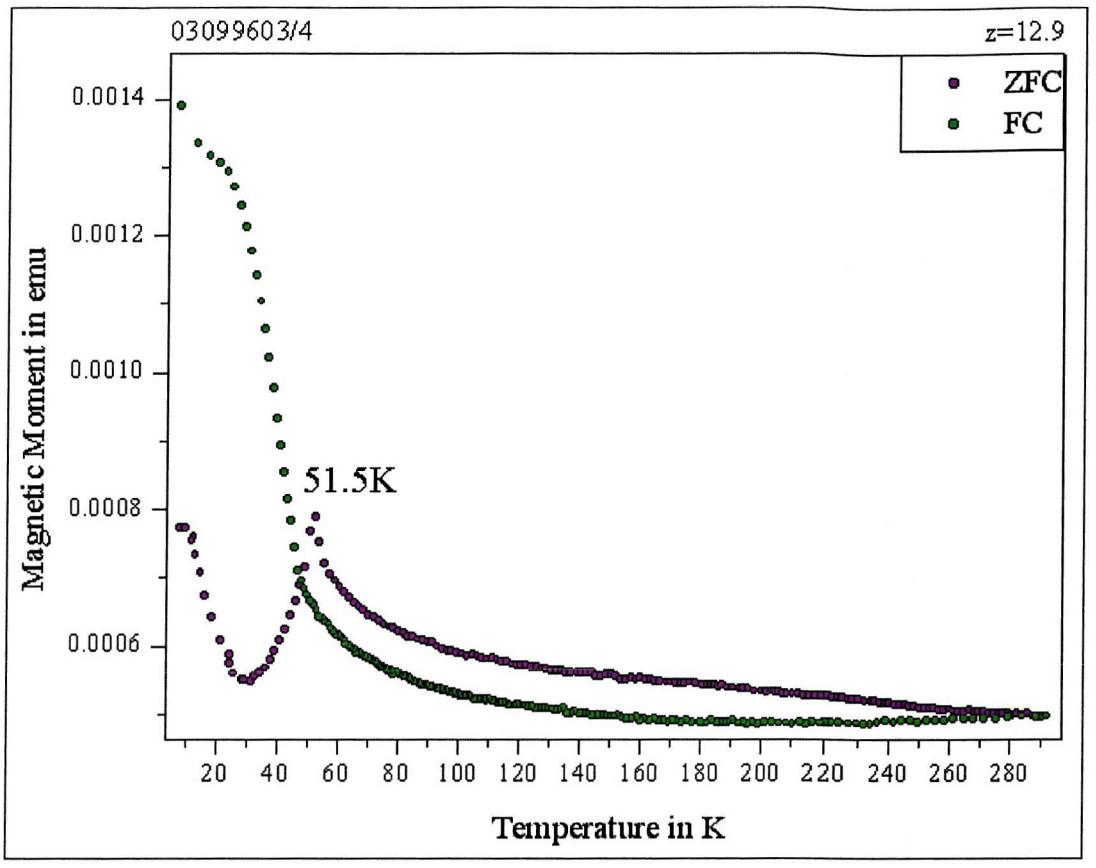

Figure A-14. Magnetic Moment as a function of temperature with 0.1T applied magnetic field parallel to the c-axis for SL703 $(Tm_{20}/Y_{20})_{60}$

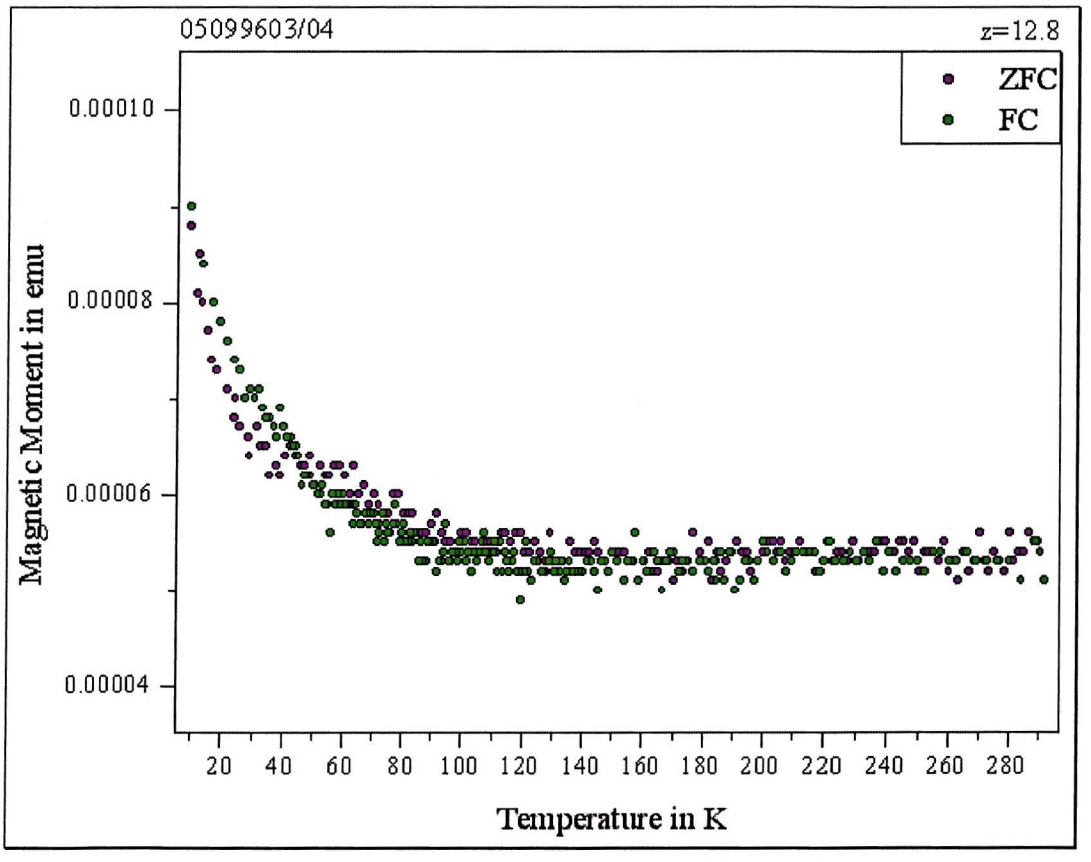

Figure A-15. Magnetic Moment as a function of temperature with 0.1T applied magnetic field parallel to the b-axis for SL703 $(Tm_{20}/Y_{20})_{60}$

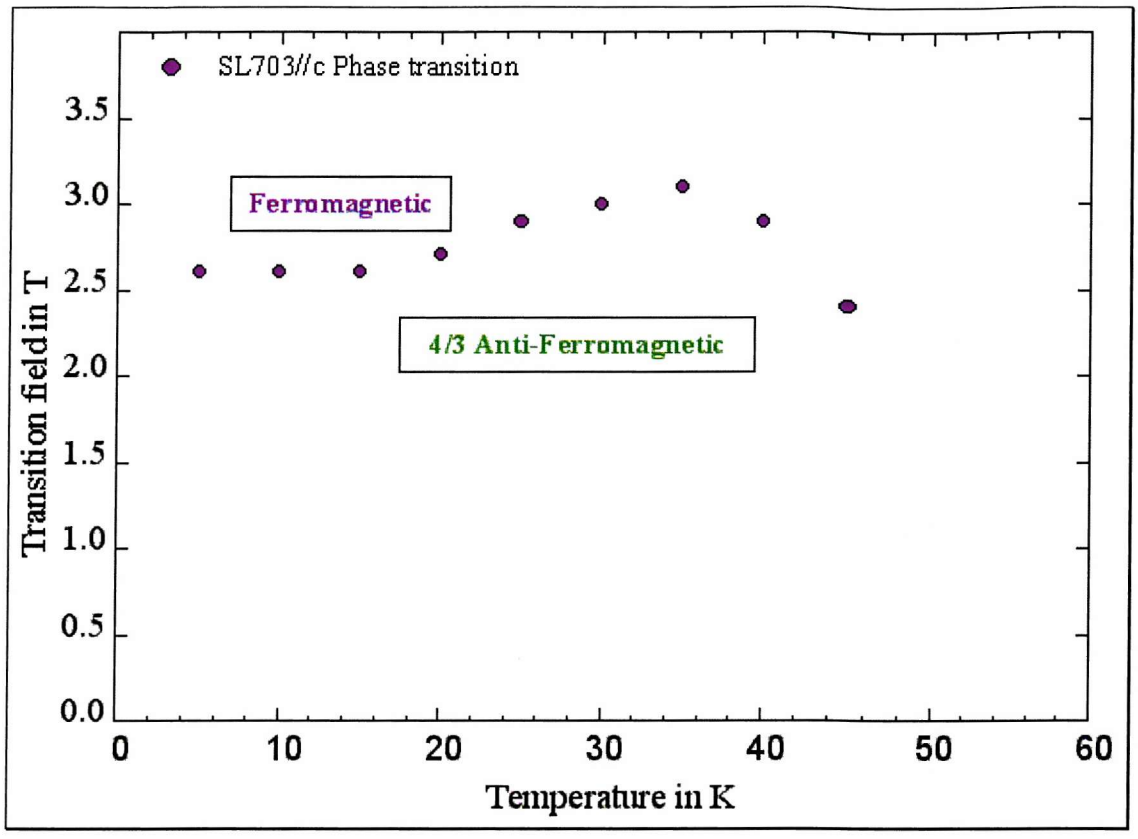

Figure A-16. Phase diagram for SL703 $(Tm_{20}/Y_{20})_{60}$ with field parallel to c-axis.

The magnetisation as a function of applied field does not suggest a detectable phase transition. No phase diagram is, therefore, presented for SL703 $(Tm_{20}/Y_{20})_{60}$ with field parallel to b-axis.

SL706 Tm film, 2000 atomic planes

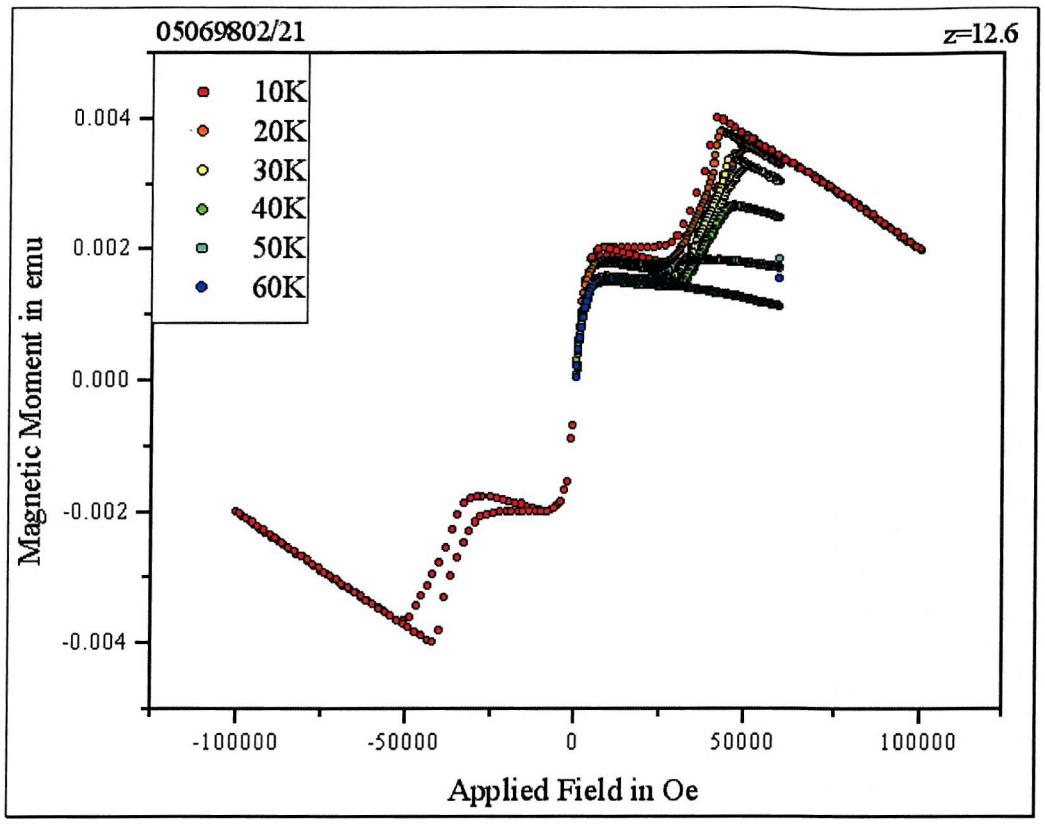

Figure A-17. Magnetic Moment as a function of c-axis applied magnetic field at a range of temperatures for SL706 (Tm film, 2000 atomic planes)

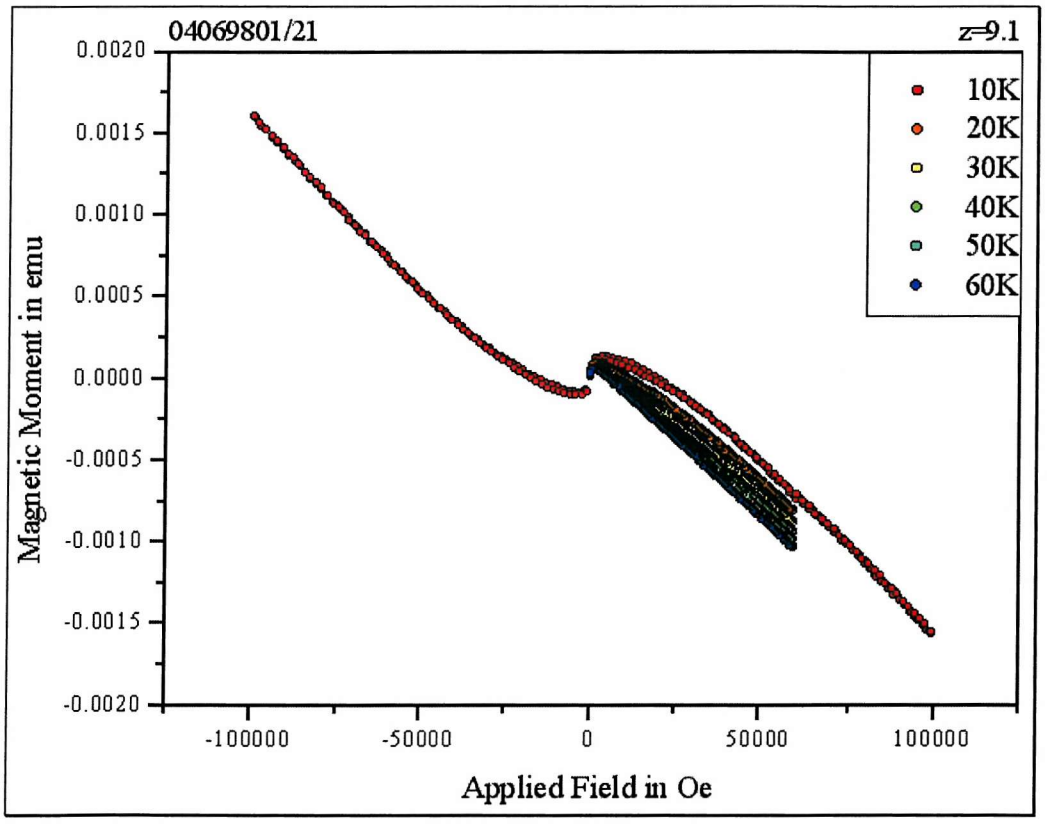

Figure A-18. Magnetic Moment as a function of b-axis applied magnetic field at a range of temperatures for SL706 (Tm film, 2000 atomic planes)

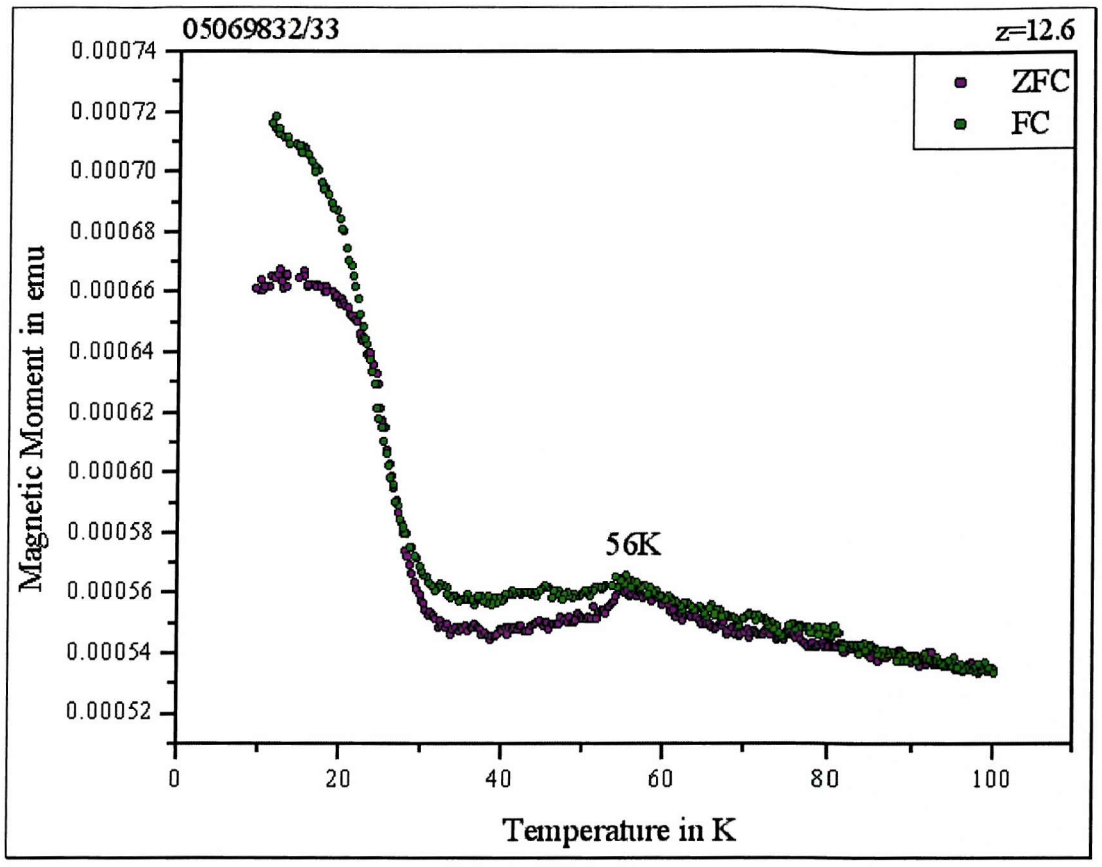

Figure A-19. Magnetic Moment as a function of temperature with 0.1T applied magnetic field parallel to the c-axis for SL706 (Tm film, 2000 atomic planes)

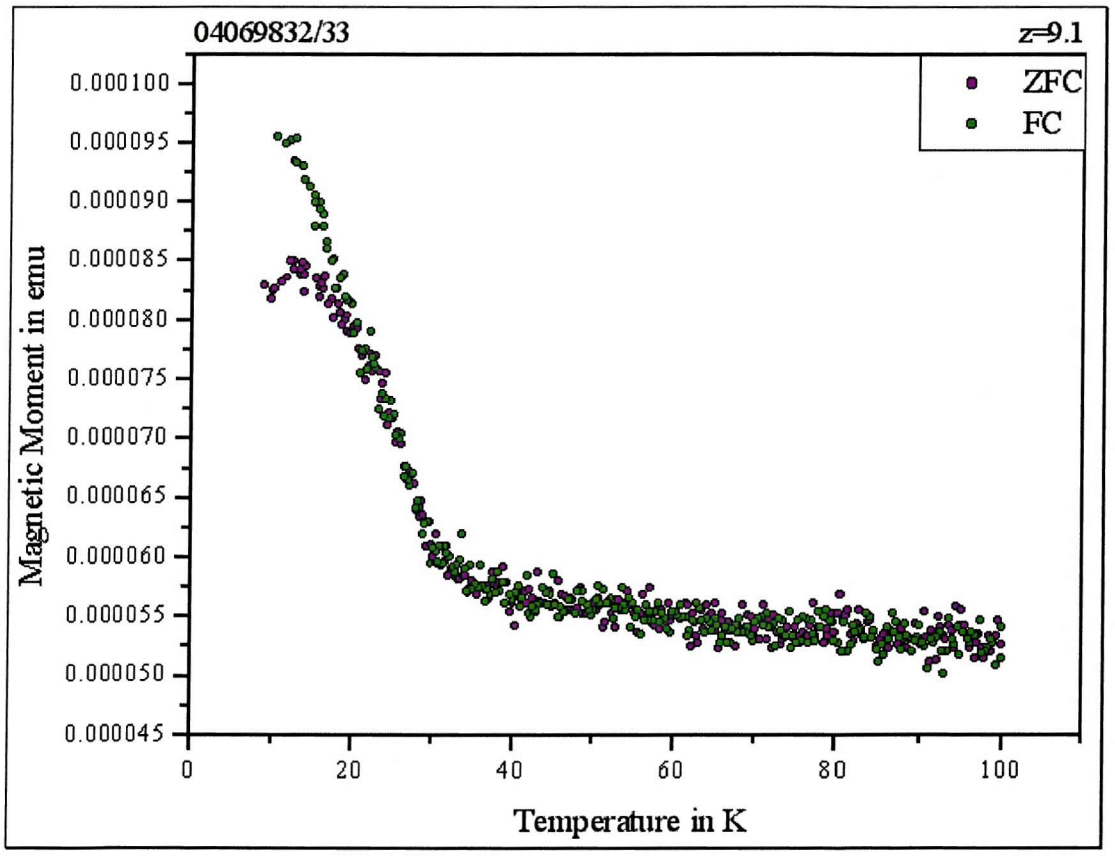

Figure A-20. Magnetic Moment as a function of temperature with 0.1T applied magnetic field parallel to the b-axis for SL706 (Tm film, 2000 atomic planes)

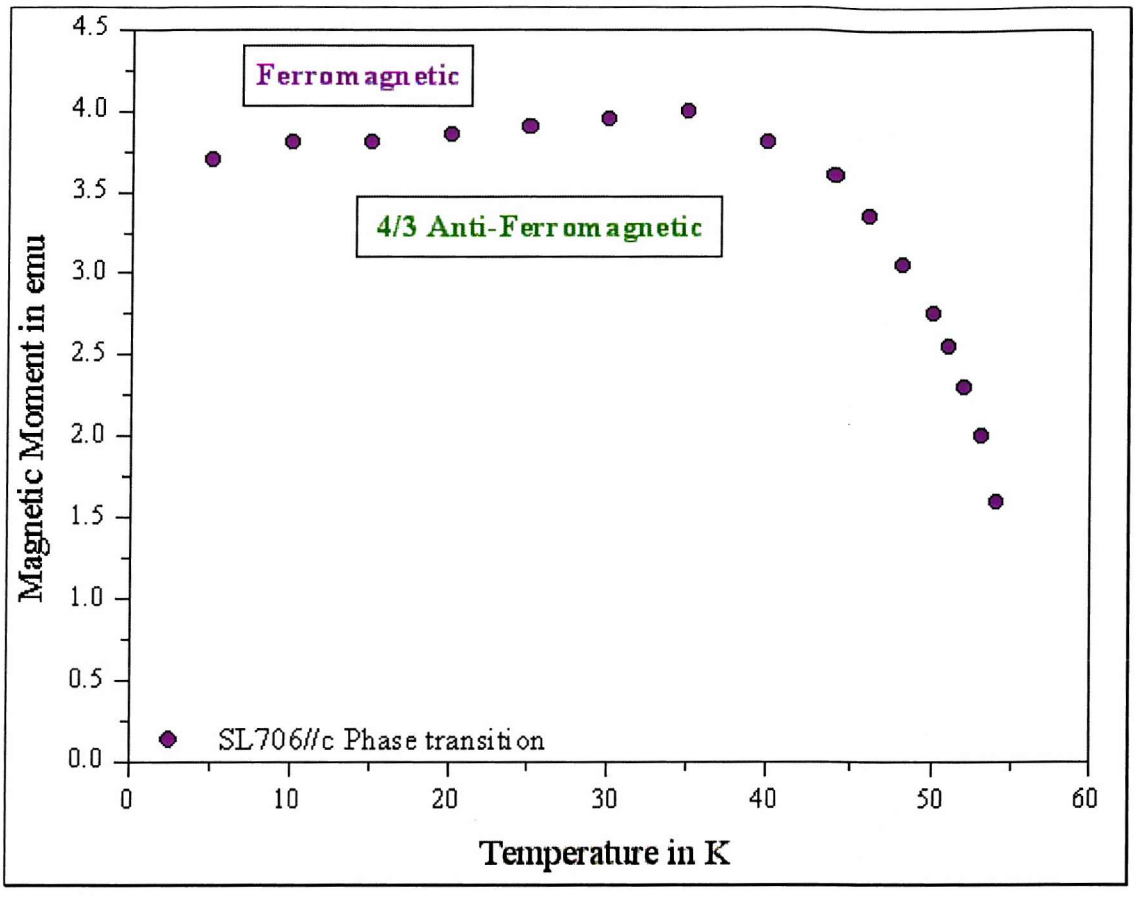

Figure A-21. Phase diagram for SL706 (Tm film, 2000 atomic planes) with field parallel to c-axis.

The magnetisation as a function of applied field does not suggest a detectable phase transition. No phase diagram is, therefore, presented for SL706 (Tm film, 2000 atomic planes) with field parallel to b-axis.

SL707 $(Tm_{40}/Y_{20})_{50}$

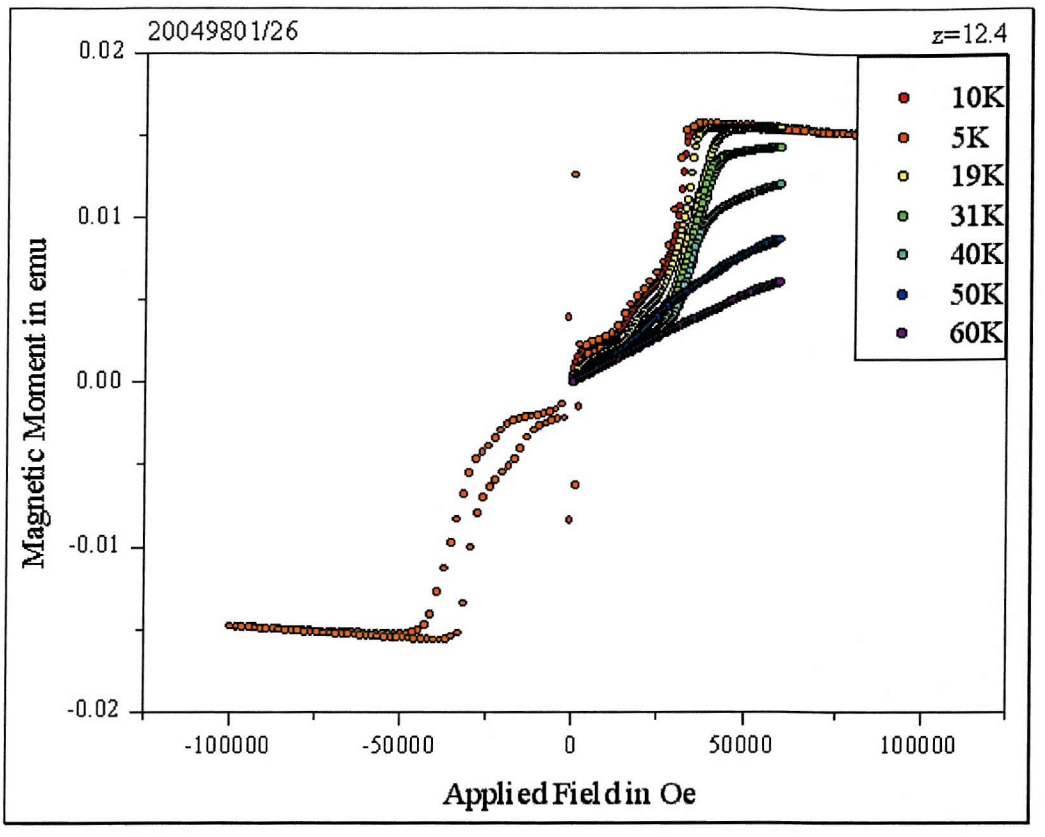

Figure A-22. Magnetic Moment as a function of c-axis applied magnetic field at a range of temperatures for SL707 $(Tm_{40}/Y_{20})_{50}$

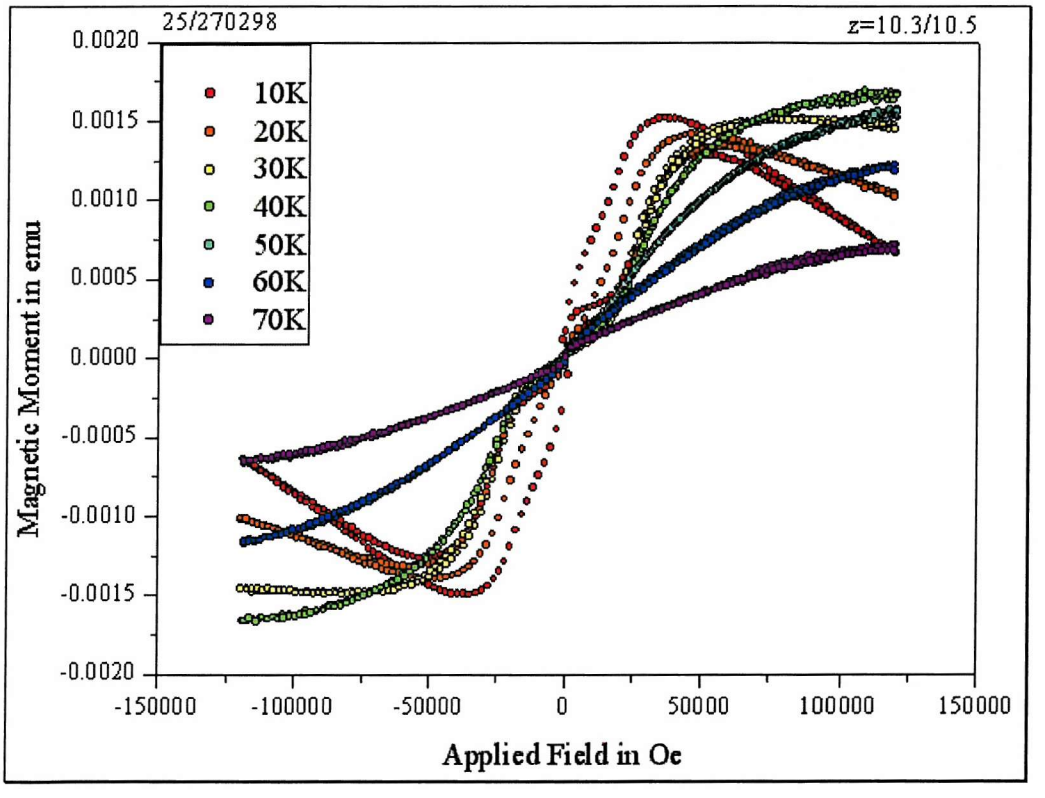

Figure A-23. Magnetic Moment as a function of b-axis applied magnetic field at a range of temperatures for SL707 $(Tm_{40}/Y_{20})_{50}$

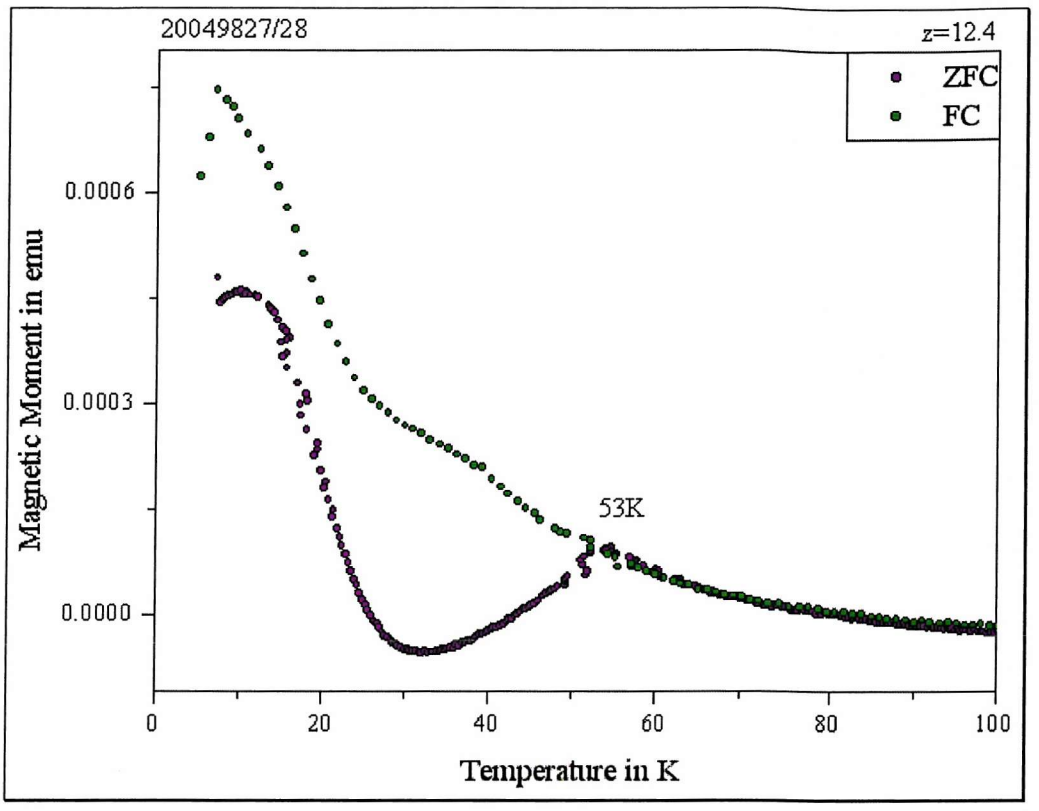

Figure A-24. Magnetic Moment as a function of temperature with 0.1T applied magnetic field parallel to the c-axis for SL707 $(Tm_{40}/Y_{20})_{50}$

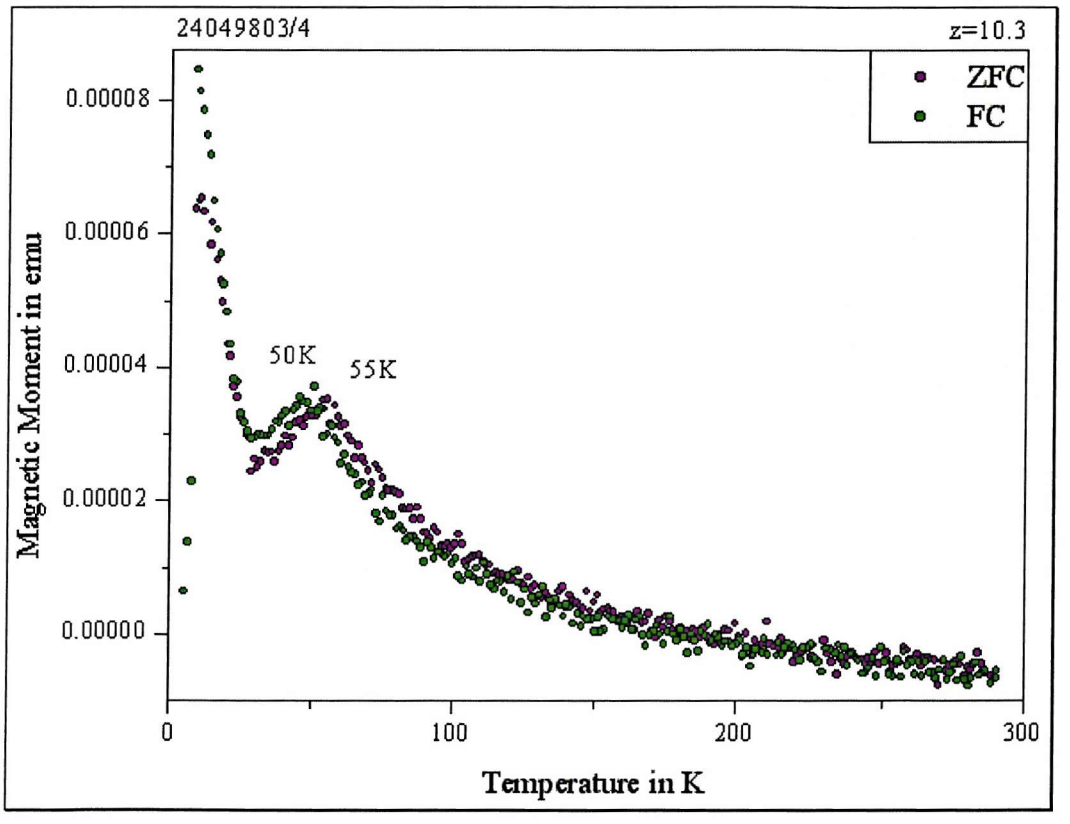

Figure A-25. Magnetic Moment as a function of temperature with 0.1T applied magnetic field parallel to the b-axis for SL707 $(Tm_{40}/Y_{20})_{50}$

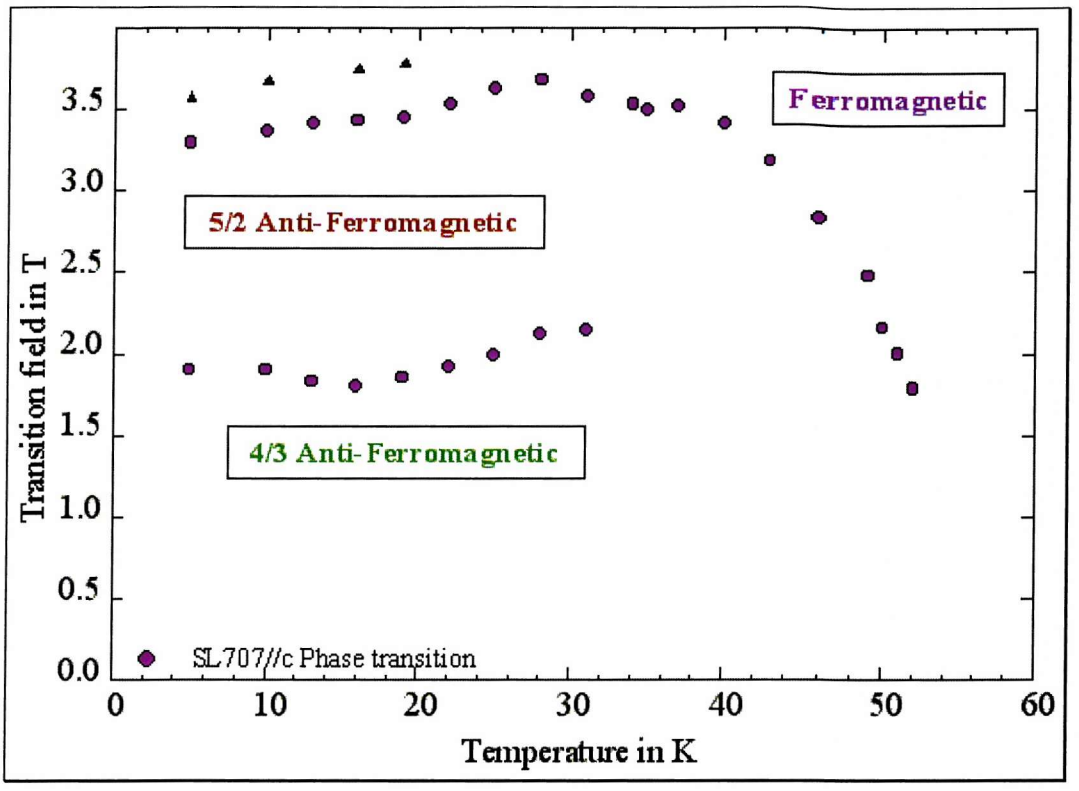

Figure A-26. Phase diagram for SL707 $(Tm_{40}/Y_{20})_{50}$ with field parallel to c-axis.

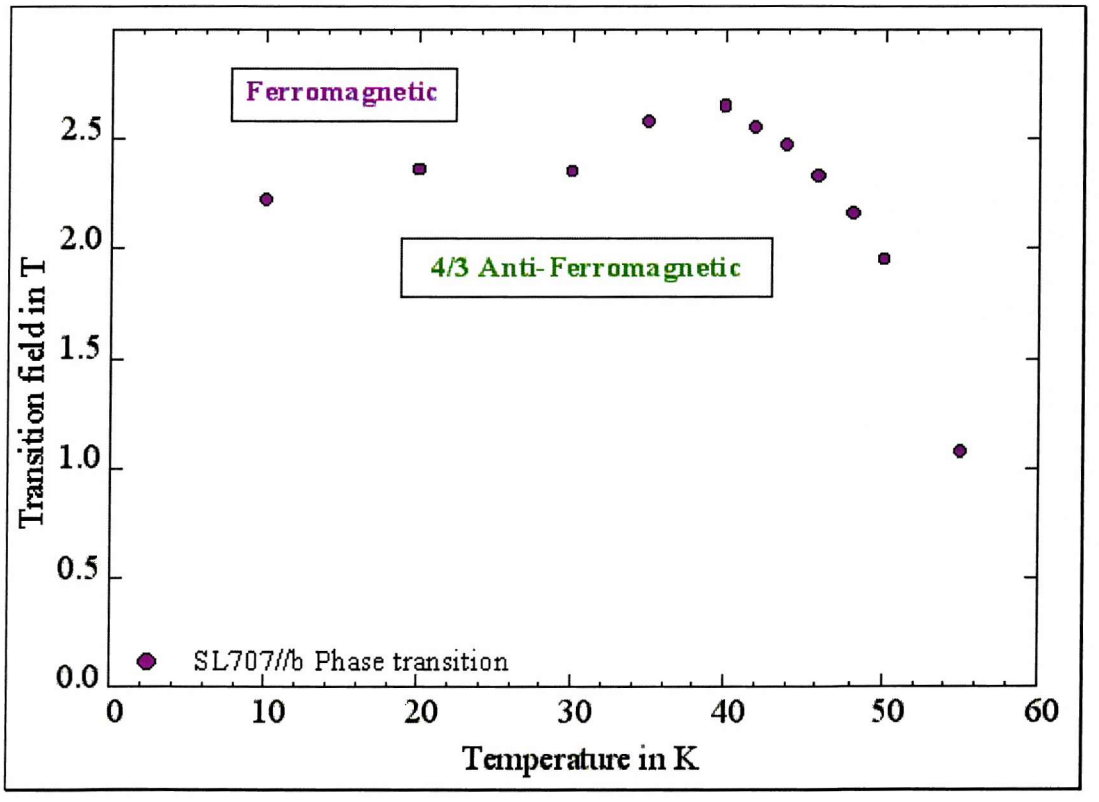

Figure A-27. Phase diagram for SL707 $(Tm_{40}/Y_{20})_{50}$ with field parallel to b-axis.

SL708 $(Tm_{20}/Y_{40})_{50}$

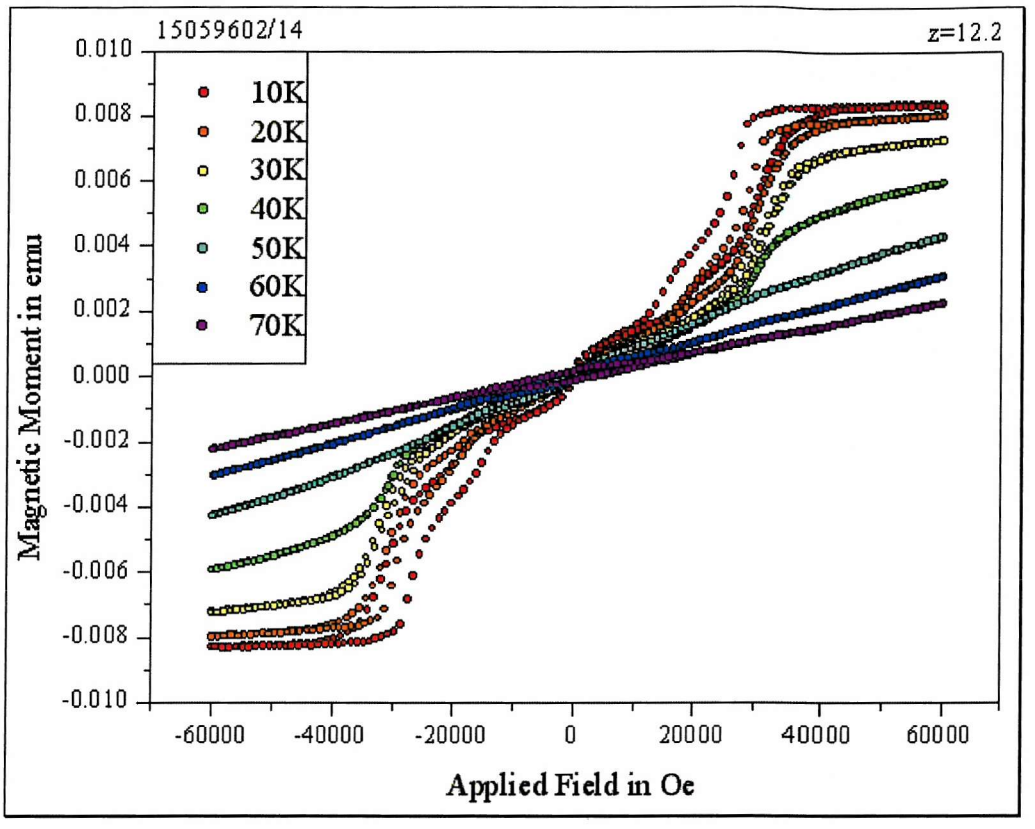

Figure A-28. Magnetic Moment as a function of c-axis applied magnetic field at a range of temperatures for SL708 $(Tm_{20}/Y_{40})_{50}$.

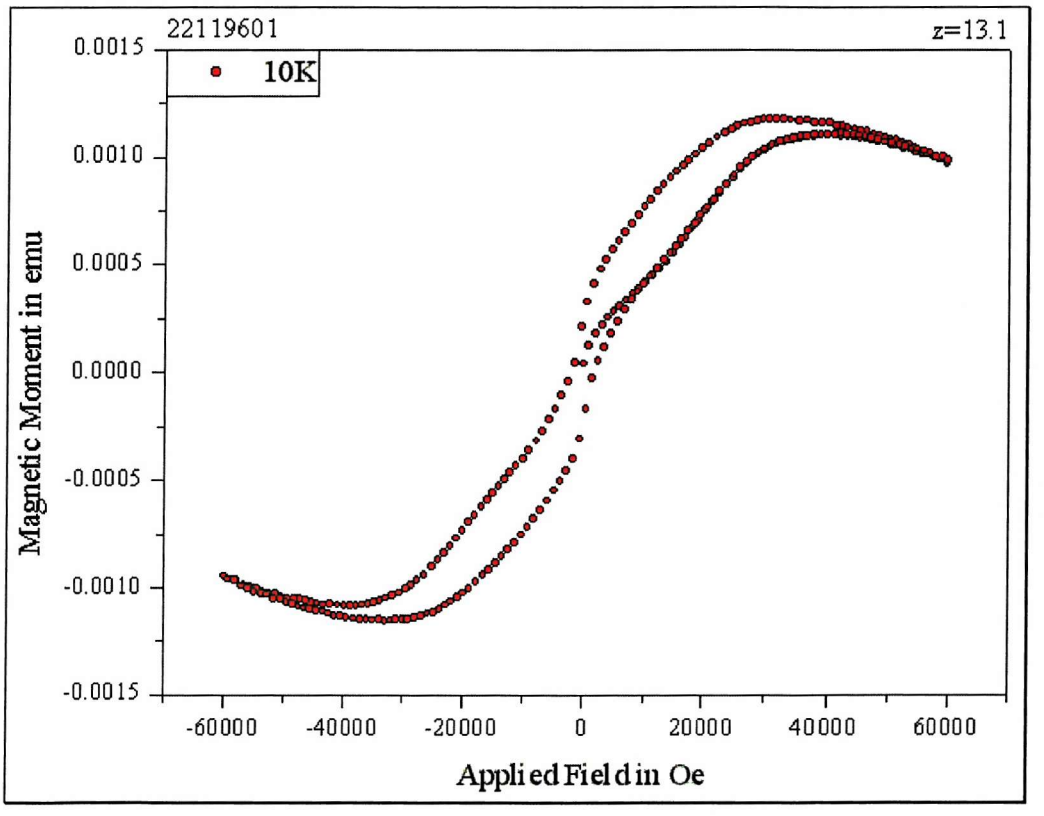

Figure A-29. Magnetic Moment as a function of b-axis applied magnetic field at 10K for SL708 $(Tm_{20}/Y_{40})_{50}$.

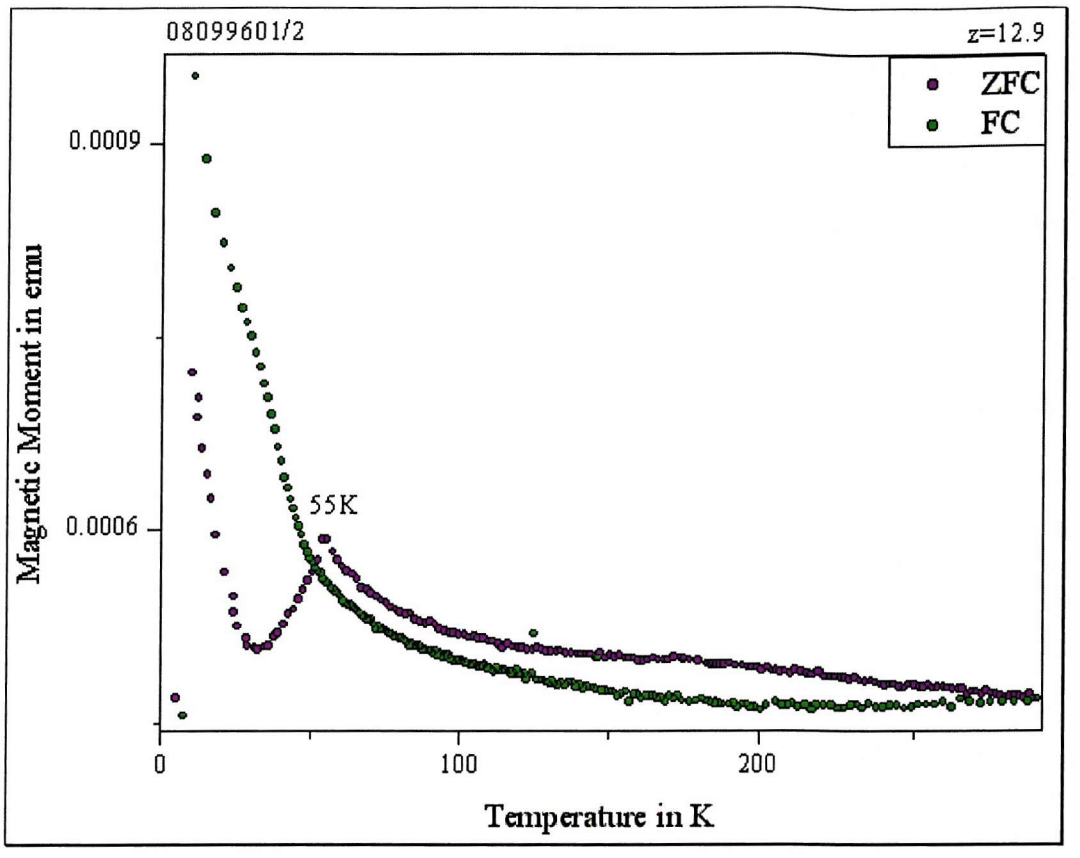

Figure A-30. Magnetic Moment as a function of temperature with 0.1T applied magnetic field parallel to the c-axis for SL708 $(Tm_{20}/Y_{40})_{50}$.

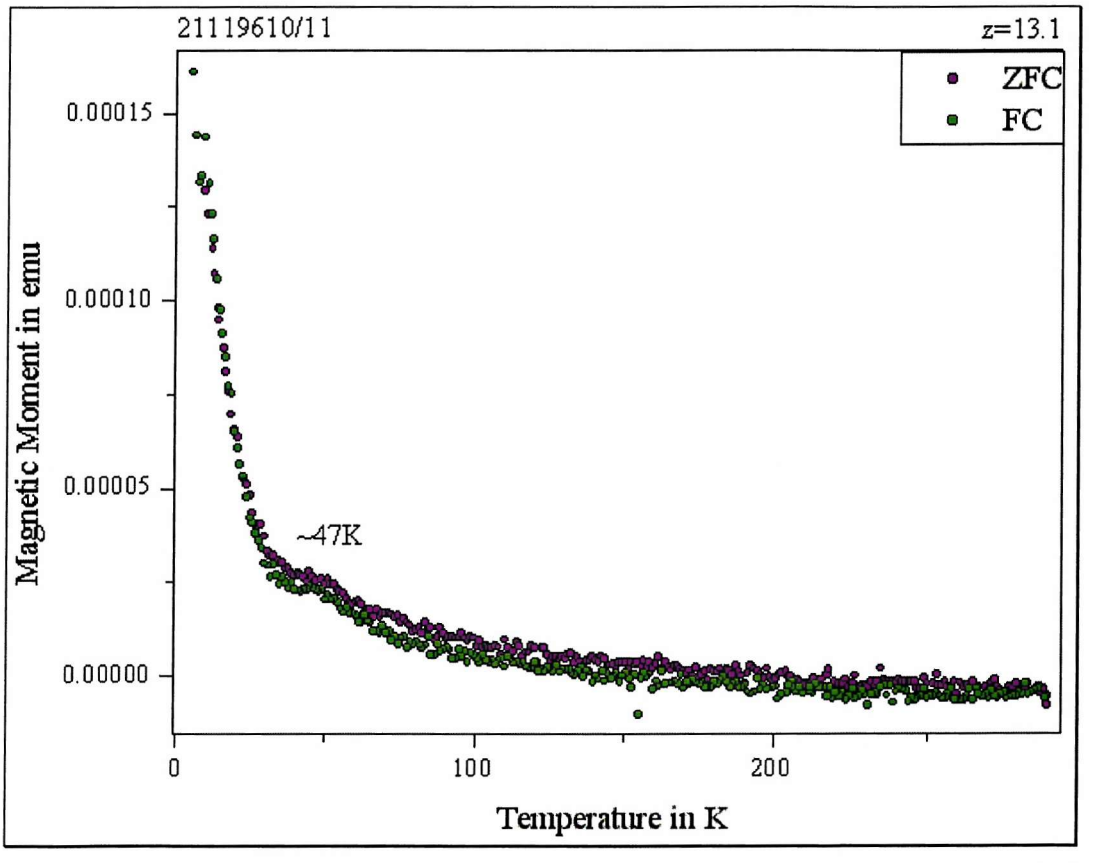

Figure A-31. Magnetic Moment as a function of temperature with 0.1T applied magnetic field parallel to the b-axis for SL708 $(Tm_{20}/Y_{40})_{50}$.

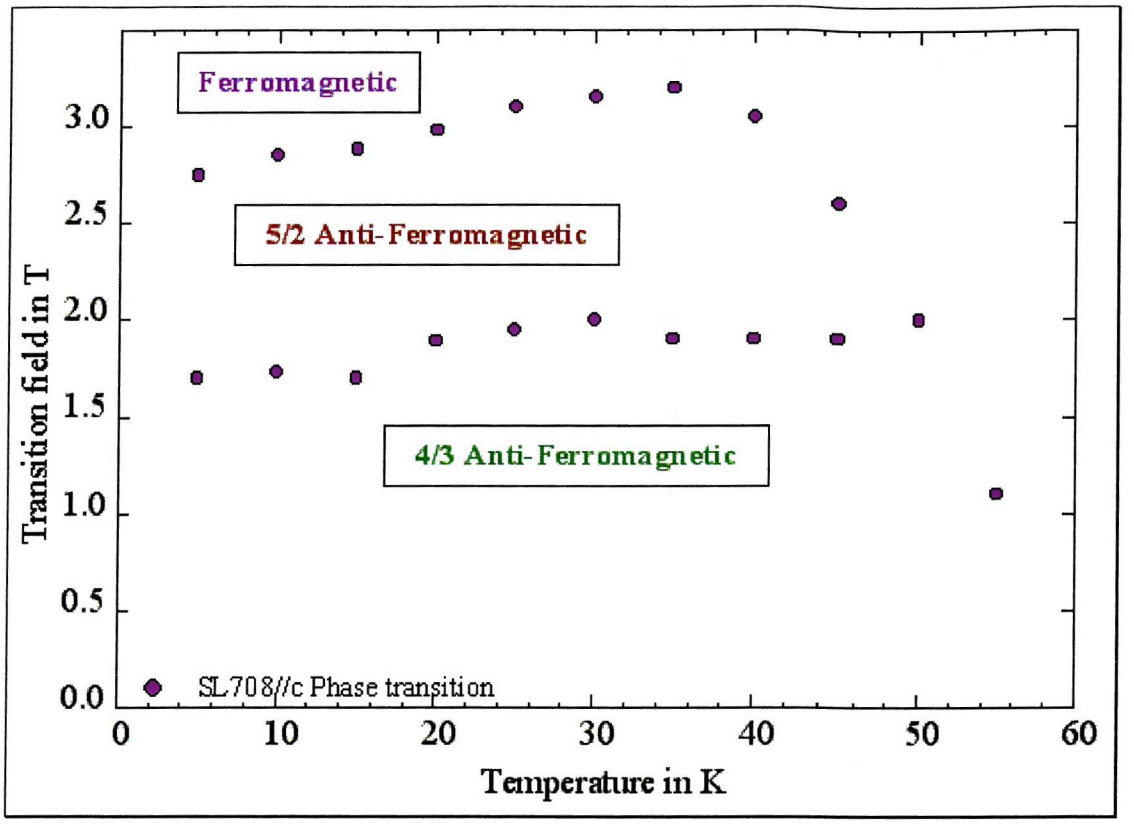

Figure A-32. Phase diagram for SL708 $(Tm_{20}/Y_{40})_{50}$ with field parallel to c-axis.

Whilst the magnetisation as a function of *b*-axis applied field does suggest a phase transition, much of the magnetisation data obtained for this sample was dominated by the sample holder contribution. It was not possible to deduce phase transition fields with reasonable accuracy. No phase diagram is, therefore, presented for SL708 $(Tm_{20}/Y_{40})_{50}$ with field parallel to b-axis.

SL717 $(Tm_{50}/Y_{10})_{52}$

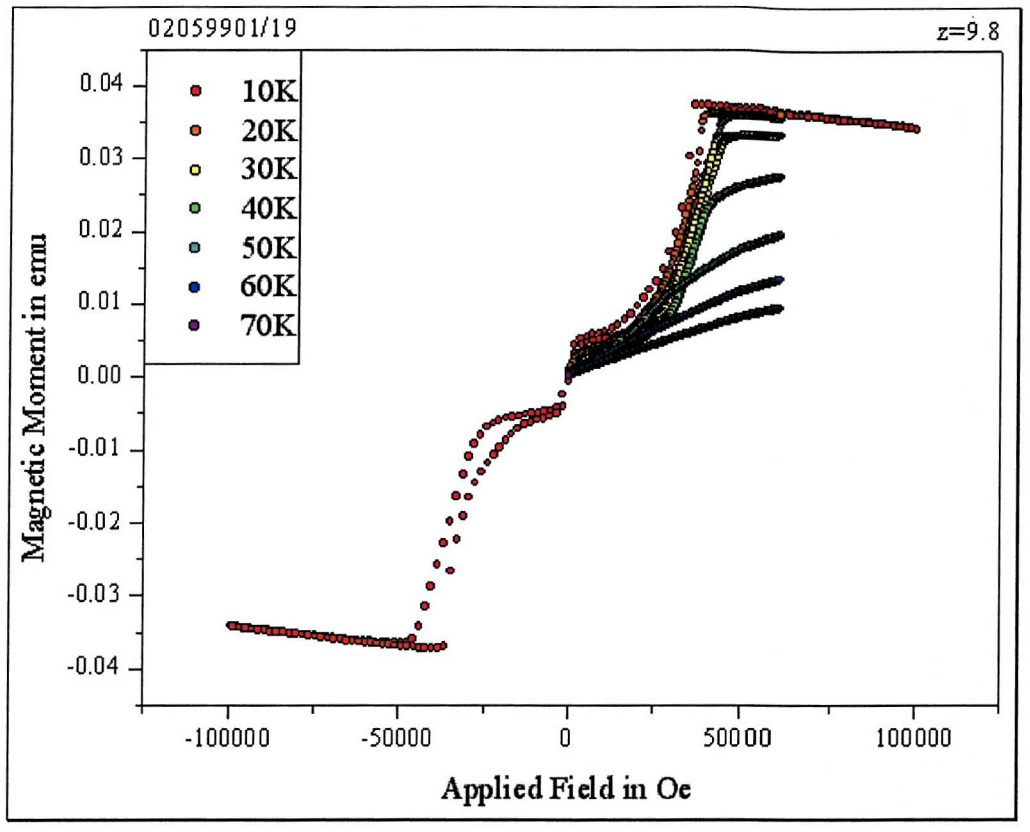

Figure A-33. Magnetic Moment as a function of c-axis applied magnetic field at a range of temperatures for SL717 $(Tm_{50}/Y_{10})_{52}$.

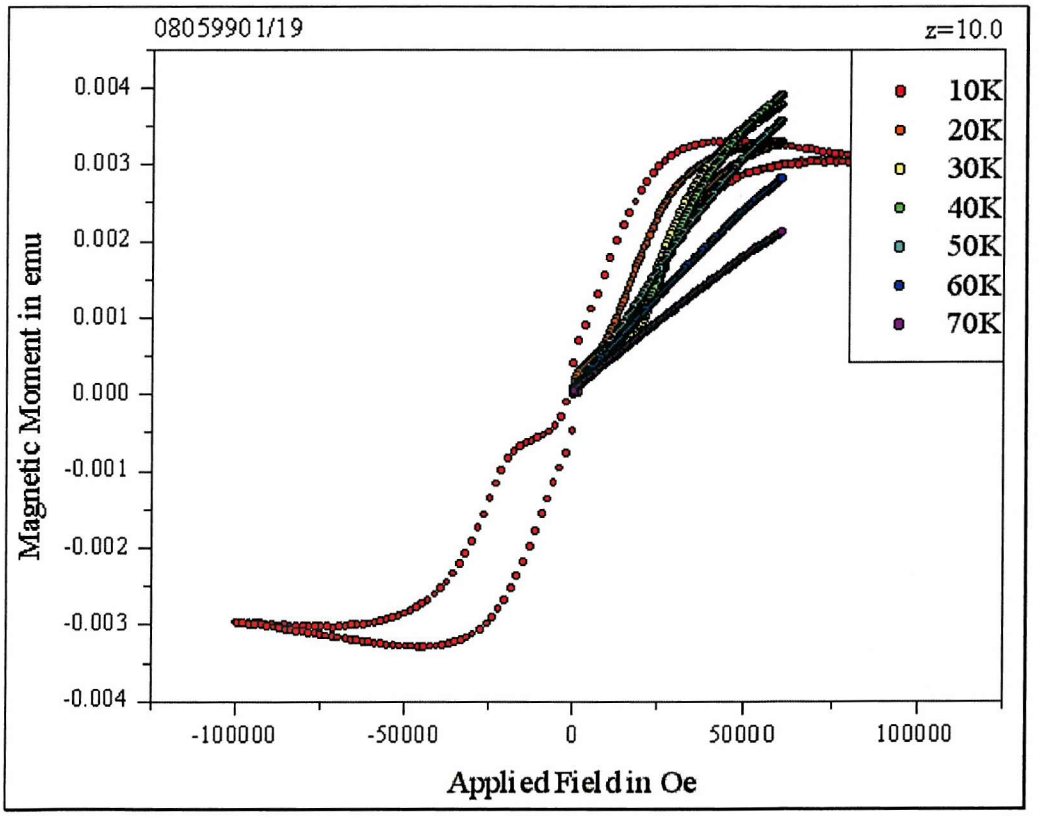

Figure A-34. Magnetic Moment as a function of b-axis applied magnetic field at a range of temperatures for SL717 $(Tm_{50}/Y_{10})_{52}$.

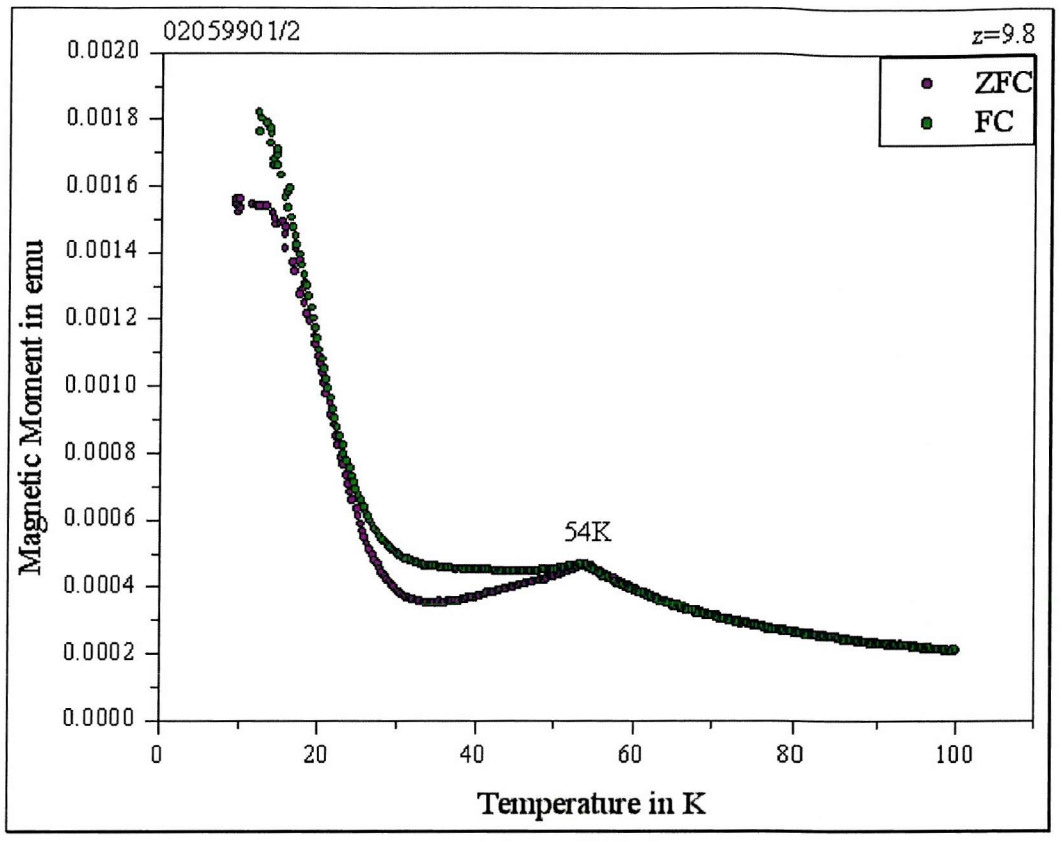

Figure A-35. Magnetic Moment as a function of temperature with 0.1T applied magnetic field parallel to the c-axis for SL717 $(Tm_{50}/Y_{10})_{52}$.

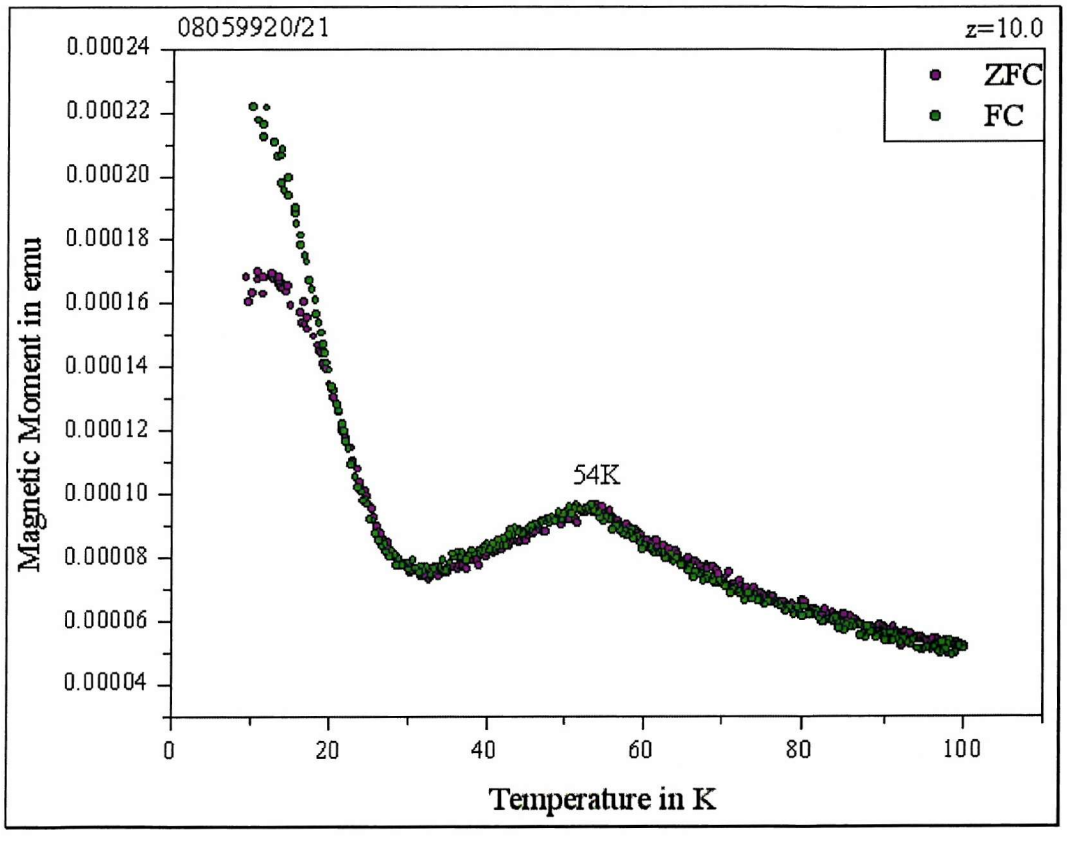

Figure A-36. Magnetic Moment as a function of temperature with 0.1T applied magnetic field parallel to the b-axis for SL717 $(Tm_{50}/Y_{10})_{52}$.

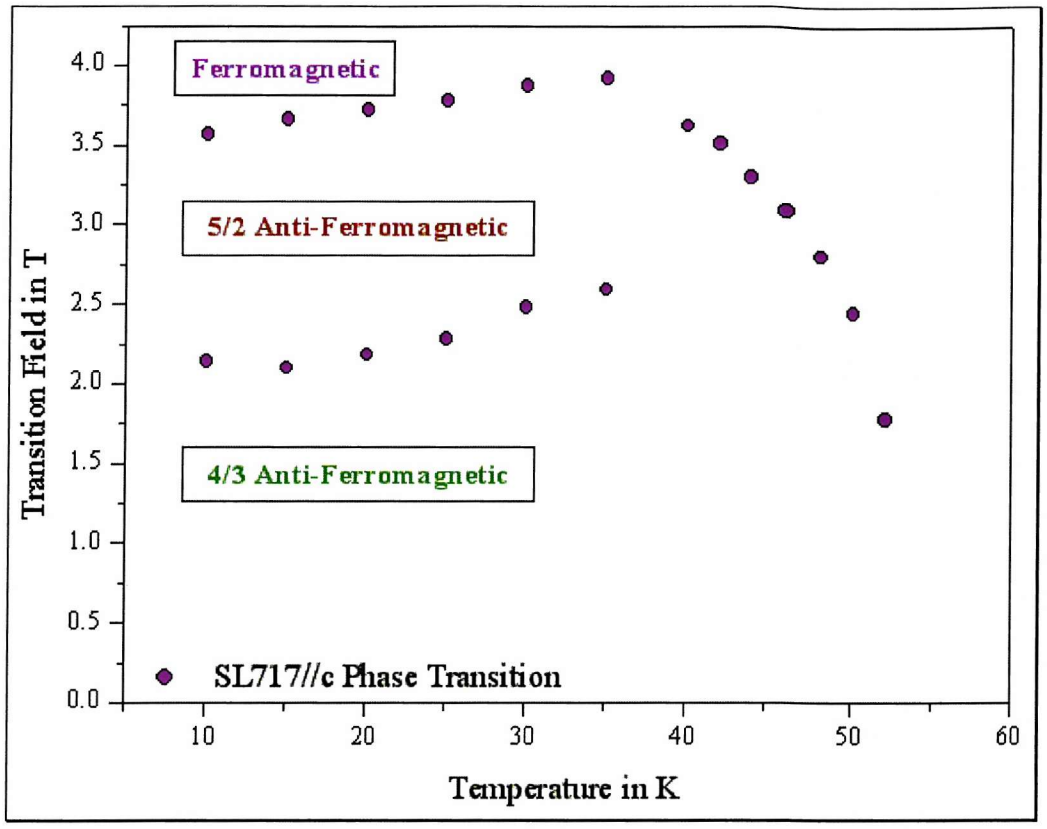

Figure A-37. Phase diagram for SL717 $(Tm_{50}/Y_{10})_{52}$ with field parallel to c-axis.

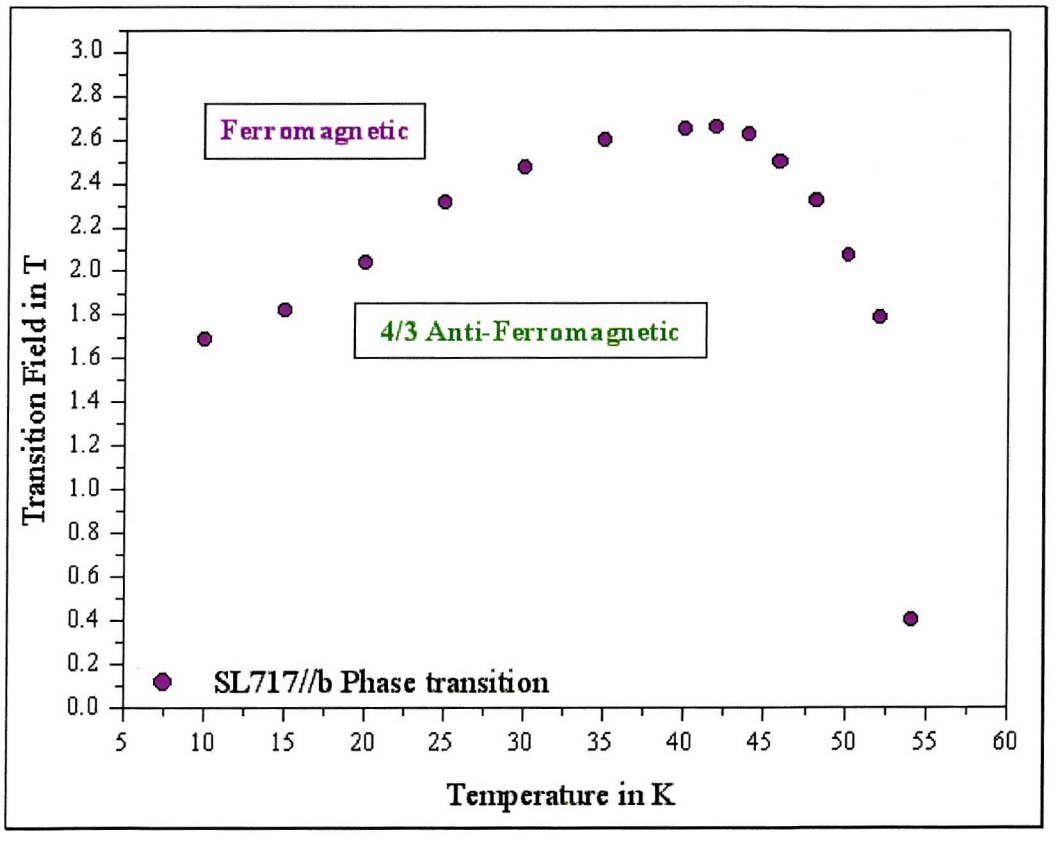

Figure A-38. Phase diagram for SL717 $(Tm_{50}/Y_{10})_{52}$ with field parallel to b-axis.

SL709 $(Tm_{20}/Lu_6)_{60}$

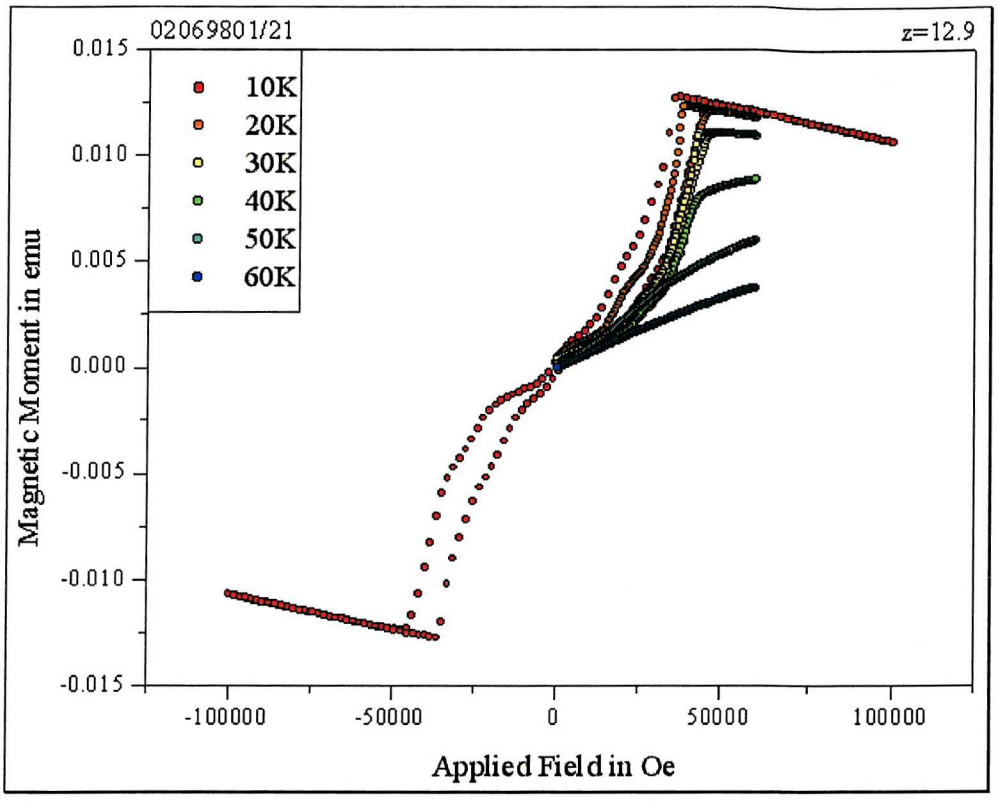

Figure A-39. Magnetic Moment as a function of c-axis applied magnetic field at a range of temperatures for SL709 $(Tm_{20}/Lu_6)_{60}$.

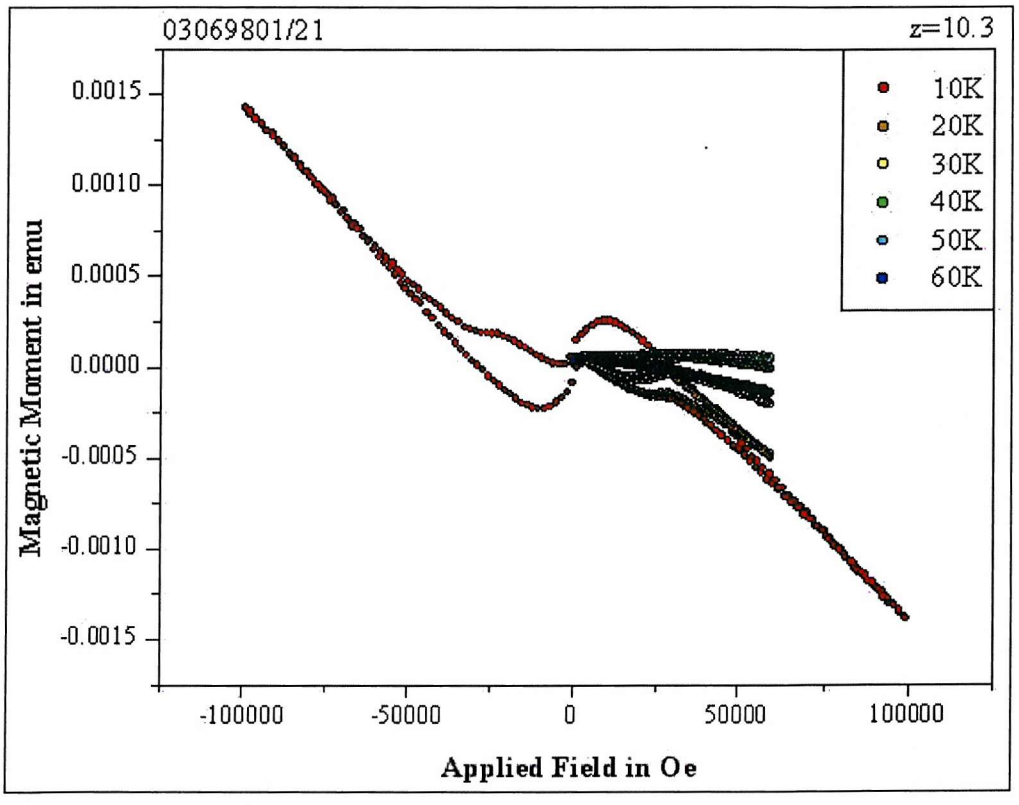

Figure A-40. Magnetic Moment as a function of b-axis applied magnetic field at a range of temperatures for SL709 $(Tm_{20}/Lu_6)_{60}$.

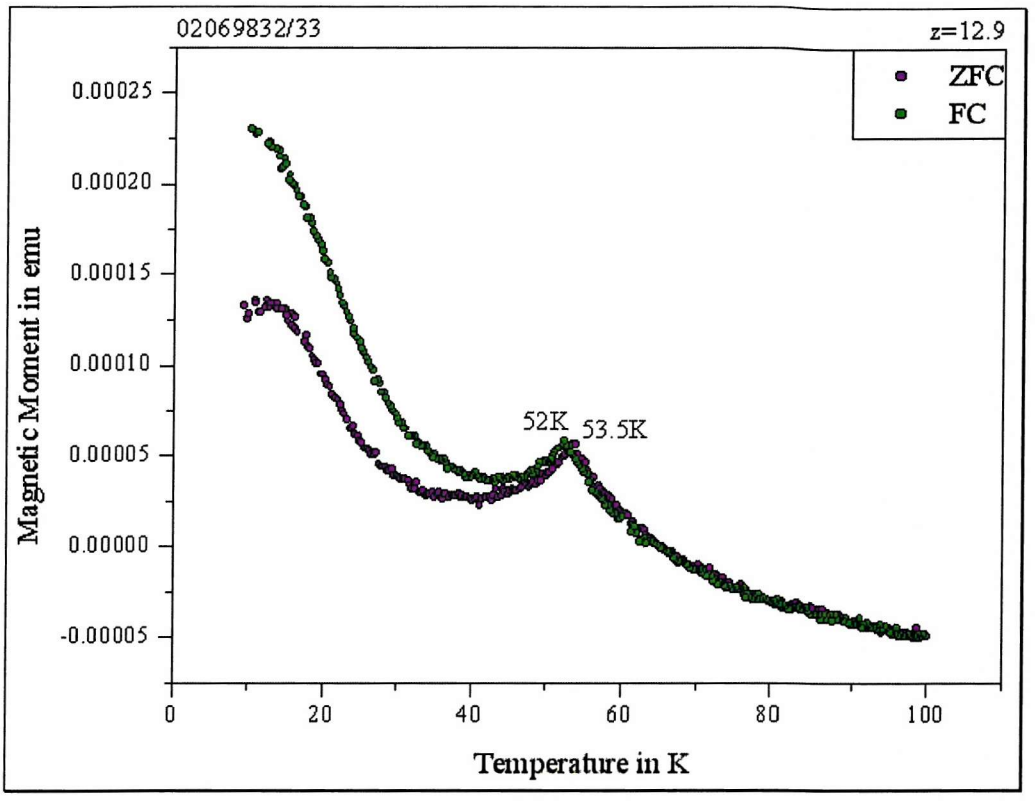

Figure A-41. Magnetic Moment as a function of temperature with 0.1T applied magnetic field parallel to the c-axis for SL709 $(Tm_{20}/Lu_6)_{60}$.

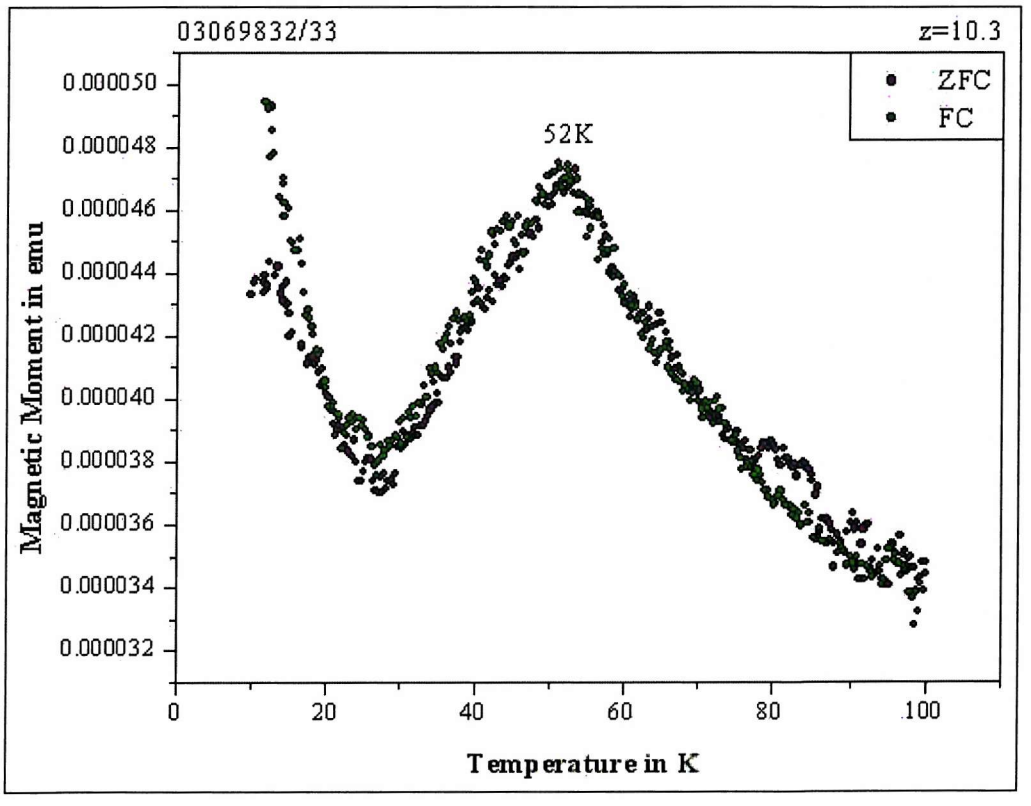

Figure A-42. Magnetic Moment as a function of temperature with 0.1T applied magnetic field parallel to the b-axis for SL709 $(Tm_{20}/Lu_6)_{60}$.

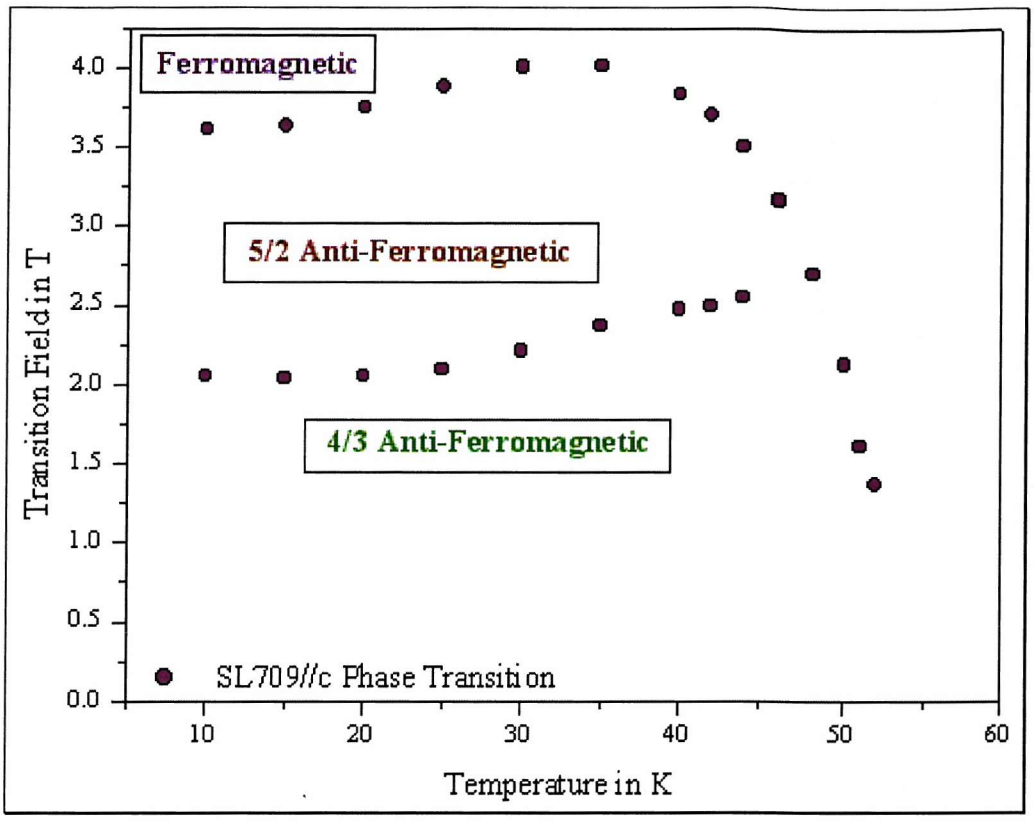

Figure A-43. Phase diagram for SL709 $(Tm_{20}/Lu_6)_{60}$ with field parallel to c-axis.

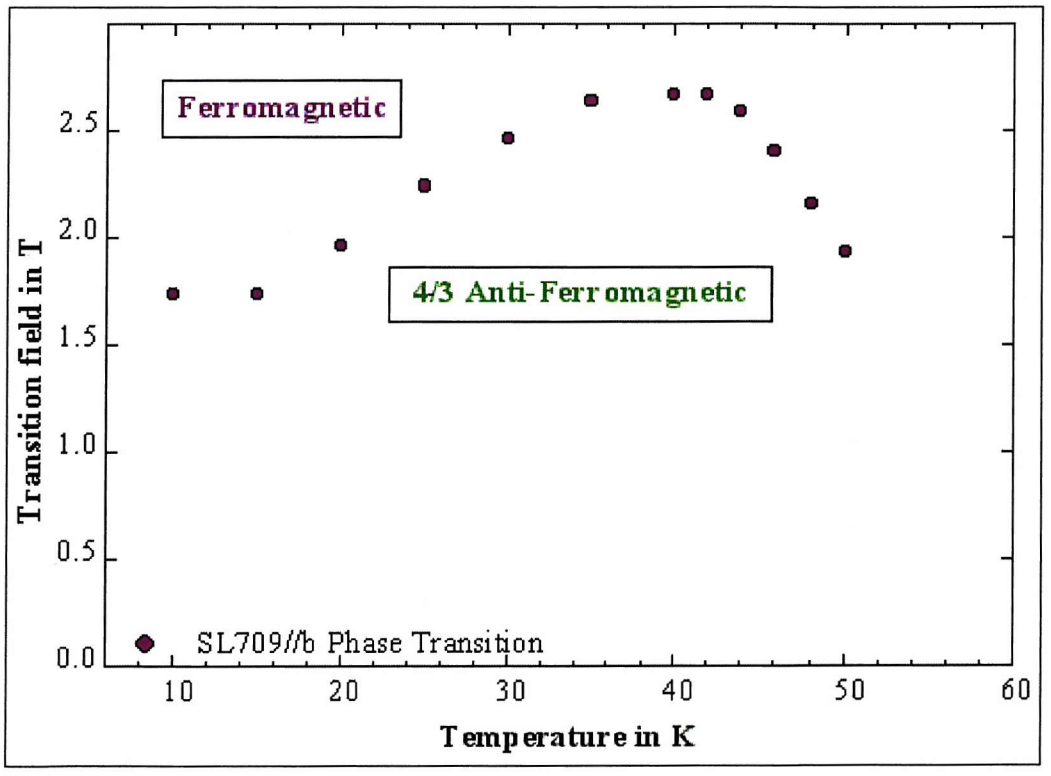

Figure A-44. Phase diagram for SL709 $(Tm_{20}/Lu_6)_{60}$ with field parallel to b-axis.

SL710 $(Tm_6/Lu_{20})_{60}$

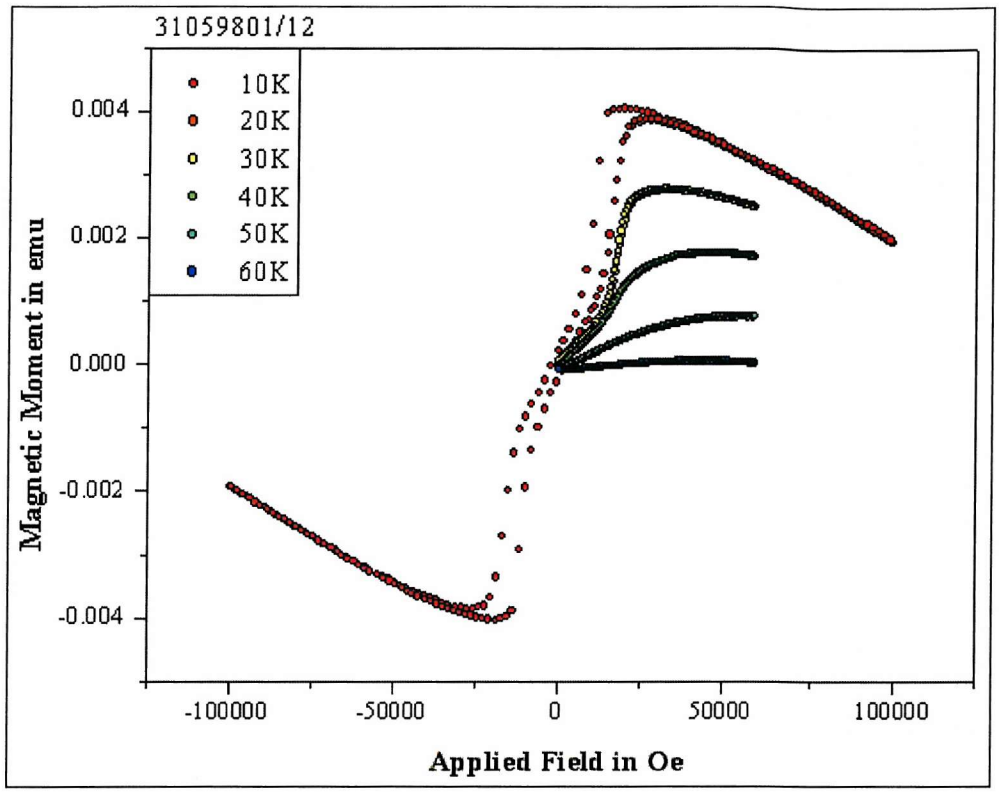

Figure A-45. Magnetic Moment as a function of c-axis applied magnetic field at a range of temperatures for SL710 $(Tm_6/Lu_{20})_{60}$.

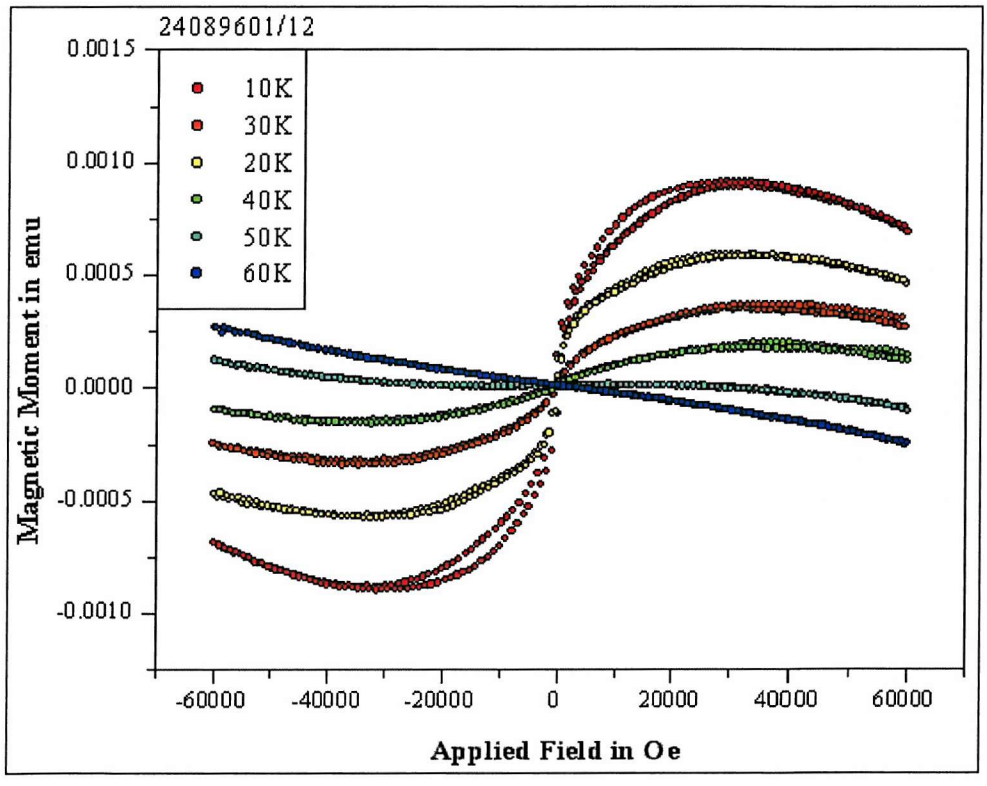

Figure A-46. Magnetic Moment as a function of b-axis applied magnetic field at a range of temperatures for SL710 $(Tm_6/Lu_{20})_{60}$.

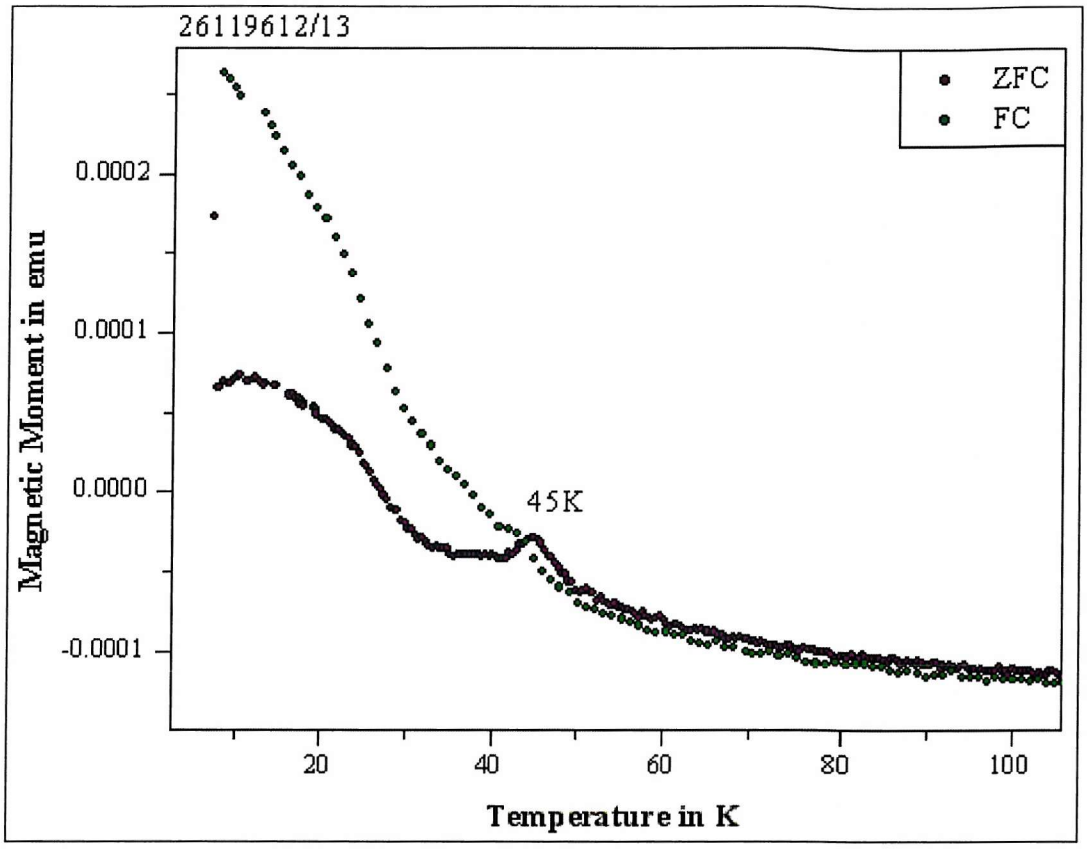

Figure A-47. Magnetic Moment as a function of temperature with 0.1T applied magnetic field parallel to the c-axis for SL710 $(Tm_6/Lu_{20})_{60}$.

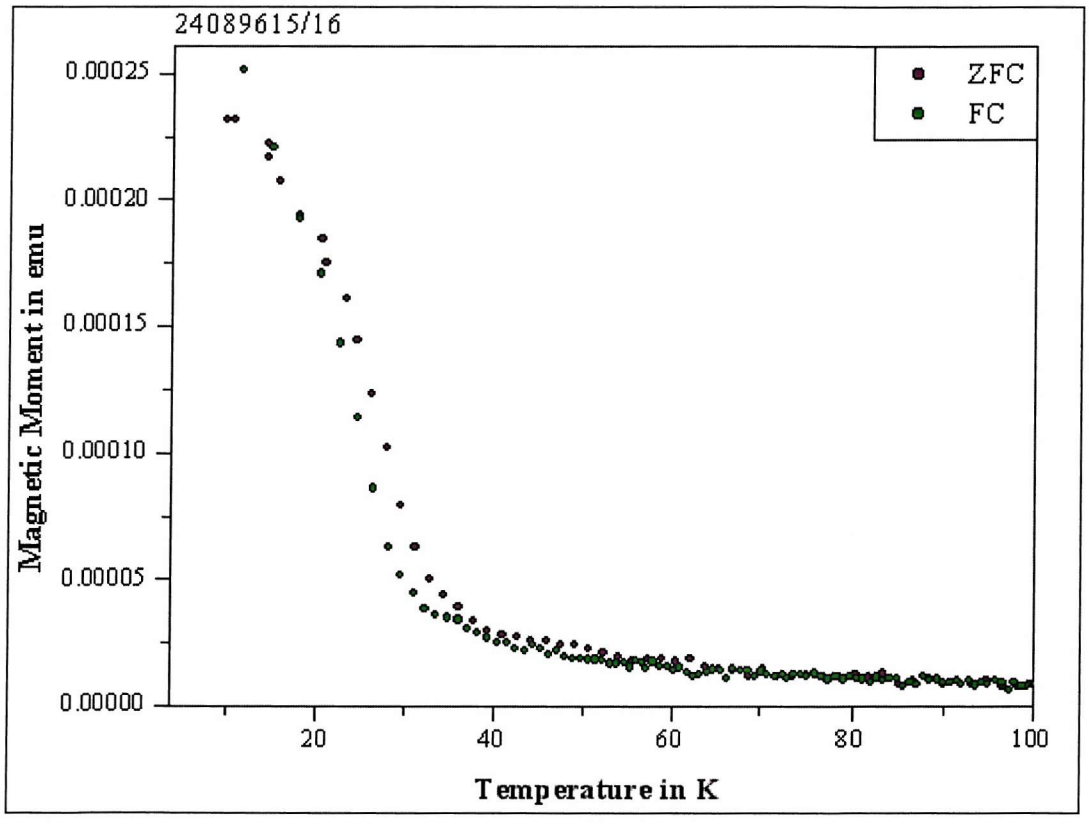

Figure A-48. Magnetic Moment as a function of temperature with 0.1T applied magnetic field parallel to the b-axis for SL710 $(Tm_6/Lu_{20})_{60}$.

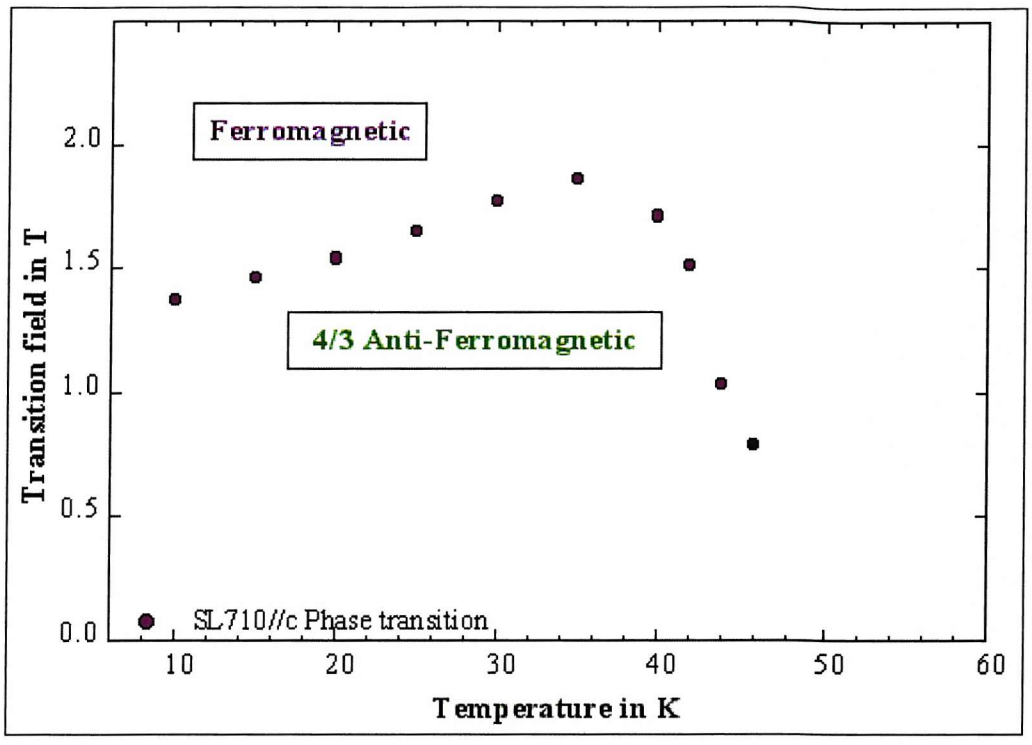

Figure A-49. Phase diagram for SL710 $(Tm_6/Lu_{20})_{60}$ with field parallel to c-axis.

The magnetisation as a function of applied field does not suggest a detectable phase transition. No phase diagram is, therefore, presented for SL710 $(Tm_6/Lu_{20})_{60}$ with field parallel to b-axis.

SL711 $(Tm_{20}/Lu_{20})_{60}$

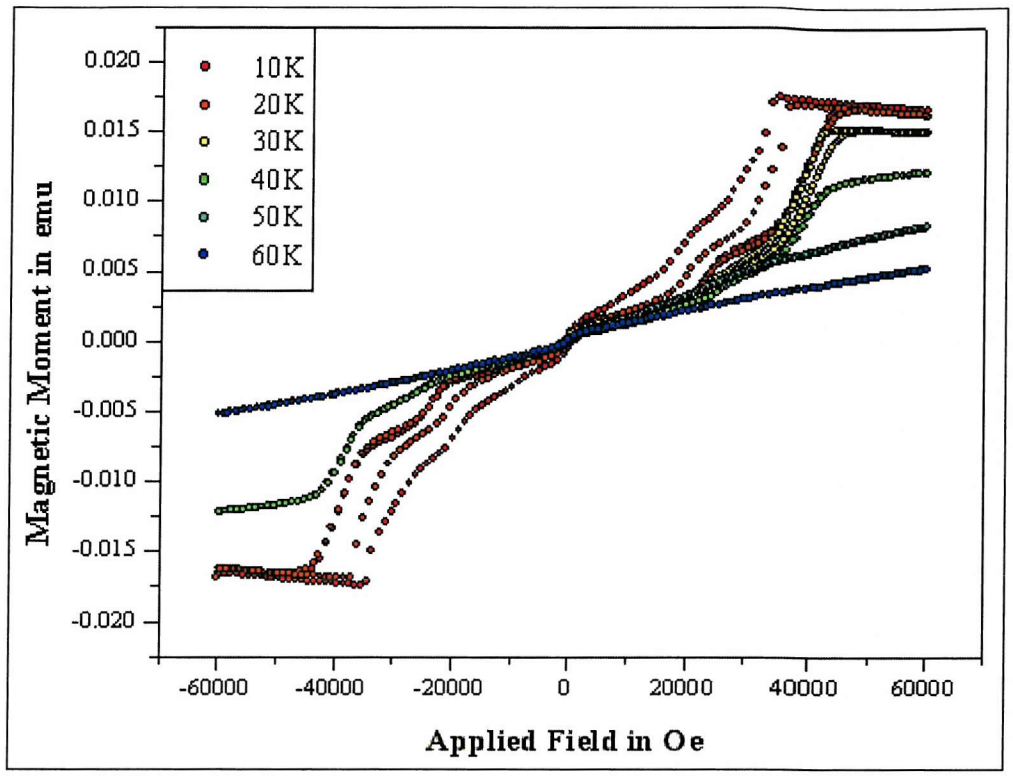

Figure A-50. Magnetic Moment as a function of c-axis applied magnetic field at a range of temperatures for SL711 $(Tm_{20}/Lu_{20})_{60}$.

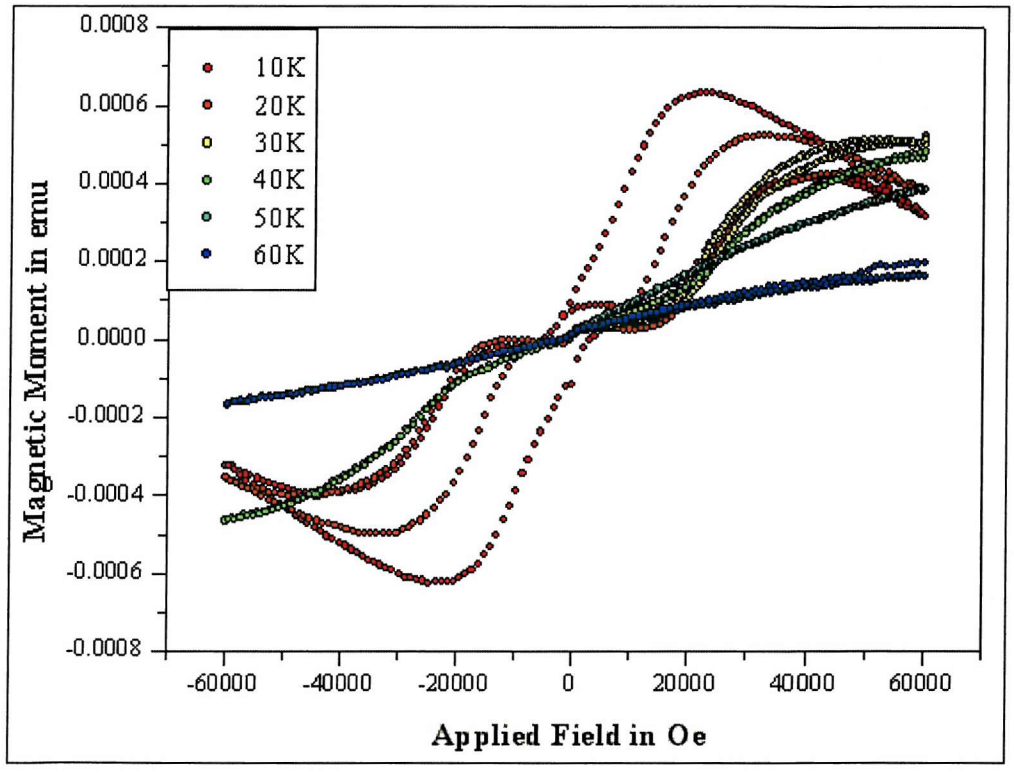

Figure A-51. Magnetic Moment as a function of b-axis applied magnetic field at a range of temperatures for SL711 $(Tm_{20}/Lu_{20})_{60}$.

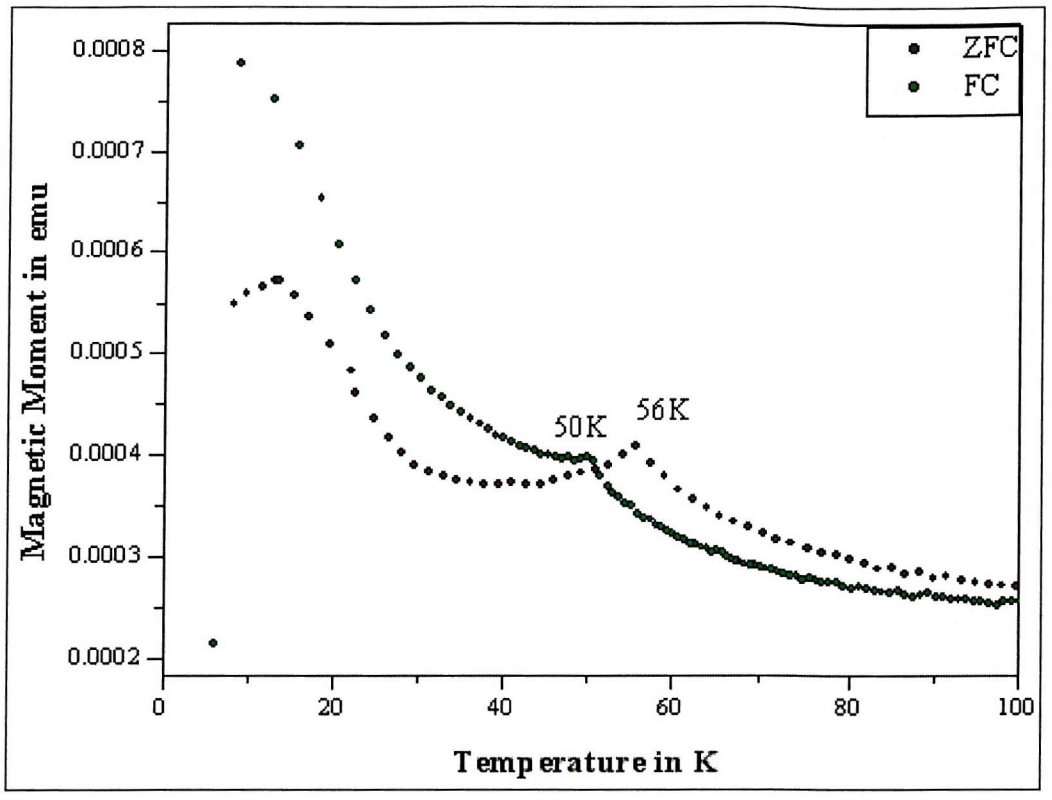

Figure A-52. Magnetic Moment as a function of temperature with 0.1T applied magnetic field parallel to the c-axis for SL711 $(Tm_{20}/Lu_{20})_{60}$.

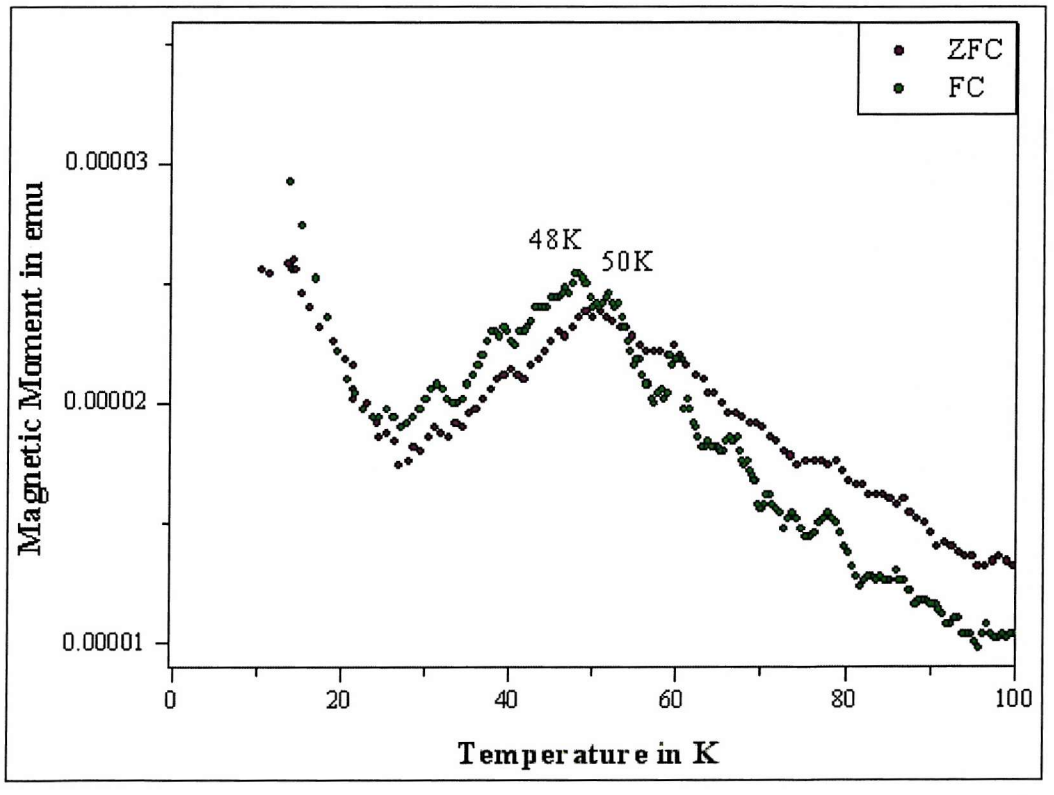

Figure A-53. Magnetic Moment as a function of temperature with 0.1T applied magnetic field parallel to the b-axis for SL711 $(Tm_{20}/Lu_{20})_{60}$.

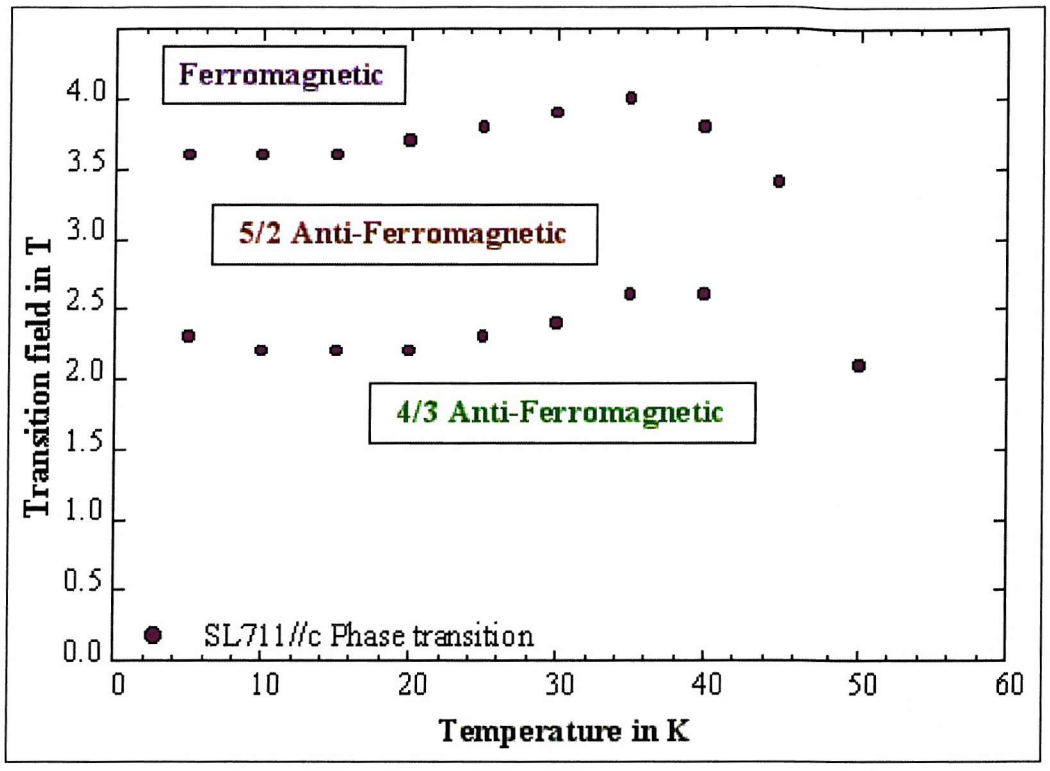

Figure A-54. Phase diagram for SL711 $(Tm_{20}/Lu_{20})_{60}$ with field parallel to c-axis.

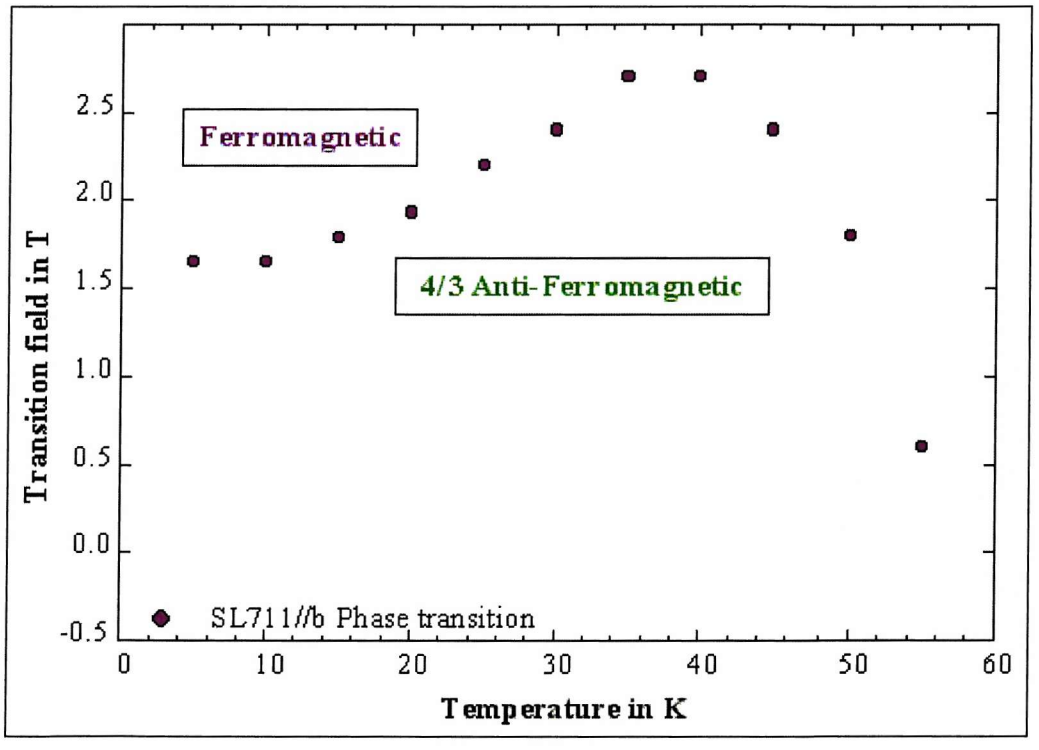

Figure A-55. Phase diagram for SL711 $(Tm_{20}/Lu_{20})_{60}$ with field parallel to b-axis.

SL712 $(Tm_{40}/Lu_{20})_{50}$

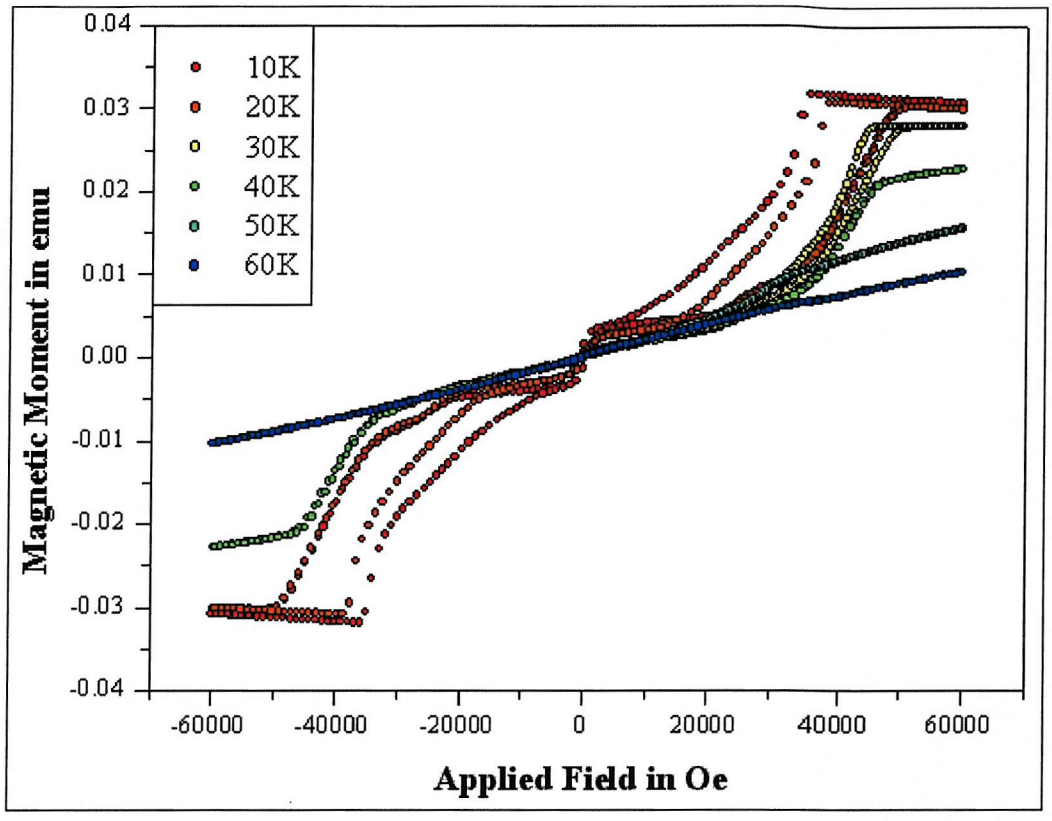

Figure A-56. Magnetic Moment as a function of c-axis applied magnetic field at a range of temperatures for SL712 $(Tm_{40}/Lu_{20})_{50}$.

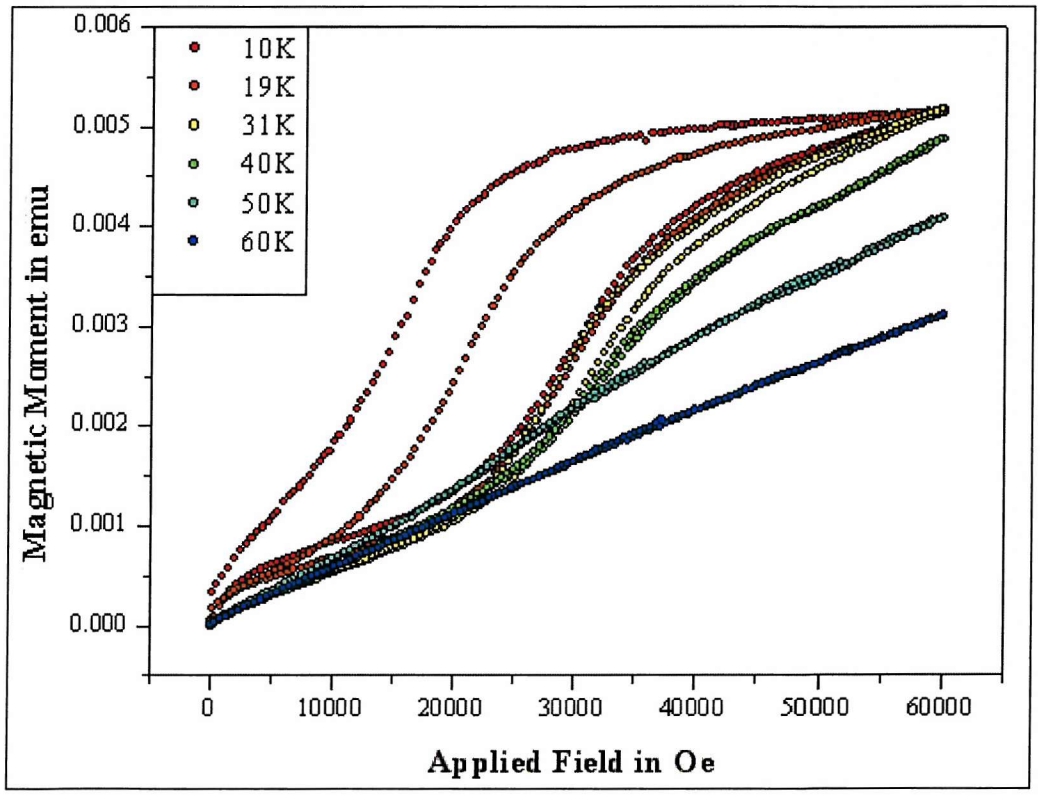

Figure A-57. Magnetic Moment as a function of b-axis applied magnetic field at a range of temperatures for SL712 $(Tm_{40}/Lu_{20})_{50}$.

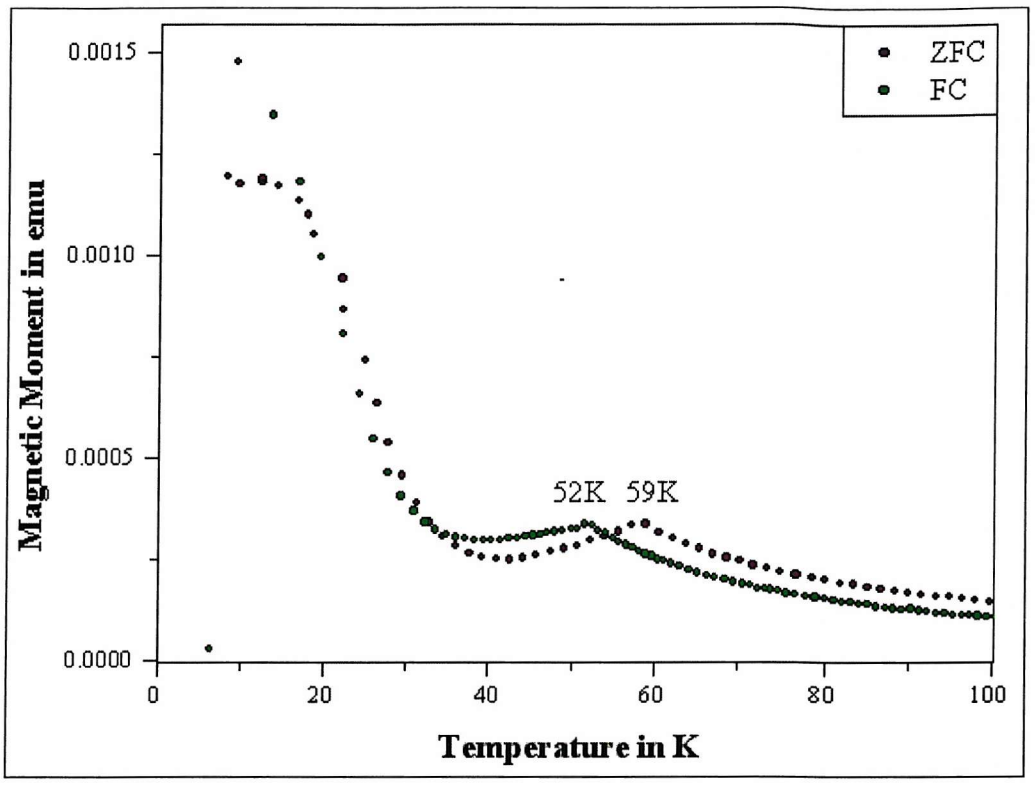

Figure A-58. Magnetic Moment as a function of temperature with 0.1T applied magnetic field parallel to the c-axis for SL712 $(Tm_{40}/Lu_{20})_{50}$.

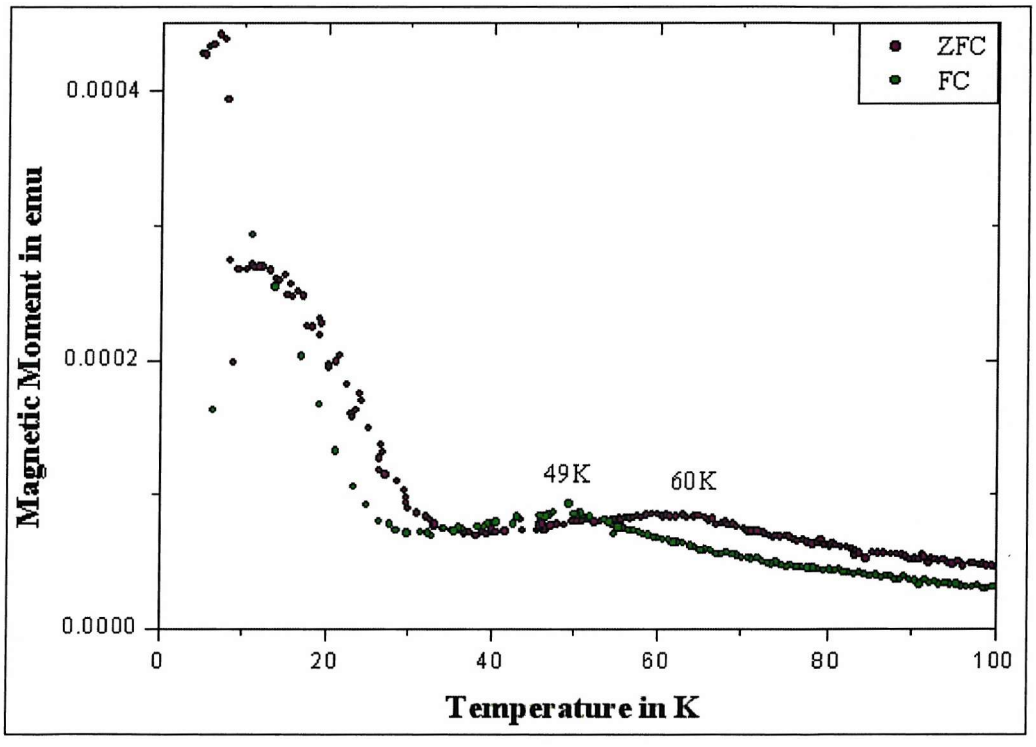

Figure A-59. Magnetic Moment as a function of temperature with 0.1T applied magnetic field parallel to the b-axis for SL712 $(Tm_{40}/Lu_{20})_{50}$.

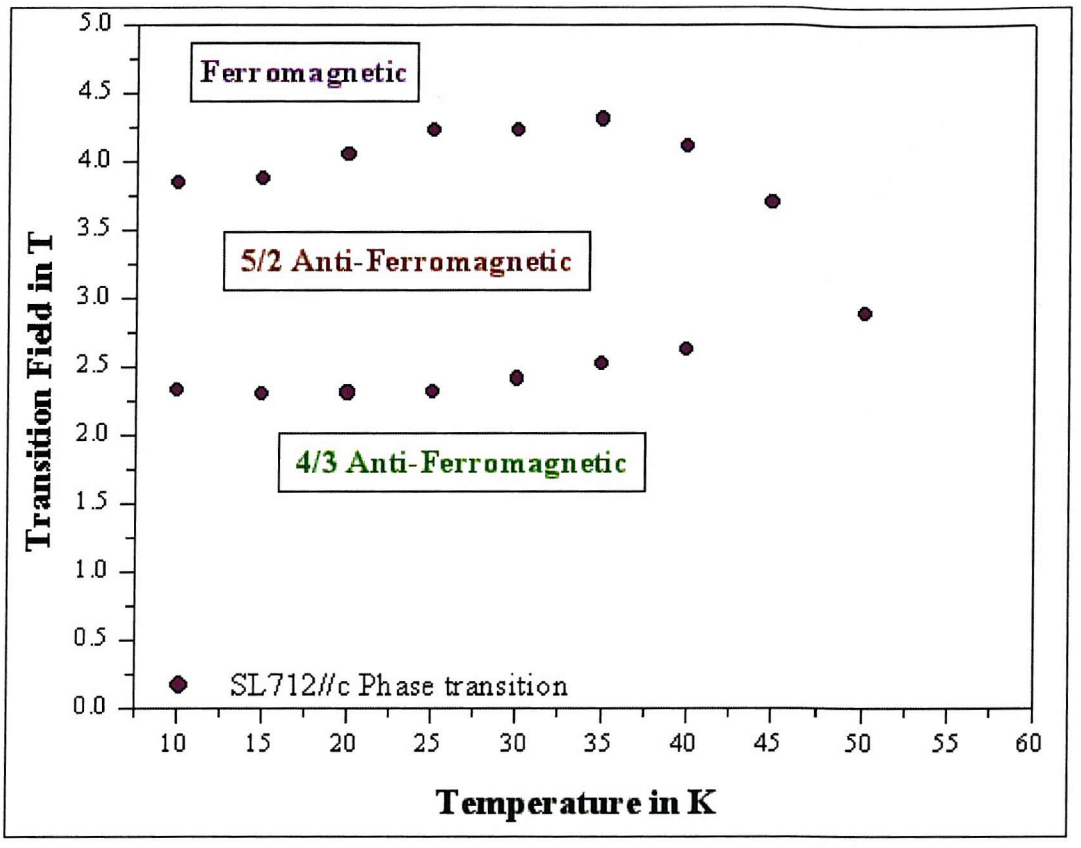

Figure A-60. Phase diagram for SL712 $(Tm_{40}/Lu_{20})_{50}$ with field parallel to c-axis.

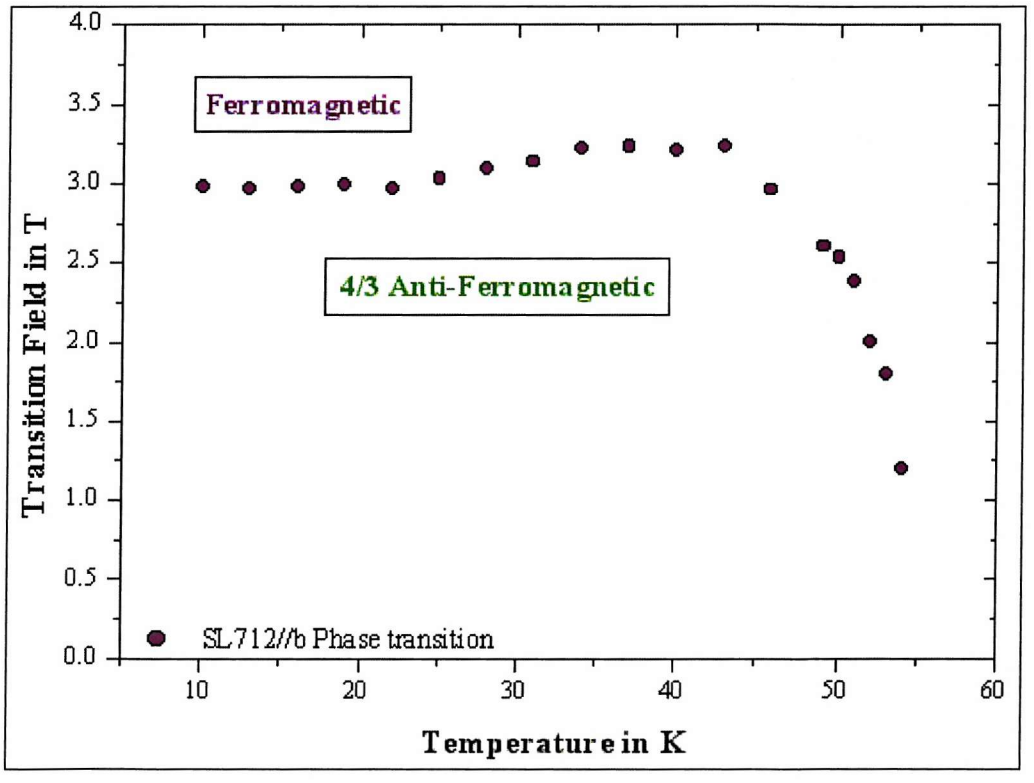

Figure A-61. Phase diagram for SL712 $(Tm_{40}/Lu_{20})_{50}$ with field parallel to b-axis.

SL713 $(Tm_{20}/Lu_{40})_{50}$

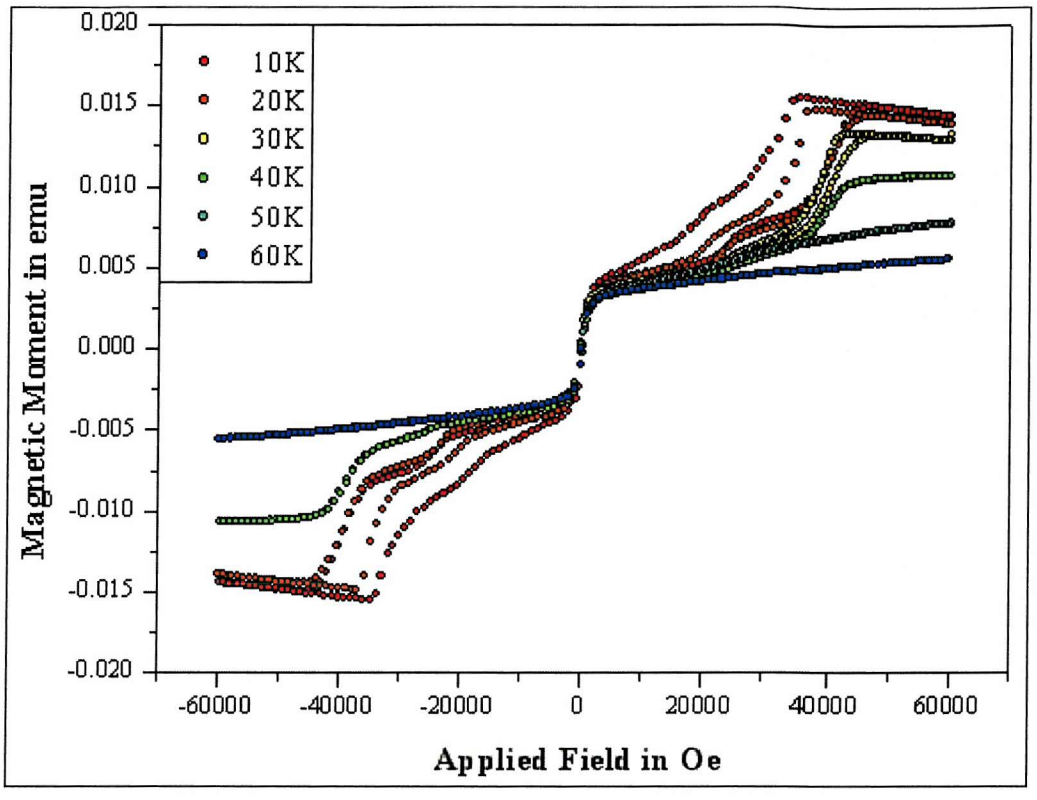

Figure A-62. Magnetic Moment as a function of c-axis applied magnetic field at a range of temperatures for SL713 $(Tm_{20}/Lu_{40})_{50}$.

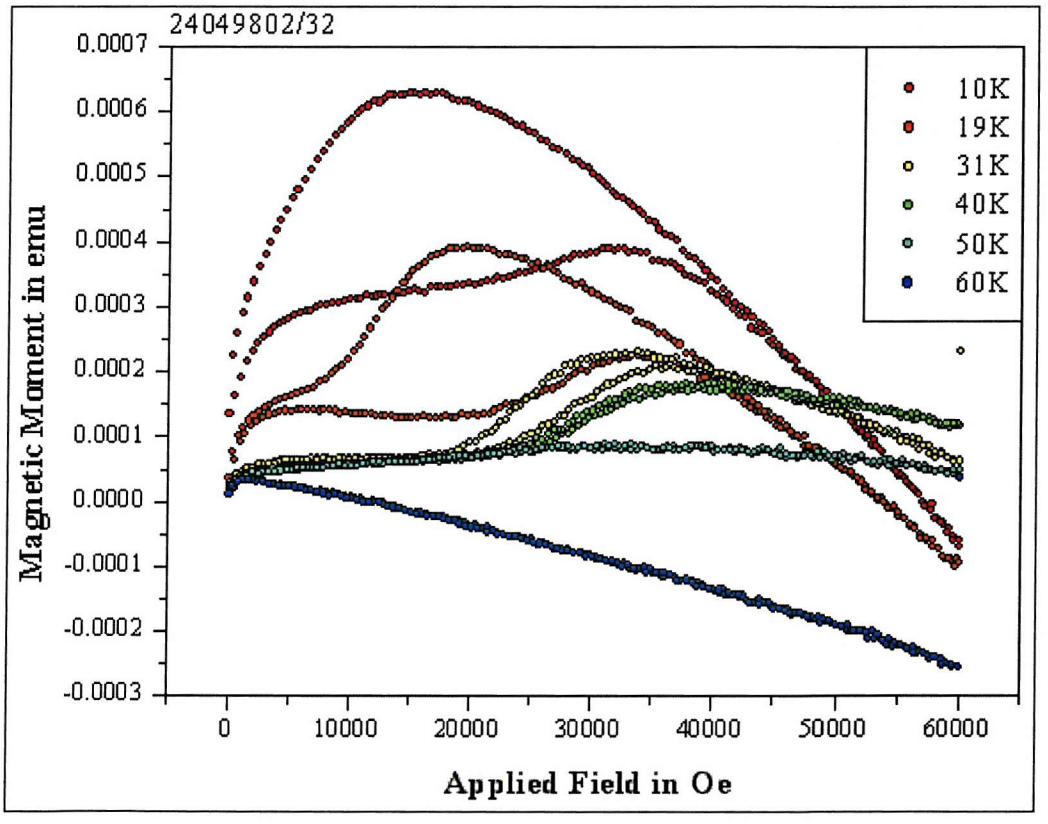

Figure A-63. Magnetic Moment as a function of b-axis applied magnetic field at a range of temperatures for SL713 $(Tm_{20}/Lu_{40})_{50}$.

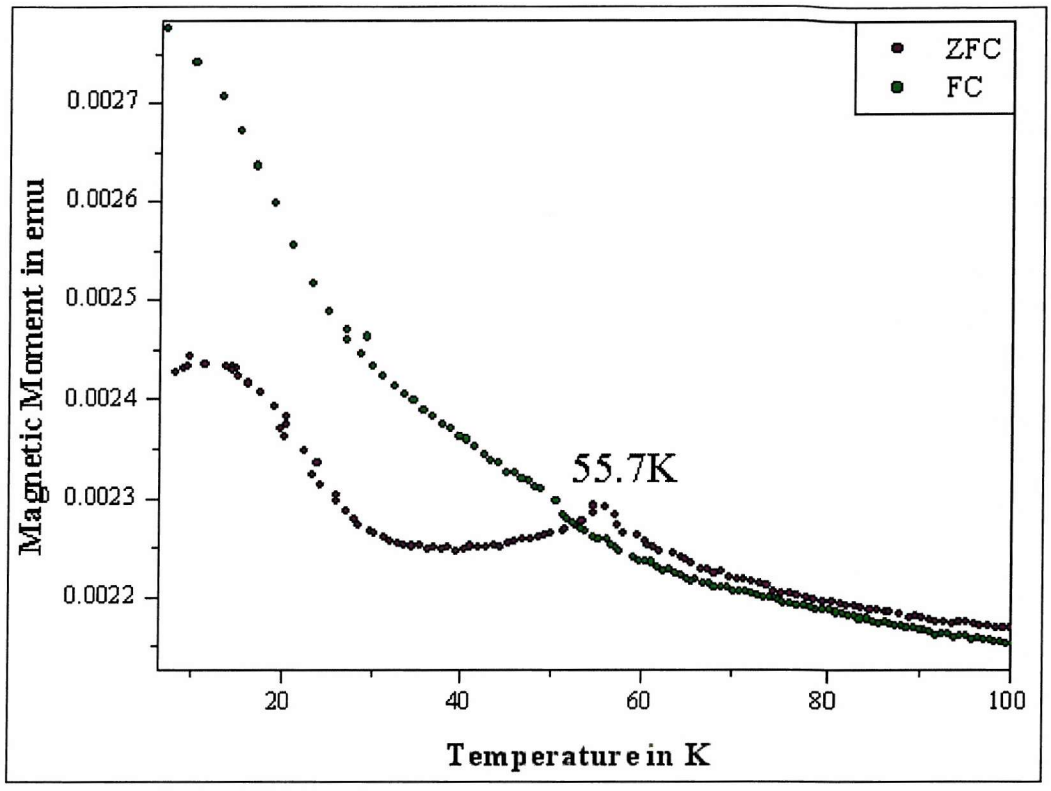

Figure A-64. Magnetic Moment as a function of temperature with 0.1T applied magnetic field parallel to the c-axis for SL713 $(Tm_{20}/Lu_{40})_{50}$.

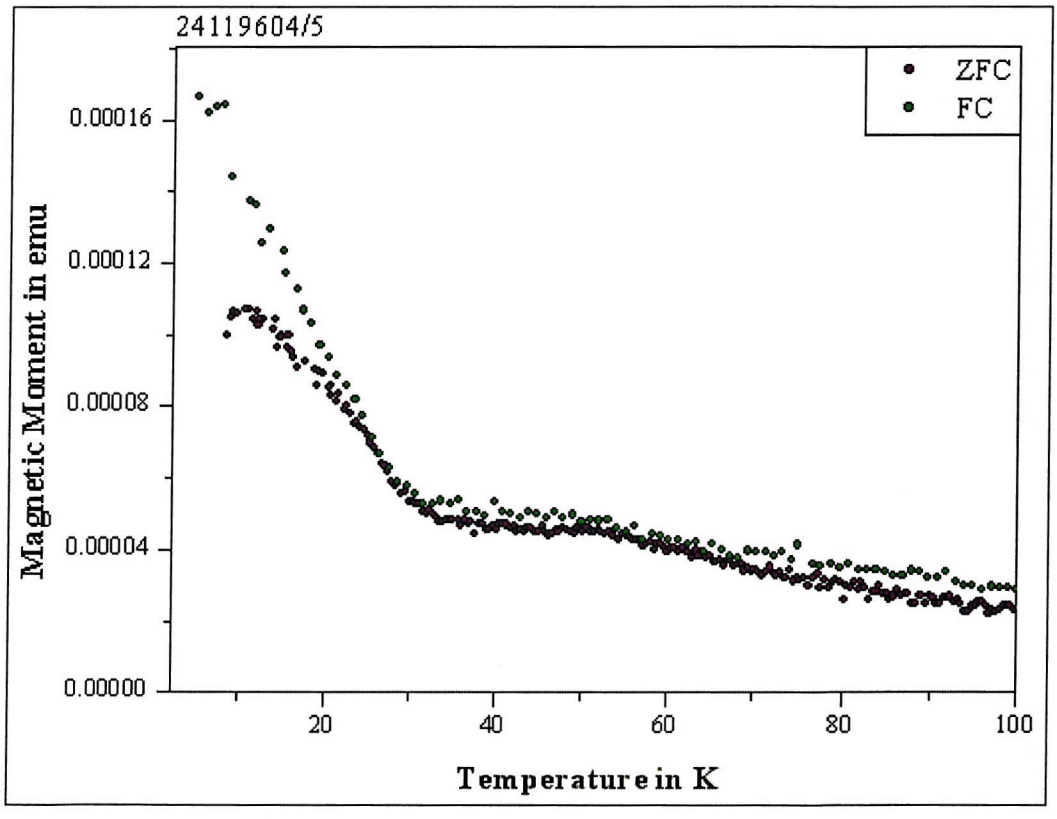

Figure A-65. Magnetic Moment as a function of temperature with 0.1T applied magnetic field parallel to the b-axis for SL713 $(Tm_{20}/Lu_{40})_{50}$.

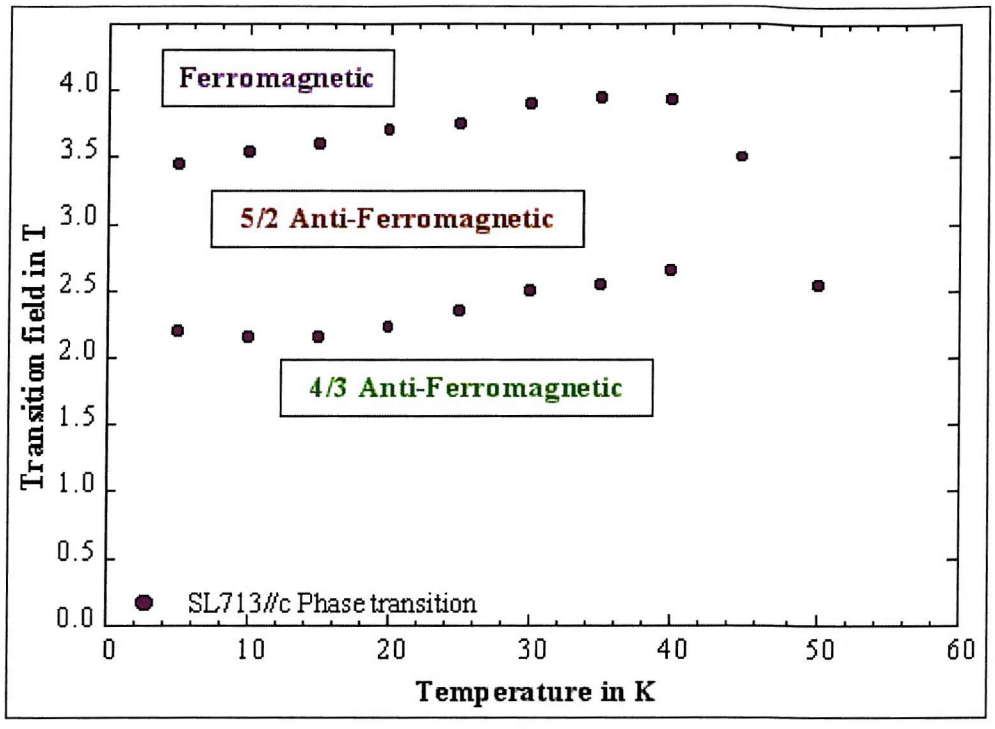

Figure A-66. Phase diagram for SL713 $(Tm_{20}/Lu_{40})_{50}$ with field parallel to c-axis.

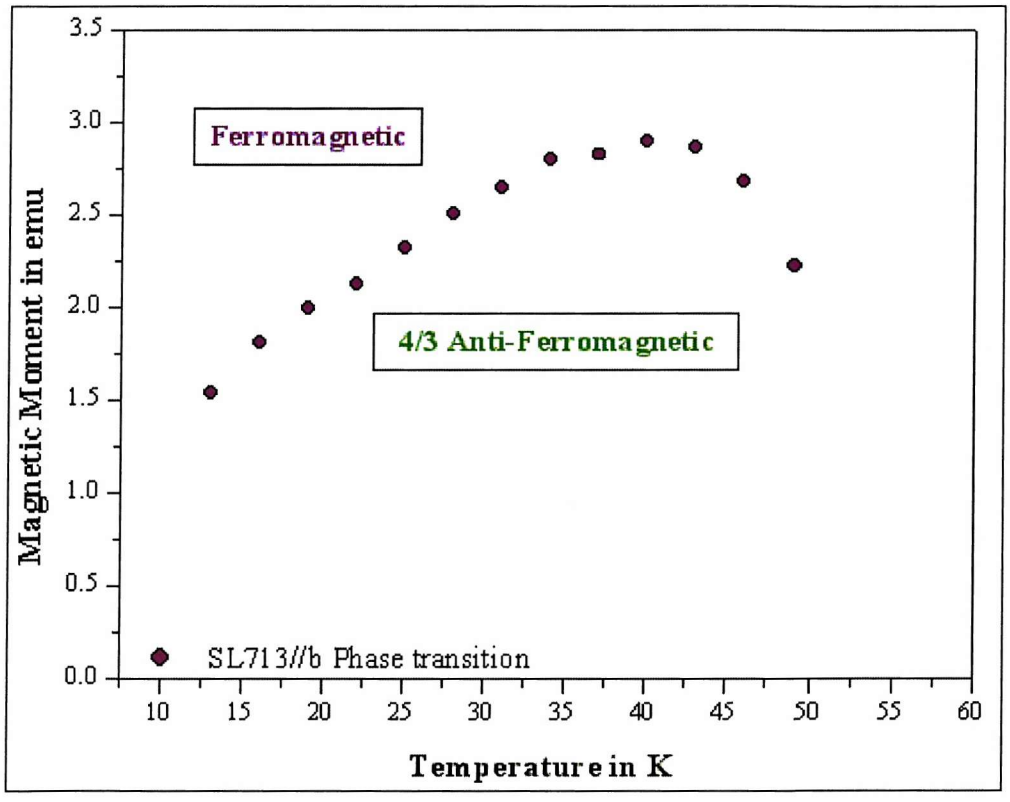

Figure A-67. Phase diagram for SL713 $(Tm_{20}/Lu_{40})_{50}$ with field parallel to b-axis.

SL719 $(Tm_{50}/Lu_{10})_{48}$

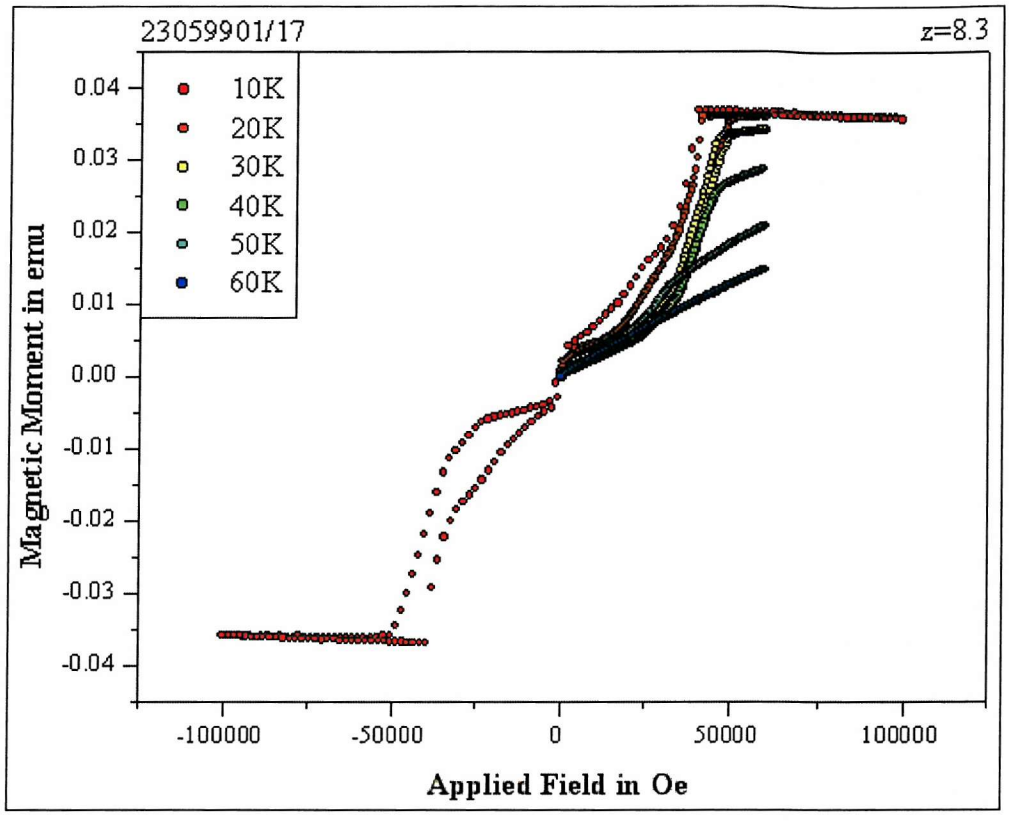

Figure A-68. Magnetic Moment as a function of c-axis applied magnetic field at a range of temperatures for SL719 $(Tm_{50}/Lu_{10})_{48}$.

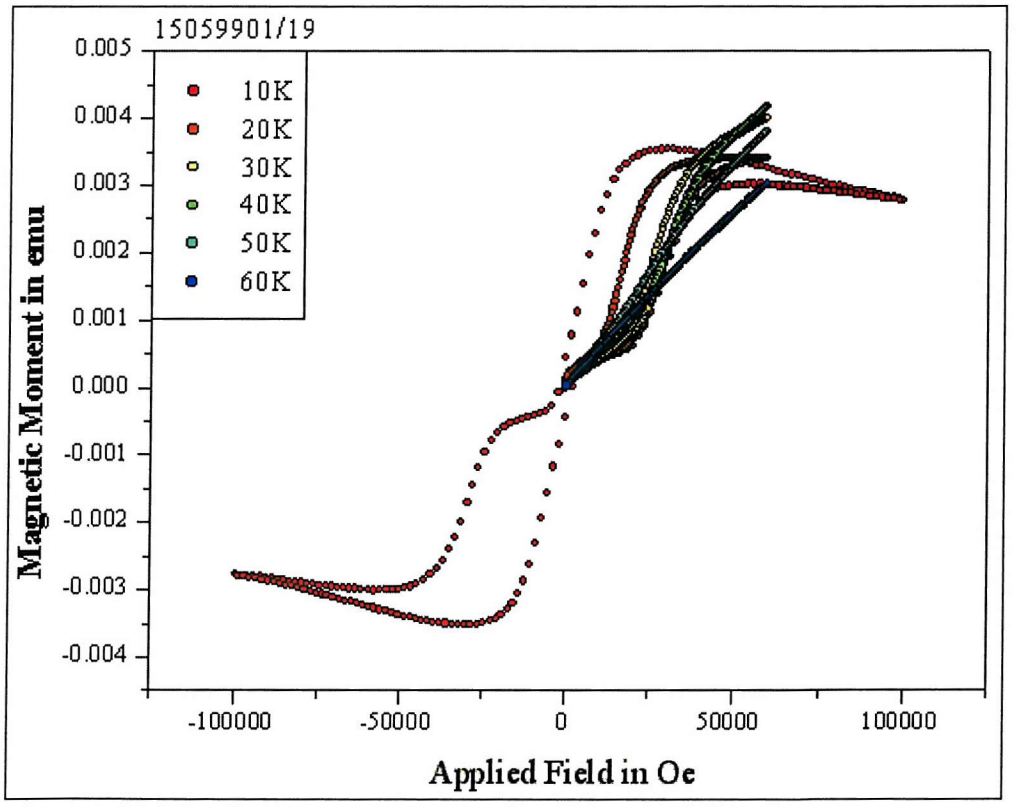

Figure A-69. Magnetic Moment as a function of b-axis applied magnetic field at a range of temperatures for SL719 $(Tm_{50}/Lu_{10})_{48}$.

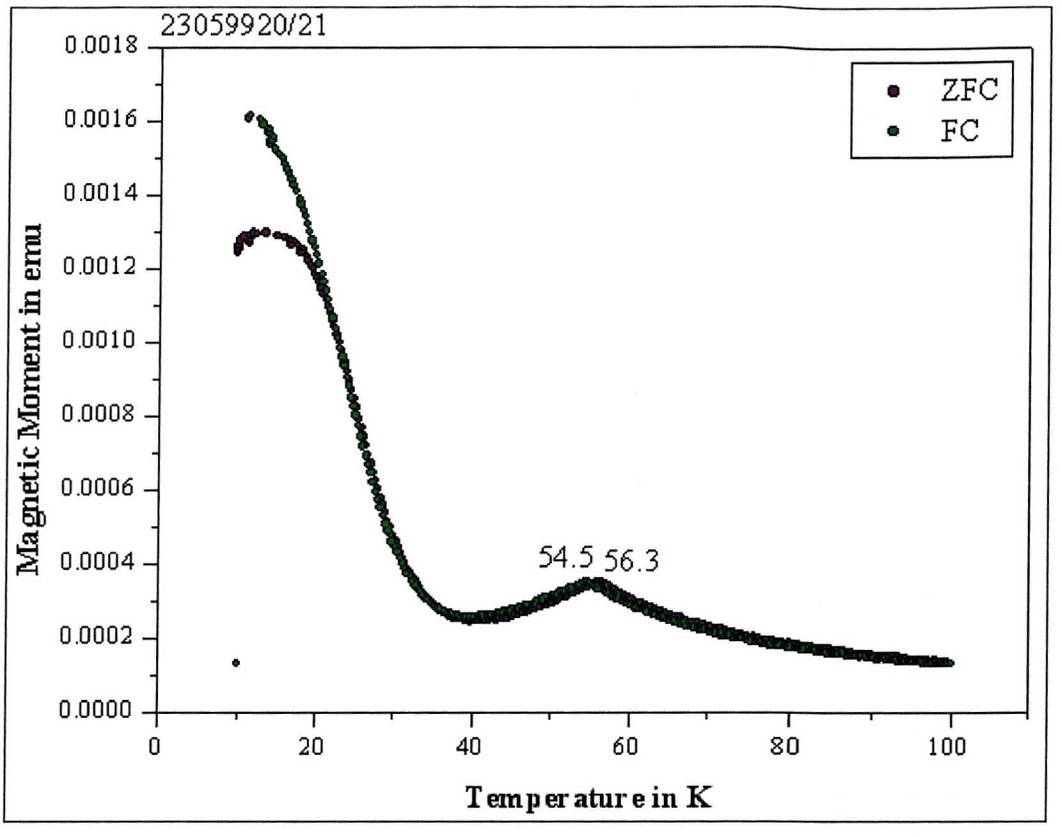

Figure A-70. Magnetic Moment as a function of temperature with 0.1T applied magnetic field parallel to the c-axis for SL719 $(Tm_{50}/Lu_{10})_{48}$.

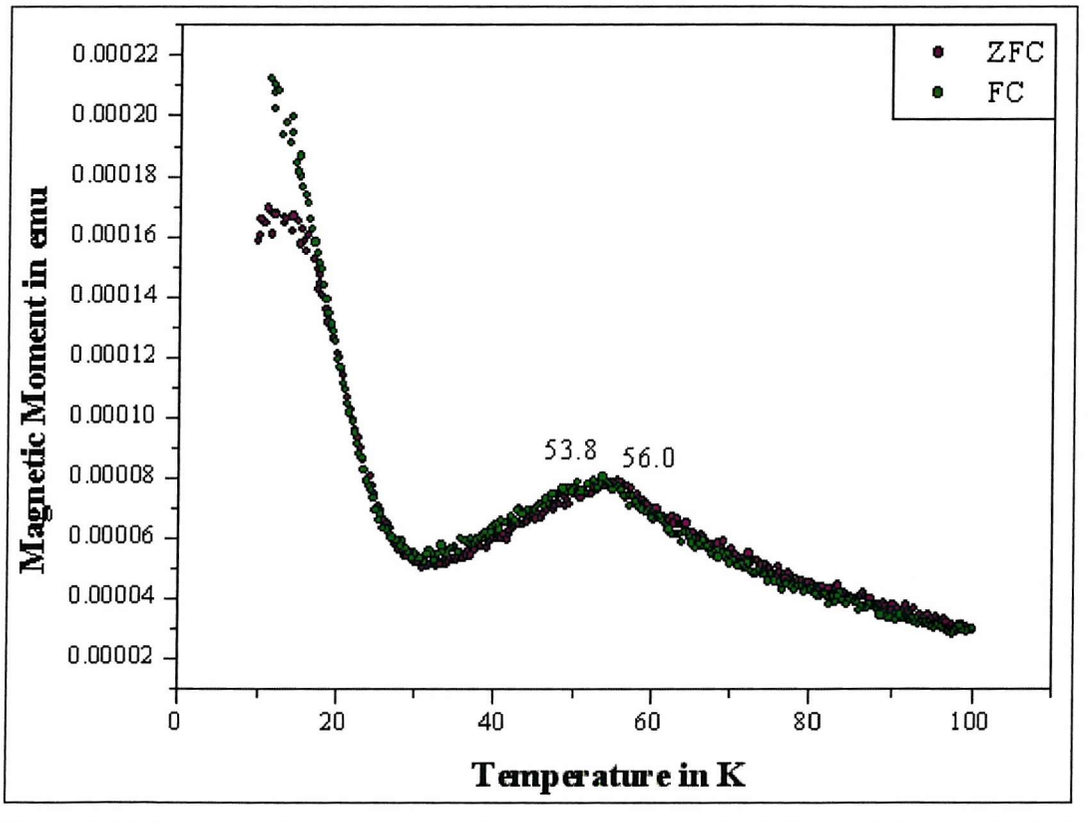

Figure A-71. Magnetic Moment as a function of temperature with 0.1T applied magnetic field parallel to the b-axis for SL719 $(Tm_{50}/Lu_{10})_{48}$.

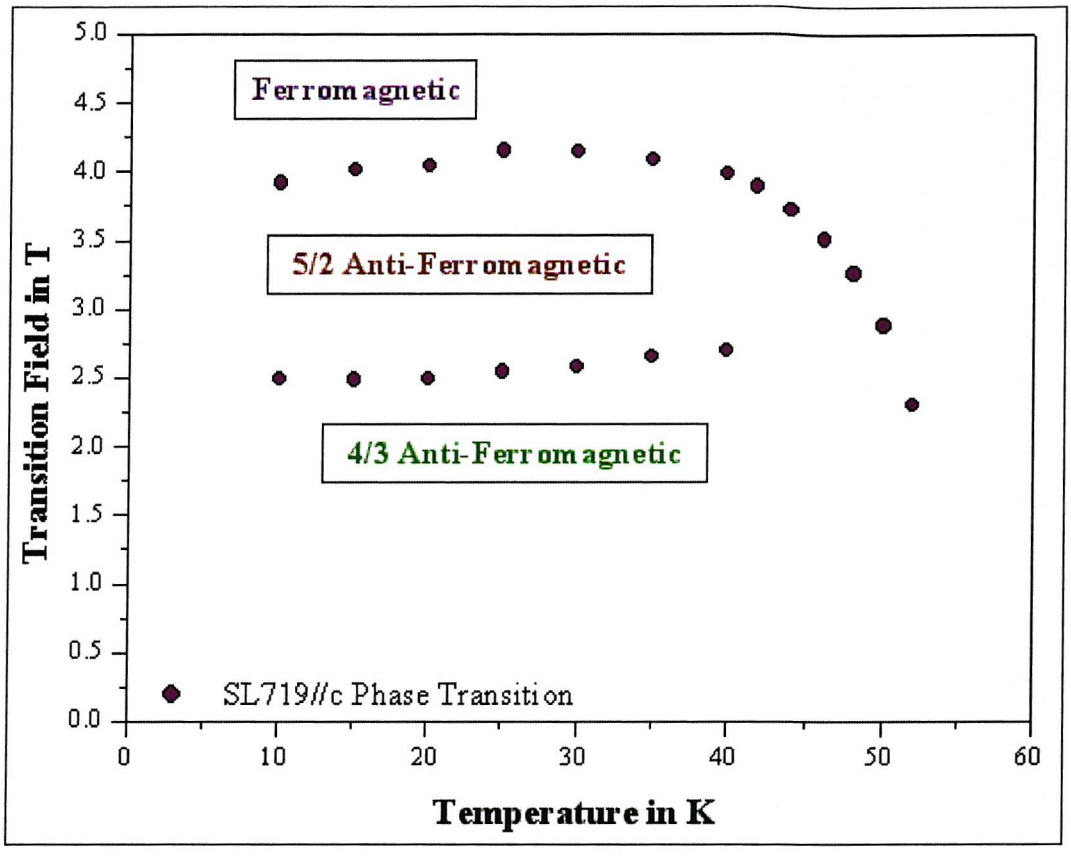

Figure A-72. Phase diagram for SL719 $(Tm_{50}/Lu_{10})_{48}$ with field parallel to c-axis.

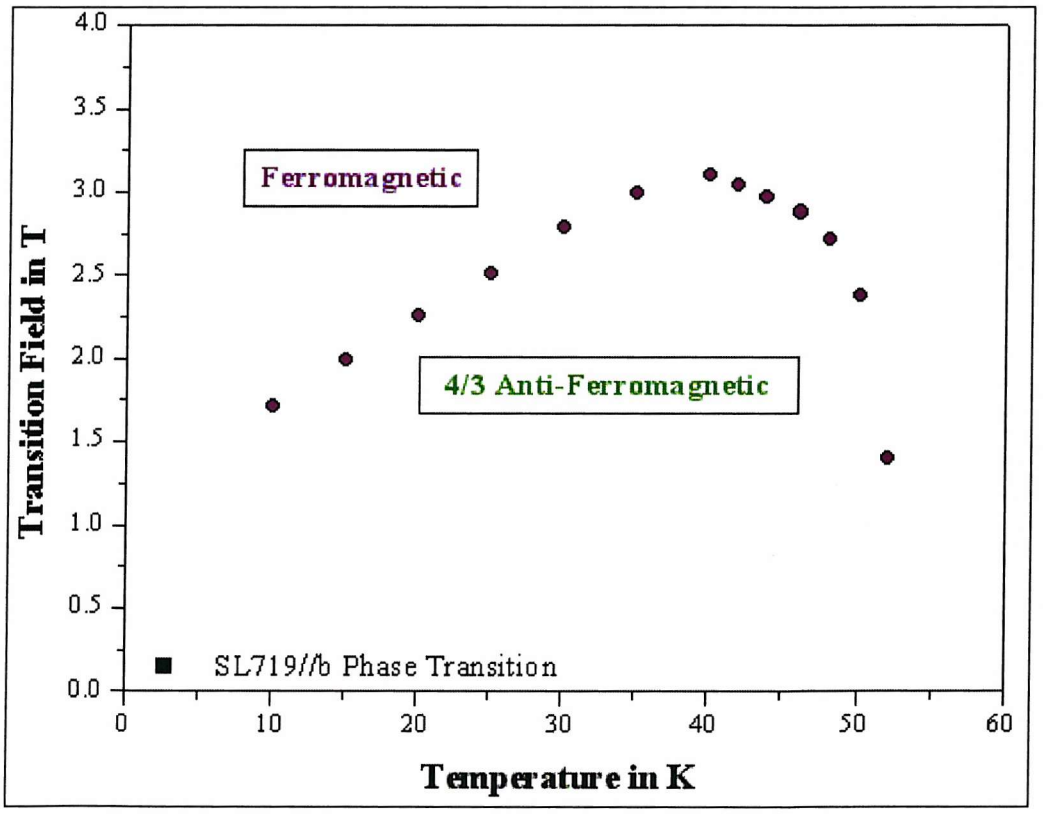

Figure A-73. Phase diagram for SL719 $(Tm_{50}/Lu_{10})_{48}$ with field parallel to b-axis.

References

1. C. F. Majkrzak, J. Kwo, M. Hong, Y. Yafet, Doon Gibbs, C. L. Chien, J. Bohr, *Advances in Physics*, **40** (1991) 99-189
2. J. Jensen and A. Mackintosh, *Rare Earth Magnetism* (Oxford Science Publications, 1991)
3. M.A. Ruderman and C. Kittel, *Physical Review*, **96** (1954) 99 - 102
4. T. Kasuya, *Progress of Theoretical Physics*, **Vol. 16,** No. 1, (July 1956) 45 - 57
5. K. Yosida, *Physical Review*, **106** (1957) 893 - 898
6. F. H. Spedding, B. J. Beaudry, J. J. Croat and P. E. Palmer, *Les Elements des Terres Rares* (Colloques Intern. du C.N.R.S. No. 180, 1970).
7. D. B. Richards and S. Legvold, *Physical Review*, **186** No. 2 (1969) 508 - 514
8. K. A. McEwen, U. Steigenberger, J. Jensen, *Physical Review*, **B43** No. 4 (1991) 3298 - 3310
9. C. Zener, *Physical Review*, **81** (1951) 446; **82** (1951) 403; **83** (1951) 299, **85** (1951) 324.
10. Y. Yafet, J. Kwo, M. Hong, C. Majkrzak and T. O'Brien, *Journal of Applied Physics*, **63** (1988) 3453
11. H. U. Åstrom, J. Nogues, G.K. Nicolaides, K. V. Rao and G. Benediktson, *Journal of Physics: Condensed Matter*, **3** (1991) 7395-7402
12. S. W, Zochowski and K. A. McEwen, *Journal of Magnetism and Magnetic Materials*, **104-107** (1992) 1515-1516
13. J. A. Fernandes-Baca, R. M. Nicklow and J. J. Rhyne, *Journal of Applied Physics*, **67** (1990) 5283-5285
14. S. Legvold, *Ferromagnetic Materials*, Vol. **1**, edited by E.P. Wohlfarth (Amsterdam: North-Holland, 1980), p. 183
15. M. Salamon, S.Sinha, J. Ryne, J. Cunningham, R.Erwin, J. Borchers and C. Flynn, *Phys. Rev. Lett.* **56** (1986) 259
16. R. A. Cowley, J. A. Simpson, R. C. C. Ward, M. R. Wells and D. F. McMorrow, *J. Phys.:Condens. Matter* **10** (1998) 2115-2124
17. J. Jensen and A. Mackintosh, *Rare Earth Magnetism* (Oxford Science Publications, 1991) p. 17

18. M. Baibich, J. Broto, A. Fert, F. Nguyen Van Dau, F. Petroff, P. Eitenne, G. Creuzet, A. Friederich and J. Chazelas, *Phys. Rev. Lett.* **61** (1988) 2472
19. A. Modak, D. Smith and S. Parkin, *Phys. Rev.* B **50** (1994) 4232
20. G. Binasch, P. Grünberg, F. Saurenbach and W. Zinn, *Phys. Rev. B* **39** (1989) 4828
21. B. Dieny, V. Speriosu, S. Metin, S. Parkin, B. Gurney, P. Baumgart and D. Wilhoit, *J. Appl. Phys* **69** (1991) 4774
22. H. Fujiwara and M. Parker, *J. Magn. Magn. Matter* **135** (1994) L23
23. P. Eitenne, J. Chazelas, G. Creuzet, A. Friederich, J. Massies, F. Nguyen-Van-Dau and A. Fert, *Journal of Crystal Growth* **95** (1989) 410
24. P. Levy, K. Ounadjela, S. Zhang, Y. Whang, C. Sommers and A. Fert, *J. Appl. Phys*. **67** (1990) 5914
25. S. Parkin, N. More and K. Roche, *Phys. Rev. Lett.* **64** (1990) 2304
26. D. Mosca, F. Petroff, A. Fert, P. Schroeder, W. Pratt Jr. and R. Laloee, *J. Magn. Magn. Mater.* **94** (1991) L1
27. S. Parkin, R. Bhadra and K. Roche, *Phys. Rev. Lett.* **66** (1991) 2152
28. A. Fuß, S. Demokritov, P. Grünberg and W. Zinn, J. Magn. Magn. Mater. **103** (1992) L221
29. J. Kwo, E. M. Gyorgy, D.B. McWhan, M. Hong, F. J. DiSalvo, C. Vettier and J. E. Bower, *Phys. Rev. Lett.*, **55**, 1402
30. J. Kwo, M. Hong, F. DiSalvo, J. Waszczak and C. Majkrzak, *Phys. Rev. B*, **35** (1987) 7295
31. C. Majkrzak, J. Cable, J. Kwo, M. Hong, D. McWhan, Y. Yafet, J. Waszczak and C. Vettier, *Phys. Rev. Lett.* **56** (1986) 2700
32. Z. Tun, W. Buyers, I. Swainson, M. Sutton and R. Cochrane, *J. Appl. Phys.* **76** (1994) 7075
33. F. Petroff, A. Barthélemy, D. Mosca, D. Lottis, A. Fert, P. Schroeder, W. Pratt Jr., R. Loloee and S. Lequien, *Phys. Rev. B* **44** (1991) 5355
34. W. Bennett, W. Schwarzacher and W. Egelhoff, Jr, *Phys. Rev. Lett.* **65** (1990) 3169
35. P. Grünberg, R. Schreiber and Y. Pang, M. Brodsky and H. Sowers, *Phys. Rev. Lett.* **57** (1986) 2442
36. Z. Qiu, J. Pearson and S. Bader, *Phys. Rev. B* **46** (1992) 8659
37. P. Bruno, *Europhys. Lett.*, **23** (1993) 615

38. J. Barnas, *J. Magn. Magn. Matter*, **128** (1994) 171
39. P. Bloemen and M. van de Vorst, *J. Appl. Phys.* **76** (1994) 7081
40. P. Bloemen, M. Johnson, M. van de Vorst, R. Coehoorn, J. de Vries, R. Jungblut, J. aan de Stegge, A. Reinders and W. de Jonge, *Phys. Rev. Lett.* **72** (1994) 764
41. S. Okuno and K. Inomata, *Phys. Rev. Lett.* **72** (1994) 1553
42. L. Zhou, Z. Zhang, P. Wigen and K. Ounadjela, *J. Appl. Phys.* **76** (1994) 7078
43. J. Borchers, S. Sinha, M. B. Salamon, R. Du, C. P. Flynn, J. J. Rhyne and R. W. Erwin, *J. Appl. Phys* **61** (1987) 4049
44. R. W. Erwin, J. J. Rhyne, M. B. Salamon, J. Borchers, S. Sinha, R. Du, J. E. Cunningham and C. P. Flynn, *Phys Rev. B* **35** (1987) 6808
45. M. Hong, R. M. Fleming, J. Kwo, L. F. Schneemyer, J. V. Waszczak, J. P. Mannaerts, C. F. Majkrzak, D. Gibbs and J. Bohr, *J. Appl. Phys.* **61** (1987) 4054
46. R. W. Erwin, J. J. Rhyne, J. Borchers, R. Du, M. B. Salamon and C. P. Flynn, *Physica B*, **161** (1989) 260
47. J. J. Rhyne, R. W. Erwin, J. Borchers, S. Sinha, M. B. Salamon, , R. Du and C. P. Flynn, *J. Appl. Phys.* **61** (1987) 4043
48. W. C. Koehler, J. W. Cable, M. K. Wilkinson, and E. O. Wollan, *Phys. Rev.* **151** (1966) 414
49. W. C. Koehler, J. W. Cable, H. R. Child, M. K. Wilkinson, and E. O. Wollan, *Phys. Rev.* **158** (1967) 450
50. G. P. Felcher, G. H. Lander, T. Arai, S. K. Sinha and F. H. Spedding, *Phys. Rev. B* **13** (1976) 3034
51. D. Gibbs, D. E. Moncton, K. L. D'Amico, J. Bohr and B. H. Grier, *Phys. Rev. Lett.* **55** (1985) 234
52. J. Bohr, D. Gibbs, D. E. Moncton and K. L. D'Amico, *Physica A,* **140** (1986) 349
53. J. Bohr, D. Gibbs, J. D. Axe, D. E. Moncton, K. L. D'Amico, C. F. Majkrzak, J. Kwo, M. Hong, C. Chien and J. Jensen *Physica B,* **159** (1989) 93
54. R. A. Cowley and S. J. Bates, *J. Phys C*, **21** (1988) 4113
55. J. W. Cable, E. O. Wollan, W. C. Koehler and M. K. Wilkinson, *Phys. Rev.* **140** (1965) 1896
56. D. Gibbs, J. Bohr , J. D. Axe, D. E. Moncton and K. L. D'Amico, *Phys. Rev. B.* **34** (1986) 8182
57. M. Habenschuss, C. Stassis, S. K. Sinha, H. W. Deckman and F. H. Spedding *Phys. Rev.* , **10** (1974) 1010

58. R. W. Erwin, J. J. Rhyne, J. Borchers, R. Du, M. B. Salamon, R. Du and C. P. Flynn, *J. Phys. B*, 49 (1988) 260

59. T. O. Brun, S. K. Sinha, N. Wakabayashi, G. H. Lander, L. R. Edwards and F. H. Spedding, *Phys. Rev. B* **1** (1970) 1251

60. G.L. Squires, *Introduction to the theory of Thermal Neutron Scattering*,(1997) Dover, p2.

61. G. L. Squires, *Introduction to the theory of Thermal Neutron Scattering*,(1997) Dover, p5.

62. D. A. Jehan, D. F. McMorrow, R. A. Cowley, R. C. C. Ward, M. R. Wells, N. Hagmann and K. N. Clausen, Physical Review B, 48 (1993) 5594-5606

63. VSM documentation by Oxford Instruments

64. *The International Tables for Crystallography*, edited by U. Shmueli, (Kluwer Academic Publishers, The Netherlands, 1995) Vol. C

65. G.L. Squires, Introduction to the theory of Thermal Neutron Scattering,(1997) Dover, p34.

66. C. P. Flynn, *J Phys F* **18** L195 1988

67. R. C. C. Ward and M. R. Wells (private communication)

68. G. J. Tomka, P. A. de Groot, B. D. Rainford, M. R. Wells, R. C. C. Ward and A. del Moral, *J. Magn. Magn. Mater.* **140-144** (1995) 777.

69. G. J. Tomka, B. D. Rainford, P. A. de Groot, M. Ciria, R. C. C. Ward and M. R. Wells, *J. Magn. Magn. Mater.* **156** (1996) 431.

70. William H. Press, *Numerical Recipes,* Cambridge University Press (1993)

71. J. A. Osborn, *Phys. Rev.* **67** (1945) 351

72. G. J. Tomka, P. A. de Groot, B. D. Rainford, M. R. Wells, R. C. C. Ward and J. I. Arnaudas, *J. Magn. Magn. Mater.* **140-144** (1995) 785.

73. C. J. T. Wilkins, B. D. Rainford, J. P. Goff,R. C. C. Ward, M. R. Wells, D. F. McMorrow and G. I. McIntyre, *J. Magn. Magn Mater.* **199** (1999) 509-512

74. M. Sawicki, C. J. T. Wilkins, P. A. J. de Groot, B. D. Rainford, M. R. Wells and R. C. C. Ward, *J. Magn. Magn Mater.* **199** (1999) 98-100

75. J. P. Goff, R. S. Sarthour, C. Micheletti, S. Langridge, C. J. T. Wilkins, R. C. C. Ward and M. R. Wells, *J. Magn. Magn Mater.* **199** (1999) 309-311

76. J. P. Goff, R. S. Sarthour, D. F. McMorrow, B. D. Rainford, C. J. T. Wilkins, R. C. C. Ward, M. R. Wells, *Physica B* **241** (1997) 714-716

77. J. Jensen and A. Mackintosh, *Rare Earth Magnetism* (Oxford Science Publications, 1991) p. 77

78. J. Jensen and A. Mackintosh, *Rare Earth Magnetism* (Oxford Science Publications, 1991) p. 46, Eq. 1.4.20

79. W. C. Koehler, J. W. Cable, E. O. Wollan and M. K. Wilkinson, Phys. Rev. **126** (1962) 1672